Theories of Experimentally Observed Excitation Spectra of Square Lattice Antiferromagnets

THÈSE N^{O} 6090 (2014)

PRÉSENTÉE LE 28 MARS 2014

À LA FACULTÉ DES SCIENCES DE BASE
LABORATOIRE DE MAGNÉTISME QUANTIQUE
PROGRAMME DOCTORAL EN PHYSIQUE

ÉCOLE POLYTECHNIQUE FÉDÉRALE DE LAUSANNE

POUR L'OBTENTION DU GRADE DE DOCTEUR ÈS SCIENCES

PAR

Bastien DALLA PIAZZA

acceptée sur proposition du jury:

Prof. O. Schneider, président du jury
Prof. H. M. Rønnow, Dr D. Ivanov, directeurs de thèse
Prof. C. L. Broholm, rapporteur
Prof. F. Mila, rapporteur
Prof. S. Sorella, rapporteur

ÉCOLE POLYTECHNIQUE
FÉDÉRALE DE LAUSANNE

Suisse
2014

Acknowledgements

My first thanks go to my supervisor Prof. Henrik Rønnow for welcoming me in his group the Laboratory for Quantum Magnetism. Throughout all my PhD, Henrik has been a constant source of inspiration and wonder, especially for his incredible creativity and purposeful questioning. While I was easily caught into intricate nets of barely controlled theoretical technicalities, he would always point out at the greater picture and, through apparently innocent questions, shatter the crumbling mess of the inadequate concepts I was trapped in.

I am also greatly indebted to Dr. Dmitri Ivanov who, during the second part of my thesis, acted as a co-supervisor before becoming formally one in the end. As a theoretically oriented student in an otherwise experimental group, the support from Dima has been essential to build the theoretical work presented in the first part of this thesis.

At the start of my PhD where I was still balancing between theory and experiments, I had the great pleasure to accompany Marco Guarise to Resonant Inelastic X-ray Scattering experiments. I want to thank Marco and his former supervisor Prof. Marco Grioni for giving me the opportunity to participate to these fascinating experiments.

I am extremely grateful to all the members and former members of the Laboratory for Quantum Magnetism for the friendly atmosphere and great coffee breaks. Among those, I am especially indebted to Martin Mourigal who helped me a lot getting started in spin-wave theory. I am grateful to Neda Nikseresht and Julian Piatek to let me have first hand experience of Neutron scattering, taking the risk that I would ruin it all, which in some times I did. These experiences let me appreciate how intricate and complex the experimental setups are and how remarkable it is that accurate experimental data may be acquired.

I am very grateful to the members and former members of the Chair of Condensed Matter Theory Tommaso Coletta, Frédéric Michaud, Tamas Toth and to Prof. Frédéric Mila for fruitful theoretical discussions.

Je tiens également à remercier mes parents Anne et Aldo ainsi que mes frères et soeurs Jonas, Joëlle et Thomas pour leur soutien et leur affection. Ces années de thèse auraient été bien ternes sans mes amis et colocataires Romuald Curdy, Karine et Dominique Julsaint-Nussbaum, Patrice Soom, Sacha et Michaël Hertig-Trotsenko, Xuan et Jean-Marie Droz, Yoann Pfluger, Sami Gocke, Alice Bürckel et Anouk André.

Finalement, je tiens à exprimer toute ma reconnaissance à ma femme Céline à qui je dédie ma thèse.

Lausanne, February 18, 2014 B. D. P.

Abstract

The first part of this thesis presents the theoretical study of an anomaly of unknown origin in the excitation spectrum of the Quantum spin-1/2 Heisenberg Square lattice Anti-Ferromagnet. The anomaly manifests itself in Inelastic Neutron Scattering data for short wavelength/high energy excitations. Instead of the expected sharp semi-classical harmonic modes, a broad continuum emerges suggesting the possibility of fractionalized excitations. A theoretical framework based on the Gutzwiller projection is developed and allows to link the observed continuum to *unbound* fractional quasiparticle pairs while the sharp harmonic excitations may be described by *bound* ones.

The second part of this thesis presents the detailed theoretical modeling of the spin-wave dispersion relation measured in insulating cuprate materials. Starting from the one-band Hubbard model with extended hopping amplitudes, an effective low-energy theory is derived allowing to describe on the same footing different insulating cuprate magnetic excitation spectra. The effective theory is fitted against experimental data and microscopic model parameters are extracted. The high level of details included in our effective theory allows a consistent characterization of the studied materials as measured by various magnetic or electronic experimental techniques.

Keywords : Quantum magnetism, square lattice antiferromagnet, spin-waves, fractionalization, insulating parent compounds (cuprate superconductors).

Résumé

La première partie de cette thèse présente l'étude théorique d'une anomalie d'origine inconnue trouvée dans le spectre des excitations magnétiques de l'anti-ferro-aimant de spin-1/2 sur le réseau carré. L'anomalie se manifeste dans les données provenant d'expériences de diffusion de neutron inélastique pour les excitations de courte longueur d'onde et de haute énergie. En lieux et place des excitations harmoniques discrètes attendues, un continuum émerge suggérant la possible présence d'excitations fractionnelles. Une théorie basée sur la projection de Gutzwiller est développée. Elle permet de lier le continuum observé à l'émergence de paires non-liées de quasi-particules fractionnaires alors que les excitations harmoniques conventionnelles sont reproduites par des paires liées.

La seconde partie de cette thèse présente la modélisation détaillée de la dispersion des ondes de spin mesurée dans une sélection de matériaux isolants de la famille des cuprates. En partant d'un modèle de Hubbard à une bande incluant des amplitudes de saut étendues, une théorie effective de basse énergie est dérivée permettant de décrire les différents spectres d'excitations magnétiques des cuprates isolants sélectionnés. La théorie effective est ajustée de façon à correspondre aux données expérimentales et les paramètres du modèle microscopique sont extraits. Le haut niveau de détails inclus dans la théorie effective permet une caractérisation cohérente des matériaux étudiés, tels que mesurés par différentes techniques de mesures magnétiques ou électroniques.

Mot-clés : Magnétisme quantique, antiferroaimant sur réseau carré, ondes de spin, fractionalisation, composés isolants parents (superconducteurs cuprates)

Contents

Abbreviations

ARPES Angle-Resolved Photo-Emission Spectroscopy. 4, 30, 82, 88–90, 92–95, 106, 128, 131, 136–138, 144

BLAS Basic Linear Algebra Subroutines. 53, 168

BSYCO $Bi_2Sr_2YCu_2O_8$. 20, 89, 126, 129–132, 137, 138, 144

CFTD $Cu(DCOO)_2 \cdot 4D_2O$. 6, 20–23, 61

CSCS Swiss National Supercomputing Center. 53, 168

DO Double Occupancy. 100, 101

INS Inelastic Neutron Scattering. 5, 6, 22–24, 88, 89, 95–97, 123, 124, 126, 127, 130, 136, 142, 144

LCO La_2CuO_4. 6, 20, 21, 88, 89, 126, 129, 130, 132, 138–140, 144

MBZ Magnetic Brillouin Zone. 36, 46, 66

MBZB Magnetic Brillouin Zone Boundary. 20–23, 61, 65

MPI Message Passing Interface. 53, 168

QHSAF Quantum spin-1/2 Heisenberg Square lattice Anti-Ferromagnetic model. 5, 19, 20, 22, 25–27, 83

QSL Quantum Spin Liquid. 5, 54, 56, 65, 66, 70, 74, 80

RIXS Resonant Inelastic X-ray Scattering. 88–90, 97–99, 127, 129–131, 136, 138, 139, 141–144

RMS Root Mean Square. 77, 78

RPA Random Phase Approximation. 34, 97

RVB Resonating Valence Bonds. 5, 30, 33, 70, 71, 82, 85

SCOC $Sr_2CuO_2Cl_2$. 6, 20, 89, 126, 130–132, 134, 137, 138, 141–144

SF Staggered Flux. 31, 33, 55–58, 62, 66, 68, 70, 73–75, 78, 80, 81

SF+N Staggered Flux plus Néel. 34, 36, 37, 41, 43, 48, 53–59, 62, 66, 72, 74, 75, 80, 81

SWT Spin Wave Theory. 5–7, 14, 19–23, 25, 28, 34, 54, 56, 58, 59, 61, 63, 67, 68, 70, 80, 81, 88, 89

VMC Variational Monte Carlo. 38, 39, 46, 49, 51, 55, 58, 68

1 Introduction

This thesis is divided into two main chapters which correspond to originally separated projects. The two topics broadly relate to the square lattice antiferromagnet, and more precisely to its excitation spectrum as measured by different techniques. I nonetheless felt it would be artificial to shape the two topics into a single one. I thus chose to present the two topics separately in their dedicated chapters.

It then falls upon this introduction to provide some link between these chapters. A strong link is contained first into the scientific approach which gave birth to these works. Both topics were motivated by prior experimental results on specific materials which raised questions about their theoretical interpretation. It just so happened that the materials considered were all realizations of the square lattice antiferromagnet. Of course calling this a coincidence is an exaggeration. Indeed the magnetic properties of the square lattice antiferromagnet is one of the fundamental problems of the quantum magnetism research domain and, in a broader context, a possible key-ingredient into the still controversial high temperature superconductivity problem. The mentioned experimental results allowed to characterize with unprecedented accuracy the magnetic excitation spectrum, which then required a detailed theoretical modeling.

While the two topics share many aspects, they also represent different complementary piece of work of scientific research. The first topic in chapter 2 studies theoretically the fundamental Heisenberg model for which a variety of physical realizations exists. The emphasis is on developing original theoretical methods and using those to extract some fundamental properties of this model, hopefully improving its understanding. On the other hand the second topic in chapter 3 is geared towards using established theoretical tools in order to give a detailed theoretical characterization of materials. The emphasis there is on reaching a high level of detail in existing theories in order to allow a quantitative interpretation of experimentally measured quantities. This quantitative analysis then allows comparison across different experimental techniques helping to build an overall consistent experimental picture.

The occurrence of these two approaches in a single thesis is reminiscent of the position which was mine in the Laboratory for Quantum Magnetism. As a theoretically oriented student in an otherwise experimental laboratory, it often fell on me to provide some simple “first order ” theoretical description, using conventional theoretical tools such as the mean-field approximation, or spin-wave theory. Upon the success or failure of such simple approach, more sophisticated approach could be undertaken. In the case of the first project in chapter 2, the established failure of spin-wave theory to capture some striking aspects of measurements lead into undertaking a completely different theoretical approach. On the other hand the relative success of spin-wave theory in the context of the second project in chapter 3 lead into refining it accounting for fine details of specific materials. Overall I believe the two projects make for an equilibrated picture of what has been my work as a theorist in the Laboratory for Quantum Magnetism.

2 Variational Study of the Square Lattice Antiferromagnet Magnetic Zone-Boundary Anomaly

2.1 Introduction

A constant trend in modern physics has been the prediction and experimental validation of the existence of hidden degrees of freedom found in nature. Coincidentally a perfect illustration is the 2013 physics Nobel price rewarding the theoretical prediction of the Higgs boson following its experimental validation at CERN's Large Hadron Collider (LHC). While the discoveries of such hidden degrees of freedom have most often been accomplished by carrying out experiments in extraordinarily high energy regimes, it is tempting to put it in parallel with the phenomenon known as *emergence* found in condensed matter physics at comparatively extremely low energy scales. The constituents of any condensed matter physics system are by definition the building blocks of cold matter: nuclei and electrons. The energy scale at which such systems are considered is adequately set by the thermal motion energy at room temperature of 25meV, 14 orders of magnitude less than the collisions produced in the LHC. At such low energies, the hidden degrees of freedom found for instance in the nucleus are invisible. There are nevertheless hidden degrees of freedom which *emerge* in such systems but only when regarding it as a whole, strongly interacting indivisible set of particles. In such cases there have been many observations of new degrees of freedom characterized as *fractional* as they can only be described as fractions of the degrees of freedom found in the system in its non-interacting limit. Perhaps the most iconic example is the spin-charge separation [Lieb and Wu, 1968] in quasi-1D electronic systems. The low-energy excitations can be characterized by quasi-particles carrying either a charge degree of freedom (holon) or a spin degree of freedom (spinon). But for the particles constituting the non-interacting system – the electrons – the charge and spin degrees of freedom are indivisible. Angle-Resolved Photo-Emission Spectroscopy (ARPES) experiments could observe this spin-charge separation [Kim et al., 1996]. In the removal of an electron through the photoemission process, the spin-1/2 charge $+e$ hole left in the system can thus be understood as a bound state of a holon and a spinon which, due to the special nature of 1D physics, deconfine into two truly independent degrees of freedom.

In the area of quantum magnetism, the prototypical emergent degree of freedom is the fractional spin-1/2 quasiparticle often called *spinon*. Taking a system of non-interacting spin-1/2 degrees of freedom, the fundamental spin deviation is to flip a spin for instance from $S = -1/2$ to $S = 1/2$, corresponding to a $\Delta S = 1$ excitation. But in an interacting system, spin-1/2 excitations are known to emerge such that, in a similar fashion as in the spin-charge separation phenomenon, a $\Delta S = 1$ excitation deconfines into two unbound fractional spin-1/2 quasiparticles. The deconfinement of fractional spin-1/2 quasi-particle has been exactly predicted [Faddeev and Takhtajan, 1981; Müller et al., 1981] and experimentally observed [Tennant et al., 1995; Lake et al., 2005; Mourigal et al., 2013] in 1D systems. In higher dimensions, the theoretical characterization of deconfined fractional quasi-particle excitations and their experimental observation is an ongoing challenge [Balents, 2010] with the most prominent candidates being the frustrated triangular lattice [Coldea et al., 2001b] and the kagomé lattice [de Vries et al., 2009; Han et al., 2012; Jeong et al., 2011] antiferromagnets. These systems are characterized by a strong magnetic frustration – the impossibility to minimize classically a set of conflicting

interaction energies – which is a key feature favoring non-magnetic groundstates composed of highly correlated fluctuating spins called Quantum Spin Liquid (QSL). So far fractional excitations have been searched for in systems where the groundstate was thought to be such a QSL or very close to it. In contrast we take in this work another route and look at the *unfrustrated* square lattice antiferromagnet.

The Quantum spin-1/2 Heisenberg Square lattice Anti-Ferromagnetic model (QHSAF) groundstate has a spontaneously broken spin symmetry which exhibits a finite staggered magnetization comparable to the classical Néel order state where each neighboring spins point in opposite directions. Despite the existence of a classical order parameter attached to it, the groundstate also contains large quantum fluctuations around the classical Néel state which reduces the staggered magnetization to 62% of its classicla value[Reger and Young, 1988; Hamer et al., 1992]. The low energy excitations are well described by fluctuations of the ordered spins either in the *transverse* or *longitudinal* directions with respect to the ordering axis. These excitations can be adequately derived by the Spin Wave Theory (SWT) approximation [Bloch, 1930; Anderson, 1952; Kubo, 1952]. The transverse excitations are found to be dominantly spin-1 bosonic modes called magnons with crystal momentum $\boldsymbol{q}$ and the longitudinal ones spin-0 weakly interacting pairs of magnons. In the SWT approximation a weak magnon-magnon interaction arises which can be treated perturbatively. The small parameter is $1/S$, where S is the spin quantum number of the magnetic sites. In the spin-1/2 case, we are thus in the strongest interacting limit of SWT and it remains a question whether the perturbative treatment of the magnon-magnon interaction is appropriate, as hinted by the slowly, if at all, convergent quantum corrections to the magnon energy for the specific momentum $\boldsymbol{q} = (\pi, 0)$[Syromyatnikov, 2010].

While there is a strong consensus for the groundstate of the square lattice Heisenberg antiferromagnet to be Néel ordered, the nature of its quantum fluctuations is much less clear. An alternate proposal is the so-called Resonating Valence Bonds (RVB) state, a superposition of various lengths' singlets arrangements on the lattice. The RVB state is a prototypical QSL first proposed as a possible ground state of the triangular lattice antiferromagnet [Anderson, 1973]. Interest for this state arose dramatically following the discovery of high-temperature superconductivity in the cuprate materials. In the generic cuprate phase-diagram (see for instance fig. 3.2), the small doping necessary to destroy the antiferromagnetic order suggests that QSL states such as the RVB state might be very close to the Néel ordered groundstate [Anderson, 1987]. Analytical work of the RVB state elementary excitations showed that they can be described as fractional fermionic [Hsu, 1990; Ho et al., 2001] or bosonic [Auerbach and Arovas, 1988] quasi-particles. The possibility thus exists that, even for a Néel ordered groundstate, the square lattice Heisenberg antiferromagnet retains fractional excitations for some specific momenta.

Experimentally, the SWT predictions proved to be accurate, even in the spin-1/2 case. The Inelastic Neutron Scattering (INS) technique in particular could unambiguously characterize both the instantaneous [Greven et al., 1995; Birgeneau et al., 1999; Rønnow et al., 1999] and the low-energy/long wavelength dynamical [Yamada et al., 1989] properties of the square lattice Heisenberg antiferromagnet in excellent agreement with SWT. Due to their importance for

high-temperature superconductivity, experiments focused at first on the cuprate insulating parent compounds La_2CuO_4 (LCO)[Birgeneau et al., 1999; Yamada et al., 1989] or $Sr_2CuO_2Cl_2$ (SCOC)[Greven et al., 1995]. These compounds have the technical disadvantage that the magnetic interaction energy is rather large $J \sim 1500K$ which makes it difficult for INS to probe the top of the magnon dispersion relation. INS measurements carried out on the much lower energy model material $Cu(DCOO)_2 \cdot 4D_2O$ (CFTD)[Rønnow et al., 2001] systematically evidenced important deviations from SWT found at the high energy/small wavelength part of the magnon dispersion [Rønnow et al., 2001; Christensen et al., 2007]. More precisely, these deviations happen for momenta $\boldsymbol{q}$ on the magnetic Brillouin zone boundary $|\boldsymbol{q}| = \pi$ and are hereafter mentioned as the magnetic zone boundary quantum anomaly. The anomaly has more recently been found to exist in La_2CuO_4[Headings et al., 2010]. In particular, a key-feature is the observation of a continuum of excitations found at the momentum $\boldsymbol{q} = (\pi, 0)$, in strong contrast with the SWT predictions. A possible interpretation of this unexpected feature is that the states constituting the continuum correspond to different pairs of fractional excitations. In the following work, we use a combination of analytical and numerical calculations to provide a new theoretical description of the high energy/small wavelength excitations of the square lattice Heisenberg antiferromagnet in terms of *bound* or *unbound* fractional spin-1/2 particles pair and compare it to newly available polarized inelastic neutron scattering results.

2.1.1 Overview

We provide here as bullet points a quick overview of this study, pointing to the dedicated sections for additional details.

– **Experimental status:** There are many physical realizations of the square lattice antiferromagnets (see section 2.3). The CFTD material is one of those with the distinct advantage of the energy scale being the most favorable for thermal neutron scattering. This allowed an accurate determination of the excitation spectrum to first order well accounted for by SWT (see section 2.4.1). However with respect to SWT, a glaring anomaly appears at the short wavelength/high enery part of the magnetic excitation spectrum (see section 2.3.1). The anomaly appears for the $\boldsymbol{q} = (\pi, 0)$ momentum of the Brillouin zone of unit length 2π. It is characterized by a reduction of 7% of the $\boldsymbol{q} = (\pi, 0)$ magnon energy with respect to $\boldsymbol{q} = (\pi/2, \pi/2)$, a dramatic loss of intensity of the main magnon peak and the development of a continuum of excitations extending to higher energies from the main magnon peak. In strong contrast, the $\boldsymbol{q} = (\pi/2, \pi/2)$ magnetic spectrum stays sharp indicative of a long-lived single-particle excitation.

– **Postulate and theoretical framework:** We postulate that the observed continuum might be a manifestation of fractional quasiparticle deconfinement happening in the vicinity of the $\boldsymbol{q} = (\pi, 0)$ momentum. To tackle theoretically this idea, we start from the Heisenberg model written in the fermionic operators (see section 2.4.2) which we treat using a mean-field decoupling (see section 2.4.3). The obtained mean-field groundstate contains double occupancies which are not part of the original physical Hilbert space associated with the Heisenberg model. We thus consider the Gutzwiller-projected mean-field groundstate

$P_G \left|\psi_{\mathrm{MF}}\right\rangle$ as a trial wavefunction for the Heisenberg model groundstate depending on two variational parameters, one being the so-called flux θ_0 and the other the Néel order (see section 2.4.6).

– **Numerical evalutation of the projected mean-field wavefunction:** Using variational Monte Carlo (see section 2.5), we optimize the variational energy obtained by varying the projected mean-field wavefunction parameters and consider only two distinct trial wavefunctions, the Néel ordered $|\mathrm{SF}+\mathrm{N}\rangle$ and the spin liquid $|\mathrm{SF}\rangle$ wavefunctions (see section 2.7.1). The $|\mathrm{SF}+\mathrm{N}\rangle$ state has the best variational energy but exponentially decaying transverse spin correlations which is inconsistent with the robust SWT prediction of algebraic decay. On the other hand the $|\mathrm{SF}\rangle$ state has a higher variational energy, no magnetic order but a consistent algebraic decay of the transverse spin correlations.
– **Construction of variational magnetic excitations:** Using either the $|\mathrm{SF}+\mathrm{N}\rangle$ or $|\mathrm{SF}\rangle$ trial wavefunctions, we construct the magnetic excitations as projected particle-hole pairs (see section 2.6.1). Defining $\gamma^{\dagger}_{\boldsymbol{k}\sigma b}$ and $\gamma_{\boldsymbol{k}\sigma b}$ the creation and annihilation operators diagonalizing the mean-field Hamiltonian, $\boldsymbol{k}$ being the momentum, σ the spin and $b \in \{+,-\}$ a band index, the projected particle-hole pairs

$$\left|\boldsymbol{k},\sigma\sigma',\boldsymbol{q}\right\rangle = P_G \gamma^{\dagger}_{\boldsymbol{k}\sigma+} \gamma_{\overline{\boldsymbol{k}-\boldsymbol{q}}\sigma'-} \left|\psi_{\mathrm{MF}}\right\rangle \tag{2.1.1}$$

span a subspace of magnetic excitations on which we numerically project the Heisenberg model (see section 2.6.2). We then diagonalize the projected Heisenberg model obtaining projected particle-hole eigenstates which allow to calculate the dynamic spin structure factor (see section 2.6.4).
– **Dynamic structure factor for the trial wavefunctions:** The two different trial wavefunctions $|\mathrm{SF}+\mathrm{N}\rangle$ and $|\mathrm{SF}\rangle$ give a complementary picture of the experimentally observed anomaly (see section 2.7.2). The former recovers the magnon dispersion with the 7% reduction of the energy but shows no continuum. The latter develops a strong continuum at $\boldsymbol{q} = (\pi, 0)$ in strong contrast with $\boldsymbol{q} = (\pi/2, \pi/2)$ where the magnetic excitation spectrum stays sharp as seen in experiments.
– **Fractional quasiparticle deconfinement:** With the complete knowledge of the projected particle-hole excitation eigenstates, we develop quantities to characterize the degree of fractional quasiparticle deconfinement (see section 2.8.3 and 2.8.4). We find that for the $|\mathrm{SF}+\mathrm{N}\rangle$ trial wavefunction, the magnetic spectrum corresponds to *bound* pairs of fractional quasiparticles recovering the conventional magnon excitation. On the other hand for the $|\mathrm{SF}\rangle$ trial wavefunction, we find that the continuum of excitations corresponds to *unbound* fractional quasiparticle pairs (see section 2.8.5).

2.1.2 The Heisenberg Model

The Heisenberg model is the foundation of the quantum magnetism physics field. It is a very general model describing magnetic interacting systems which can arise as the effective

low-energy description of many strongly correlated electron systems. It is simply written as

$$\mathscr{H} = \frac{1}{2}\sum_{i,j} J_{ij}\boldsymbol{S}_i \cdot \boldsymbol{S}_j \tag{2.1.2}$$

where i, j index sites with a magnetic degree of freedom characterized by a quantum spin S, J_{ij} is the magnetic coupling energy and $\boldsymbol{S}_i$ are the spin operator vectors as defined below. The magnetic degree of freedom of a site can be any of the $2S+1$ states:

$$\{|m=-S\rangle, |m=-S+1\rangle, \ldots, |m=S-1\rangle, |m=S\rangle\}. \tag{2.1.3}$$

The Hilbert space can be generated by the ladder operators $\{S^+, S^-\}$

$$S^+|m\rangle = \sqrt{S(S+1)-m(m+1)}\,|m+1\rangle \tag{2.1.4}$$

$$S^-|m\rangle = \sqrt{S(S+1)-m(m-1)}\,|m-1\rangle. \tag{2.1.5}$$

It is customary to regroup these spin operators in a vector whose quantum average represents the magnetic dipole moment of the site:

$$\boldsymbol{S} = \begin{pmatrix} S^x \\ S^y \\ S^z \end{pmatrix} \tag{2.1.6}$$

with

$$S^x = \frac{1}{2}\left(S^+ + S^-\right) \tag{2.1.7}$$

$$S^y = \frac{1}{2i}\left(S^+ - S^-\right) \tag{2.1.8}$$

$$S^z = \frac{1}{2}\left(S^+S^- - S^-S^+\right) \tag{2.1.9}$$

The Hilbert space for N sites is spanned by the basis states that we will hereafter call real space spin configuration:

$$\Omega_{\mathrm{H}} = \{|m_1, \ldots, m_N\rangle\} \qquad m_i \in \{-S, \ldots, S\}. \tag{2.1.10}$$

Compared to other many-body quantum states, the magnetic sites are distinguishable thus there is no redundancy in the state labeling eq. 2.1.10.
The Heisenberg model will arise as the effective theory of electronic systems. We first note that the only magnetic interaction for electrons as described by electrodynamics is the weak dipole-dipole interaction which would couple the electron intrinsic magnetic moment and angular momentum. Unlike the magnetic coupling J_{ij} in eq. 2.1.2, this interaction is highly

anisotropic as characterized by the dipole-dipole tensor $\overline{D}(\boldsymbol{r})$:

$$\mathscr{H}_{D-D} = \sum_{ij} \boldsymbol{S}_i^T \overline{D}(\boldsymbol{r}_2 - \boldsymbol{r}_1) \boldsymbol{S}_j \tag{2.1.11}$$

$$\overline{D}^{\alpha\beta}(\boldsymbol{r}) \propto \frac{r_\alpha r_\beta - \delta_{\alpha\beta}|\boldsymbol{r}|^2}{|\boldsymbol{r}|^5}. \tag{2.1.12}$$

In most materials this coupling can be safely neglected especially for low-spin systems where the magnitude of this interaction is very small. The Heisenberg model therefore does not arise from a bare magnetic electron-electron interaction but as an effective theory. We give below two examples.

The Heitler-London Method

The Heitler-London method was developed in the context of the covalent molecular bonding theory. We consider only two "sites", for instance the two protons held fixed of an H_2 molecule. Labeling the sites a and b we only consider one orbital state per site $|a\rangle$ and $|b\rangle$ and a separation of $\boldsymbol{R}_{ab}$ between the two sites. We study the 2-electrons problem. The Hamiltonian only contains the electron kinetic energy and the Coulomb repulsion. The spin degree of freedom of the electron does not enter the Hamiltonian at all. If the two sites are held at a very large distance, the orbital states become eigenstates of the single electron problem:

$$H_{\boldsymbol{R}_{ab}\to\infty}|a,\sigma\rangle = E_0|a,\sigma\rangle \tag{2.1.13}$$

$$H_{\boldsymbol{R}_{ab}\to\infty}\left|b,\sigma'\right\rangle = E_0\left|b,\sigma'\right\rangle \tag{2.1.14}$$

where σ and σ' label the electron spins. In this limit, the $|a,\sigma\rangle$ and $\left|b,\sigma'\right\rangle$ states are orthogonal regardless of their spin σ and σ'. Defining the electron i position-spin coordinate $(\boldsymbol{r}_i, s_i) = \boldsymbol{x}_i$, the two-electron anti-symmetrized states are given by the Slater determinant:

$$\psi^{\sigma\sigma'}(\boldsymbol{x}_1,\boldsymbol{x}_2) = \begin{vmatrix} \langle \boldsymbol{x}_1|a,\sigma\rangle & \langle \boldsymbol{x}_2|a,\sigma\rangle \\ \left\langle \boldsymbol{x}_1\right|b,\sigma'\rangle & \left\langle \boldsymbol{x}_2\right|b,\sigma'\rangle \end{vmatrix}, \tag{2.1.15}$$

where we have omitted the (two) polar states where the two electrons sit on the same site with opposite spin. We now turn towards the finite $\boldsymbol{R}_{ab}$ limit. As the Hamiltonian has no explicit spin dependence, it will be possible to factorize the total wavefunction into a spatial and a spin part. In the following we will consider only the spatial part in a first step and will introduce the spin part and the antisymmetry requirement in a later step. We will consider the variational non-symmetrized states:

$$|c_1, c_2\rangle = c_1|ab\rangle + c_2|ba\rangle \tag{2.1.16}$$

where $|ab\rangle$ has electron 1 in orbital state a and electron 2 in orbital state b and $|ba\rangle$ the converse. We want to evaluate the correction to the $\boldsymbol{R}_{ab}\to\infty$ energy E_0 as we bring the two

sites closer. We define the following quantities:

$$L^2 = \langle ab|ba\rangle \tag{2.1.17}$$

$$V = \langle ab|\,H\,|ab\rangle = \langle ba|\,H\,|ba\rangle \tag{2.1.18}$$

$$X = \langle ab|\,H\,|ba\rangle \tag{2.1.19}$$

and find the variational energy

$$\frac{\langle c_1, c_2|\,H\,|c_1, c_2\rangle}{\langle c_1, c_2|c_1, c_2\rangle} = \frac{(c_1^2 + c_2^2)V + 2c_1c_2X}{c_1^2 + c_2^2 + 2c_1c_2L^2}. \tag{2.1.20}$$

The extrema are found for $c_1 = \pm c_2$ with the energies

$$E_\pm = \frac{V \pm X}{1 \pm L^2}. \tag{2.1.21}$$

Interestingly, the $c_1 = c_2$ solution imply that the spatial part of the wavefunction is symmetrical and the $c_1 = -c_2$ anti-symmetrical upon electron interchange. Introducing the spin part and enforcing the global anti-symmetry of the wavefunction leads to the following spatial-spin wavefunctions with their associated energies:

$$E_+ \longrightarrow (|ab\rangle + |ba\rangle)\,(|\uparrow\downarrow\rangle - |\downarrow\uparrow\rangle) \tag{2.1.22}$$

$$E_- \longrightarrow (|ab\rangle - |ba\rangle)\begin{cases} |\uparrow\downarrow\rangle + |\downarrow\uparrow\rangle \\ |\uparrow\uparrow\rangle \\ |\downarrow\downarrow\rangle \end{cases}. \tag{2.1.23}$$

Up to a constant energy shift, this is the same spectrum one would get from the dimer Heisenberg model:

$$\mathscr{H} = \boldsymbol{S}_1 \cdot \boldsymbol{S}_2 \tag{2.1.24}$$

with $J = E_- - E_+$. The sign of J will depend of the L^2, V and X parameters in the following way:

$$\text{J>0} \Leftrightarrow X - VL^2 < 0. \tag{2.1.25}$$

We have thus found that a pure Coulomb Hamiltonian leads to an effective Heisenberg Hamiltonian. The required ingredients were a finite overlap L^2 and exchange integral X and most importantly the antisymmetry requirement for the wavefunction. The particle statistics thus plays an essential role into the emergence of quantum magnetism.

The Hubbard model

Probably the most known example for the Heisenberg model derivation is from the Hubbard model:

$$\mathscr{H} = \underbrace{-t\sum_{ij\sigma} c^\dagger_{i\sigma}c_{j\sigma}}_{T} + \underbrace{U\sum_i c^\dagger_{i\uparrow}c_{i\uparrow}c^\dagger_{i\downarrow}c_{i\downarrow}}_{V}. \tag{2.1.26}$$

We give a more extended description of this model in section 3.3.1. It describes fermions on a lattice with one orbital and two spin states per site. The operator $c^\dagger_{i\sigma}$ and $c_{i\sigma}$ respectively create and destroy a fermion of spin-σ on site i. The first term is the kinetic energy and the second one counts the number of doubly occupied sites which cost an energy U due to Coulomb repulsion. If we compare to the Heitler-London method, the hopping amplitude t is linked to the overlap integral L^2 and the energy U corresponds to the polar states that were disregarded due to their too high energy. We consider this model in the half-filled case where there are as many fermions as there are sites and in the strong coupling limit $t/U \ll 1$. In this limit, the Coulomb interaction defines sectors of the Hilbert space with a given number of doubly occupied sites and corresponding empty sites (because of half filling). These sectors are separated by the large energy U such that in the Hamiltonian eq. 2.1.26 the interaction part V is block-diagonal in the subspace of real space spin configurations with a given number of double occupancies. However the kinetic term

$$K = -t\sum_{ij} c^\dagger_{i\sigma}c_{j\sigma} \tag{2.1.27}$$

is not block-diagonal on this subspace since it might increase or decrease the number of double occupancies. The usual approach is to introduce it as a perturbation as t/U is a small parameter. The lowest energy subspace corresponds to the real space spin configurations with only one fermion on every sites. Let $|\alpha\rangle$ be one of these we have

$$V|\alpha\rangle = 0. \tag{2.1.28}$$

To the first order the perturbation will not bring any matrix elements between an $|\alpha\rangle$ and a $|\beta\rangle$ state as

$$\langle\alpha|\mathscr{H}^{(1)}|\beta\rangle = \langle\alpha|T|\beta\rangle = 0 \tag{2.1.29}$$

since the kinetic operator T will necessarily create a double occupancy. To the second order however we have:

$$\langle\alpha|\mathscr{H}^{(2)}|\beta\rangle = \sum_\gamma \frac{\langle\alpha|T|\gamma\rangle\langle\gamma|T|\beta\rangle}{-U} \tag{2.1.30}$$

where $|\gamma\rangle$ are the states with one double occupancy and one hole. As $T|\beta\rangle$ belongs to these states, the sum over the $|\gamma\rangle$ states resolves the identity on this subspace thus we have:

$$\mathscr{H}^{(2)} = -\frac{t^2}{U}\sum_{ij\sigma}\sum_{i'j'\sigma'} c^{\dagger}_{i\sigma}c_{j\sigma}c^{\dagger}_{i'\sigma'}c_{j'\sigma'}. \tag{2.1.31}$$

By inspection it is seen that the above Hamiltonian will only contribute on the real space spin configuration space without double occupancies only if

$$j' = i \tag{2.1.32}$$

$$i' = j \tag{2.1.33}$$

giving the effective second order perturbation theory Hamiltonian

$$\mathscr{H}^{(2)} = -\frac{t^2}{U}\sum_{ij}\sum_{\sigma\sigma'} c^{\dagger}_{i\sigma}c_{j\sigma}c^{\dagger}_{j\sigma'}c_{i\sigma'}. \tag{2.1.34}$$

If we now consider the (ij) part of the above applied on a state $|\alpha_{\sigma\sigma'}\rangle$, there are four cases to consider:

1. $|\alpha_{\uparrow\uparrow}\rangle = \left|\ldots \overset{i}{\uparrow} \ldots \overset{j}{\uparrow} \ldots\right\rangle$

$$\mathscr{H}^{(2)}|\alpha_{\uparrow\uparrow}\rangle = 0 \tag{2.1.35}$$

2. $|\alpha_{\downarrow\downarrow}\rangle = \left|\ldots \overset{i}{\downarrow} \ldots \overset{j}{\downarrow} \ldots\right\rangle$

$$\mathscr{H}^{(2)}|\alpha_{\downarrow\downarrow}\rangle = 0 \tag{2.1.36}$$

3. $|\alpha_{\uparrow\downarrow}\rangle = \left|\ldots \overset{i}{\uparrow} \ldots \overset{j}{\downarrow} \ldots\right\rangle$

$$\mathscr{H}^{(2)}|\alpha_{\uparrow\downarrow}\rangle = \left|\ldots \overset{i}{\uparrow} \ldots \overset{j}{\downarrow} \ldots\right\rangle - \left|\ldots \overset{i}{\downarrow} \ldots \overset{j}{\uparrow} \ldots\right\rangle \tag{2.1.37}$$

4. $|\alpha_{\downarrow\uparrow}\rangle = \left|\ldots \overset{i}{\downarrow} \ldots \overset{j}{\uparrow} \ldots\right\rangle$

$$\mathscr{H}^{(2)}|\alpha_{\downarrow\uparrow}\rangle = \left|\ldots \overset{i}{\downarrow} \ldots \overset{j}{\uparrow} \ldots\right\rangle - \left|\ldots \overset{i}{\uparrow} \ldots \overset{j}{\downarrow} \ldots\right\rangle \tag{2.1.38}$$

where the negative sign in front of the off-diagonal elements come from the fermionic sign rule. On the $\{|\alpha_{\uparrow\uparrow}\rangle, |\alpha_{\uparrow\downarrow}\rangle, |\alpha_{\downarrow\uparrow}\rangle, |\alpha_{\downarrow\downarrow}\rangle\}$ states the effective Hamiltonian thus reads

$$\langle \alpha_{\sigma_1\sigma_2} | \mathscr{H}^{(2)} | \alpha_{\sigma_3\sigma_4} \rangle = -\frac{t^2}{U} \begin{pmatrix} 0 & 0 & 0 & 0 \\ 0 & 1 & -1 & 0 \\ 0 & -1 & 1 & 0 \\ 0 & 0 & 0 & 0 \end{pmatrix} \tag{2.1.39}$$

which can be recast as

$$\langle \alpha_{\sigma_1\sigma_2} | \mathscr{H}^{(2)} | \alpha_{\sigma_3\sigma_4} \rangle = \frac{2t^2}{U} \left[\begin{pmatrix} \frac{1}{4} & 0 & 0 & 0 \\ 0 & -\frac{1}{4} & \frac{1}{2} & 0 \\ 0 & \frac{1}{2} & -\frac{1}{4} & 0 \\ 0 & 0 & 0 & \frac{1}{4} \end{pmatrix} - \frac{1}{4} \right] \tag{2.1.40}$$

$$= \frac{2t^2}{U} \left(\boldsymbol{S}_i \cdot \boldsymbol{S}_j - \frac{1}{4} \right). \tag{2.1.41}$$

Putting back the sum over the sites, we obtain the Heisenberg model up to a constant:

$$\langle \alpha | \mathscr{H}^{(2)} | \beta \rangle = \frac{4t^2}{U} \sum_{\langle i,j \rangle} \left(\boldsymbol{S}_i \cdot \boldsymbol{S}_j - \frac{1}{4} \right). \tag{2.1.42}$$

As was the case for the Heitler-London method, we see that a Hamiltonian which has no explicit spin-spin interaction as the Hubbard model results in an effective spin Hamiltonian in some limit. Again a critical ingredient was the correct application of the fermionic statistics, here applied through the fermionic sign coming along with the $c^\dagger_{i\sigma}$ and $c_{i\sigma}$ operators. We show in figure 2.1 the exchange process which underlies the second-order perturbation process highlighting the importance of the Pauli exclusion principle, yet another expression of the fermionic statistics.

2.2 The 1D spin-$\frac{1}{2}$ Heisenberg chain

Despite its simplicity the Heisenberg Hamiltonian hosts an extremely rich physics. In eq. 2.1.2, neither the lattice, the quantum spin number S nor the magnetic couplings J_{ij} are explicitly defined. Depending on those, the ground state and the excitations can be of an entirely different nature. In particular some choices of lattice and/or magnetic couplings result in magnetic frustration leading to macroscopically degenerate or exotic quantum entangled ground states and fractional excitations [Balents, 2010]. Key-examples are for instance quantum spin-liquid/valence bond solid and fractionalized excitations in the Kagomé lattice [Marston and Zeng, 1991; Lecheminant et al., 1997; Singh and Huse, 2007; de Vries et al., 2009; Yan et al., 2011; Han et al., 2012] and spin ice and magnetic monopoles in the pyrochlore lattice [Bramwell and Gingras, 2001; Castelnovo et al., 2008; Jaubert and Holdsworth, 2009; Bramwell et al., 2009]. But even when considering simpler lattices without frustration, the Heisenberg model already

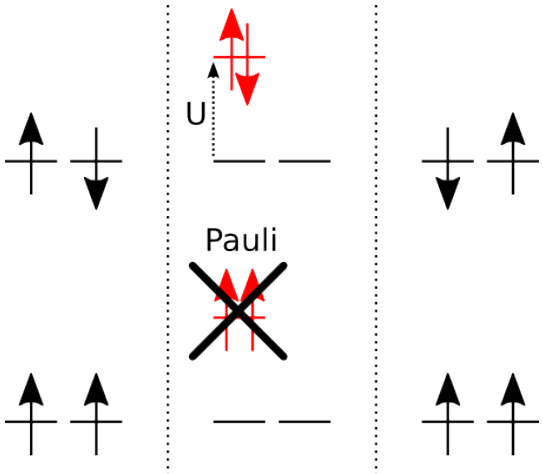

Figure 2.1 – Illustration of the second order perturbation theory matrix elements from eq. 2.1.34. Through the virtual hopping, neighboring up side down spins can gain kinetic energy by exchanging (top) while the process is forbidden for neighboring up or down spins (bottom) due to the Pauli exclusion principle.

produces a wide range of phenomena. In the following we review the case of the 1D spin-$\frac{1}{2}$ chain.

2.2.1 Theoretical overview

We consider the Hamiltonian

$$\mathscr{H} = \sum_i J_{xy}\left(S^x_{i+1}S^x_i + S^y_{i+1}S^y_i\right) + J_z S^z_{i+1}S^z_i \tag{2.2.1}$$

known as the XXZ model. We first consider the $J_{xy} = J_z = J$ which is simply the Heisenberg model. The classical ground state is simply the antiferromagnetic arrangement where $S^z_i|\text{GS}\rangle = \frac{1}{2}(-1)^i$. However the system has a continuous spin rotational symmetry which means it cannot be spontaneously broken at finite temperature (the Mermin-Wagner theorem [Mermin and Wagner, 1966]) so the antiferromagnetic order is absent at any finite temperature. That still leaves the possibility of $T = 0$ long-range order. If the system is ordered at zero temperature, then it is reasonable to use the semi-classical SWT (see section 2.4.1) to approximately diagonalize the Hamiltonian and calculate the predicted staggered magnetization. Such a calculation leads to

$$S^z_{(\pi,\pi)} = S - \frac{1}{2\pi}\int_0^{\pi/a} dk\left(1 - \frac{J}{\omega_k}\right) \tag{2.2.2}$$

$$\omega_k = J\sqrt{1-\cos^2(ka)} \tag{2.2.3}$$

where ω_k is the so-called spin-wave dispersion and, for small k, $\omega_k \sim k$ such that the integral 2.2.2 diverges. The SWT for the 1D chain, even at zero temperature, therefore is not self-

consistent suggesting that there is no order at $T = 0$ as well. The same approach in higher dimensions leads to a finite, although reduced, staggered magnetization at $T = 0$ for 2D systems and to a finite temperature long range order in 3D systems. The importance of the quantum fluctuations thus critically depend on the dimensionality.
The isotropic Heisenberg case can in fact be exactly solved by the so-called Bethe Ansatz [Bethe, 1931], an inspired guess of the ground state wavefunction which turns out to be exact! The ground state has quasi-long-range order and is a realization of a Luttinger liquid [Giamarchi, 2004]. However the great complexity of the ground state wavefunction makes it very difficult to extract physical quantities especially where it comes to correlation functions [Giamarchi, 2004]. To illustrate the nature of 1D spin-$\frac{1}{2}$ chain physics, we turn towards the simpler case where we set $J_z = 0$. In this limit the model becomes the so-called XY model and can be solved exactly in a simple fashion. Since the commutation relations for the spin operators are quite inconvenient, a good idea is to find a mapping from spin operators to fermionic or bosonic quasiparticles. We can set the vacuum of particles to be the completely polarized state

$$S_i^z |0\rangle = -\frac{1}{2}. \tag{2.2.4}$$

As one can create many bosonic quasiparticles in the same state, we see that it would corresponds to successive raising of the spin which is not allowed for spin-$\frac{1}{2}$. Representing the change in magnetization using bosons thus requires an additional constraint which prevents to create two or more bosons on the same site. This is the so-called hard-core boson mapping. Another idea is to use the Pauli exclusion principle to implement this constraint using spin-less fermionic quasi-particles. The mapping

$$S_i^+ = c_i^\dagger \tag{2.2.5}$$

$$S_i^z = c_i^\dagger c_i - \frac{1}{2} \tag{2.2.6}$$

fulfills the local spin commutation relation. However spin operators on different sites should commute, while this is not the case using the simple mapping eq. 2.2.5 and 2.2.6. To solve this issue one uses the Jordan-Wigner transformation [Jordan and Wigner, 1928]:

$$S_i^+ = c_i^\dagger \exp\left(i\pi\phi_i\right) \tag{2.2.7}$$

$$S_i^z = c_i^\dagger c_i - \frac{1}{2} \tag{2.2.8}$$

where ϕ_i is the string operator:

$$\phi_i = \sum_{j=-\infty}^{i-1} c_j^\dagger c_j \tag{2.2.9}$$

The XXZ model Hamiltonian becomes:

$$\mathscr{H}_{XXZ} = \frac{J_{xy}}{2} \sum_i \left[c_{i+1}^\dagger c_i + c_i^\dagger c_{i+1} \right] + J_z \sum_i \left(c_{i+1}^\dagger c_{i+1} - \frac{1}{2} \right) \left(c_i^\dagger c_i - \frac{1}{2} \right) \tag{2.2.10}$$

which, upon the gauge transformation $c_i \rightarrow (-1)^i c_i$ becomes

$$\mathscr{H}_{XXZ} = -t\sum_i \left[c^\dagger_{i+1}c_i + c^\dagger_i c_{i+1}\right] + V\sum_i \left(c^\dagger_{i+1}c_{i+1} - \frac{1}{2}\right)\left(c^\dagger_i c_i - \frac{1}{2}\right) \tag{2.2.11}$$

describing spinless fermions hopping on a chain with amplitude $t = \frac{J_{xy}}{2}$ subjected to a nearest neighbor repulsion $V = J_z$. In the XY limit the Hamiltonian is quadratic and can be diagonalized by a Fourier transform:

$$\mathscr{H}_{XY} = \sum_k \epsilon_k c^\dagger_k c_k \tag{2.2.12}$$

$$\epsilon_k = -2t\cos(ka) \tag{2.2.13}$$

which describes free fermions on a chain. The S^z_{tot} sector defines the fermion filling with $S^z_{\text{tot}} = 0$ corresponding to half-filling. The ground state is then a half-filled Fermi sea up to the Fermi energy ϵ_F. The most important outcome of this calculation is the fractional nature of the excitations which, in the so-called longitudinal channel where excitations do not change the S^z_{tot} sector, will be made of particle-hole spinless fermion pairs. We show in fig. 2.2 the evolution of a local particle-hole excitation $c^\dagger_i c_{i+1}$ applied on a Néel ordered cluster. This allows to identify the particle-hole excitation as the creation of two domain walls which will propagate freely on the chain as their movement does not change the overall energy of the system. Another important outcome is that, for a given momentum transfer $\boldsymbol{q}$, there will be many particle-hole pairs which one can create with this net momentum. It follows that the excitations will not be like for instance a harmonic oscillator mode where for each momentum there corresponds a discret number of bosonic excitations. Instead, a continuum of excitations $\left|k,q\right\rangle$ will correspond to each momentum:

$$\left|k,q\right\rangle = c^\dagger_k c_{k-q}\left|\text{GS}\right\rangle \quad \epsilon_{k-q} < \epsilon_F < \epsilon_k \tag{2.2.14}$$

$$\left|GS\right\rangle = \prod_{\{k|\epsilon_k \leq \epsilon_F\}} c^\dagger_k \left|0\right\rangle. \tag{2.2.15}$$

Because of the simplicity of the S^z operator in the spinless fermion representation (eq. 2.2.8), the dynamic spin structure factor is identical to the particle-hole excitation density of states [Imambekov et al., 2012]:

$$D(\boldsymbol{q},\omega) = \sum_{\{k|\epsilon_{k-q}<\epsilon_F<\epsilon_k\}} \delta(\omega - \epsilon_{k-q} + \epsilon_k) \tag{2.2.16}$$

which we show in fig. 2.3 for the half-filled case where the delta-functions are widened by a gaussian with a finite width. Of course the XY model is strongly anisotropic and the dynamic spin structure factor will be different for instance in the transverse excitation channel where the total spin is increased by $\Delta S = 1$. However because of the string operator entering the spinless fermion representation of the $S^\pm_i$ operators, the calculation of the transverse dynamic spin structure factor is more complicated and can be looked up for instance in Imambekov et al. [2012].

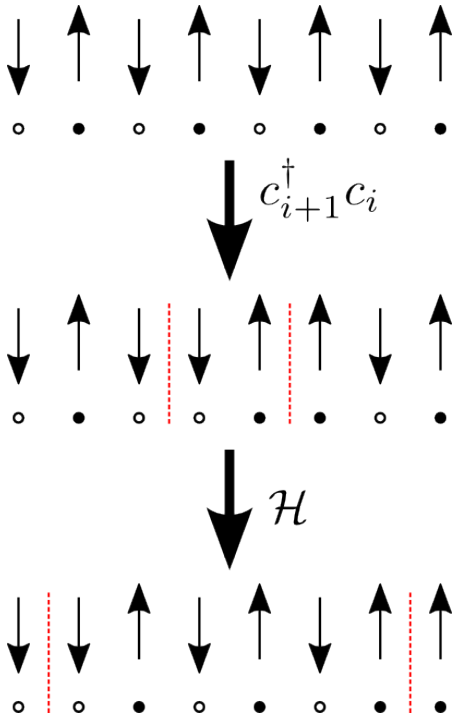

Figure 2.2 – Real space representation of a spinon particle-hole pair. Arrows are for spin representation and plain and hollow dots for spinless fermion representation. The particle-hole fermionic pair flips two neighbouring spins creating two domain walls. The Hamiltonian applied on this state will move away the domains walls which behave like free quasiparticles.

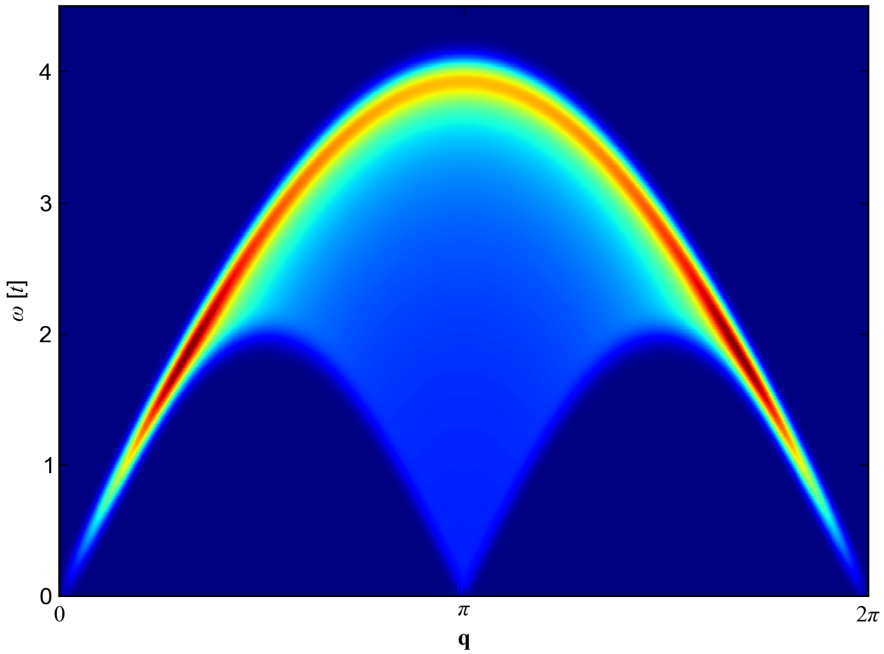

Figure 2.3 – Particle-hole excitation density of states for the XY model in the half-filled case.

Turning on the longitudinal coupling $J_z \to J_{xy}$ in a perturbative way, the interaction between spinless fermions will mix higher order n-particles n-holes into the longitudinal dynamic structure factor. In the Heisenberg limit $J_z = J_{xy}$ the exactly calculated two-spinons contribution amounts for 73% of the total spectral weight [Karbach et al., 1997] while including 4-spinon excitations produces 98% [Caux and Hagemans, 2006]. These theoretical predictions have been confirmed experimentally [Mourigal et al., 2013].

2.2.2 Experimental realizations

There have been many physical realizations of the 1D spin-$\frac{1}{2}$ chain. We can mention $KCuF_3$ [Tennant et al., 1995], Sr_2CuO_3 [Walters et al., 2009] and $CuSO_4 \cdot 5D_2O$ [Mourigal et al., 2013]. All these materials features nearly isolated spin-$\frac{1}{2}$ chains. Below some critical temperature, the inter-chain couplings will become relevant. The system thus turns into a three-dimensional one which will realize some magnetic order. Above this temperature however, the thermal fluctuations will effectively decouple the chains while leaving the chain physics itself nearly unaffected, thus realizing an effective one-dimensional system. We show in fig. 2.4 a comparison between an inelastic neutron scattering measurement of the dynamic spin structure factor and the predicted spectrum. This figure is taken from Mourigal et al. [2013]. The one-dimensional spin-$\frac{1}{2}$ Heisenberg chain is a great example where a theoretically exact theory could be successfully confronted to experimental measurements in great details.

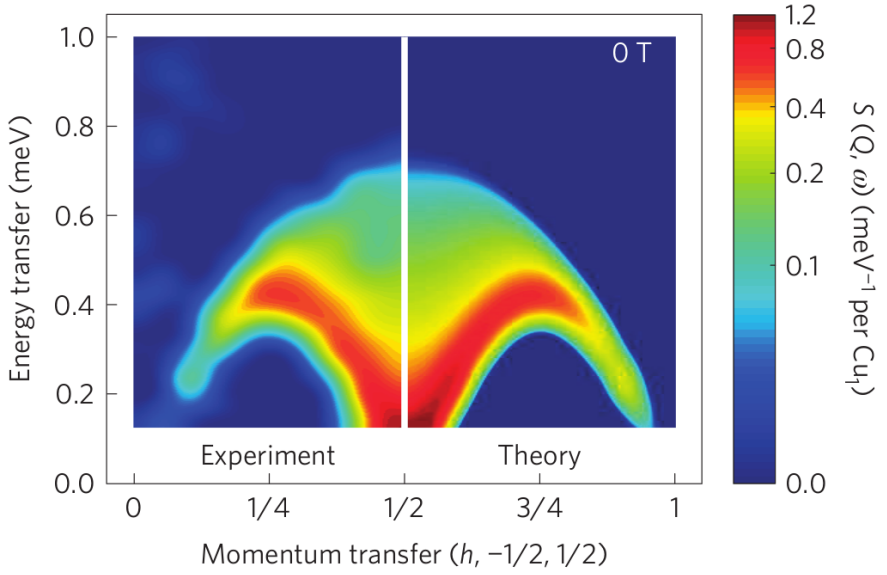

Figure 2.4 – Figure from Mourigal et al. [2013]. Experimental colormap of the dynamic spin structure factor of the spin-$\frac{1}{2}$ chain material $CuSO_4 \cdot 5D_2O$ (left) compared to a two- plus four-spinons excitation calculation from the isotropic Heisenberg model.

2.3 The square lattice Heisenberg model

The Quantum spin-1/2 Heisenberg Square lattice Anti-Ferromagnetic model (QHSAF) is probably the simplest Heisenberg model one can think of in two dimensions. We only consider a nearest-neighbour antiferromagnetic coupling J such that the model is usually written as

$$\mathscr{H} = J \sum_{\langle i,j \rangle} \boldsymbol{S}_i \cdot \boldsymbol{S}_j \tag{2.3.1}$$

where $i = (i_x, i_y)$ and j index the sites of the lattice and the sum runs over the $\langle i, j \rangle$ nearest-neighbours bonds. Since the system still has a continuous rotational symmetry and is two-dimensional, the Mermin-Wagner theorem still applies and predicts that the system should be disordered at any finite temperature. However there is theoretical and numerical agreement [Manousakis, 1991] that the zero-temperature system should be ordered. Since in real materials there always is some weak inter-plane coupling making the system marginally three-dimensional, physical realizations will order at some finite temperature.
At a first glance, this renders the problem simpler since its ground state seems to be close to a classical state with a local order parameter. However there is to date no exact solution such as in the one-dimensional case and approximations must be used. To allow comparison between the different theoretical approaches and experimental results, one resorts on instantaneous and dynamical quantities respectively relating to the ground state and to the excitations properties. The quantities which will be thoroughly studied in this work are:
– the staggered magnetization:

$$\left\langle S^z_{\boldsymbol{Q}} \right\rangle = \frac{1}{N} \sum_i e^{i \boldsymbol{R}_i \cdot \boldsymbol{Q}} \left\langle S^z_i \right\rangle \tag{2.3.2}$$

  where $\boldsymbol{Q} = (\pi, \pi)$ is the antiferromagnetic ordering vector (in reciprocal unit cell units),
– the longitudinal ($\alpha = z$) and transverse ($\alpha \in \{x, y\}$) instantaneous spin correlation in real and reciprocal space:

$$S^{\alpha\alpha}(\boldsymbol{r}) = \left\langle S^\alpha_{i+\boldsymbol{r}} S^\alpha_i \right\rangle \tag{2.3.3}$$

$$S^{\alpha\alpha}(\boldsymbol{q}) = \left\langle S^\alpha_{-\boldsymbol{q}} S^\alpha_{\boldsymbol{q}} \right\rangle, \tag{2.3.4}$$

– and the longitudinal and transverse dynamic spin structure factor:

$$S^{zz}(\boldsymbol{q}, \omega) = \int dt e^{i\omega t} \left\langle S^z_{-\boldsymbol{q}}(t) S^z_{\boldsymbol{q}}(0) \right\rangle \tag{2.3.5}$$

$$S^{\pm}(\boldsymbol{q}, \omega) = \int dt e^{i\omega t} \left\langle S^-_{\boldsymbol{q}}(t) S^+_{\boldsymbol{q}}(0) \right\rangle. \tag{2.3.6}$$

Probably the most established theory to tackle the QHSAF is SWT which we quickly review in section 2.4.1. Before going into a review of the experimental results available, it is useful to point out a few SWT results for comparison.
– The staggered magnetization: For spin-$\frac{1}{2}$, SWT predicts a $T = 0$ ordered phase with a staggered magnetization reduced to 62% of its classical value.

– Transverse instantaneous spin correlation functions: in linear SWT one can calculate $S^{\pm}(\boldsymbol{q})$ and the corresponding alternating real space transverse spin-spin correlation $S^{\pm}(\boldsymbol{r}) = \int e^{i(\boldsymbol{q}+\boldsymbol{Q})\boldsymbol{r}} S^{\pm}(\boldsymbol{q})$. An important outcome for the coming discussion is that the alternated real space transverse spin-spin correlation decays algebraically with distance (fig. 2.5). This is a long wave-length property and we will see that the spin-wave approximation is the most robust in this regime.

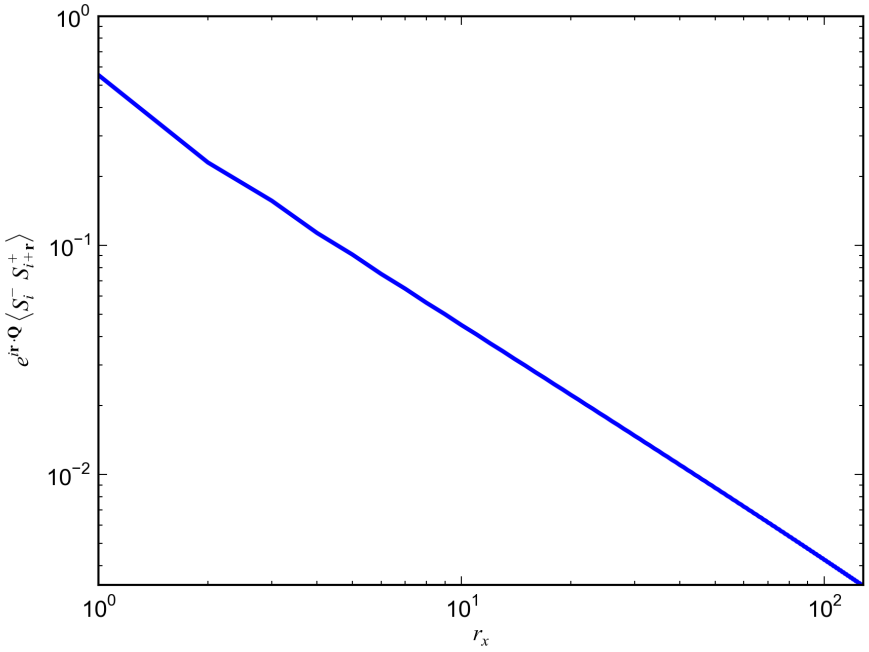

Figure 2.5 – Instantaneous transverse correlation function $S^{\pm}(\boldsymbol{r}) = e^{i\boldsymbol{Q}\boldsymbol{r}}\langle S_i^- S_{i+\boldsymbol{r}}^+\rangle$ from linear SWT. The log-log plot evidences the algebraic decay of the correlation function.

– Transverse dynamic spin structure factor: In linear SWT, the transverse dynamic structure factor consists only of a magnon mode $\omega_{\boldsymbol{q}}$ gapless at $\boldsymbol{q} = (0,0)$ and $\boldsymbol{q} = (\pi,\pi)$. The important facts are that i) the spin-wave magnon mode energy $\omega_{\boldsymbol{q}}$ is constant along the Magnetic Brillouin Zone Boundary (MBZB) $|q_x| + |q_y| = \pi$ and ii) its intensity $I(\boldsymbol{q})$ in the transverse dynamic structure factor $S^{\pm}(\boldsymbol{q},\omega) = I(\boldsymbol{q})\delta(\omega - \omega_{\boldsymbol{q}})$ is also constant along the MBZB. We show these observations in fig. 2.6 along the high-symmetry directions.

2.3.1 Physical realizations and statement of the problem

There exists many realizations of the QHSAF: the metal-organics CFTD [Burger et al., 1980; Yamagata et al., 1981; Clarke et al., 1992; Rønnow et al., 1999; Christensen et al., 2007] and $Cu(pz)_2(ClO_4)_2$ [Tsyrulin et al., 2009], the vanadate $K_2V_3O_8$ [Lumsden et al., 2006], the insulating parent compound of the high-temperature superconducting cuprate materials for instance LCO[Coldea et al., 2001a; Headings et al., 2010], $Sr_2Cu_3O_4Cl_2$ [Kim et al., 1999], SCOC or $Bi_2Sr_2YCu_2O_8$ (BSYCO)[Guarise et al., 2010; Dalla Piazza et al., 2012] and the monolayer

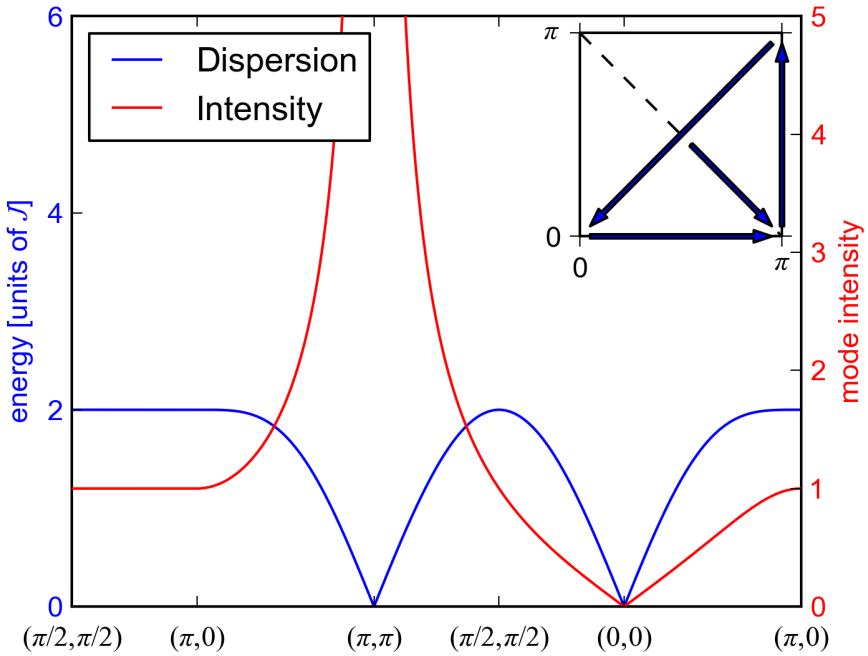

Figure 2.6 – Linear SWT magnon dispersion $\omega_{\boldsymbol{q}}$ and intensity $I(\boldsymbol{q})$ in the dynamic structure factor $S(\boldsymbol{q},\omega) = I(\boldsymbol{q})\delta(\omega - \omega_{\boldsymbol{q}})$. The inset shows the chosen high-symmetry path $\boldsymbol{q} = (q_x, q_y)$.

iridate Sr_2IrO_4 [Kim et al., 2012]. A key quantity which is accessible to neutron scattering experiments is the dynamic spin structure factor. Overall the SWT predictions proved to be surprisingly accurate, but a few experiments nonetheless reported significant deviations [Rønnow et al., 2001; Christensen et al., 2007; Headings et al., 2010; Kim et al., 2001]. These deviations occur at the high-energy/short wavelength part of the excitation spectrum which coincides with the MBZB, where SWT is consistently expected to be less robust. Dubbed hereafter "quantum effects", the observed deviations can be summarized as follow:

1. A downward dispersion of the magnon mode energy of 7% along the MBZB from $\boldsymbol{q} = (\pi/2, \pi/2)$ (highest) to $\boldsymbol{q} = (\pi, 0)$ (lowest).
2. A reduction of the magnon intensity of 50% at $\boldsymbol{q} = (\pi, 0)$ compared to $\boldsymbol{q} = (\pi/2, \pi/2)$.
3. The emergence of a continuum of excitations extending towards higher energies above the magnon line at $\boldsymbol{q} = (\pi, 0)$. This feature results in an asymmetrical lineshape of the dynamic spin structure factor peak for this momentum as a function of energy.

Feature 1 has been observed in CFTD and $Sr_2Cu_3O_4Cl_2$[Rønnow et al., 2001; Christensen et al., 2007; Kim et al., 2001] but not in LCO. This can be explained by the extended magnetic couplings present in the cuprate materials, in particular the cyclic ring exchange, which qualitatively modifies the SWT prediction for the magnon dispersion (see chapter 3). Therefore feature 1 is rendered unobservable in LCO due to these extended magnetic coupling. Otherwise features 2 and 3 could both be observed in CFTD[Christensen et al., 2007], LCO[Headings et al., 2010] and $Cu(pz)_2(ClO_4)_2$ [Tsyrulin et al., 2009] while we are not aware of an experimental work evidencing it in $Sr_2Cu_3O_4Cl_2$. These effects thus appear in very different materials

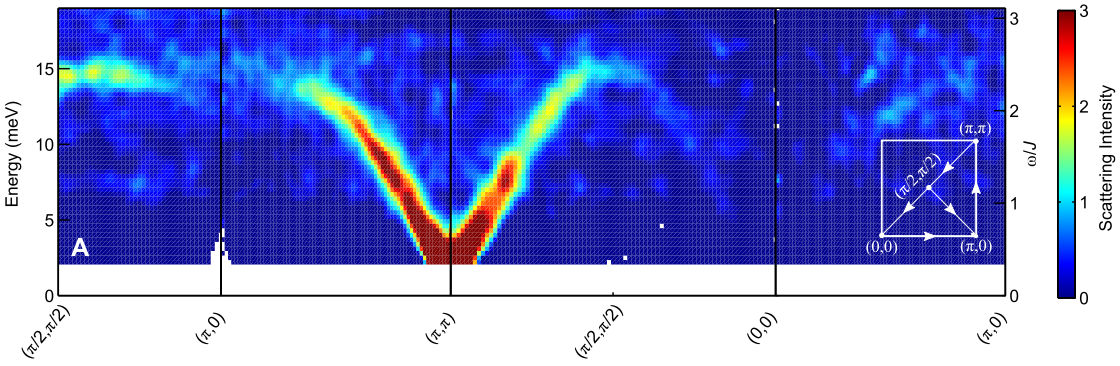

Figure 2.7 – Unpolarized INS spectrum for the CFTD materials from Mourigal [2011] as a function of momentum and energy.

supporting the idea that they are intrinsic quantum effects of the nearest-neighbour QHSAF. The dispersion quantum effect 1 could be numerically reproduced by series expansion around the Ising limit of the QHSAF[Zheng et al., 2005] and quantum Monte Carlo [Syljuåsen and Rønnow, 2000; Sandvik and Singh, 2001] strengthening the proposal of its QHSAF intrinsic nature. 3rd order $1/S$ SWT also predicted a dispersion along the MBZB but only of 3% [Syromyatnikov, 2010] as a result of an apparently very slowly, if at all convergent $1/S$ perturbative expansion. The intensity and the continuum quantum effects 2 and 3 are linked in the sense that the energy-integrated intensity is almost constant along the MBZB such that the intensity going into the continuum at $\boldsymbol{q} = (\pi,0)$ necessarily lowers the main magnon peak intensity. Series expansion could reproduce a 20% reduction of the $\boldsymbol{q} = (\pi,0)$ intensity with respect to $\boldsymbol{q} = (\pi/2,\pi/2)$. Quantum Monte Carlo on the other hand is a difficult tool when going to dynamical properties as the analytical continuation of noisy numerical data either results in an insufficient frequency resolution or requires some a-priori knowledge/postulate of the lineshape [Sandvik and Singh, 2001].

To illustrate the experimental quantum effect, we will focus on experimental data coming from CFTD due to i) the absence of extended magnetic interactions, ii) the availability of extended time-of-flight neutron data and iii) the availability of polarized neutron scattering data for the $\boldsymbol{q} = (\pi,0)$ and $\boldsymbol{q} = (\pi/2,\pi/2)$ momenta which importantly allow to disentangle the longitudinal $S^{zz}(\boldsymbol{q},\omega)$ from the transverse $S^{\pm}(\boldsymbol{q},\omega)$ experimental contributions. This yet unpublished data can be found in Martin Mourigal PhD thesis [Mourigal, 2011]. We show a colormap of the unpolarized neutron scattering data along the high-symmetry directions in fig. 2.7 which nicely evidences features 2. The 7% dispersion feature 1 is better seen in fig. 2.8, data extracted from ref. Christensen et al. [2007]. We now take a closer look at the specific momenta $\boldsymbol{q} = (\pi,0)$ and $\boldsymbol{q} = (\pi/2,\pi/2)$ from polarized neutron scattering in fig. 2.9. The measurement by polarized neutron scattering from two different Brillouin zones allowed to decouple the transverse (fig. 2.9 B and F) and longitudinal (fig. 2.9 C and G) channels. In the transverse channel, the $\boldsymbol{q} = (\pi,0)$ (fig. 2.9 B) and the $\boldsymbol{q} = (\pi/2,\pi/2)$ (fig. 2.9) nicely evidence all the quantum anomaly features. The main peak is shifted down by 7% for $\boldsymbol{q} = (\pi,0)$ compared to $\boldsymbol{q} = (\pi/2,\pi/2)$ and its intensity is reduced as more weight is pushed into the tail going to

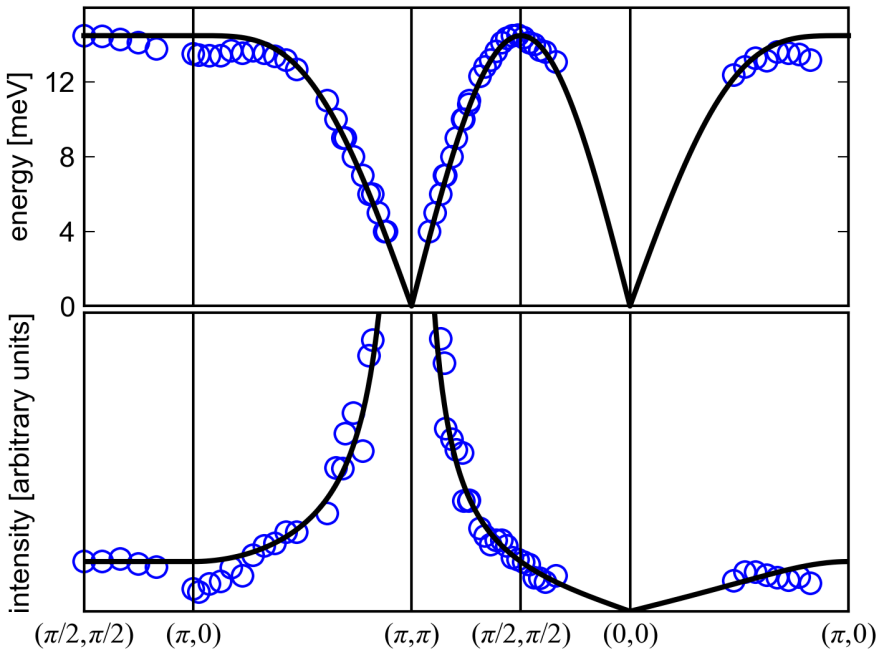

Figure 2.8 – Magnon-like dispersion relation (top) and intensity (bottom) as measured by INS on the CFTD material [Christensen et al., 2007] (blue open circles) compared to linear SWT (black solid line) with J adjusted such that $\omega(\pi/2,\pi/2)$ matches experiments.

higher energies. The longitudinal spectrum (fig. 2.9 C and G) also shows important differences between the two momenta. If one subtracts from the transverse channel the magnon-like peak as fitted by a resolution-limited gaussian, one obtains the blue open points in fig. 2.9 D and H. The dashed red lines are twice the longitudinal lineshapes from fig. 2.9 C and G. While the subtraction at $\boldsymbol{q} = (\pi/2,\pi/2)$ leaves almost no spectral weight, at $\boldsymbol{q} = (\pi,0)$ it results in a lineshape which overlaps perfectly the longitudinal channel data. This surprising observation hints that the excitations found in the high energy tail of the $\boldsymbol{q} = (\pi,0)$ spectrum might be spin-isotropic with $S^{xx}(\boldsymbol{q},\omega) = S^{zz}(\boldsymbol{q},\omega) = \frac{1}{2}S^{\pm}(\boldsymbol{q},\omega)$. It is not possible to reconciliate the observed lineshapes with SWT. In SWT, magnon-magnon interaction do push about 20% of the MBZB magnon peak weight into a higher energy three-magnon continuum [Canali and Wallin, 1993]. But the resulting lineshape is radically different, does not coincide with the (two-magnon) longitudinal lineshape at $\boldsymbol{q} = (\pi,0)$ and more importantly is only weakly momentum-dependent while the experimental data shows very important differences between the $\boldsymbol{q} = (\pi,0)$ and $\boldsymbol{q} = (\pi/2,\pi/2)$.

In this thesis, we propose that all these experimental deviations mark a departure from the conventional SWT at short wavelengths/high energies and that the measured excitations must be described differently. The total spin dynamic structure factor shown in fig. 2.9 A for $\boldsymbol{q} = (\pi,0)$ is reminiscent of the one-dimensional spin-$\frac{1}{2}$ chain dynamic structure factor. It inspired us to consider the proposal that the excitations at $\boldsymbol{q} = (\pi,0)$ should in fact be understood as emergent fractional quasiparticles-pair excitations just as in the one-dimensional case. In the

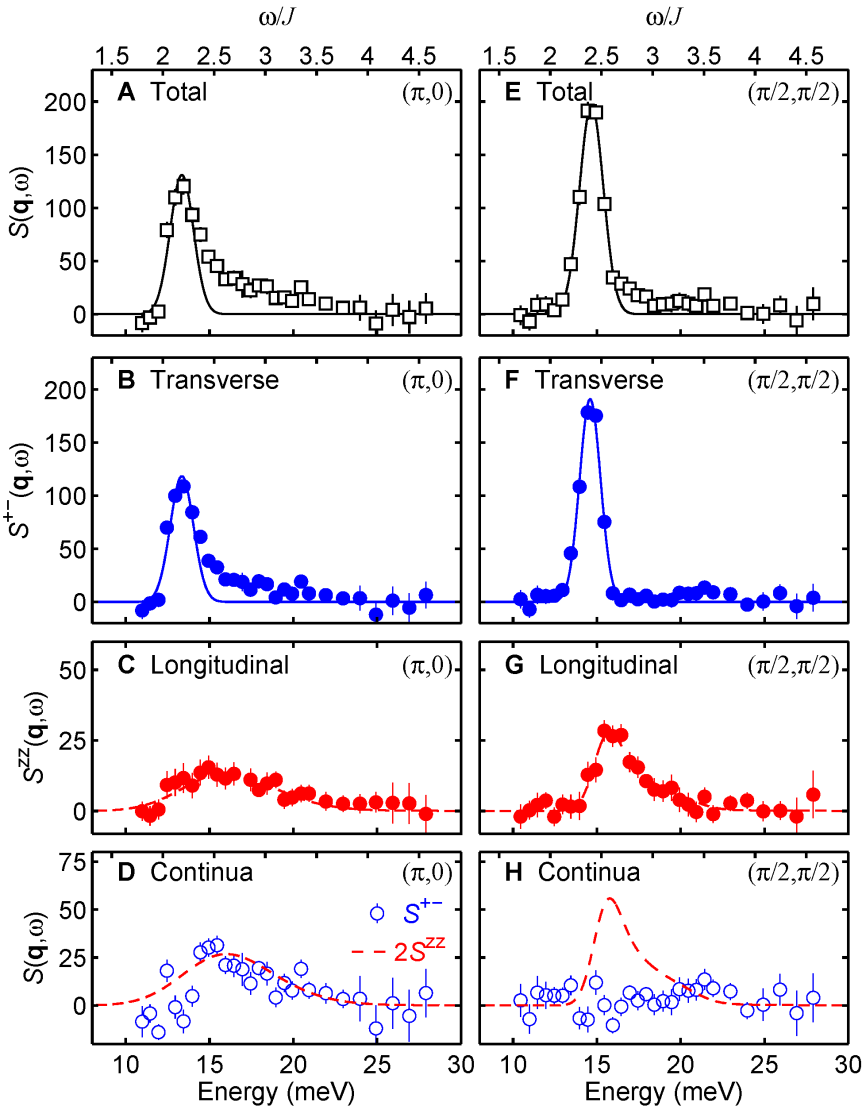

Figure 2.9 – Polarized INS spectra for the $\boldsymbol{q} = (\pi,0)$ (A-D) and $\boldsymbol{q} = (\pi/2,\pi/2)$ (E-H) momenta [Mourigal, 2011]. First line from the top indicate the total dynamic structure factor $S(\boldsymbol{q}.\omega) = S^{xx}(\boldsymbol{q},\omega) + S^{yy}(\boldsymbol{q},\omega) + S^{zz}(\boldsymbol{q},\omega)$, the Néel ordering axis taken along the z axis. Second line shows the transverse spectra with solid blue line being resolution-limited gaussian fits. Third line shows the longitudinal spectra with dashed red lines guides for the eye, and fourth line shows together twice the longitudinal red dashed guide to the eye line with the transverse spectrum where the fitted resolution-limited gaussian solid blue line have been subtracted.

following we set up a formalism and numerical techniques to tackle this idea.

2.4 Analytical approaches

In this section we first set up the linear SWT and extract from it quantities that can be compared to experiments and to our spinon-pair calculation. Then we move towards reviewing the fermionic mean-field theories of the QHSAF and setup the mathematical foundations of our later numerical work.

2.4.1 The Spin-Wave approximation

We quickly review linear SWT for the sake of the coming discussion. A more in depth discussion in particular considering bi-layered materials and the first order quantum corrections is carried out in chapter 3 section 3.5. We start by introducing a staggered rotation of the spin frame of reference around the y axis:

$$S_i^x \to e^{i\boldsymbol{Q}\boldsymbol{R}_i} S_i^x, \tag{2.4.1}$$
$$S_i^y \to S_i^y, \tag{2.4.2}$$
$$S_i^z \to e^{i\boldsymbol{Q}\boldsymbol{R}_i} S_i^z. \tag{2.4.3}$$

In this rotated frame of reference the classical ground state is *ferromagnetic*. Using the Holstein-Primakov transform we describe the deviations from this ground state using the bosonic spin-wave creation and annihilation operators:

$$S_i^z = \frac{1}{2} - a_i^\dagger a_i \tag{2.4.4}$$
$$S_i^+ = \left[\sqrt{2S - a_i^\dagger a_i}\right] a_i \approx \sqrt{2S} a_i \tag{2.4.5}$$
$$S_i^- = a_i^\dagger \left[\sqrt{2S - a_i^\dagger a_i}\right] \approx \sqrt{2S} a_i^\dagger \tag{2.4.6}$$

where the approximation of the square root term prepares the $1/S$ approximation of the spin-wave Hamiltonian. Neglecting the quartic boson operator terms (the 1/S approximation) we obtain a quadratic Hamiltonian

$$\mathscr{H}_{\mathrm{SW}}^{(2)} = JS^2 \frac{1}{2} \sum_i \sum_{\boldsymbol{\tau}} \left[-1 + \frac{1}{S} \left(a_i^\dagger a_i + a_{i+\boldsymbol{\tau}}^\dagger a_{i+\boldsymbol{\tau}} - a_{i+\boldsymbol{\tau}}^\dagger a_i^\dagger - a_{i+\boldsymbol{\tau}} a_i \right) \right] + \mathscr{O}\left(\frac{1}{S^0}\right) \tag{2.4.7}$$

which upon a Fourier transform

$$a_i = \sum_{\boldsymbol{k}} e^{i\boldsymbol{k}\boldsymbol{R}_i} a_{\boldsymbol{k}} \tag{2.4.8}$$
$$a_i^\dagger = \sum_{\boldsymbol{k}} e^{-i\boldsymbol{k}\boldsymbol{R}_i} a_i^\dagger \tag{2.4.9}$$

becomes

$$\mathscr{H}_{\mathrm{SW}}^{(2)} = -S^2 zJ\frac{N}{2} + SJ\sum_{\boldsymbol{k}}\sum_{\boldsymbol{\tau}} a_{\boldsymbol{k}}^\dagger a_{\boldsymbol{k}} - \frac{1}{2}e^{i\boldsymbol{k}\boldsymbol{\tau}} a_{\boldsymbol{k}}^\dagger a_{-\boldsymbol{k}}^\dagger - \frac{1}{2}e^{i\boldsymbol{k}\boldsymbol{\tau}} a_{\boldsymbol{k}} a_{-\boldsymbol{k}} \tag{2.4.10}$$

$$= -S^2 zJ\frac{N}{2} + SJ\sum_{\boldsymbol{k}} A_{\boldsymbol{k}} a_{\boldsymbol{k}}^\dagger a_{\boldsymbol{k}} + \frac{1}{2}B_{\boldsymbol{k}}\left(a_{\boldsymbol{k}}^\dagger a_{-\boldsymbol{k}}^\dagger + a_{\boldsymbol{k}} a_{-\boldsymbol{k}}\right). \tag{2.4.11}$$

with $z = 4$ the number of nearest neighbors and

$$A_{\boldsymbol{k}} = z \tag{2.4.12}$$

$$B_{\boldsymbol{k}} = \sum_{\boldsymbol{\tau}} \cos(\boldsymbol{k}\boldsymbol{\tau}). \tag{2.4.13}$$

At last a standard Bogoliubov transform diagonalize the quadratic spin-wave Hamiltonian with

$$\alpha_{\boldsymbol{k}} = u_{\boldsymbol{k}} a_{\boldsymbol{k}} + v_{\boldsymbol{k}} a_{-\boldsymbol{k}}^\dagger \tag{2.4.14}$$

$$u_{\boldsymbol{k}} = \sqrt{\frac{1}{2}\left(1 + \frac{A_{\boldsymbol{k}}}{\omega_{\boldsymbol{k}}}\right)} \tag{2.4.15}$$

$$v_{\boldsymbol{k}} = \mathrm{sign}\,(B_{\boldsymbol{k}})\sqrt{\frac{1}{2}\left(1 - \frac{A_{\boldsymbol{k}}}{\omega_{\boldsymbol{k}}}\right)} \tag{2.4.16}$$

$$\omega_{\boldsymbol{k}} = \sqrt{A_{\boldsymbol{k}}^2 - B_{\boldsymbol{k}}^2} \tag{2.4.17}$$

giving

$$\mathscr{H}_{\mathrm{SW}}^{(2)} = -JS(S+1)z\frac{N}{2} + SJ\sum_{\boldsymbol{k}} \omega_{\boldsymbol{k}}\left(\alpha_{\boldsymbol{k}}^\dagger \alpha_{\boldsymbol{k}} + \frac{1}{2}\right). \tag{2.4.18}$$

The ground state is the vacuum of the $\alpha_{\boldsymbol{k}}$ harmonic oscillator modes and the excitations are the creation of one or more spin-waves through the $\alpha_{\boldsymbol{k}}^\dagger$ creation operator. Inversing the transformations, we can express the spin operators in terms of the $\alpha_{\boldsymbol{k}}$ operators thus we can express the various zero-temperature physical quantities such as:

– The staggered magnetization:

$$M_{\boldsymbol{Q}} = \left\langle \sum_i S_i^z \right\rangle_{T=0} = \frac{1}{2} - \langle a_i^\dagger a_i \rangle \tag{2.4.19}$$

$$\frac{1}{2} - \sum_{\boldsymbol{k}} v_{\boldsymbol{k}}^2 \simeq 0.3. \tag{2.4.20}$$

– The transverse instantaneous spin-spin correlation:

$$\left\langle S_{\boldsymbol{q}}^- S_{\boldsymbol{q}}^+ \right\rangle = (u_{\boldsymbol{k}} - v_{\boldsymbol{k}})^2. \tag{2.4.21}$$

We show the Fourier transform $\left\langle S_i^- S_{i+\boldsymbol{r}}^+ \right\rangle = \sum_{\boldsymbol{q}} e^{i\boldsymbol{q}\boldsymbol{r}} \left\langle S_{\boldsymbol{q}}^- S_{\boldsymbol{q}}^+ \right\rangle$ in the case of the spin-$\frac{1}{2}$ QHSAF in fig. 2.5

– The transverse dynamic spin structure factor:

$$S^{\pm}(\boldsymbol{q},\omega) = \int dt e^{i\omega t} \sum_{ij} e^{\boldsymbol{q}(R_j - R_i)} \left\langle S_i^-(t) S_j^+(0) \right\rangle \tag{2.4.22}$$

$$= (u_{\boldsymbol{k}} - v_{\boldsymbol{k}})^2 \delta(\omega - \omega_{\boldsymbol{k}}). \tag{2.4.23}$$

We see that the transverse excitations are made out of single spin-waves which corresponds to a change of angular momentum $\Delta S = 1$. In reality magnon-magnon interaction will give rise to a continuum of three-magnons, five-magnons and so on. We show in fig. 2.6 the one-magnon dispersion $\omega_{\boldsymbol{q}}$ along with its intensity $I_{\boldsymbol{q}} = (u_{\boldsymbol{k}} - v_{\boldsymbol{k}})^2$ in the case of the spin-$\frac{1}{2}$ QSHAF.

– The longitudinal dynamic spin structure factor:

$$S^{zz}(\boldsymbol{q},\omega) = M_{\boldsymbol{Q}}^2 \delta(\boldsymbol{q} - \boldsymbol{Q}) \delta(\omega) + \frac{1}{2} \sum_{\boldsymbol{k}} (u_{\boldsymbol{k}} v_{\boldsymbol{k}-\boldsymbol{q}} - u_{\boldsymbol{k}-\boldsymbol{q}} v_{\boldsymbol{k}})^2 \delta(\omega - \omega_{\boldsymbol{k}} - \omega_{\boldsymbol{k}-\boldsymbol{q}}) \tag{2.4.24}$$

whose inelastic part corresponds to the creation of two spin-waves giving rise to a longitudinal continuum of excitations. We show this longitudinal continuum for the spin-$\frac{1}{2}$ QHSAF later on in fig. 3.22.

Magnon-magnon interaction

From equation 2.4.4 to 2.4.7 we truncated the expansion of the spin Hamiltonian in terms of the a_i and $a_i^\dagger$ bosonic operators such that only the quadratic bosonic terms were left. This corresponds to an expansion in $1/S$ where terms of order $1/S^0$, giving rise to quartic bosonic terms, where disregarded. Introducing these terms can be done in various perturbative schemes. In section 3.5.5 for instance we treat those through an Hartree-Fock procedure which for nearest-neighbour coupling J leads to a uniform quantum renormalization of the one-magnon energy $\omega_{\boldsymbol{k}} \to Z_c \omega_{\boldsymbol{k}}$ with $Z_c \simeq 1.15$.
To calculate the effect of these magnon-magnon interactions on the various correlation functions, the preferred approach is to rewrite the interacting part of the spin-wave Hamiltonian into the quasi-particle $\alpha_{\boldsymbol{k}}$ operators diagonalizing the quadratic part and to carry out a perturbative expansion in the interaction through the Feynman diagram formalism for instance [Igarashi, 1992; Canali and Wallin, 1993; Igarashi and Nagao, 2005; Syromyatnikov, 2010]. Following Igarashi [1992] the correlation functions can be written in terms of the Green functions:

$$G_{11} = -i\langle T\alpha_{\boldsymbol{k}}(t)\alpha_{\boldsymbol{k}}^\dagger(0)\rangle \tag{2.4.25}$$

$$G_{12} = -i\langle T\alpha_{\boldsymbol{k}}(t)\alpha_{-\boldsymbol{k}}(0)\rangle \tag{2.4.26}$$

$$G_{21} = -i\langle T\alpha_{-\boldsymbol{k}}^\dagger(t)\alpha_{\boldsymbol{k}}^\dagger(0)\rangle \tag{2.4.27}$$

$$G_{22} = -i\langle T\alpha_{-\boldsymbol{k}}^\dagger(t)\alpha_{-\boldsymbol{k}}(0)\rangle. \tag{2.4.28}$$

The perturbed Green functions may be calculated from the Fourier-transformed unperturbed ones $G^0_{\mu\nu}(\boldsymbol{k},\omega)$ through the Dyson equation:

$$G_{\mu\nu}(\boldsymbol{k}\omega) = G^0_{\mu\nu}(\boldsymbol{k},\omega) + \sum_{\mu'\nu'} G^0_{\mu\mu'}(\boldsymbol{k}\omega)\Sigma_{\mu'\nu'}(\boldsymbol{k},\omega)G_{\nu'\nu}(\boldsymbol{k},\omega) \tag{2.4.29}$$

where $\Sigma_{\mu\nu}(\boldsymbol{k},\omega)$ is the self-energy which quantifies how the magnon-magnon interaction will mix together the unperturbed Green functions and is calculated through perturbation theory. The reason we recall this calculation is that it has been shown that the self-energy $\Sigma_{\mu\nu}(\boldsymbol{k},\omega)$ vanishes for long wavelength $\boldsymbol{k}\to 0$[Igarashi, 1992] which justifies the SWT being accounted for as a long wavelength theory. This is important for the coming discussion as some spin-wave results are therefore robust such as for instance the long distance algebraic decay of the transverse spin-spin correlation function $\langle S^-_i S^+_{i+\boldsymbol{r}}\rangle$. On the other hand the measured anomalies precisely happen at the short wavelength/high energy part of the spectrum where the convergence of the perturbation series is less robust. Indeed while Series Expansion [Zheng et al., 2005] and Quantum Monte Carlo [Sandvik and Singh, 2001; Syljuåsen and Rønnow, 2000] could obtain the 7% MBZ boundary dispersion, a 3rd order spin-wave expansion could only recover a dispersion of about 3%, raising doubts about the convergence of the perturbation series.

2.4.2 Fermionized Heisenberg model

In order to tackle the idea of fractional excitations in the QSHAF, we first need to somehow express the Heisenberg Hamiltonian in a language with fractional spin-1/2 quasiparticle creation and annihilation operators. Note that, in the XY model in 1D one could achieve this using the Jordan-Wigner transformation and map the spin operators to spinless fermions. But this mapping relied on the uniqueness of the string operator definition eq. 2.2.9 and the nearest-neighbour restriction of the interaction [Giamarchi, 2004]. In 2D the string operator attached to the Jordan-Wigner transformation may be defined in many ways and the "magic" cancellation of the string operator found in the 1D XY model would not happen here anymore. We thus turn towards a much less inspired transformation and simply express the spin-$\frac{1}{2}$ operators in second-quantized form:

$$S^\alpha_i \to \sum_{\sigma,\sigma'} c^\dagger_{i\sigma}\left(S^\alpha_i\right)_{\sigma\sigma'} c_{i\sigma'}. \tag{2.4.30}$$

The Heisenberg Hamiltonian then becomes:

$$\mathscr{H} = \sum_{\langle i,j\rangle} \sum_{\alpha} \sum_{1234} c^{\dagger}_{i\sigma_1} \left(S^{\alpha}_i\right)_{\sigma_1\sigma_2} c_{i\sigma_2} c^{\dagger}_{j\sigma_3} \left(S^{\alpha}_j\right)_{\sigma_3\sigma_4} c_{j\sigma_4} \tag{2.4.31}$$

$$= \sum_{\langle i,j\rangle} \left[\frac{1}{4} \left(n_{i\uparrow} n_{j\uparrow} + n_{i\downarrow} n_{j\downarrow} - n_{i\uparrow} n_{j\downarrow} - n_{i\downarrow} n_{j\uparrow} \right) + \frac{1}{2} \left(c^{\dagger}_{i\uparrow} c_{i\downarrow} c^{\dagger}_{j\downarrow} c_{j\downarrow} + c^{\dagger}_{i\downarrow} c_{i\uparrow} c^{\dagger}_{j\uparrow} c_{j\downarrow} \right) \right] \tag{2.4.32}$$

$$= -\frac{1}{2} \sum_{\langle i,j\rangle} \left[n_i \left(\frac{1}{2} n_i - 1 \right) + \sum_{\alpha\beta} c^{\dagger}_{i\alpha} c_{j\alpha} c^{\dagger}_{j\beta} c_{i\beta} \right] \tag{2.4.33}$$

In this fermionic formulation, doubly occupied and empty sites now belong to the enhanced Hilbert space. The Heisenberg Hamiltonian eq. 2.3.1 and its fermionized version 2.4.33 might only be equivalent on the subspace corresponding to half-filling $N_\uparrow = N_\downarrow = N/2$ and $D = 0$ double occupancies or empty sites (note that in this subspace the first term in eq. 2.4.33 is a constant and will be omitted hereafter). It turns out that eq. 2.4.33 commutes with $\hat{D} = \sum_i n_{i\uparrow} n_{i\downarrow}$ thus the two formulations are equivalent on the physical Hilbert space. But when applying approximations we might break this property. A way to enforce it a priori is to add explicitly the constraint into the fermionic spin operators:

$$c_{i\sigma} \rightarrow \tilde{c}_{i\sigma} = c_{i\sigma}(1 - n_{i\bar{\sigma}}) \tag{2.4.34}$$

$$c^{\dagger}_{i\sigma} \rightarrow \tilde{c}^{\dagger}_{i\sigma} = (1 - n_{i\bar{\sigma}}) c^{\dagger}_{i\sigma} \tag{2.4.35}$$

as one can verify that $\left[\tilde{c}_{i\sigma}, \hat{D}\right] = 0$. Another way to enforce the constraint of no-double occupancies is through the so-called Gutzwiller projection:

$$P_{D=0} = \prod_i \left(1 - n_{i\uparrow} n_{i\downarrow}\right). \tag{2.4.36}$$

Applying this projector left-hand and right-hand side of an approximate of eq. 2.4.33 will cure a posteriori the non-commuting parts of an approximated Hamiltonian such that

$$\left[P_{D=0} \mathscr{H}_{\text{approx}} P_{D=0}, \hat{D}\right] = 0. \tag{2.4.37}$$

Equivalently, the Gutzwiller projection may simply be applied to the eigenstates found in a particular approximation. In the following we will heavily use the Gutzwiller projection which we will implement numerically.

2.4.3 Projected Mean Field theories

The simplest approximation one can think of to diagonalize the fermionized Heisenberg Hamiltonian is to define mean-fields such that it becomes quadratic in fermion operators. There are many ways one can define the mean fields and we review some of those below. When doing a mean-field approximation, we might break the no-double occupancies constraint

introducing matrix elements between the half-filled $D = 0$ subspace and other $D > 0$ subspaces which are not relevant for approximating the Heisenberg model. As a result, the obtained eigenstates of the mean-field Hamiltonian will contain states belonging to $D > 0$ subspaces. We cure this a-posteriori using the Gutzwiller projection such that a mean-field eigenstate $\left|\psi_{\mathrm{M-F}}\right\rangle$ become

$$\left|\psi_{\mathrm{M-F}}\right\rangle \rightarrow P_{D=0}\left|\psi_{\mathrm{M-F}}\right\rangle. \tag{2.4.38}$$

These kinds of projected wavefunctions were first used by Gutzwiller [Gutzwiller, 1963] to study the Hubbard model in the metallic phase. They have been later put forward in the context of high-temperature superconductivity along with the RVB proposal [Anderson, 1987]. When defining the mean-fields, we must be careful that they obey the symmetries present in the Heisenberg model in particular we want the total z-component of the total spin to be conserved. We define the three mean-fields:

$$h_{i\sigma} = -h_{i\bar{\sigma}} = \langle c^{\dagger}_{i\sigma} c_{i\sigma}\rangle \tag{2.4.39}$$

$$\chi_{ij} = \chi^{*}_{ji} = 2\langle c^{\dagger}_{i\sigma} c_{j\sigma}\rangle \tag{2.4.40}$$

$$\Delta_{ij} = \Delta_{ji} = \langle c_{i\uparrow} c_{j\downarrow}\rangle. \tag{2.4.41}$$

Introducing those in eq. 2.4.33 we obtain the following mean-field Hamiltonian where constants have been omitted:

$$\begin{aligned}\mathscr{H}_{\mathrm{M-F}} = -\frac{1}{4}\sum_{\langle i,j\rangle}\sum_{\sigma}\Big[&\chi_{ij} c^{\dagger}_{j\sigma} c_{j\sigma} + \Delta_{ij}\epsilon_{\sigma\bar{\sigma}} c^{\dagger}_{i\bar{\sigma}} c^{\dagger}_{j\sigma} + \mathrm{H.C.} \\ &+ h_{j\sigma} c^{\dagger}_{i\sigma} c_{i\sigma} + h_{i\sigma} c^{\dagger}_{j\sigma} c_{i\sigma}\Big].\end{aligned} \tag{2.4.42}$$

The definition of the different mean-fields is then guided by physical insight and results in various mean-field Ansätze. For instance as we know that the classical Heisenberg model favours antiferromagnetism, we will choose for $h_{i\sigma}$ an antiferromagnetic order parameter:

$$h_{i\sigma} = \sigma h e^{i\boldsymbol{Q}\cdot\boldsymbol{R}_i} \quad \boldsymbol{Q} = (\pi,\pi). \tag{2.4.43}$$

The choice of a good form of the other two mean-fields is less obvious. The first one we present is the so-called d-wave RVB Ansatz. It is inspired by the Bardeen-Cooper-Schrieffer mean-field decoupling of the effective electron-phonon Hamiltonian found to govern conventional superconductivity [Bardeen et al., 1957]. The 'd-wave' name comes from the similarity of the chosen mean-field symmetries with the one of a d-shell electronic orbital. It was inspired by the superconducting gap symmetry found in the cuprate family by ARPES measurements [Lee

et al., 2006]. The mean-fields Ansatz is:

$$\chi_{ij} = \chi_0 \in \mathbb{R} \tag{2.4.44}$$

$$\Delta_{ij} = \begin{cases} \Delta_0 & j = i \pm \hat{\boldsymbol{e}}_x \\ -\Delta_0 & j = i \pm \hat{\boldsymbol{e}}_y \\ 0 \text{ otherwise} \end{cases} . \tag{2.4.45}$$

An alternative Ansatz is the so-called Staggered Flux (SF) mean-field as it describes free fermions on a lattice with staggered fluxes threading the plaquettes (fig. 2.10). The mean-field is parametrized by the two parameters t and θ_0. While t only sets an energy scale, θ_0 describes the phase a fermion would acquire by circulating around a plaquette ($\pm 4\theta_0$). This mean-field decoupling was first proposed by Affleck and Marston [Marston and Affleck, 1989] as it turns out it is the exact solution of eq. 2.4.33 in the limit where, instead of $\sigma \in \{\uparrow, \downarrow\}$ the spin index takes $n \to \infty$ flavors. The mean-fields definition is:

$$\chi_{ij} = t e^{i\theta_{ij}} \quad \theta_{ij} = \theta_0 (-1)^{i_x + j_y} \tag{2.4.46}$$

$$\Delta_{ij} = 0. \tag{2.4.47}$$

Although it seems at first sight that these two mean-fields definitions are very different from each others, it turns out that they produce exactly the same eigenvalues. This is explained in the following section.

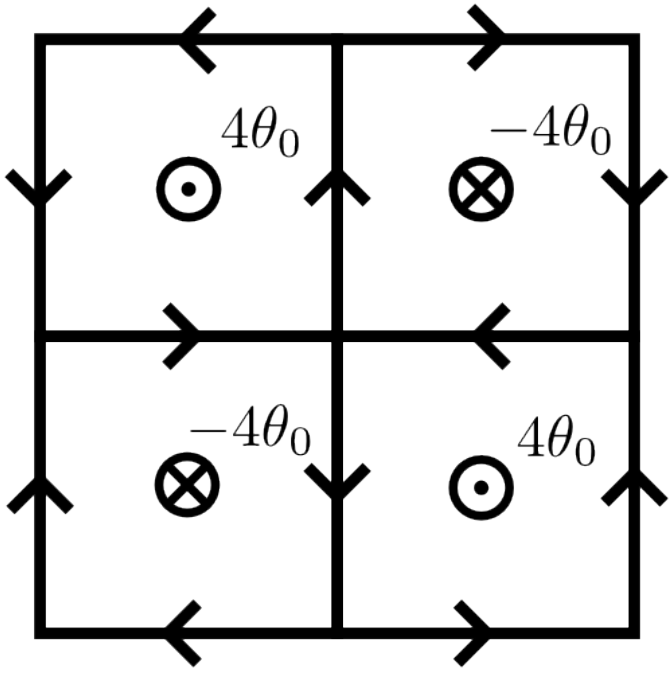

Figure 2.10 – representation of the staggered flux mean-field solution. Fluxes of $\pm 4\theta_0$ threads the square lattice plaquettes in a staggered manner.

2.4.4 Equivalences between mean field theories

When going to the fermionized version of the Heisenberg Hamiltonian, there are actually many ways one can define the fermions in the new enhanced Hilbert space. For instance an obvious transformation that leaves the Heisenberg model invariant is a local U(1) gauge transformation:

$$c_{i\sigma} \rightarrow e^{i\omega_i} c_{i\sigma}. \tag{2.4.48}$$

However there is more. Introducing $\boldsymbol{\psi}_i$

$$\boldsymbol{\psi}_i = \begin{pmatrix} c_{i\uparrow} \\ c^\dagger_{i\downarrow} \end{pmatrix} \tag{2.4.49}$$

we remark that the spin operators can be rewritten as [Lee and Feng, 1988]:

$$S^+_i = \frac{1}{2} \boldsymbol{\psi}^T_i \begin{pmatrix} 0 & 1 \\ -1 & 0 \end{pmatrix} \boldsymbol{\psi}_i \tag{2.4.50}$$

$$S^z_i = \frac{1}{2} \left[\boldsymbol{\psi}^\dagger_i \boldsymbol{\psi}_i - 1 \right]. \tag{2.4.51}$$

such that it is easy to see that the SU(2) transformation

$$\boldsymbol{\psi}_i \rightarrow W_i \boldsymbol{\psi}_i \quad W_i \in \mathrm{SU}(2) \tag{2.4.52}$$

does leave the spin operator unchanged since for a SU(2) matrix W_i

$$W^T_i \begin{pmatrix} 0 & 1 \\ -1 & 0 \end{pmatrix} W_i = \begin{pmatrix} 0 & 1 \\ -1 & 0 \end{pmatrix} \tag{2.4.53}$$

$$W^H_i W_i = \mathbb{1}. \tag{2.4.54}$$

Therefore there are many ways to fermionize the Heisenberg Hamiltonian which, when considered on the half-filled with no double occupancies subspace, are equivalent. To be physically relevant, the mean-field Ansatz must also exhibit this symmetry. If we introduce the $\boldsymbol{\psi}_i$ operators in the mean-field Hamiltonian eq. 2.4.42 then we obtain:

$$\mathscr{H}_{\mathrm{M-F}} = -\frac{1}{4} \sum_{\langle i,j \rangle} \left[\boldsymbol{\psi}^\dagger_i U_{ij} \boldsymbol{\psi}_j + \mathrm{H.C.} + \boldsymbol{\psi}^\dagger_i H_j \boldsymbol{\psi}_i + \boldsymbol{\psi}^\dagger_j H_i \boldsymbol{\psi}_j \right] \tag{2.4.55}$$

with

$$U_{ij} = \begin{pmatrix} \chi^*_{ij} & -\Delta_{ij} \\ -\Delta^*_{ij} & -\chi_{ij} \end{pmatrix} = -\left\langle \boldsymbol{\psi}_i \boldsymbol{\psi}^\dagger_j \right\rangle \tag{2.4.56}$$

and

$$H_i = \begin{pmatrix} h_{i\uparrow} & 0 \\ 0 & h_{i\uparrow} \end{pmatrix} = \frac{1}{2}\left(\left\langle \boldsymbol{\psi}_i^\dagger \boldsymbol{\psi}_i \right\rangle - 1\right)\begin{pmatrix} 1 & 0 \\ 0 & 1 \end{pmatrix} \tag{2.4.57}$$

We now consider the local SU(2) transformations

$$\boldsymbol{\psi}_i \rightarrow W_i \boldsymbol{\psi}_i \tag{2.4.58}$$

$$\boldsymbol{\psi}_j \rightarrow W_j \boldsymbol{\psi}_j. \tag{2.4.59}$$

We see that the mean-field Hamiltonian remains invariant. Using such an SU(2) transformation it has been shown [Affleck et al., 1988] that the d-wave RVB and SF Ansätze are in fact equivalent with

$$t = \sqrt{\chi_0^2 + \Delta_0^2} \tag{2.4.60}$$

$$\theta_0 = \tan^{-1}\left(\frac{\Delta_0}{\chi_0}\right). \tag{2.4.61}$$

2.4.5 Projected mean-field magnetic excitation spectrum

We shortly review here previous efforts into predicting the excitation spectrum of the square lattice antiferromagnet based on the mean-field approach.
Following the mean-field decoupling of eq. 2.4.33 omitting the Gutzwiller projection, one can simply diagonalize the Hamiltonian and write down self-consistent equations defining the mean-fields. In the staggered flux gauge, it has been shown that the self-consistent flux is $4\theta_0 = \pi$ [Marston and Affleck, 1989] such that the staggered pattern from fig. 2.10 is lost since the phase acquired by circulating around a plaquette is $e^{i\pi} = e^{-i\pi}$. Of course neglecting the Gutzwiller projection renders the mean-field results doubtful at best. A strategy is to consider the following Hamitlonian treated in the mean-field approach:

$$\mathscr{H} = -J_{eff} \sum_{\langle i,j\rangle,\sigma} \left[e^{i\theta_{ij}} c_{i\sigma}^\dagger c_{j\sigma} + \text{h.c.} \right] + V \sum_i n_{i\uparrow} n_{i\downarrow} \tag{2.4.62}$$

with θ_{ij} as defined in eq. 2.4.46 with $\theta_0 = \pi/4$. V is an added on-site repulsion, a strategy to account to some level for the Gutzwiller projection. The mean-field solution gives the eigenvalues as

$$E_{\boldsymbol{k}} = J_{eff}\sqrt{\cos^2 k_x + \cos^2 k_y + m^2} \tag{2.4.63}$$

where m is a Néel field. The self-consistent relation between m and V is given by

$$V^{-1} = N^{-1} \sum_{|\boldsymbol{k}|<\pi} E_{\boldsymbol{k}}^{-1} \tag{2.4.64}$$

The strategy then is to find some scheme such that the choice of parameters J_{eff} and m (or equivalently V) reflects the effect of the Gutzwiller projection. In Hsu [1990], $J_{eff} = J$ and m is the optimal value from variational Monte Carlo while the Gutzwiller projection still is accounted for in some approximate way. In Ho et al. [2001] the values of J_{eff} and m are obtained from a self-consistent approach first developped in Laughlin [1995]. The effect of the particle repulsion V is then accounted for in a Random Phase Approximation (RPA) fashion. The generalized magnetic susceptibility is obtained as:

$$\chi^{\pm}(\boldsymbol{q},\omega) = \frac{\chi_0^{\pm}(\boldsymbol{q},\omega)}{1 - V\chi_0^{\pm}(\boldsymbol{q},\omega)} \tag{2.4.65}$$

where $\chi_0^{\pm}$ is the transverse susceptibility calculated in the mean-field solution. Importantly, in both approach the excitations are made out of projected mean-field particle-hole pairs which form a bound state with a dispersion similar to the magnon one from SWT. Additionally the calculation in Ho et al. [2001] evidences the emergence of a continuum of high-energy excitations which, at $\boldsymbol{q} = (\pi, 0)$ merges with the otherwise sharp magnon mode.
However the approximate treatement of the Gutzwiller projection in the two approaches obviously is a source of uncertainties. In Hsu [1990], the complications induced by the approximate Gutzwiller projection only allowed for the calculation of the poles of the excitation spectrum – similar to a single-mode approximation – such that the question of the possibility of a continuum could not be addressed. In Ho et al. [2001], the RPA treatment of the Gutzwiller projection allows for a finite number of double occupancies such that the spin sum rule $\boldsymbol{S}^2 = S(S+1)$ is not fullfilled. In that case it is impossible to tell whether the calculated spectrum exhaust the spectral weight.

2.4.6 The Staggered Flux + Néel Wavefunction

The coming numerical calculations will be based on the Staggered Flux plus Néel (SF+N) mean-field Ansatz which we describe here. The staggered flux gauge is convenient because in the mean-field Hamiltonian there are no pairing terms such as $c^{\dagger}_{i\sigma} c^{\dagger}_{j\bar{\sigma}}$. The resulting quasiparticle operators diagonalizing it therefore do not contain superposition of creation and annihilation operators such that the number of particles is conserved and the wavefunction can simply be factorized such as

$$\left|\psi\right\rangle = \prod_{\boldsymbol{k},\sigma} \gamma^{\dagger}_{\boldsymbol{k},\sigma} \left|0\right\rangle . \tag{2.4.66}$$

The mean-field Hamiltonian is:

$$\mathscr{H}_{\mathrm{SF+N}} = \mathscr{H}_{\mathrm{SF}} + \mathscr{H}_{\mathrm{N}} \tag{2.4.67}$$

$$\mathscr{H}_{\mathrm{SF}} = -\frac{1}{2}\sum_{i\,\mathrm{even},\sigma}\left(e^{i\theta_0}c^{\dagger}_{i\sigma}c_{i+\boldsymbol{x}\sigma} + e^{-i\theta_0}c^{\dagger}_{i\sigma}c_{i+\boldsymbol{y}\sigma} + \mathrm{H.C.}\right)$$
$$-\frac{1}{2}\sum_{i\,\mathrm{odd},\sigma}\left(e^{-i\theta_0}c^{\dagger}_{i\sigma}c_{i+\boldsymbol{x}\sigma} + e^{i\theta_0}c^{\dagger}_{i\sigma}c_{i+\boldsymbol{y}\sigma} + \mathrm{H.C.}\right) \tag{2.4.68}$$

$$\mathscr{H}_{\mathrm{N}} = -h_{\mathrm{N}}\sum_{\sigma}\sigma\left(\sum_{i\,\mathrm{even}}c^{\dagger}_{i\sigma}c_{i\sigma} - \sum_{i\,\mathrm{odd}}c^{\dagger}_{i\sigma}c_{i\sigma}\right) \tag{2.4.69}$$

Where $\sigma \in \{-1,1\}$. Using the Fourier transform of the creation and annihilation operators we obtain a more compact form:

$$\mathscr{H}_{\mathrm{SF+N}} = \sum_{\boldsymbol{k}\in\mathrm{MBZ},\sigma} -\boldsymbol{\alpha}^{\dagger}_{\boldsymbol{k}\sigma}\begin{pmatrix}\sigma h_{\mathrm{N}} & \Delta^{*}_{\boldsymbol{k}}\\ \Delta_{\boldsymbol{k}} & -\sigma h_{\mathrm{N}}\end{pmatrix}\boldsymbol{\alpha}_{\boldsymbol{k}\sigma} \tag{2.4.70}$$

with

$$\boldsymbol{\alpha}_{\boldsymbol{k}\sigma} = \frac{1}{\sqrt{2}}\begin{pmatrix}c_{\boldsymbol{k}\sigma} + c_{\boldsymbol{k}+\boldsymbol{Q}\sigma}\\ c_{\boldsymbol{k}\sigma} - c_{\boldsymbol{k}+\boldsymbol{Q}\sigma}\end{pmatrix} \tag{2.4.71}$$

and

$$\Delta_{\boldsymbol{k}} = \frac{1}{2}\left(e^{i\theta_0}\cos(k_x) + e^{-i\theta_0}\cos(k_y)\right). \tag{2.4.72}$$

We thus look for a unitary transformation $P^{-1}_{\boldsymbol{k}\sigma} = P^{H}_{\boldsymbol{k}\sigma}$ such that

$$\Omega_{\boldsymbol{k}\sigma} = P^{-1}_{\boldsymbol{k}\sigma}\begin{pmatrix}\sigma h_{\mathrm{N}} & \Delta^{*}_{\boldsymbol{k}}\\ \Delta_{\boldsymbol{k}} & -\sigma h_{\mathrm{N}}\end{pmatrix}P_{\boldsymbol{k}\sigma} \tag{2.4.73}$$

is a diagonal matrix. Defining the transformation matrix as

$$P_{\boldsymbol{k}\sigma} = \begin{pmatrix}u_{\boldsymbol{k}\sigma-} & u_{\boldsymbol{k}\sigma+}\\ v_{\boldsymbol{k}\sigma-} & v_{\boldsymbol{k}\sigma+}\end{pmatrix} \tag{2.4.74}$$

we achieve this with the following definitions:

$$u_{\boldsymbol{k}\sigma-} = \sqrt{\frac{1}{2}\left(1 + \frac{\sigma h_{\mathrm{N}}}{\omega_{\boldsymbol{k}}}\right)} \tag{2.4.75}$$

$$v_{\boldsymbol{k}\sigma-} = \frac{\Delta_{\boldsymbol{k}}}{|\Delta_{\boldsymbol{k}}|}\sqrt{\frac{1}{2}\left(1 - \frac{\sigma h_{\mathrm{N}}}{\omega_{\boldsymbol{k}}}\right)} \tag{2.4.76}$$

$$u_{\boldsymbol{k}\sigma+} = -v^{*}_{\boldsymbol{k}\sigma-} \tag{2.4.77}$$

$$v_{\boldsymbol{k}\sigma+} = u_{\boldsymbol{k}\sigma-} \tag{2.4.78}$$

where $\omega_{\boldsymbol{k}}$ is the quasiparticle eigen-energy:

$$\Omega_{\boldsymbol{k}\sigma} = \begin{pmatrix} -\omega_{\boldsymbol{k}} & 0 \\ 0 & \omega_{\boldsymbol{k}} \end{pmatrix} \tag{2.4.79}$$

$$\omega_{\boldsymbol{k}} = \sqrt{|\Delta_{\boldsymbol{k}}|^2 + h_{\mathrm{N}}^2}. \tag{2.4.80}$$

We have thus diagonalized the SF+N Hamiltonian eq. 2.4.67 using a canonical transformation which defines two quasiparticle bands. The reason there are two bands is because in eq. 2.4.67 the original lattice translation symmetry is broken. The resulting lattice has a doubled unit cell containing two sites thus the obtained two bands with the corresponding quasi-particle operators. We note that the doubling of the unit cell is uniquely due to the Néel mean field. While $\mathscr{H}_{\mathrm{SF}}$ eq. 2.4.68 seems to break the translational symmetry (along with some 90° crystal rotation symmetry), this transformation can in fact be written as an SU(2) transformation which is a symmetry of the mean-field Hamiltonian in the physical Hilbert space. However the same is not true for $\mathscr{H}_{\mathrm{N}}$ eq. 2.4.69. There an SU(2) transformation cannot account for a translation by one unit cell resulting into the changing the sign of the h_{N} mean-field parameter. With respect to the original Hamiltonian creation and annihilation operators $c_{\boldsymbol{k}\sigma}$, the canonical transform reads:

$$\begin{pmatrix} \gamma_{\boldsymbol{k}\sigma-} \\ \gamma_{\boldsymbol{k}\sigma+} \end{pmatrix} = \frac{1}{\sqrt{2}} \begin{pmatrix} u_{\boldsymbol{k}\sigma-} & v^*_{\boldsymbol{k}\sigma-} \\ u^*_{\boldsymbol{k}\sigma+} & v_{\boldsymbol{k}\sigma+} \end{pmatrix} \begin{pmatrix} c_{\boldsymbol{k}\sigma} + c_{\boldsymbol{k}+\boldsymbol{Q}\sigma} \\ c_{\boldsymbol{k}\sigma} - c_{\boldsymbol{k}+\boldsymbol{Q}\sigma} \end{pmatrix} \tag{2.4.81}$$

where $\boldsymbol{k}$ is restricted to the Magnetic Brillouin Zone (MBZ) $|\boldsymbol{k}| \leq \pi$. Expressed with the new quasi-particle operators the real space fermion operators are

$$c_{i\sigma} = \sqrt{2} \sum_{\boldsymbol{k}\in\mathrm{MBZ}} e^{i\boldsymbol{k}\boldsymbol{R}_i} \left[\left(\epsilon_{\boldsymbol{R}_i} u_{\boldsymbol{k}\sigma-} + \bar{\epsilon}_{\boldsymbol{R}_i} v_{\boldsymbol{k}\sigma-} \right) \gamma_{\boldsymbol{k}\sigma-} + \left(\epsilon_{\boldsymbol{R}_i} u_{\boldsymbol{k}\sigma+} + \bar{\epsilon}_{\boldsymbol{R}_i} v_{\boldsymbol{k}\sigma+} \right) \gamma_{\boldsymbol{k}\sigma+} \right] \tag{2.4.82}$$

where $\epsilon_{\boldsymbol{R}_i}$ and $\bar{\epsilon}_{\boldsymbol{R}_i}$ tell whether site i is even or odd:

$$\epsilon_{\boldsymbol{R}_i} = \frac{1}{2}\left(1 + e^{i\boldsymbol{Q}\boldsymbol{R}_i}\right) \tag{2.4.83}$$

$$\bar{\epsilon}_{\boldsymbol{R}_i} = \frac{1}{2}\left(1 - e^{i\boldsymbol{Q}\boldsymbol{R}_i}\right). \tag{2.4.84}$$

We show in fig. 2.11 the obtained energy bands. For $h_{\mathrm{N}} = 0$ the bands are gapless with Dirac cones at $\boldsymbol{k} = (\pm\pi/2, \pm\pi/2)$. The effect of the Néel mean field h_{N} is to gap the two bands turning the Dirac cones into minima/maxima of the bands. We note that the canonical transformation is ill-defined at $\boldsymbol{k} = (\pm\pi/2, \pm\pi/2)$ since the phase $\Delta_{\boldsymbol{k}}/|\Delta_{\boldsymbol{k}}|$ has no well-defined limit when $\boldsymbol{k} \to (\pm\pi/2, \pm\pi/2)$. This will have technical consequences when implementing the numerical calculation.

The ground state of the SF+N mean field Hamiltonian at half-filling and in the $S^z_{\mathrm{tot}} = 0$ sector corresponds into completely filling the bottom band. The mean-field ground-state is thus:

$$\left|\psi_{\mathrm{GS}}\right\rangle = \prod_{\boldsymbol{k}\in\mathrm{MBZ}} \gamma^\dagger_{\boldsymbol{k}\uparrow-} \gamma^\dagger_{\boldsymbol{k}\downarrow-} \left|0\right\rangle. \tag{2.4.85}$$

Looking at the definition of the quasi-particle operators eq. 2.4.81, one immediately sees that the mean-field ground state will contain many double occupancies and thus cannot be as such an approximation of the Heisenberg model ground state. Only the Gutzwiller-projected mean-field ground-state is significant:

$$|\mathrm{GS}(\theta_0, h_\mathrm{N})\rangle = P_{D=0}\left|\psi_\mathrm{GS}(\theta_0, h_\mathrm{N})\right\rangle \tag{2.4.86}$$

where we have explicitly put back the mean-fields definition dependence. How good an approximation of the Heisenberg model ground state is it and for which parameters θ_0 and h_N? To answer this we can try to calculate the variational energy of this state:

$$E_\mathrm{GS}(\theta_0, h_\mathrm{N}) = \frac{\langle \mathrm{GS}|\mathscr{H}|\mathrm{GS}\rangle}{\langle \mathrm{GS}|\mathrm{GS}\rangle} = \frac{\left\langle \psi_\mathrm{GS}\right| P_{D=0}\mathscr{H}P_{D=0}\left|\psi_\mathrm{GS}\right\rangle}{\left\langle \psi_\mathrm{GS}\right| P_{D=0}\left|\psi_\mathrm{GS}\right\rangle}. \tag{2.4.87}$$

Due to the complexity of the Gutzwiller projection, there is no simple way to evaluate eq. 2.4.87. Analytically one can use further approximation such as the Gutzwiller approximation [Gros, 1989]. In this thesis we choose to treat exactly the Gutzwiller projection using the variational Monte Carlo numerical technique presented in the following section.

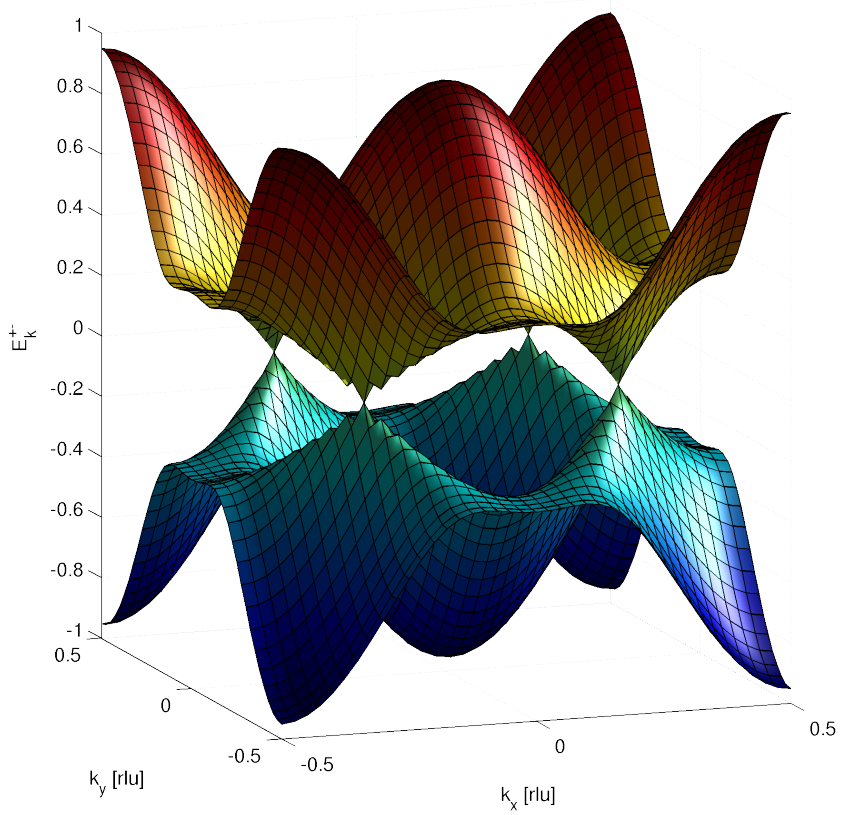

Figure 2.11 – Quasi-particle bands from the SF+N mean-field Hamiltonian.

2.5 Variational Monte Carlo

In a broad context Variational Monte Carlo (VMC) is a numerical technique to calculate the zero-temperature quantum average of some quantities using a motivated approximation of the ground state called the trial wavefunction $|\psi_{\text{trial}}\rangle$. If we are able to calculate the overlap of the trial wavefunction with some complete basis of the Hilbert space $\{|\alpha\rangle\}$ and also are able in this basis to calculate the matrix elements of the quantity under interest $\langle\alpha|O|\beta\rangle$, then the quantum average is:

$$\langle O\rangle_{\text{trial}} = \sum_{\alpha\beta} \frac{\langle\psi_{\text{trial}}|\alpha\rangle\langle\alpha|O|\beta\rangle\langle\beta|\psi_{\text{trial}}\rangle}{\langle\psi_{\text{trial}}|\psi_{\text{trial}}\rangle}. \tag{2.5.1}$$

As the sum over the states $\{|\alpha\rangle\}$ surely is much too large to be evaluated by some regular sampling, we turn towards a Monte Carlo approach. For a quantity F

$$F = \sum_{\alpha} \rho(\alpha) f(\alpha) \tag{2.5.2}$$

where $\rho(\alpha)$ is a normalized probability distribution, one can design a Markov chain Monte Carlo using the Metropolis-Hastings algorithm [Metropolis et al., 1953; Hastings, 1970] to evaluate the sum. In the case of eq. 2.5.1, it is simple to turn it into a form suitable for a Metropolis Monte Carlo evaluation [Gros, 1989; Foulkes et al., 2001]:

$$\langle O\rangle = \sum_{\alpha} \underbrace{\frac{|\langle\alpha|\psi_{\text{trial}}\rangle|^2}{\langle\psi_{\text{trial}}|\psi_{\text{trial}}\rangle}}_{\rho(\alpha)} \underbrace{\left(\sum_{\beta}\langle\alpha|O|\beta\rangle\frac{\langle\beta|\psi_{\text{trial}}\rangle}{\langle\alpha|\psi_{\text{trial}}\rangle}\right)}_{f(\alpha)} \tag{2.5.3}$$

where

$$\rho(\alpha) = \frac{|\langle\alpha|\psi_{\text{trial}}\rangle|^2}{\langle\psi_{\text{trial}}|\psi_{\text{trial}}\rangle} \tag{2.5.4}$$

is a normalized probability distribution and

$$f(\alpha) = \sum_{\beta}\langle\alpha|O|\beta\rangle\frac{\langle\beta|\psi_{\text{trial}}\rangle}{\langle\alpha|\psi_{\text{trial}}\rangle} \tag{2.5.5}$$

is the quantity of interest for the point or state α. We give a short description of the Metropolis Monte Carlo in the appendix A.1.

The quantity thus sampled will be for instance the variational energy $\langle\mathscr{H}\rangle_{\text{trial}}$ of a state $|\psi_{\text{trial}}\rangle$ which may depend on some undetermined set of parameters. An associated problem often is to find the proper set of parameters such that the variational energy is minimized, thus providing an approximate of the system ground state. An important aspect of the VMC technique is that the sampled quantities entirely rely on the trial wavefunction. Thus if one seeks exact numerical estimates of physical quantities for a given problem, the VMC technique might

not be the most suitable approach as it introduces an explicit bias by choosing a more or less well motivated trial wavefunction. But this disadvantage can be turned around in the case we actually are focused on the trial wavefunction per se. There are many cases where the choice of a trial wavefunction contains deep physical motivations. This choice then is a physical Ansatz and the VMC technique allows to draw its consequences in term of physical, and potentially measurable, quantities. In this perspective, the VMC technique is not aimed at providing a numerical way of *simulating* the physics of some problem. Rather it may be understood as a semi-analytical tool which allows to draw the physical consequences of some theoretical hypotheses as encompassed in the trial wavefunction. The focus therefore is more about establishing an effective theory for a system than about simulating its physical properties.

2.5.1 Average quantities for projected wavefunctions

In the context of projected wavefunctions, the trial wavefunction is simply the projected mean-field ground state $\left|\psi_{\text{trial}}\right\rangle = P_{D=0}\left|\psi_{\text{GS}}\right\rangle$, or any other filling of the mean-field bands $P_{D=0}\left|\psi\right\rangle$. The idea is to deal with the projection by simply considering the Hilbert space of singly occupied sites when introducing the projector $\sum_\alpha |\alpha\rangle\langle\alpha|$. More precisely the $|\alpha\rangle$ are states where spin-$\frac{1}{2}$ particles are arranged on the system sites without double occupancies:

$$|\alpha\rangle = |(\boldsymbol{R}_1,\sigma_1),(\boldsymbol{R}_2,\sigma_2),\ldots,(\boldsymbol{R}_N,\sigma_N)\rangle \quad \boldsymbol{R}_i \neq \boldsymbol{R}_j \;\forall i,j \tag{2.5.6}$$

where $\sigma_i \in \{\uparrow,\downarrow\}$ is the spin index. The Gutzwiller projection then takes the simple form:

$$P_{D=0} = \sum_\alpha |\alpha\rangle\langle\alpha|. \tag{2.5.7}$$

On the other hand the mean field wavefunction can be written as

$$\left|\psi\right\rangle = |(\boldsymbol{k}_1,\sigma_1,b_1),(\boldsymbol{k}_2,\sigma_1,b_2),\ldots,(\boldsymbol{k}_N,\sigma_N,b_N)\rangle \tag{2.5.8}$$

where $b_i \in \{+,-\}$ is the band index. In using the spin σ_i in these notations we assume that S^z_{tot} is a good quantum number in the mean-field theory. From eq. 2.5.3 we see that the random walk probability distribution is

$$\rho(\alpha) = \frac{\left|\left\langle\alpha\middle|\psi\right\rangle\right|^2}{\left\langle\psi\middle|\psi\right\rangle}. \tag{2.5.9}$$

A nice feature of the Metropolis random walk is that the normalization must not be known as only ratios of the probability distribution enter the transition matrix eq. A.1.2. The averaged quantities calculated that way also are implicitly normalized as well. The key-quantity is then the amplitude $\left\langle\alpha\middle|\psi\right\rangle$. The states eq. 2.5.6 and 2.5.8 are written in a particles state basis, not in Fock space. The random walk in the $|\alpha\rangle$ states will consist into moving these particles respecting the no-double occupancies condition. But because the particles are fermions, the states written in the particles state basis must be anti-symmetrized. As a result the amplitudes

$\langle\alpha|\psi\rangle$ must be calculated as a Slater determinant:

$$\langle\alpha|\psi\rangle = \mathrm{Det}_{ij}\langle \boldsymbol{R}_i,\sigma_i|\boldsymbol{k}_j,\sigma_j,b_j\rangle \tag{2.5.10}$$

where $\langle \boldsymbol{R}_i,\sigma_i|\boldsymbol{k}_j,\sigma_j,b_j\rangle$ are the single-particle amplitudes. Because S^z_{tot} is a good quantum number, the determinant can be further split in two since it is block-diagonal as $\langle \boldsymbol{R}_i,\uparrow|\boldsymbol{k}_j,\downarrow,b_j\rangle = 0$:

$$\langle\alpha|\psi\rangle = \left(\mathrm{Det}_{i_\uparrow j_\uparrow}\langle \boldsymbol{R}_{i_\uparrow},\uparrow|\boldsymbol{k}_{j_\uparrow},\uparrow,b_{j_\uparrow}\rangle\right)\left(\mathrm{Det}_{i_\downarrow j_\downarrow}\langle \boldsymbol{R}_{i_\downarrow},\downarrow|\boldsymbol{k}_{j_\downarrow},\downarrow,b_{j_\downarrow}\rangle\right). \tag{2.5.11}$$

The numerical calculation of a $N\times N$ determinant is of complexity $\mathcal{O}(N^3)$. We explain in appendix A.2 how one can improve the determinant calculation complexity.

The projected SF+N wavefunction

For the specific case of the staggered flux mean-field wavefunction, the unprojected ground state trial wavefunction simply is $|\psi_{\mathrm{GS}}\rangle$ and depends upon two parameters $(\theta_0, h_{\mathrm{N}})$. An approximate of the ground state may then be obtained by optimizing the variational energy of the trial wavefunction with respect to those parameters. We come back at the issue that the magnetic Brillouin zone does contain special points – the nodes – $\boldsymbol{q} = (\pm\pi/2, \pm\pi/2)$ where the quasi-particles are ill-defined (see eq. 2.4.75-2.4.78). If we take a finite square system of $L\times L$ sites with periodic boundary conditions, then the reciprocal wavevector will be of the form $\boldsymbol{k} = \left(n_x\frac{2\pi}{L}, n_y\frac{2\pi}{L}\right)$ and if L is even then the wavevectors corresponding to the nodes will be included leading to numerical difficulties. A solution is to choose a finite system slightly tilted which results in tilted wavevectors avoiding the nodal points [Gros, 1989]. This has the disadvantage to break some of the lattice symmetries in particular the four-fold rotational symmetry of the square lattice. The approach we chose is to consider a finite square system of $L\times L$ sites but with anti-periodic boundary conditions. For the single-particle Bloch waves this means:

$$\psi_{\boldsymbol{k}n}(\boldsymbol{r}) = e^{i\boldsymbol{k}\boldsymbol{r}}u_{\boldsymbol{k}n}(\boldsymbol{r}) \tag{2.5.12}$$

$$\psi_{\boldsymbol{k}n}(\boldsymbol{r}+L\hat{\boldsymbol{e}}_\alpha) = -\psi_{\boldsymbol{k}n}(\boldsymbol{r}) \tag{2.5.13}$$

which leads to the definition of the wavevector:

$$k_\alpha = \left(n_\alpha + \frac{1}{2}\right)\frac{2\pi}{L}. \tag{2.5.14}$$

The anti-periodicity thus leads into shifting the wavevectors by $\frac{\pi}{L}$ which will make them avoid the nodes. We show a real space/reciprocal space finite system pair in fig. 2.12 where antiperiodic boundary conditions are taken in both the $\hat{\boldsymbol{e}}_x$ and $\hat{\boldsymbol{e}}_y$ directions.

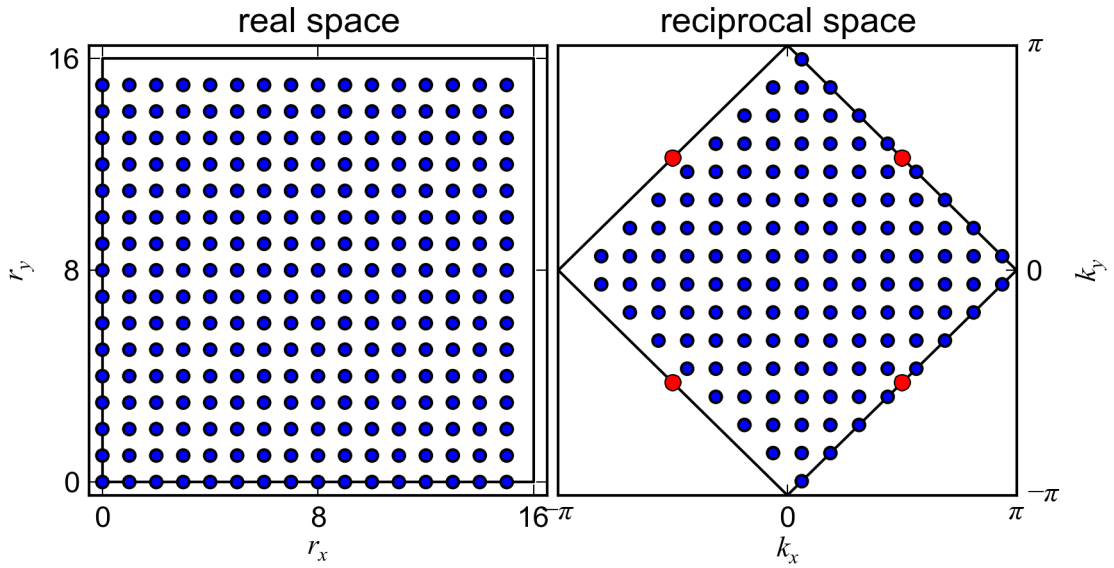

Figure 2.12 – Real space/reciprocal space pair where doubling of the unit cell is assumed. The boundary conditions are anti-periodic in both the $\hat{\boldsymbol{e}}_x$ and $\hat{\boldsymbol{e}}_y$ directions. Red points indicate the position of the SF+N nodes.

2.5.2 Monte Carlo Random Walk

We specifically describe here the Metropolis Monte Carlo random walk for half-filled $S^z_{\text{tot}} = 0$ mean-field wavefunctions. The $|\alpha\rangle$ states have no empty sites and a simple choice for the proposal function generating the random walk is to simply swap neighbouring spins if they are anti-parallel and do nothing if they are parallel. The conditional probability from the proposal function has therefore the property:

$$\mathscr{P}(\alpha|\alpha') = \mathscr{P}(\alpha'|\alpha) \tag{2.5.15}$$

which simplifies the definition of the transition matrix eq. A.1.2. A slight disadvantage is that it artificially increases the acceptance rate as many proposed states are actually identical to the previous one. Another proposal matrix would be to only generate states by swapping nearest neighbour anti-parallel spins, then the conditional probability would be:

$$\mathscr{P}(\alpha'|\alpha) = \frac{1}{N_\alpha^{\uparrow\downarrow}} \tag{2.5.16}$$

where $N_\alpha^{\uparrow\downarrow}$ is the number of nearest-neighbour anti-parallel spins in the state $|\alpha\rangle$. Defined that way the proposal matrix requires to keep track of $N_\alpha^{\uparrow\downarrow}$. In our implementation we do not tune the proposal function in order to optimize the acceptance ratio thus use the first proposal function.

What does the swap of to anti-parallel spins mean for the amplitude $\langle\alpha|\psi\rangle \to \langle\alpha'|\psi\rangle$. Labeling the moving spin-$\uparrow$ particle $l_\uparrow$ and the moving spin-$\downarrow$ particle $l_\downarrow$, we see that the swap only

means a change if the $l_\uparrow$'th line in the $\langle \boldsymbol{R}_{i_\uparrow}, \uparrow | \boldsymbol{k}_{j_\uparrow}, \uparrow, b_{j_\uparrow} \rangle$ spin-$\uparrow$ Slater matrix and the same thing for the spin-$\downarrow$ Slater matrix. We then use a determinant update formula to efficiently calculate the new amplitude from the old one exploiting this fact. This procedure is explained in details in appendix A.2. Here we will only mention that the calculation of the new determinant will only be of $\mathcal{O}(N)$ complexity if N is the size of the matrix instead of the cubic complexity for calculating the determinant from scratch. Due to additional book-keepings of the determinant update formula, the acceptance of a proposed state also has a numerical cost and will be of order $\mathcal{O}(N^2)$.
The random walk can thus be efficiently generated and samples of the measured quantity will be collected every L^2 steps in order to make them independent. The measurement will also have a significant computational cost. Considering the specific case of the Heisenberg model:

$$\mathscr{H} = \sum_{\langle i,j \rangle} S_i^z S_j^z + \frac{1}{2}\left(S_i^+ S_j^- + S_i^- S_j^+ \right) \tag{2.5.17}$$

we see that the off-diagonal part will generate new states $|\beta\rangle \neq |\alpha\rangle$ for which a new amplitude $\langle \beta | \psi \rangle$ must be calculated according to eq. 2.5.5. The associated determinant update with the sum over nearest-neighbour will make the measurement cost of quadratic complexity $\mathcal{O}(N^2)$. Finally important quantities like the transverse spin-spin correlation function will turn out to be pretty expensive:

$$\left\langle S_{\boldsymbol{q}}^- S_{\boldsymbol{q}}^+ \right\rangle = \sum_{ij} e^{i\boldsymbol{q}(\boldsymbol{R}_j - \boldsymbol{R}_i)} \left\langle S_i^- S_j^+ \right\rangle \tag{2.5.18}$$

as they must then be of cubic complexity due to the double sum.

2.5.3 Jastrow factors

We mention here another degree of freedom into defining a variational wavefunction, the so-called Jastrow factor [Jastrow, 1955]. The idea is to allow for more correlation into the trial wavefunction Ansatz than the one directly induced by the Gutzwiller projection. In practice the Jastrow factor is an operator diagonal into the sampling subspace, that is the real space spin configuration in our case. A popular generic form [Edegger et al., 2007] is for instance the spin-spin correlator:

$$\mathscr{J}_s = \exp\left[\sum_{ij} V\left(\boldsymbol{r}_{ij}\right) S_i^z S_j^z \right] \tag{2.5.19}$$

where the different components of $V(\boldsymbol{r})$ potential are independent variational parameters. In the context of the square lattice Heisenberg antiferromagnet, an interesting simple Jastrow factor would be for instance using a staggered potential

$$V(\boldsymbol{r}) = \lambda e^{i\boldsymbol{Q}\cdot\boldsymbol{r}} \tag{2.5.20}$$

where as usual $\boldsymbol{Q} = (\pi, \pi)$ and λ is a variational parameter. The staggered potential will cause antiferromagnetic order in the wavefunction and will artificially break the spin rotation symmetry as is the case in the SF+N trial wavefunction. In the process of this work, we also looked at the even simpler antiferromagnetic Jastrow factor:

$$\mathscr{J}_{\text{AFM}} = \exp\left[\lambda \sum_i e^{i\boldsymbol{Q}\boldsymbol{R}_i} S_i^z\right] \tag{2.5.21}$$

which, in contrast to eq. 2.5.19 with a potential of the form of eq. 2.5.20 will favor only one of the two sublattice magnetization. That is, if $\lambda > 0$ even sites $e^{i\boldsymbol{Q}\boldsymbol{R}_i} = 1$ will have negative magnetization while odd $e^{i\boldsymbol{Q}\boldsymbol{R}_i} = -1$ will have positive magnetization. We will briefly mention later in section 2.7.1 and in section 2.7.2 how such Jastrow antiferromagnetically ordered wavefunctions compare to the SF+N mean-field one.

2.5.4 Other numerical methods

We review here only two other numerical methods mainly because our results will often be compared to those. In strong contrast these two methods provide a way to give an estimate of various quantities corresponding to a physical model while our approach does find those as corresponding to an Ansatz for the ground state wavefunction. Agreement between these approaches strengthen the validity of a given ground state Ansatz, but in the following discussion it is ultimately agreement with experimental results that will be the most important. Although we did not develop yet our formalism for calculating dynamical quantities we will briefly mention how adequate these other numerical techniques are in that respect.

Perturbative Series Expansion

The series expansion technique takes some known limit of the model Hamiltonian and uses it as the basis for a perturbation expansion. The most relevant one for the square lattice Heisenberg model is the Ising limit:

$$\mathscr{H} = \sum_{\langle i,j \rangle} S_i^z S_j^z + \Delta\left(S_i^x S_j^x + S_i^y S_j^y\right). \tag{2.5.22}$$

In the limit where $\Delta = 0$ the model has a classical Néel ground state. One might then attempt to treat the transverse part of the Hamiltonian in a perturbative way for finite Δ. A so-called cluster expansion allows a systematic derivation of the expansion which can be carried out computationally [Gelfand et al., 1990]. Of course, being a perturbation expansion, this technique cannot predict quantum phase transition as a function of Δ as it relies on the assumption one can adiabatically relate the perturbed ground state with the unperturbed one although divergences in the correction might indicate the proximity to a phase transition [Gelfand et al., 1990]. This is probably not an issue in the case of the Heisenberg model on the square lattice as its ground-state does have long-range Néel order and as such should be adiabatically

connected to the classical Néel order state.
The system excitations may be also calculated either using the single mode approximation [Singh, 1993] or in a perturbative way [Singh and Gelfand, 1995]. However the excitations obtained perturbatively also rely on the assumption that the perturbed excited states can be adiabatically connected to those of the unperturbed system. In the case of the Ising limit, the unperturbed excitations of the Néel classical ground state are local spin-flips with a constant energy over the whole magnetic Brillouin zone. Calculating the excitation spectrum from there naturally leads to spin-waves but it has to be noted that it does carry an explicit bias from the adiabaticity assumption.

Stochastic Series Expansion Quantum Monte Carlo

The stochastic series expansion (SSE) quantum Monte Carlo method is a finite temperature method based on an expansion of the partition function. Finite temperature quantum Monte Carlo starts from the thermal average formula:

$$\langle A\rangle = \frac{1}{Z}\mathrm{Tr}\left(Ae^{-\beta H}\right) \tag{2.5.23}$$

$$Z = \mathrm{Tr}\left(e^{-\beta H}\right) \tag{2.5.24}$$

and expand it in order to turn it into a form suitable for Monte Carlo sampling such as eq. 2.5.2. Probably the most famous expansion scheme is the imaginary time-slicing:

$$\langle A\rangle = \frac{1}{Z}\sum_{\alpha}\langle\alpha|\, e^{-\beta H}\,|\alpha\rangle \tag{2.5.25}$$

$$= \frac{1}{Z}\sum_{\alpha_0,\ldots,\alpha_{L-1}}\langle\alpha_0|\, e^{-\Delta_\tau H}\,|\alpha_1\rangle\langle\alpha_1|\ldots|\alpha_{L-1}\rangle\langle\alpha_{L-1}|\, e^{-\Delta_\tau H} A\,|\alpha_0\rangle \tag{2.5.26}$$

with $\Delta_\tau = \beta/L$ which, when $\Delta_\tau \to 0$ leads to the path integral formulation of quantum statistical mechanics. The expansion used in SSE Monte Carlo is a simple Taylor expansion:

$$\sum_{\alpha_0}\langle\alpha_0|\, e^{-\beta H} A\,|\alpha_0\rangle = \sum_{n=0}^{\infty}\frac{(-\beta)^n}{n!}\sum_{\{\alpha\}_{n+1}}\langle\alpha_0|\, H\,|\alpha_n\rangle\langle\alpha_n|\ldots|\alpha_2\rangle\langle\alpha_2|\, H\,|\alpha_1\rangle\langle\alpha_1|\, A\,|\alpha_0\rangle \tag{2.5.27}$$

and uses the fact quantum models on lattices are expressed in terms of bond operators:

$$H = \sum_{pb} H_{p,b} \tag{2.5.28}$$

where b index the bonds and p some "parts" of the Hamiltonian. One can then formulate the above expansion in terms of a sum over α_0 and over bonds operators products $S_n = \prod_{i=1}^{n} H_{p_i,b_i}$ and use importance sampling to carry it out [Sandvik, 1999]. An important prerequisite is that it must be possible to make the matrix elements of the S_n operators positive definite which is generally the case on non-frustrated lattices.
In principle this method is exact modulo the numerical uncertainties thus can provide many

of the physical properties of lattice quantum models. In particular for the Heisenberg model it provides important quantities such as the ground state energy and the staggered magnetization. However when turning towards dynamical quantities, important difficulties arise. For instance the dynamic spin structure factor is the space and time Fourier transform of the dynamical spin-spin correlation function:

$$S^{\alpha\beta}(\boldsymbol{r},t) = \langle S^{\alpha}_{\boldsymbol{R}_i+\boldsymbol{r}}(t) S^{\beta}_{\boldsymbol{R}_i}(0)\rangle \tag{2.5.29}$$

where the time-dependant operator is

$$S^{\alpha}_{\boldsymbol{R}}(t) = e^{itH} S^{\alpha}_{\boldsymbol{R}} e^{-itH}. \tag{2.5.30}$$

Introducing this quantity in eq. 2.5.23 might be done using some expansion scheme but then the complex exponent itH will break the positive definite condition. The work-around is to consider the dynamical quantity in imaginary time $\tau = it$:

$$G^{\alpha\beta}(\boldsymbol{q},\tau) = \sum_{ij} e^{i\boldsymbol{q}(\boldsymbol{R}_j-\boldsymbol{R}_i)} \langle S^{\alpha}_{\boldsymbol{R}_i}(\tau) S^{\beta}_{\boldsymbol{R}_j}(0)\rangle. \tag{2.5.31}$$

The imaginary-time spin-spin correlation function can now be sample through a quantum Monte Carlo method and the dynamic spin structure factor is linked to it by a Laplace transform:

$$G^{\alpha\beta}(\boldsymbol{q},\tau) = \frac{1}{\pi}\int_{-\infty}^{\infty} d\omega S^{\alpha\beta}(\boldsymbol{q},\omega) e^{-\tau\omega}. \tag{2.5.32}$$

In principle one should then invert this relation, a problem which is known as the analytical continuation. But in practice this inversion is rendered highly unstable by the numerical noise contained within the sampled quantity $G(\boldsymbol{q},\tau)$ and schemes to regularize the transform must be designed [Jarrell and Gubernatis, 1996] which will be costly in terms of frequency resolution [Sandvik and Singh, 2001]. Fine details such as the square lattice Heisenberg model zone boundary anomaly will prove very difficult to reproduce with an acceptable confidence. Another approach is to assume some functional form of $S(\boldsymbol{q},\omega)$ allowing to invert eq. 2.5.32[Syljuåsen and Rønnow, 2000; Sandvik and Singh, 2001]. Although the results obtained this way are numerically stable, they are then tied to the assumption chosen for the lineshape and are therefore explicitly biased.

2.6 Dynamical Spin Structure Factor in the Variational Monte Carlo method

The dynamic spin structure factor is a fundamental quantity in the context of quantum magnetism both theoretically and experimentally. Experimentally because it turns out to be very accessible through the inelastic neutron scattering technique. Theoretically because it is linked to probably the simplest quantity describing the dynamical properties of a spin system,

the spin-spin correlation function:

$$S^{\alpha}(\boldsymbol{r},t) = \langle S^{\alpha}_{\boldsymbol{R}_i+\boldsymbol{r}}(t) S^{\alpha}_{\boldsymbol{R}_i}(0)\rangle. \tag{2.6.1}$$

It asks the simple question of the time and space correlation of two successive spin measurement. Since the system under study are usually space and time-translation invariant, it is natural to study the time and space Fourier transform of this quantity which defines the dynamic spin structure factor:

$$S^{\alpha}(\boldsymbol{q},\omega) = \int dt \sum_{i,\boldsymbol{r}} e^{i\boldsymbol{q}\boldsymbol{r}+i\omega t} \langle S^{\alpha}_{\boldsymbol{R}_i+\boldsymbol{r}}(t) S^{\alpha}_{\boldsymbol{R}_i}(0)\rangle. \tag{2.6.2}$$

An elementary calculation then leads to the zero-temperature expression:

$$S^{\alpha}(\boldsymbol{q},\omega) = \sum_{\lambda} \left|\langle\lambda| S^{\alpha}_{\boldsymbol{q}} |\mathrm{GS}\rangle\right|^2 \delta(\omega - E_{\lambda} + E_{\mathrm{GS}}) \tag{2.6.3}$$

with λ the system eigenstates. This quantity thus has a form quite different from the quantum averages we based the VMC technique on. We will see below that it is still suitable for VMC as evidenced in Li and Yang [2010].

2.6.1 Excitation subspace

The first thing to do is to define what the system eigenstates $|\lambda\rangle$ are. In that respect it is instructive to look at the state:

$$\left|\boldsymbol{q},+\right\rangle = S^{+}_{\boldsymbol{q}} P_{D=0} \left|\psi_{\mathrm{GS}}\right\rangle \tag{2.6.4}$$

and write it in the basis of the mean-field eigenstates. Written in fermionic operators, $S^{+}_{\boldsymbol{q}}$ is:

$$S^{+}_{\boldsymbol{q}} = \sum_{\boldsymbol{k}} c^{\dagger}_{\boldsymbol{k}\uparrow} c_{\boldsymbol{k}-\boldsymbol{q}\downarrow} \tag{2.6.5}$$

and can be expressed in the mean-field quasiparticle basis using the canonical transform eq. 2.4.81. This gives:

$$\left|\boldsymbol{q},+\right\rangle = P_{D=0} \sum_{\boldsymbol{k}} \phi^{\boldsymbol{q}+}_{\boldsymbol{k}} \gamma^{\dagger}_{\boldsymbol{k}\uparrow+} \gamma_{\overline{\boldsymbol{k}-\boldsymbol{q}}\downarrow-} \left|\psi_{\mathrm{GS}}\right\rangle \tag{2.6.6}$$

where we have used the fact that $[S^{+}_{\boldsymbol{q}}, P_{D=0}] = 0$ and where $\overline{\boldsymbol{k}-\boldsymbol{q}}$ means folding back in the MBZ. The coefficients $\phi^{\boldsymbol{q}+}_{\boldsymbol{k}}$ are:

$$\phi^{\boldsymbol{q}+}_{\boldsymbol{k}} = u^{*}_{\boldsymbol{k}\uparrow+} u_{\boldsymbol{k}-\boldsymbol{q}\downarrow-} + v^{*}_{\boldsymbol{k}\uparrow+} v_{\boldsymbol{k}-\boldsymbol{q}\downarrow-}. \tag{2.6.7}$$

The excited state $\left|\boldsymbol{q},+\right\rangle$ can thus be written as a sum of the particle-hole excitations $\left|\boldsymbol{k},\uparrow\downarrow,\boldsymbol{q}\right\rangle$ (fig. 2.13):

$$\left|\boldsymbol{k},\uparrow\downarrow,\boldsymbol{q}\right\rangle = P_{D=0}\gamma^{\dagger}_{\boldsymbol{k}\uparrow+}\gamma_{\overline{\boldsymbol{k}-\boldsymbol{q}}\downarrow-}\left|\psi_{\mathrm{GS}}\right\rangle \tag{2.6.8}$$

and suggests that the transverse $\Delta S = 1$ eigenstates $|\lambda\rangle = \left|n,\boldsymbol{q},+\right\rangle$ might as well be expressed the same way:

$$\left|n,\boldsymbol{q},+\right\rangle = \sum_{\boldsymbol{k}} \phi^{\boldsymbol{q}+}_{\boldsymbol{k}n}\left|\boldsymbol{k},\uparrow\downarrow,\boldsymbol{q}\right\rangle \tag{2.6.9}$$

where the $\phi^{\boldsymbol{q}+}_{\boldsymbol{k}n}$ are some coefficients that remains to be determined. We can in the same way define longitudinal $\Delta S = 0$ particle-hole excitations:

$$\left|\boldsymbol{k},\sigma\sigma,\boldsymbol{q}\right\rangle = P_{D=0}\gamma^{\dagger}_{\boldsymbol{k}\sigma+}\gamma_{\overline{\boldsymbol{k}-\boldsymbol{q}}\sigma-}\left|\psi_{\mathrm{GS}}\right\rangle \tag{2.6.10}$$

and find that the state $\left|\boldsymbol{q},0\right\rangle = S^{z}_{\boldsymbol{q}}P_{D=0}\left|\psi_{\mathrm{GS}}\right\rangle$ can be written as

$$\left|\boldsymbol{q},0\right\rangle = \frac{1}{2}\sum_{\boldsymbol{k}}\sum_{\sigma}\phi^{\boldsymbol{q}0}_{\boldsymbol{k}\sigma}\left|\boldsymbol{k},\sigma\sigma,\boldsymbol{q}\right\rangle + \delta_{\boldsymbol{q}\boldsymbol{Q}}\sum_{\boldsymbol{k}}\frac{h_{\mathrm{N}}}{\omega_{\boldsymbol{k}}}P_{D=0}\left|\psi_{\mathrm{GS}}\right\rangle \tag{2.6.11}$$

with

$$\phi^{\boldsymbol{q}0}_{\boldsymbol{k}\sigma} = \sigma\left(u^{*}_{\boldsymbol{k}\sigma+}u_{\boldsymbol{k}-\boldsymbol{q}\sigma-} + v^{*}_{\boldsymbol{k}\sigma+}v_{\boldsymbol{k}-\boldsymbol{q}\sigma-}\right). \tag{2.6.12}$$

which also suggests we can look for longitudinal eigenstates $\left|n,\boldsymbol{q},0\right\rangle$ of the form:

$$\left|n,\boldsymbol{q},0\right\rangle = \sum_{\boldsymbol{k}\sigma}\phi^{\boldsymbol{q}0}_{\boldsymbol{k}\sigma n}\left|\boldsymbol{k},\sigma\sigma,\boldsymbol{q}\right\rangle. \tag{2.6.13}$$

In the end considering the S^{z}_{tot} sector and the momentum $\boldsymbol{q}$, we see that we can construct subspaces of particle-hole excitations:

$$\Omega_{\boldsymbol{q},\Delta S=+1} = \left\{\left|\boldsymbol{k},\uparrow\downarrow,\boldsymbol{q}\right\rangle \middle| \boldsymbol{k}\in\mathrm{MBZ}\right\} \tag{2.6.14}$$

$$\Omega_{\boldsymbol{q},\Delta S=0} = \left\{\left|\boldsymbol{k},\sigma\sigma,\boldsymbol{q}\right\rangle \middle| \boldsymbol{k}\in\mathrm{MBZ},\sigma\in\{\uparrow,\downarrow\}\right\}. \tag{2.6.15}$$

While the unprojected particle-hole excitations are true eigenstates of the mean-field Hamiltonian, the projected ones are probably very far from being eigenstates from the Heisenberg model itself. Therefore the individual states in themselves may not really have physical relevance but we will show later on that the subspace they span in fact does.
In principle we could also construct higher order excitations by considering multiple particle-hole pairs. We choose here to restrict ourselves to the one particle-hole pair under the assumption that the number of particle-hole pair is approximately a good quantum number of the Heisenberg model, as it is the case for its SF+N mean-field version. But this claim might be challenged, although carrying out calculations containing these higher order terms becomes numerically intractable.

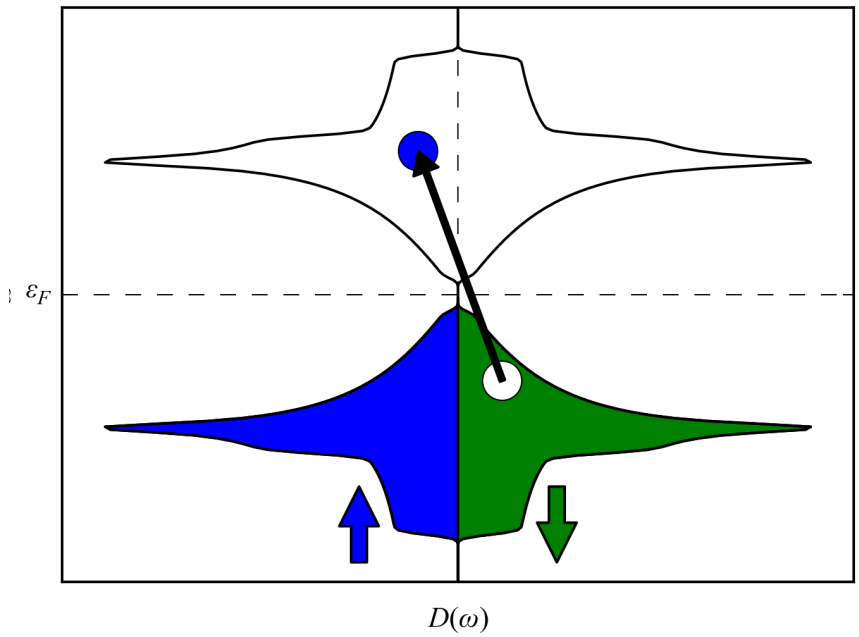

Figure 2.13 – Representation of the transverse particle-hole pair excitation. A spin-↓ is taken from the filled spin-↓ band, flipped and put in the spin-↑ empty band. The integrated density of states $D(\omega) = \sum_{\boldsymbol{q}\in \mathrm{MBZ}} D(\boldsymbol{q},\omega)$ is calculated from the (gapped) SF+N state.

2.6.2 The Heisenberg Hamiltonian on the Excitation Subspace

With the excitation subspaces defined, we can now define the variational eigenstates $|\lambda\rangle$ entering the definition of the dynamic spin structure factor. For the $\left|n,\boldsymbol{q},\Delta S\right\rangle$ to be eigenstates we require that:

$$\left\langle n,\boldsymbol{q},\Delta S\right|\mathscr{H}\left|n,\boldsymbol{q},\Delta S\right\rangle = E_n^{\boldsymbol{k}\Delta S}\left\langle n,\boldsymbol{q},\Delta S\right|\left.n,\boldsymbol{q},\Delta S\right\rangle \tag{2.6.16}$$

$$\left\langle n',\boldsymbol{q},\Delta S\right|\left.n,\boldsymbol{q},\Delta S\right\rangle = \delta_{nn'} \tag{2.6.17}$$

where $\mathscr{H}$ is the Heisenberg model eq. 2.1.2. For the transverse excitations, this defines the following generalized eigenvalue problem:

$$\sum_{\boldsymbol{k}\boldsymbol{k}'} \phi_{\boldsymbol{k}'n}^{\boldsymbol{q}+*} H_{\boldsymbol{k}'\boldsymbol{k}}^{\boldsymbol{q}+}\phi_{\boldsymbol{k}n}^{\boldsymbol{q}+} = E_n^{\boldsymbol{q}+}\sum_{\boldsymbol{k}\boldsymbol{k}'} \phi_{\boldsymbol{k}'n}^{\boldsymbol{q}+*} O_{\boldsymbol{k}'\boldsymbol{k}}^{\boldsymbol{q}+}\phi_{\boldsymbol{k}n}^{\boldsymbol{q}+} \tag{2.6.18}$$

where

$$H_{\boldsymbol{k}\boldsymbol{k}'}^{\boldsymbol{q}+} = \left\langle \boldsymbol{k},\uparrow\downarrow,\boldsymbol{q}\right|\mathscr{H}\left|\boldsymbol{k}',\uparrow\downarrow,\boldsymbol{q}\right\rangle \tag{2.6.19}$$

$$O_{\boldsymbol{k}\boldsymbol{k}'}^{\boldsymbol{q}+} = \left\langle \boldsymbol{k},\uparrow\downarrow,\boldsymbol{q}\right|\left.\boldsymbol{k}',\uparrow\downarrow,\boldsymbol{q}\right\rangle \tag{2.6.20}$$

and in a similar way for the longitudinal excitations:

$$\sum_{\boldsymbol{k}\boldsymbol{k}'\sigma\sigma'} \phi^{\boldsymbol{q}0^*}_{\boldsymbol{k}'\sigma' n} H^{\boldsymbol{q}0}_{\boldsymbol{k}'\boldsymbol{k}\sigma'\sigma} \phi^{\boldsymbol{q}0}_{\boldsymbol{k}\sigma n} = E^{\boldsymbol{q}0}_n \sum_{\boldsymbol{k}\boldsymbol{k}'\sigma\sigma'} \phi^{\boldsymbol{q}0^*}_{\boldsymbol{k}'\sigma' n} O^{\boldsymbol{q}0}_{\boldsymbol{k}'\boldsymbol{k}\sigma'\sigma} \phi^{\boldsymbol{q}0}_{\boldsymbol{k}\sigma n} \tag{2.6.21}$$

where

$$H^{\boldsymbol{q}0}_{\boldsymbol{k}\boldsymbol{k}'\sigma\sigma'} = \langle \boldsymbol{k}, \sigma\sigma, \boldsymbol{q} | \mathscr{H} | \boldsymbol{k}', \sigma'\sigma', \boldsymbol{q} \rangle \tag{2.6.22}$$

$$O^{\boldsymbol{q}0}_{\boldsymbol{k}\boldsymbol{k}'\sigma\sigma'} = \langle \boldsymbol{k}, \sigma\sigma', \boldsymbol{q} | \boldsymbol{k}', \sigma'\sigma', \boldsymbol{q} \rangle . \tag{2.6.23}$$

Finding the particle-hole excitations eigenstates therefore amount into diagonalizing the Heisenberg model projected into the non-orthonormal bases $\Omega_{\boldsymbol{q},\Delta S}$. Once the matrices $O^{\boldsymbol{q}\Delta S}$ and $H^{\boldsymbol{q}\Delta S}$ are known, this is a simple numerical problem that can be solved with standard diagonalization routines. Indeed the size of these matrices is small being simply the number of particle-hole pair one can form. For a $L \times L$ system, there are only $L^2/2$ particle-hole excitations in the transverse channel and L^2 in the longitudinal one. The matrices size thus grows linearly with the number of sites considered. Li and Yang showed how these matrices can be evaluated through the VMC technique [Li and Yang, 2010] as we will show below.

2.6.3 Modified Monte Carlo Random Walk

In order to perform the Gutzwiller projection, the idea still is to expand the quantities $H^{\boldsymbol{q}\Delta S}$ and $O^{\boldsymbol{q}\Delta S}$ into the basis of spin-$\frac{1}{2}$ particles in real space positions with no double occupancies. This can be readily done for instance in the transverse channel:

$$H^{\boldsymbol{q}+}_{\boldsymbol{k}\boldsymbol{k}'} = \sum_{\alpha\beta} \langle \boldsymbol{k}, \uparrow\downarrow, \boldsymbol{q} | \alpha \rangle \langle \alpha | \mathscr{H} | \beta \rangle \langle \beta | \boldsymbol{k}', \uparrow\downarrow, \boldsymbol{q} \rangle . \tag{2.6.24}$$

which can simply be put back in a form suitable for Metropolis Monte Carlo using the same approach than before:

$$\frac{H^{\boldsymbol{q}+}_{\boldsymbol{k}\boldsymbol{k}'}}{\langle \boldsymbol{k}, \uparrow\downarrow, \boldsymbol{q} | \boldsymbol{k}, \uparrow\downarrow, \boldsymbol{q} \rangle} = \sum_{\alpha} \underbrace{\frac{|\langle \boldsymbol{k}, \uparrow\downarrow, \boldsymbol{q} | \alpha \rangle|^2}{\langle \boldsymbol{k}, \uparrow\downarrow, \boldsymbol{q} | \boldsymbol{k}, \uparrow\downarrow, \boldsymbol{q} \rangle}}_{\rho(\alpha)} \underbrace{\sum_{\beta} \langle \alpha | \mathscr{H} | \beta \rangle \frac{\langle \beta | \boldsymbol{k}', \uparrow\downarrow, \boldsymbol{q} \rangle}{\langle \alpha | \boldsymbol{k}, \uparrow\downarrow, \boldsymbol{q} \rangle}}_{f(\alpha)} . \tag{2.6.25}$$

This formulation allows to calculate $H^{\boldsymbol{q}+}_{\boldsymbol{k}\boldsymbol{k}'}$ but normalized to the $|\boldsymbol{k}, \uparrow\downarrow, \boldsymbol{q}\rangle$ wavefunction. If one aims at doing exact diagonalization of the $H^{\boldsymbol{q}+}$ then we would need all matrix elements normalized to the same arbitrarily chosen wavefunction $|\boldsymbol{k}_0, \uparrow\downarrow, \boldsymbol{q}\rangle$ leading to

$$\frac{H^{\boldsymbol{q}+}_{\boldsymbol{k}\boldsymbol{k}'}}{\langle \boldsymbol{k}_0, \uparrow\downarrow, \boldsymbol{q} | \boldsymbol{k}_0, \uparrow\downarrow, \boldsymbol{q} \rangle} = \sum_{\alpha} \underbrace{\frac{|\langle \alpha | \boldsymbol{k}_0, \uparrow\downarrow, \boldsymbol{q} \rangle|^2}{\langle \boldsymbol{k}_0, \uparrow\downarrow \boldsymbol{q} | \boldsymbol{k}_0, \uparrow\downarrow, \boldsymbol{q} \rangle}}_{\rho(\alpha)} \underbrace{\sum_{\beta} \frac{\langle \boldsymbol{k}, \uparrow\downarrow, \boldsymbol{q} | \alpha \rangle}{\langle \boldsymbol{k}_0, \uparrow\downarrow, \boldsymbol{q} | \alpha \rangle} \langle \alpha | \mathscr{H} | \beta \rangle \frac{\langle \beta | \boldsymbol{k}', \uparrow\downarrow, \boldsymbol{q} \rangle}{\langle \alpha | \boldsymbol{k}_0, \uparrow\downarrow, \boldsymbol{q} \rangle}}_{f(\alpha)} . \tag{2.6.26}$$

This formulation is however rather unstable. Suppose $\langle \boldsymbol{k}_0, \uparrow\downarrow, \boldsymbol{q} | \alpha \rangle \to 0$ and $\langle \boldsymbol{k}, \uparrow\downarrow, \boldsymbol{q} | \alpha \rangle$ finite. Then we have the problem that $\rho(\alpha) \to 0$ and $f(\alpha) \to \infty$ which will render a good the Monte Carlo sampling impossible. The arbitrary choice of a wavevector $\boldsymbol{k}_0$ obviously is the problem. To solve this Li and Yang [2010] developed a reweighing technique, which simply redefines the Monte Carlo random walk weight to avoid such problems: For any weight definition $W(\alpha)$ one can in principle define the weighted sum:

$$\frac{H^{\boldsymbol{q}+}_{\boldsymbol{k}\boldsymbol{k}'}}{\sum_\alpha W(\alpha)} = \sum_\alpha \underbrace{\frac{W(\alpha)}{\sum_\alpha W(\alpha)}}_{\rho(\alpha)} \underbrace{\frac{\langle \boldsymbol{k}, \uparrow\downarrow, \boldsymbol{q} | \alpha \rangle \langle \alpha | \mathscr{H} | \beta \rangle \langle \beta | \boldsymbol{k}', \uparrow\downarrow, \boldsymbol{q} \rangle}{W(\alpha)}}_{f(\alpha)} \tag{2.6.27}$$

which will be good-behaved if $\langle \boldsymbol{k}, \uparrow\downarrow, \boldsymbol{q} | \alpha \rangle \langle \beta | \boldsymbol{k}', \uparrow\downarrow, \boldsymbol{q} \rangle / W(\alpha)$ is a slowly varying function of α and β. Choosing the following weight we see this will indeed be the case:

$$W^{\boldsymbol{q}+}(\alpha) = \sum_{\boldsymbol{k} \in \mathrm{MBZ}} \left| \langle \alpha | \boldsymbol{k}, \uparrow\downarrow, \boldsymbol{q} \rangle \right|^2. \tag{2.6.28}$$

Defining the sum $W^{\boldsymbol{q}+} = \sum_\alpha W^{\boldsymbol{q}+}(\alpha)$ we have the following weighted sum defining the Monte Carlo random walk in the transverse channel:

$$\frac{H^{\boldsymbol{q}+}_{\boldsymbol{k}\boldsymbol{k}'}}{W^{\boldsymbol{q}+}} = \sum_\alpha \frac{W^{\boldsymbol{q}+}(\alpha)}{W^{\boldsymbol{q}+}} \sum_\beta \frac{\langle \boldsymbol{k}, \uparrow\downarrow, \boldsymbol{q} | \alpha \rangle \langle \alpha | \mathscr{H} | \beta \rangle \langle \beta | \boldsymbol{k}', \uparrow\downarrow, \boldsymbol{q} \rangle}{W^{\boldsymbol{q}+}(\alpha)} \tag{2.6.29}$$

$$\frac{O^{\boldsymbol{q}+}_{\boldsymbol{k}\boldsymbol{k}'}}{W^{\boldsymbol{q}+}} = \sum_\alpha \frac{W^{\boldsymbol{q}+}(\alpha)}{W^{\boldsymbol{q}+}} \frac{\langle \boldsymbol{k}, \uparrow\downarrow, \boldsymbol{q} | \alpha \rangle \langle \alpha | \boldsymbol{k}', \uparrow\downarrow, \boldsymbol{q} \rangle}{W^{\boldsymbol{q}+}(\alpha)}. \tag{2.6.30}$$

In the longitudinal channel the formulas are almost the same with a weight defined as:

$$W^{\boldsymbol{q}0}(\alpha) = \sum_{\boldsymbol{k} \in \mathrm{MBZ}, \sigma} \left| \langle \alpha | \boldsymbol{k}, \sigma\sigma, \boldsymbol{q} \rangle \right|^2 \tag{2.6.31}$$

$$W^{\boldsymbol{q}0} = \sum_\alpha W^{\boldsymbol{q}0}(\alpha). \tag{2.6.32}$$

To finish the discussion about the modified Monte Carlo random walk, we come back to the problem of efficiently calculating the overlaps $\langle \alpha | \boldsymbol{k}, \uparrow\downarrow, \boldsymbol{q} \rangle$. To do so we must calculate the determinant of the Slater matrices:

$$M^{\langle \alpha | \boldsymbol{k}, \uparrow\downarrow, \boldsymbol{q} \rangle}_{i_\uparrow j_\uparrow} = \langle \boldsymbol{R}_{i_\uparrow}, \uparrow | \boldsymbol{k}_{j_\uparrow}, \uparrow, b_{j_\uparrow} \rangle \tag{2.6.33}$$

$$M^{\langle \alpha | \boldsymbol{k}, \uparrow\downarrow, \boldsymbol{q} \rangle}_{i_\downarrow j_\downarrow} = \langle \boldsymbol{R}_{i_\downarrow}, \downarrow | \boldsymbol{k}_{j_\downarrow}, \downarrow, b_{j_\downarrow} \rangle \tag{2.6.34}$$

for which we know that an exchange of an up-spin and a down-spin $|\alpha\rangle \to |\beta\rangle$ corresponds to a single *row* change in both $M^{\langle \alpha | \boldsymbol{k}, \uparrow\downarrow, \boldsymbol{q} \rangle}_{i_\uparrow j_\uparrow}$ and $M^{\langle \alpha | \boldsymbol{k}, \uparrow\downarrow, \boldsymbol{q} \rangle}_{i_\downarrow j_\downarrow}$ for which the determinant can be efficiently updated through the formulas derived in appendix A.2. Suppose now that we already know the amplitude $\langle \alpha | \boldsymbol{k}, \uparrow\downarrow, \boldsymbol{q} \rangle$. Is there a simple way to calculate $\langle \beta | \boldsymbol{k}', \uparrow\downarrow, \boldsymbol{q} \rangle$? In fact the transition $|\boldsymbol{k}, \uparrow\downarrow, \boldsymbol{q}\rangle \to |\boldsymbol{k}', \uparrow\downarrow, \boldsymbol{q}\rangle$ simply corresponds to moving the excited spin-$\uparrow$ from wavevector $\boldsymbol{k}$ to $\boldsymbol{k}'$ and the spin-$\downarrow$ hole from $\overline{\boldsymbol{k} - \boldsymbol{q}}$ to $\overline{\boldsymbol{k}' - \boldsymbol{q}}$. This corresponds into changing a *column* in

both the up and down Slater matrices. We therefore need an efficient way to calculate the determinant update upon simultaneous *row* and *column* change. Looking into the longitudinal channel we see we actually require more. Indeed the transition $\left|\boldsymbol{k},\sigma\sigma,\boldsymbol{q}\right\rangle \rightarrow \left|\boldsymbol{k}',\sigma\sigma,\boldsymbol{q}\right\rangle$ corresponds to two simultaneous *column* changes in the σ-Slater matrix. To efficiently treat all those cases in a manageable way, we derive in appendix A.2 a determinant update formula for an arbitrary number of simultaneous *row* and *column* changes. We also expose in greater details the modified random walk in appendix A.3.

2.6.4 Evaluation of the Dynamical Spin Structure Factor

With all the above developments, we are now in a position to evaluate the dynamic spin structure factor through a VMC technique. In eq. 2.6.3, in the transverse case we have:

$$|\lambda\rangle = \left|n,\boldsymbol{q},+\right\rangle \tag{2.6.35}$$

$$S^{+}_{\boldsymbol{q}}|\mathrm{GS}\rangle = \left|\boldsymbol{q},+\right\rangle \tag{2.6.36}$$

and in the longitudinal channel:

$$|\lambda\rangle = \left|n,\boldsymbol{q},0\right\rangle \tag{2.6.37}$$

$$S^{z}_{\boldsymbol{q}}|\mathrm{GS}\rangle = \left|\boldsymbol{q},0\right\rangle \tag{2.6.38}$$

such that the dynamic structure factors are:

$$S^{\pm}(\boldsymbol{q},\omega) = \sum_{n} \left|\left\langle n,\boldsymbol{q},+\middle|\boldsymbol{q},+\right\rangle\right|^{2} \delta\left(\omega - E^{\boldsymbol{q}+}_{n} + E_{\mathrm{GS}}\right) \tag{2.6.39}$$

$$S^{zz}(\boldsymbol{q},\omega) = \sum_{n} \left|\left\langle n,\boldsymbol{q},0\middle|\boldsymbol{q},0\right\rangle\right|^{2} \delta\left(\omega - E^{\boldsymbol{q}0}_{n} + E_{\mathrm{GS}}\right). \tag{2.6.40}$$

Expanding the $\left|n,\boldsymbol{q},\Delta S\right\rangle$ and $\left|\boldsymbol{q},\Delta S\right\rangle$ states into the particle-hole bases $\Omega_{\boldsymbol{q}\Delta S}$ we obtain:

$$\frac{S^{\pm}(\boldsymbol{q},\omega)}{W^{\boldsymbol{q}+}} = \sum_{n} \left| \sum_{\boldsymbol{k}\boldsymbol{k}'} \phi^{\boldsymbol{q}+*}_{\boldsymbol{k}n} \frac{O^{\boldsymbol{q}+}_{\boldsymbol{k}\boldsymbol{k}'}}{W^{\boldsymbol{q}+}} \phi^{\boldsymbol{q}+}_{\boldsymbol{k}'} \right|^{2} \delta\left(\omega - E^{\boldsymbol{q}+}_{n} + E_{\mathrm{GS}}\right) \tag{2.6.41}$$

$$\frac{S^{zz}(\boldsymbol{q},\omega)}{W^{\boldsymbol{q}0}} = \sum_{n} \left| \sum_{\boldsymbol{k}\boldsymbol{k}'\sigma\sigma'} \phi^{\boldsymbol{q}0*}_{\boldsymbol{k}\sigma n} \frac{O^{\boldsymbol{q}0}_{\boldsymbol{k}\boldsymbol{k}'\sigma\sigma'}}{W^{\boldsymbol{q}0}} \phi^{\boldsymbol{q}0}_{\boldsymbol{k}'\sigma'} \right|^{2} \delta\left(\omega - E^{\boldsymbol{q}0}_{n} + E_{\mathrm{GS}}\right) \tag{2.6.42}$$

where we have explicitly written down the normalization from the weights $W^{\boldsymbol{q}\Delta S}$ as the matrices $O^{\boldsymbol{q}\Delta S}$ obtained from the variational Monte Carlo will necessarily be normalized to it. We thus see that the sampling of the $(H^{\boldsymbol{q}\Delta S}, O^{\boldsymbol{q}\Delta S})$ is all that is needed to obtain the dynamic structure factor. A slight issue is that the normalization $W^{\boldsymbol{q}\Delta S}$ is $\boldsymbol{q}$-dependent. In principle this renders a direct comparison of the spectral weight across different $\boldsymbol{q}$ momenta impossible. We will see in next section how the so-called sum rules will allow to solve this issue.

2.6.5 Sum Rules

By integrating the dynamic structure factor over energy, it is simple to see that one recovers the corresponding instantaneous correlation functions:

$$\int d\omega S^{\pm}(\boldsymbol{q},\omega) = \left\langle S^{-}_{\boldsymbol{q}} S^{+}_{\boldsymbol{q}} \right\rangle \tag{2.6.43}$$

$$\int d\omega S^{zz}(\boldsymbol{q},\omega) = \left\langle S^{z}_{-\boldsymbol{q}} S^{z}_{\boldsymbol{q}} \right\rangle. \tag{2.6.44}$$

In our formalism, using the property:

$$\frac{1}{W^{\boldsymbol{q}+}} \sum_{n\boldsymbol{k}} \phi^{\boldsymbol{q}+*}_{n\boldsymbol{k}_1} O^{\boldsymbol{q}+}_{\boldsymbol{k}_2\boldsymbol{k}} \phi^{\boldsymbol{q}+}_{n\boldsymbol{k}} = \delta_{\boldsymbol{k}_1\boldsymbol{k}_2} \tag{2.6.45}$$

we consistently get

$$\int d\omega \frac{S^{\pm}(\boldsymbol{q},\omega)}{W^{\boldsymbol{q}+}} = \sum_{n} \left| \phi^{\boldsymbol{q}+*}_{n\boldsymbol{k}} \frac{O^{\boldsymbol{q}+}_{\boldsymbol{k}\boldsymbol{k}'}}{W^{\boldsymbol{q}+}} \phi^{\boldsymbol{q}+}_{n\boldsymbol{k}'} \right|^2 \tag{2.6.46}$$

$$= \frac{1}{W^{\boldsymbol{q}+}} \sum_{\boldsymbol{k}\boldsymbol{k}'} \phi^{\boldsymbol{q}+*}_{\boldsymbol{k}} O^{\boldsymbol{q}+}_{\boldsymbol{k}\boldsymbol{k}'} \phi^{\boldsymbol{q}+}_{\boldsymbol{k}'} \tag{2.6.47}$$

$$= \frac{1}{W^{\boldsymbol{q}+}} \left\langle \psi_{\mathrm{GS}} \right| P_{D=0} S^{-}_{\boldsymbol{q}} S^{+}_{\boldsymbol{q}} P_{D=0} \left| \psi_{\mathrm{GS}} \right\rangle \tag{2.6.48}$$

$$= \left\langle S^{-}_{\boldsymbol{q}} S^{+}_{\boldsymbol{q}} \right\rangle_{\Omega_{\boldsymbol{q}+}} \tag{2.6.49}$$

We then see that using the sum rule will solve the issue of the $\boldsymbol{q}$-dependent normalization of the dynamic structure factor. We can thus evaluate the instantaneous transverse spin-spin correlation function in two ways, either using the groundstate wavefunction eq. 2.6.50 or the particle-hole excitation subspace eq. 2.6.51.

$$\left\langle S^{-}_{\boldsymbol{q}} S^{+}_{\boldsymbol{q}} \right\rangle_{\psi_{\mathrm{GS}}} = \frac{\left\langle \psi_{\mathrm{GS}} \right| P_{D=0} S^{-}_{\boldsymbol{q}} S^{+}_{\boldsymbol{q}} P_{D=0} \left| \psi_{\mathrm{GS}} \right\rangle}{\left\langle \psi_{\mathrm{GS}} \right| P_{D=0} \left| \psi_{\mathrm{GS}} \right\rangle} \tag{2.6.50}$$

$$\left\langle S^{-}_{\boldsymbol{q}} S^{+}_{\boldsymbol{q}} \right\rangle_{\Omega_{\boldsymbol{q}+}} = \frac{\left\langle \psi_{\mathrm{GS}} \right| P_{D=0} S^{-}_{\boldsymbol{q}} S^{+}_{\boldsymbol{q}} P_{D=0} \left| \psi_{\mathrm{GS}} \right\rangle}{W^{\boldsymbol{q}+}}. \tag{2.6.51}$$

We can carrying out both numerical evaluation, we can thus obtain the proportionality constant

$$\frac{\left\langle S^{+}_{\boldsymbol{q}} S^{-}_{\boldsymbol{q}} \right\rangle_{\Omega_{\boldsymbol{q}+}}}{\left\langle S^{+}_{\boldsymbol{q}} S^{-}_{\boldsymbol{q}} \right\rangle_{\psi_{\mathrm{GS}}}} = \frac{\left\langle \psi_{\mathrm{GS}} \right| P_{D=0} \left| \psi_{\mathrm{GS}} \right\rangle}{W^{\boldsymbol{q}+}}. \tag{2.6.52}$$

which can then be used to renormalize the dynamic structure factor such that it becomes normalized to the groundstate wavefunction for every $\boldsymbol{q}$. This reasoning can be carried out exactly the same way for the longitudinal channel. In the following, every numerical evaluation

of the dynamic structure factor is normalized such that:

$$\int d\omega \sum_{\boldsymbol{q}} \left\langle S^{zz}(\boldsymbol{q},\omega) + \frac{1}{2} S^{\pm}(\boldsymbol{q},\omega) \right\rangle = NS(S+1). \tag{2.6.53}$$

2.7 Numerical results

The variational Monte Carlo algorithm modified for measuring dynamical quantities has been implemented in the C++ programming language. The most computationally demanding part is the calculation of the determinant updates. The many matrix-matrix, matrix-vector and scalar products implied by the determinant update formulas exposed in appendix A.2 are calculated using the Basic Linear Algebra Subroutines (BLAS) interface to highly optimized platform-dependent implementations. The Monte Carlo algorithm being just about collecting statistics, it is very easy to parallelize simply by running many simultaneous random walks. The parallelization has been implemented using the standard Message Passing Interface (MPI) making the program suitable for massively parallel supercomputers. So far calculations have been performed on the EPFL Institute of Theoretical Physics cluster "itplc1", on the Swiss National Supercomputing Center (CSCS) Monte Rosa Cray XE6 cluster and on our home-made "Quantum Wolf" cluster made out of consumer parts (appendix C). Single calculations have so far used as much as 3200 computational cores simultaneously on the CSCS Monte Rosa cluster and the total CPU-time spent in the context of this project amounts for more than $5 \cdot 10^6$ CPU-hours. We discuss the Monte Carlo thermalization process and the calculation CPU-time scaling in the appendices A.4 and A.5.
In the numerical results shown below we will first establish the properties of the trial wavefunctions as a function of its parameters and then move on into the analysis of the dynamic quantities. The discussion comparing our results to other numerical or analytical techniques and to experiments will be carried out in parallel with the results presentation.

2.7.1 Ground State Average quantities

The ground state properties of the trial wavefunction are probably the easiest to obtain through the variational Monte Carlo method and have been calculated before. First of those is the ground state energy calculated as:

$$E_{\mathrm{GS}}(\theta_0, h_{\mathrm{N}}) = \frac{\left\langle \psi_{\mathrm{GS}}(\theta_0, h_{\mathrm{N}}) \right| P_{D=0} \mathscr{H} P_{D=0} \left| \psi_{\mathrm{GS}}(\theta_0, h_{\mathrm{N}}) \right\rangle}{\left\langle \psi_{\mathrm{GS}}(\theta_0, h_{\mathrm{N}}) \right| P_{D=0} \left| \psi_{\mathrm{GS}}(\theta_0, h_{\mathrm{N}}) \right\rangle} \tag{2.7.1}$$

We show in figure 2.14 a colormap of this variational energy as a function of θ_0 and h_{N}. Since $4\theta_0$ describes the phase acquired by a particle circulating around a square plaquette, The SF+N variational energy is periodic in $\theta_0 \to \theta_0 + \frac{\pi}{2}$. At zero Néel field, moving along the θ_0 axis, the energy has two minima at $\theta_0 = 0.075\pi$ and $\theta_0 = \frac{\pi}{2} - 0.075\pi$ with a reduction of 18% compared to the $\theta_0 = 0$ and $h_{\mathrm{N}} = 0$ case. On the other hand considering no flux and moving along the

Néel mean field axis, we see a broad minima about $h_N = 0.06$ with a reduction of of the energy by 19%. We took ($\theta_0 = 0.1\pi, h_N = 0.055$) with $E_{GS} = -0.664J$ as the optimal flux and Neel field hereby referred as $|\mathrm{SF}+\mathrm{N}\rangle$. This is only 4% better than the pure flux state and only 3.5% better than the pure Néel mean-field state. Thus we see that all these groundstate energies are quite close. While there is experimentally no doubts that the system ground state is ordered, the

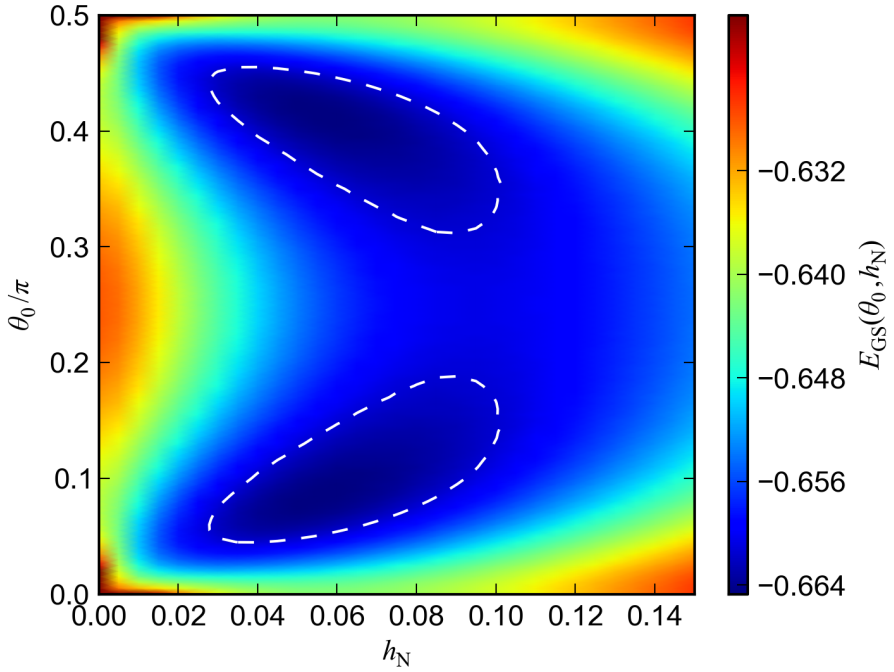

Figure 2.14 – Variational energy of the wavefunction $P_{D=0}|\psi_{GS}\rangle$ as a function of the parameters θ_0 and h_N. The dashed contour indicates the region where the variational energy varies by less than 0.5%

proximity of QSL groundstates corresponding here to the pure flux states suggests that the system excitations may not always share the spontaneously broken spin-symmetry of the groundstate.
Another elementary quantity to look at is the staggered magnetization:

$$\tilde{S}^z_{GS}(\theta_0, h_N) = \frac{\langle \psi_{GS}(\theta_0, h_N)| P_{D=0} S^z_{\boldsymbol{Q}} P_{D=0} |\psi_{GS}(\theta_0, h_N)\rangle}{\langle \psi_{GS}(\theta_0, h_N)| P_{D=0} |\psi_{GS}(\theta_0, h_N)\rangle} \tag{2.7.2}$$

which we also show on the (θ_0, h_N) plane (fig. 2.15). For a given Néel mean field, turning on the flux results into a reduction of the staggered magnetization evidencing that the flux induces additional quantum fluctuations competing with the classical Néel order. The best groundstate energy corresponds to a staggered magnetization of $\tilde{S}^z_{GS}(0.1, 0.055) = 0.71S$. This corresponds to a 29% reduction from the classical value and may be compared to SWT which predicts a 38% reduction. The energy and staggered magnetization from various numerical methods are shown in table 2.1. Regarding the above results, it seems obvious the optimal flux and Néel field, hereby denoted SF+N, is the best trial wavefunction: it has the lowest energy,

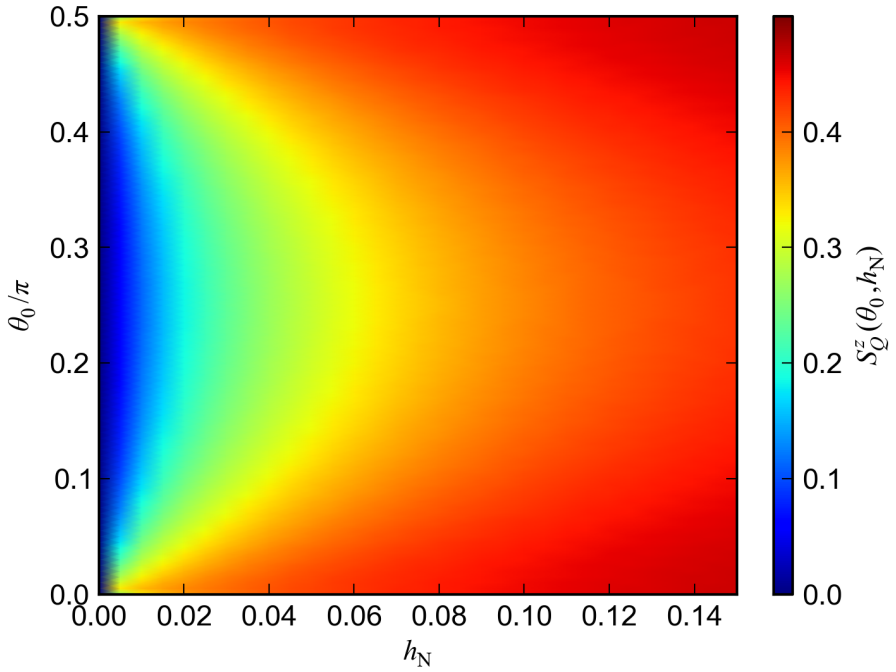

Figure 2.15 – Staggered magnetization of the wavefunction $P_{D=0}\left|\psi_{GS}\right\rangle$ as a function of the parameters θ_0 and h_N.

	$\langle\mathscr{H}\rangle$	$\langle S^z_{\mathbf{Q}}\rangle$
Green function Monte Carlo	$-0.6692J$	$0.62S$
Optimal flux	$-0.638J$	$0S$
Optimal flux and Néel field	$-0.664J$	$0.71S$

Table 2.1 – Comparison of the groundstate energies and staggered magnetization from various numerical approaches. Green function Monte Carlo from Trivedi and Ceperley [1989]; Runge [1992]; Calandra Buonaura and Sorella [1998]. Optimal flux VMC from Yokoyama and Ogata [1996] and coincide with our results for the SF state. Optimal flux and Néel field from Lee and Feng [1988] and coincides with our results for the SF+N state.

reasonably close to the Green function Monte Carlo one, and shows a staggered magnetization also in good agreement. With respect to experiments, the observed finite ordered moment also seems to favour the SF+N wavefunction. To settle the notations for the wavefunctions, let us define again the QSL state $|\mathrm{SF}\rangle$ and the Néel ordered state $|\mathrm{SF}+\mathrm{N}\rangle$:

$$|\mathrm{SF}\rangle \longrightarrow \theta_0 = 0.1\pi,\ h_\mathrm{N} = 0 \tag{2.7.3}$$

$$|\mathrm{SF}+\mathrm{N}\rangle \longrightarrow \theta_0 = 0.1\pi,\ h_\mathrm{N} = 0.055. \tag{2.7.4}$$

The minimum of the energy is quite broad and many sets of variational parameters will have very comparable energies. In the area highlighted in fig. 2.14, the groundstate energy varies at most by 0.5%. We will show later that, while the Néel mean-field parameter h_N is critical to shape the excitation spectra, these only weakly depend on the flux θ_0 in the region of minimum variational energy (see fig. 2.27 and 2.22). We quickly mention that we also have tried to use Jastrow factors to induce in a different way the Néel order into the trial wavefunctions. We defined the two different wavefunctions:

$$\left|\mathrm{SF}+\mathrm{V_Q}\right\rangle = \mathscr{J}_{\boldsymbol{Q}}\,|\mathrm{SF}\rangle \tag{2.7.5}$$

$$|\mathrm{SF}+\mathrm{AF}\rangle = \mathscr{J}_\mathrm{AF}\,|\mathrm{SF}\rangle \tag{2.7.6}$$

where $\mathscr{J}_{\boldsymbol{Q}}$ is eq. 2.5.19 with the staggered potential eq. 2.5.20 and $\mathscr{J}_\mathrm{AF}$ the antiferromagnetic Jastrow factor eq. 2.5.21. Once optimized, the two Jastrow wavefunctions essentially gave the same results as the $|\mathrm{SF}+\mathrm{N}\rangle$ state both when looking at the variational energy and the staggered magnetization.

We now turn towards the instantaneous spin-spin correlation function. We show in fig. 2.16 the instantaneous correlation functions $\langle S^x_{-\boldsymbol{q}} S^x_{\boldsymbol{q}}\rangle$ and $\langle S^z_{-\boldsymbol{q}} S^z_{\boldsymbol{q}}\rangle$ in both the SF and the SF+N case. The SF case has the full spin-symmetry but the introduction of the Néel mean field depletes the transverse $\boldsymbol{Q} = (\pi,\pi)$ peak in the transverse correlation function and develops a strong Magnetic Bragg peak in the longitudinal channel (cut out from the plot in fig. 2.16 top right panel). By Fourier-transforming with a shift of $\boldsymbol{Q}$, we get the real space staggered spin-spin correlation function:

$$S^{\alpha\alpha}(\boldsymbol{r}) = \frac{1}{N}\sum_{\boldsymbol{q}} e^{i(\boldsymbol{q}+\boldsymbol{Q})\boldsymbol{r}}\langle S^\alpha_{-\boldsymbol{q}} S^\alpha_{\boldsymbol{q}}\rangle \tag{2.7.7}$$

$$= \frac{1}{2}\sum_i e^{\boldsymbol{Q}\boldsymbol{r}}\langle S^\alpha_i S^\alpha_{i+\boldsymbol{r}}\rangle \tag{2.7.8}$$

It is interesting to look at the transverse component, recalling that SWT predict an algebraically decay of $S^x(\boldsymbol{r}) \sim |\boldsymbol{r}|^a$. We show it along both the $\boldsymbol{r} = (x,0)$ and $\boldsymbol{r} = (x,x)$ directions on a log-log plot in fig. 2.17 again in the SF and SF+N cases. Interestingly we see that the SF trial wavefunction does have an algebraic decay of the transverse (or longitudinal) spin-spin correlation as found previously [Ivanov, 2006]. But the SF+N trial wavefunction does not and has in fact an exponential decay of the transverse spin-spin correlation. Thus the Néel mean-field, while resulting into a Néel ordered state, does not have the correct long-wavelength

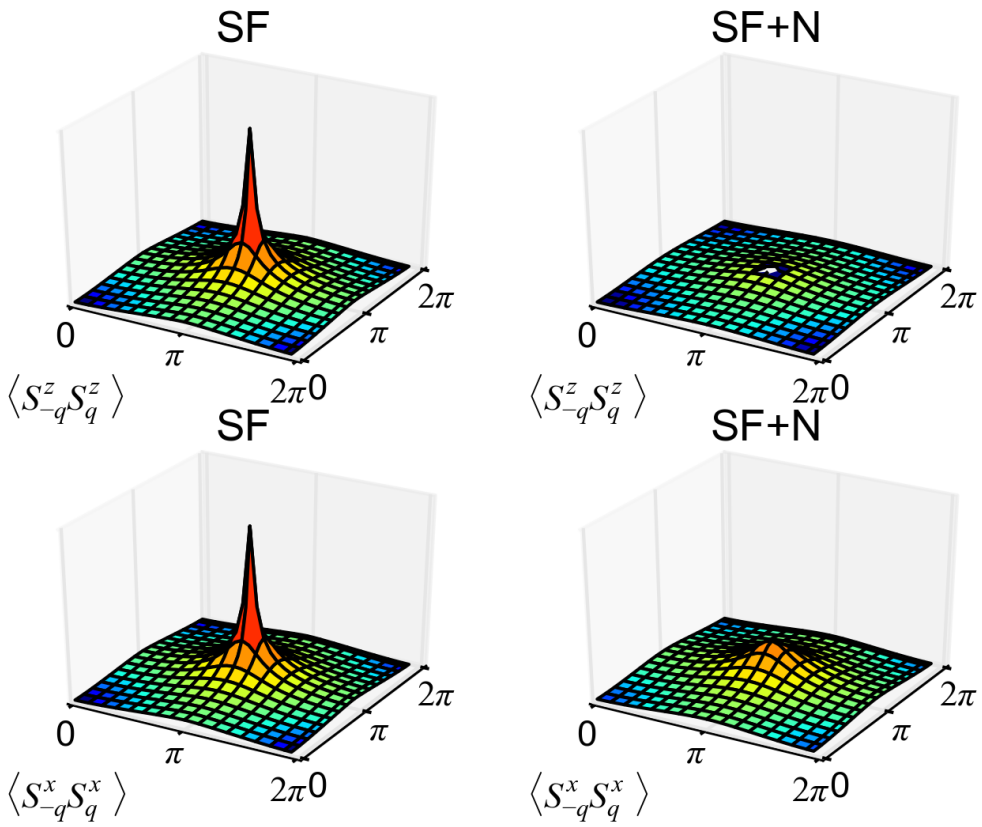

Figure 2.16 – Instantaneous longitudinal and transverse spin-spin correlation functions for both the SF and SF+N cases. In the longitudinal SF+N case the magnetic Bragg peak has been cut out of the plot.

properties expected from SWT. We recall that the spin-wave prediction should be robust as the residual magnon-magnon interaction should become negligible for long wavelength [Igarashi, 1992]. It is thus not so obvious which wavefunction between the SF and SF+N is the most physical. In the following we will therefore study both and see that they seem to capture different aspects of the square lattice Heisenberg model excitation spectrum.

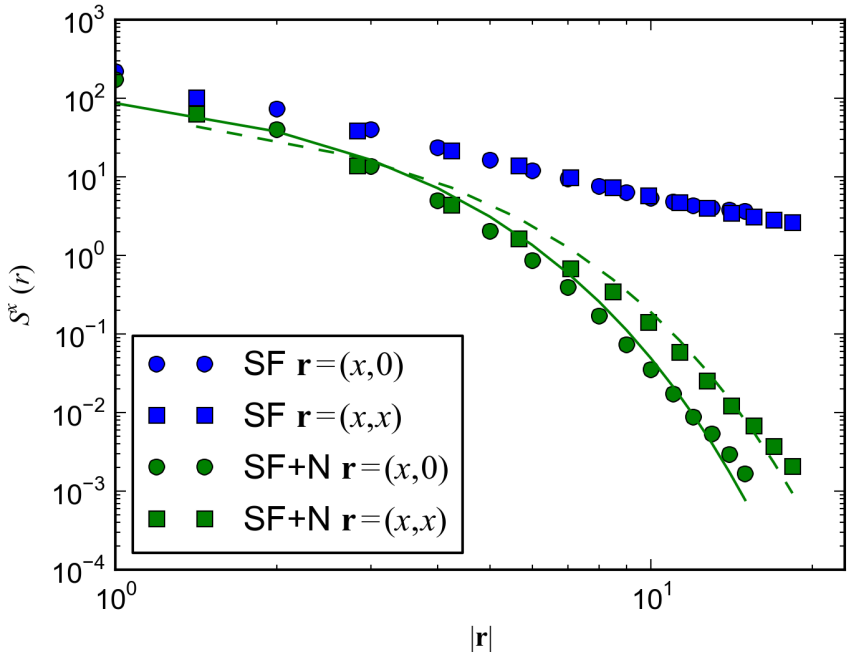

Figure 2.17 – Transverse spin-spin correlation function $S^{xx}(\boldsymbol{r})$ as defined by eq. 2.7.7 on a log-log scale. Blue (green) dots and blue (green) squares are for $\boldsymbol{r} = (x,0)$ and $\boldsymbol{r} = (x,x)$ respectively for the SF (SF+N) state calculated on a 32×32 lattice size.

2.7.2 Transverse dynamic spin structure factor

We now turn to the most important numerical results from our VMC calculation which, for the half-filled square lattice Heisenberg model, are the true new results of this work. Solving the generalized eigenvalue problem eq. 2.6.18, we obtain the transverse particle-hole excitations eigen-energies $E_n^{\boldsymbol{q}+}$ and eigenstates $\sum_{\boldsymbol{k}} \phi_{\boldsymbol{k}n}^{\boldsymbol{q}+} |\boldsymbol{k},\uparrow\downarrow,\boldsymbol{q}\rangle$. We first show in fig. 2.18 the density of states of the transverse particle-hole excitations:

$$D(\boldsymbol{q},\omega) = \sum_n \delta(\omega - E_n^{\boldsymbol{q}+} + E_{\mathrm{GS}}) \tag{2.7.9}$$

$$\simeq \sum_n \frac{1}{\sqrt{2\pi\sigma^2}} \exp\left[-\frac{1}{2}\left(\frac{\omega - E_n^{\boldsymbol{q}+} + E_{\mathrm{GS}}}{\sigma}\right)^2\right] \tag{2.7.10}$$

where we broaden the δ-function with a gaussian of variance $\sigma = 0.1J$ for better visualization. The density of states is plotted along the high-symmetry directions:

$$(\frac{\pi}{2},\frac{\pi}{2}) \rightarrow (\pi,0) \rightarrow (\pi,\pi) \rightarrow (0,0) \rightarrow (\pi,0). \tag{2.7.11}$$

The numerical data is the result of 10^6 samples of the projected Hamiltonian and the overlap matrix for a 24×24 system size. In the SF+N case it is immediately visible that the lowest-energy states follow a magnon-like dispersion with a gap at the $\boldsymbol{q} = (0,0)$ and $\boldsymbol{q} = (\pi,\pi)$ momenta of $0.38J$. In the same way as the exponentially decaying transverse spin correlations, the opening of a gap is a result of artificially breaking the spin symmetry adding the Néel mean-field h_{N}. There are higher-lying eigenstates gapped every-where from the magnon-like branch. Especially at $\boldsymbol{q} = (\pi,0)$ there is no trace of a continuum of excitations.

From the obtained eigenstates and eigen-energies, we can now take look at the transverse

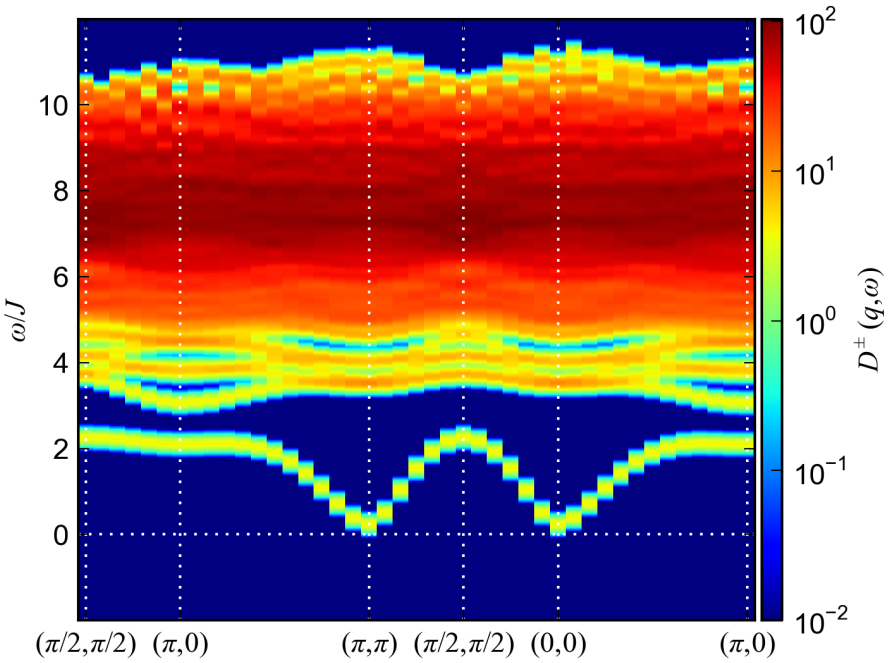

Figure 2.18 – Density of states of the transverse particle-hole excitations of the $|\mathrm{SF}+\mathrm{N}\rangle$ state for a 24×24 system.

dynamic structure factor using formula 2.6.41 and making sure that it is correctly normalized using eq. 2.6.52. The result is shown in fig. 2.19. We see that most of the high-energy states have no spectral weight while the magnon-like mode intensity is almost constant along the magnetic Brillouin zone, diverges at $\boldsymbol{q} = (\pi,\pi)$ and almost vanishes at $\boldsymbol{q} = (0,0)$. Again the reason it does not completely vanish is due to the artificial breaking of the spin-symmetry. For instance in linear SWT, a similar gapped magnon branch with a finite intensity at $\boldsymbol{q} = (0,0)$ can be obtained by including a staggered longitudinal field to the Heisenberg model.

We briefly note that, using the alternate Néel ordered wavefunctions $\left|\mathrm{SF}+\mathrm{V_Q}\right\rangle$ eq. 2.7.5 and $|\mathrm{SF}+\mathrm{AF}\rangle$ eq. 2.7.6 we essentially recovered the same results. The high-energy excitations above

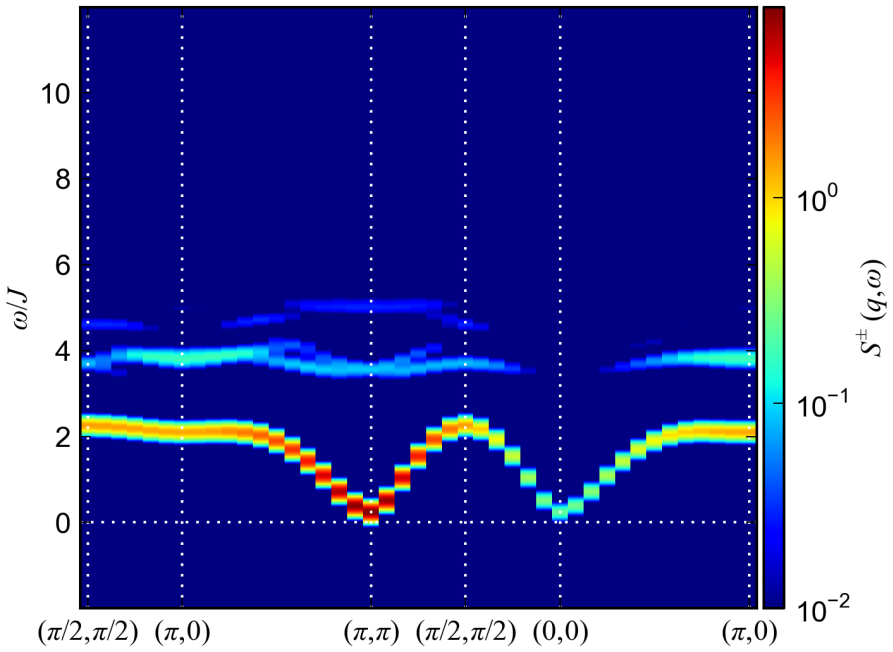

Figure 2.19 – Transverse dynamic structure factor for the particle-hole excitations of the $|\mathrm{SF}+\mathrm{N}\rangle$ state for a 24×24 system.

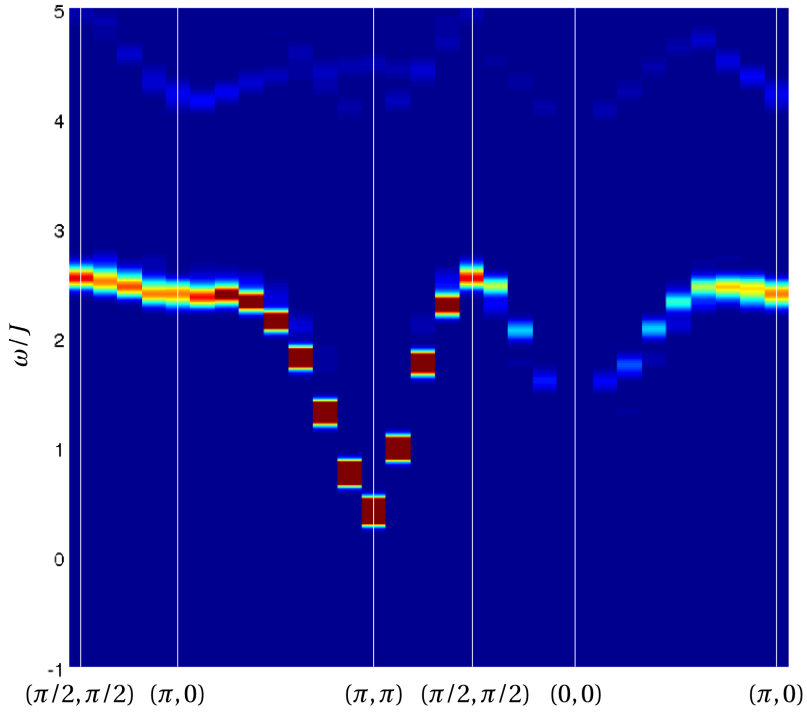

Figure 2.20 – Transverse dynamic structure factor for the projected particle-hole excitations of the $\left|\mathrm{SF}+\mathrm{V_Q}\right\rangle$ state on a 16×16 lattice.

the magnon mode were slightly different, but still gapped from the magnon mode. We show this in the case of the optimal $|\mathrm{SF}+\mathrm{V_Q}\rangle$ for a 16×16 lattice in fig. 2.20

Coming back to the $|\mathrm{SF}+\mathrm{N}\rangle$ wavefunction, we first take a closer look at the magnon-like

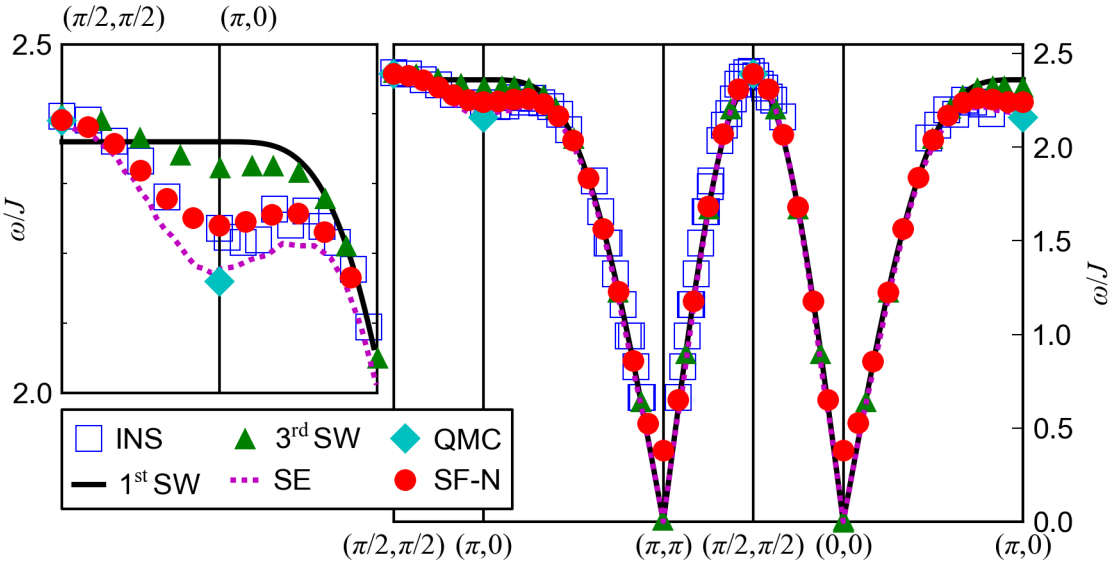

Figure 2.21 – Comparison of the magnon-like mode obtained from the $|\mathrm{SF}+\mathrm{N}\rangle$ wavefunction on a 24×24 system along the high-symmetry directions (right panel) and zoom-in of the MBZB (left panel). Blue squares: unpolarized inelastic neutron scattering from Christensen et al. [2007]. Black solid line: Spin-wave theory with first $1/S$ corrections. Green triangles: Spin-wave theory with third $1/S$ corrections [Syromyatnikov, 2010]. Dashed magenta line: Perturbation series expansion around the Ising limit [Zheng et al., 2005]. Cyan diamonds: Stochastic series expansion quantum Monte Carlo [Sandvik and Singh, 2001]. Red dots: The transverse particle-hole eigenstates from the $|\mathrm{SF}+\mathrm{N}\rangle$ variational wavefunction.

branch in fig. 2.21 where we compare it with unpolarized inelastic neutron scattering on the CFTD material [Christensen et al., 2007], with SWT with first and with third [Syromyatnikov, 2010] order $1/S$ corrections, with series expansion [Zheng et al., 2005] and with stochastic series expansion quantum Monte Carlo [Sandvik and Singh, 2001]. Overall the different theories agree very well with the experimental data. But taking a closer look at the MBZB, we see that the transverse particle-hole magnon-like mode we calculated, series expansion and quantum Monte Carlo agree very well with the 7% downward dispersion $(\pi/2,\pi/2)\rightarrow(\pi,0)$ found in the experiment while third order SWT only obtains a 3% dispersion. This remarkably good agreement of the calculated transverse particle-hole magnon-like mode comes about without any tuning parameter and is the anchor for the physical validity of our variational approach of dynamical quantities. In contrast, quantum Monte Carlo results rely on an explicit choice for the lineshape in order to carry out the analytic continuation (see section 2.5.4). In Syljuåsen and Rønnow [2000] and Sandvik and Singh [2001] the lineshape was chosen to match experiments making this approach explicitly biased. We note that in our approach the dispersion from $\boldsymbol{q}=(\pi/2,\pi/2)$ to $\boldsymbol{q}=(\pi,0)$ is only very weakly dependent on the fine

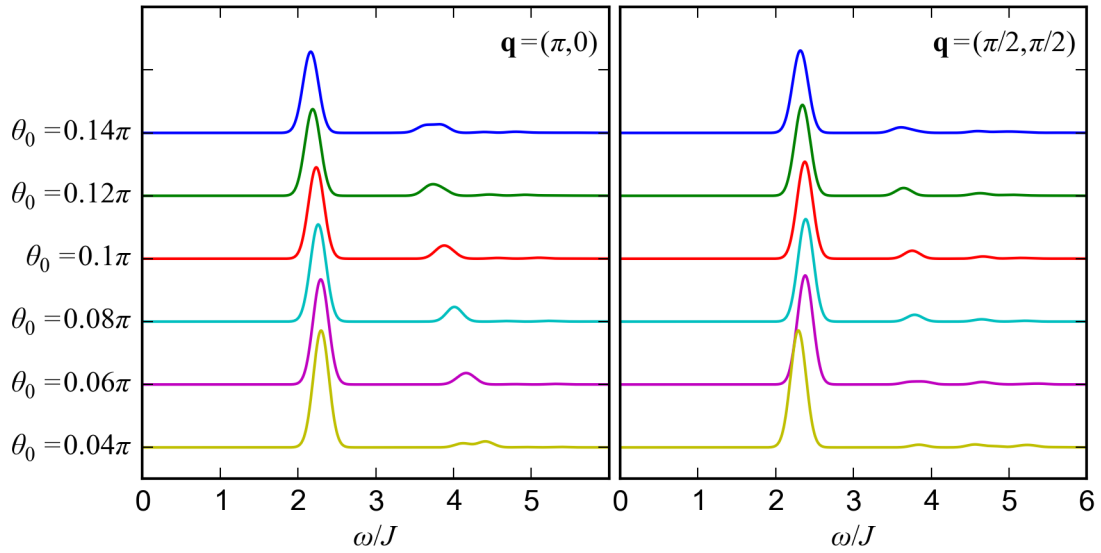

Figure 2.22 – Transverse dynamic structure factor for $\boldsymbol{q} = (\pi, 0)$ (left) and $\boldsymbol{q} = (\pi/2, \pi/2)$ (right) for the optimal Néel mean-field h_{N} and various fluxes θ_0. The calculations were carried with a 16×16 lattice size.

optimization of the variational parameter θ_0. We show in fig. 2.22 the transverse dynamic structure factor at $\boldsymbol{q} = (\pi, 0)$ and $\boldsymbol{q} = (\pi/2, \pi/2)$ for the optimal Néel mean-field $h_{\mathrm{N}} = 0.055$ but with various fluxes θ_0. In the region of lowest variational energy $\theta_0 \in [0.06\pi, 0.12\pi]$, the spectra appear to be only very weakly flux-dependent.

Looking at the magnon-like mode intensity and comparing it to experiments (fig. 2.23), we see that the 50% reduction of the $(\pi, 0)$ intensity compared to $(\pi/2, \pi/2)$ is not reproduced by the transverse particle-hole excitations of the $|\mathrm{SF} + \mathrm{N}\rangle$ state. Instead we find a small 6% reduction of the magnon intensity. This simply relates to the other important discrepancy between our variational theory and the experiments: the fact the SF+N spectrum largely misses the $(\pi, 0)$ continuum, although the high-energy excitations above the $\boldsymbol{q} = (\pi, 0)$ magnon-like mode are stronger than at $\boldsymbol{q} = (\pi/2, \pi/2)$.

We then turn towards the SF case. Looking at the density of states we see that a magnon-like branch is still visible but that a strong continuum of states appears everywhere above it. Close to $\boldsymbol{q} = (0, 0)$ and $\boldsymbol{q} = (\pi, \pi)$, the eigen-energies become negative, meaning some "excitations" have a lower energy than the groundstate. This is due to the fact the wavefunction $|\mathrm{SF}\rangle$ is energetically sub-optimal, linked to the fact there is a magnetic ordering instability. The corresponding dynamic structure factor is shown in fig. 2.25. We see that the continuum of states above the magnon-like branch has almost no spectral weight except at $\boldsymbol{q} = (\pi, 0)$ where a continuum of states clearly appears. However since the calculation is based on a finite size system, the continuum appears as a collection of discrete modes. To support the interpretation of the $\boldsymbol{q} = (\pi, 0)$ states as being part of a continuum we show in fig. 2.26 the effect of increasing system size: The particle-hole excitation subspace size is of $L^2/2$ where L^2 is the total number of sites. Then for larger systems there are more states "available" to

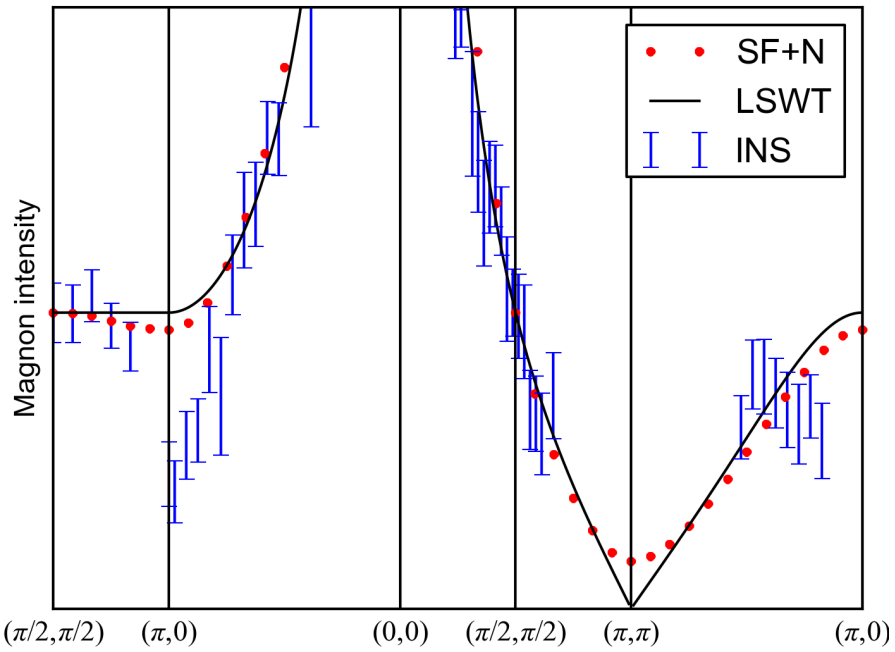

Figure 2.23 – Comparison of the magnon-like mode intensity obtained from the $|\mathrm{SF}+\mathrm{N}\rangle$ wavefunction on a 24×24 system. Red dots: the transverse particle-hole excitation intensity. Black solid line: Linear SWT. Blue error bars: unpolarized inelastic neutron scattering [Christensen et al., 2007]. The linear spin-wave intensity and the experimental intensity are scaled to match the $\boldsymbol{q}=(\pi/2,\pi/2)$ transverse particle-hole intensity. The transverse dynamic structure factor as obtained from our variational approach is itself normalized such that $\sum_{\boldsymbol{q}}\int d\omega S^{\pm}(\boldsymbol{q},\omega)=\frac{N}{2}$.

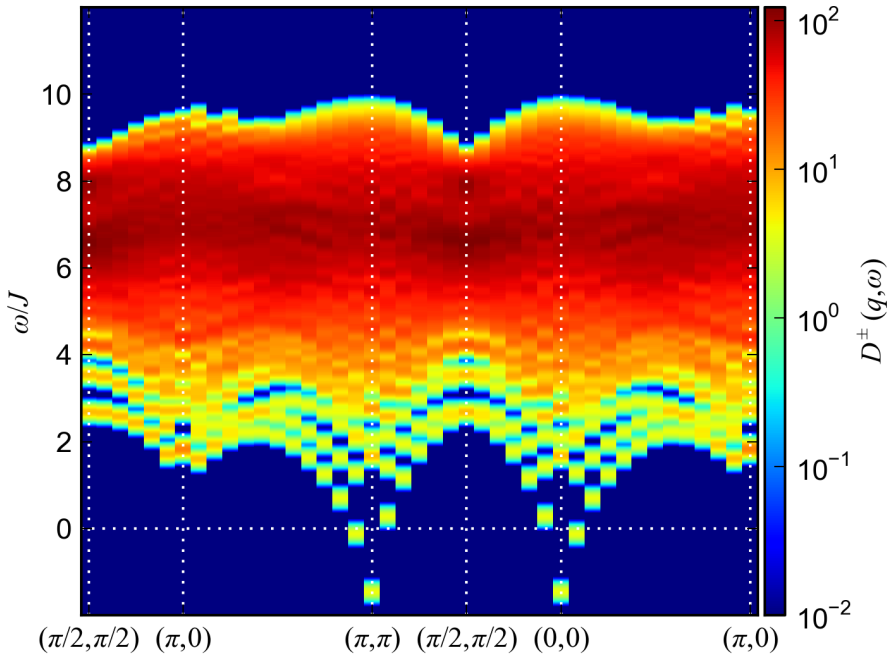

Figure 2.24 – Density of states of the transverse particle-hole excitations of the |SF⟩ state for a 24×24 system.

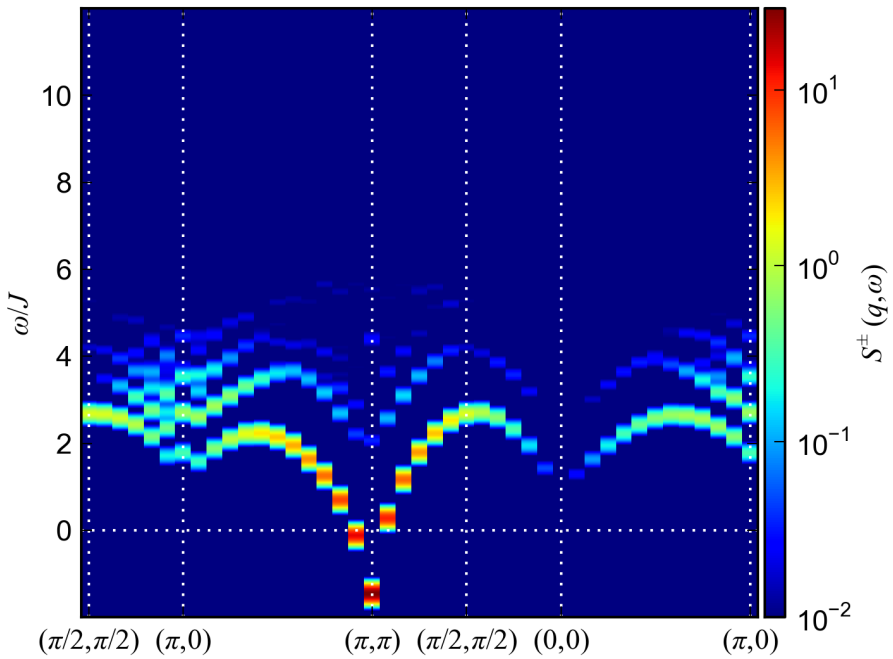

Figure 2.25 – Transverse dynamic structure factor for the particle-hole excitations spectrum of the |SF⟩ state on a 24×24 system.

populate the continuum. As a result we see that in fig. 2.26 left panel new excitations appear at larger system size and move down in energy while gaining spectral weight. This finite-size behavior is the milestone indicating the development of a continuum in the thermodynamic limit. In contrast we show in fig. 2.26 right panel the evolution of the $\boldsymbol{q} = (\pi/2, \pi/2)$ mode. It appears nearly size-independent and about twice as intense as the maximum intensity at $(\pi, 0)$, in qualitative agreement with the experimental results and thus seems to retain a magnon character even in the QSL case.

While we obtain a qualitative agreement for the appearance of the $(\pi, 0)$ continuum with the

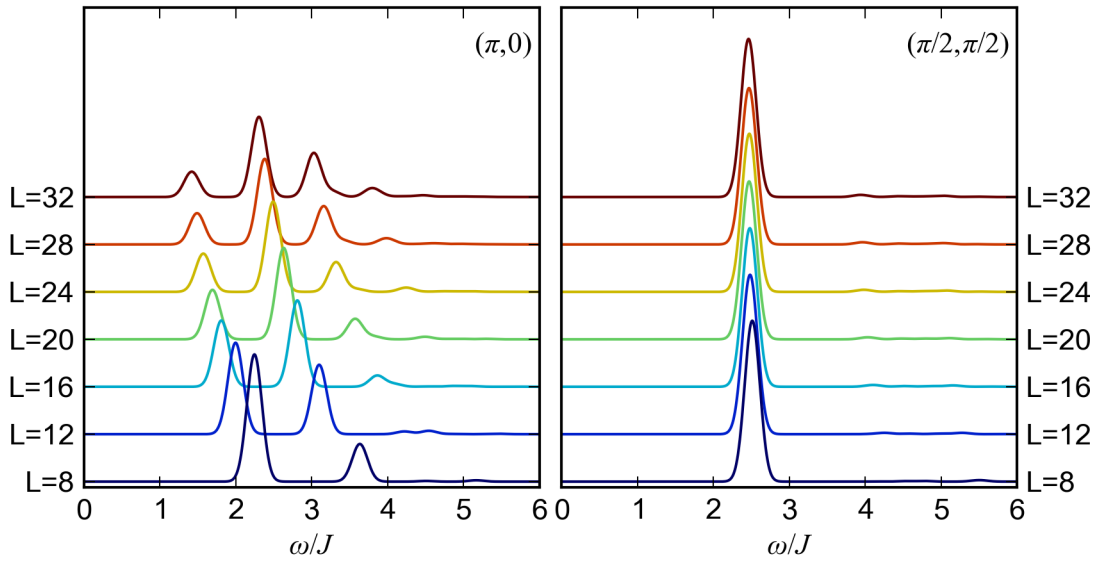

Figure 2.26 – Size dependence of the dynamic structure factor for the $|SF\rangle$ state at $\boldsymbol{q} = (\pi, 0)$ (left) and $\boldsymbol{q} = (\pi/2, \pi/2)$ (right). All spectra are normalized such that $\sum_{\boldsymbol{q}} \int d\omega S^{\pm}(\boldsymbol{q}, \omega) = \frac{L^2}{2}$.

SF wavefunction, the magnon-like branch dispersion along the MBZB is now too pronounced and it is also difficult, when moving close to $(\pi, 0)$, to clearly identify what the magnon mode is. However as the excitation spectrum is strongly dependent on the system size, it is unsure what the main magnon-like branch will look in the thermodynamic limit. Indeed in fig. 2.26 for $\boldsymbol{q} = (\pi, 0)$, the lowest energy mode seems to loose spectral weight with increasing system sizes while the dominant peak energy is 6% smaller than the sharp $\boldsymbol{q} = (\pi/2, \pi/2)$ peak energy. Based on the available numerical data, one can thus not rule out that the projected particle-hole spectrum of the QSL $|\mathrm{SF}\rangle$ state does recover all of the experimentally observed features at short wavelength/high energies in the thermodynamic limit. But for our discussion it is already enough to simply state how the Néel field selects the different observed aspects of the dynamical properties of the square lattice antiferromagnet. We show in fig. 2.27 the variation of the $\boldsymbol{q} = (\pi, 0)$ spectrum as a function of the Néel mean field. One can see it immediately results in a gap between the magnon-like branch and the higher energy excitations. Along with the experimental observation that the $\boldsymbol{q} = (\pi, 0)$ continuum seems to be spin-rotationally invariant, this would support the following interpretation of our theoretical results: The broken spin-symmetry state $|\mathrm{SF} + \mathrm{N}\rangle$ recovers spin-symmetry broken excitations (the magnons) while

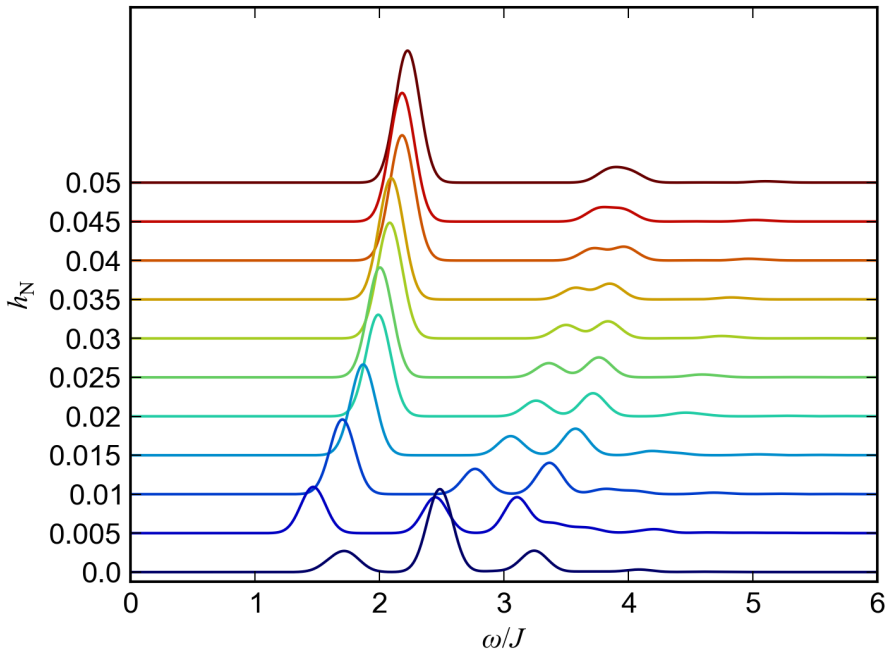

Figure 2.27 – Evolution of the $\boldsymbol{q} = (\pi, 0)$ transverse dynamic structure factor for a range of different Néel mean fields h_N. The spectra are obtained from a calculation on a 32×32 system size.

the QSL $|SF\rangle$ state recovers spin-rotationally invariant excitations. We propose to put in parallel the extinction of the continuum of excitations at $\boldsymbol{q} = (\pi, 0)$ and the exponential decay of the transverse spin correlations suggesting that the states composing the continuum are highly sensitive to the long-distance spin correlation behavior. The relation between these two aspects will be clarified in the next section 2.8. We summarize the pros and cons of the two wavefunctions on table 2.2 highlighting their complementarity.

2.7.3 Longitudinal Dynamical spin structure factor

We present here the longitudinal dynamic structure factor obtained using the eigenstates of the longitudinal particle-hole excitations of our trial wavefunction. In contrast with the transverse

$\|SF+N\rangle$	$\|SF\rangle$
+ Néel order	- QSL
+ Perfect MBZ magnon dispersion	- MBZ dispersion seems too pronounced
- Exponential correlation function	+ Algebraic correlation function
- Weak MBZ magnon intensity variation	+ Good MBZ magnon intensity variation
- No continuum	+ $(\pi, 0)$ continuum

Table 2.2 – Comparison of the SF+N and SF wavefunctions in terms of phenomenological aspects.

channel, these results must be taken as preliminary as much less work and CPU-time was dedicated to it. We will only consider the case of the $|\mathrm{SF}+\mathrm{N}\rangle$ trial wavefunction as the $|\mathrm{SF}\rangle$ one has no breaking of the spin-symmetry thus the longitudinal spectrum is identical to the transverse one. Indeed using the definition of the global rotation operator $\sum_i S_i^-$ in terms of the mean-field theory quasi-particles we find that

$$\sum_i S_i^- \left|\boldsymbol{k},\uparrow\downarrow,\boldsymbol{q}\right\rangle = \left|\boldsymbol{k},\uparrow\uparrow,\boldsymbol{q}\right\rangle + \left|\boldsymbol{k},\downarrow\downarrow,\boldsymbol{q}\right\rangle \tag{2.7.12}$$

which are the triplet states of the longitudinal channel. But when the Néel mean-field is introduced, the breaking of the spin-symmetry makes the longitudinal channel dynamic structure factor different as is the case in SWT. We show only here the result for the 24×24 $|\mathrm{SF}+\mathrm{N}\rangle$ system in fig. 2.28 top panel. Longitudinal particle-hole excitations appear gapped above the transverse magnon-like mode (dashed white line) reproduced as a guide to the eye. At $\boldsymbol{q}=(\pi,\pi)$, the magnetic Bragg peak appears at negative energy of $-0.4J$. To explain it, we recall that at $\boldsymbol{q}=(\pi,\pi)$ and at $\boldsymbol{q}=(0,0)$ the mean-field groundstate itself must be included into the excitation subspace such that longitudinal particle-hole excitations can mix with the groundstate. This leads to a further optimization of the variational groundstate, although it will be barely noticeable when considering the energy per site.

From the analysis of the transverse dynamic structure factor, it was apparent that a particle-

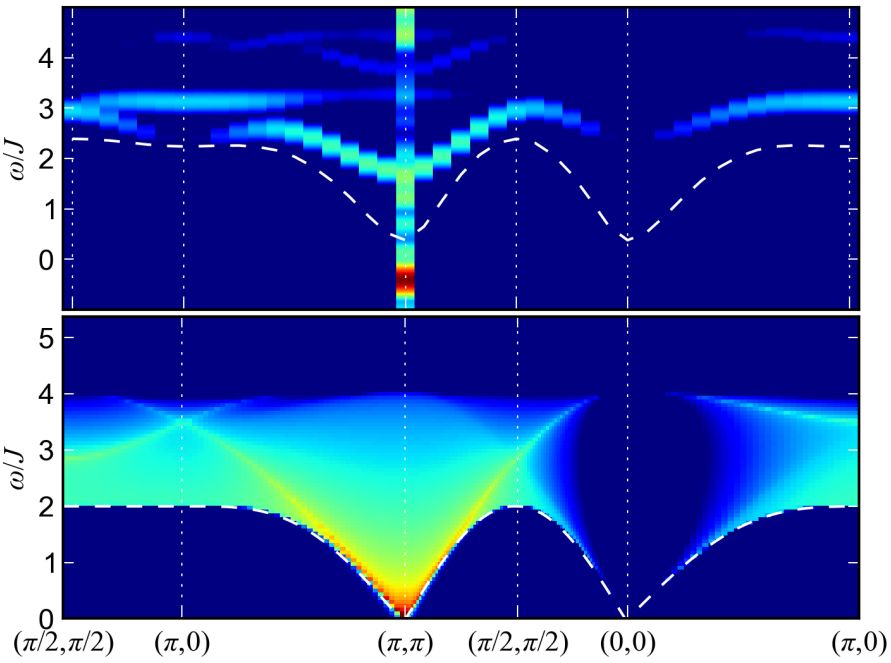

Figure 2.28 – Top: The longitudinal particle-hole dynamic structure factor in the $|\mathrm{SF}+\mathrm{N}\rangle$ state for a 24×24 system. Dashed white line indicates the position of the transverse particle-hole magnon-like dispersion. Bottom: The longitudinal dynamic structure factor in the linear spin-wave approximation. The dashed white line indicates the position of the (not renormalized) transverse magnon dispersion.

hole bound state reproduces a magnon-like excitation. But it shouldn't be inferred that the fractional particle and hole are simply internal degrees of freedom of magnons. In fact as seen in the longitudinal channel, particle-hole states do overlap with what SWT would interpret as two-magnon excitations and it is reasonable to postulate that they will overlap with states which SWT would interpret as even higher order multi-magnons. There is thus no simple relation between the SWT bosonic excitations and the particle-hole one from the projected mean-field theory. To ease the comparison with the spin-wave predictions, we show in fig. 2.28 bottom panel the longitudinal dynamic structure factor from linear SWT, thus neglecting magnon-magnon interaction.
Compared to the polarized neutron scattering data shown in fig. 2.9 panels C and G, we note the following: At $\boldsymbol{q} = (\pi/2, \pi/2)$, the calculated spectrum shows a rather sharp peak at $\omega = 3J$ which might be compared to the lower energy $\omega = 2.6J$ peak found in the experimental data. At $\boldsymbol{q} = (\pi, 0)$, while the calculated spectrum is broader than at $\boldsymbol{q} = (\pi/2, \pi/2)$ in agreement with experiments, it also has a too high energy. The calculated spectrum thus shows significant differences from the experimental data. But for the experimental interpretation of the $\boldsymbol{q} = (\pi, 0)$ continuum as spin-rotationally invariant, it is not expected to match with our spin-rotation broken symmetry calculations based on the $|\mathrm{SF} + \mathrm{N}\rangle$ state. However in the $|\mathrm{SF}\rangle$ state, the longitudinal spectrum must be identical to the transverse one. The numerical validation of this statement still requires some work. Comparing for instance fig. 2.26 to the longitudinal experimental spectrum fig. 2.9 panels C and G, we see that the sharp $\boldsymbol{q} = (\pi/2, \pi/2)$ excitation and the broad $\boldsymbol{q} = (\pi, 0)$ continuum is reproduced by the calculations.

2.8 Bound/Unbound spinon pair analysis

The possibility to obtain numerical predictions of dynamical quantities such as the dynamic structure factor is one great achievement of the VMC technique in the context of Gutzwiller-projected mean-field wavefunctions. Another great advantage is that, from the Monte Carlo sampling of the projected Hamiltonian eq. 2.6.29 and overlap matrix 2.6.30 and their diagonalization, we do obtain variational particle-hole eigenstates which we can further scrutinize. In our study so far of the transverse excitation spectrum, we mentioned dispersing excitations as "magnon-like". In the SF case, we also would like to link the collection of spin-isotropic modes forming the continuum to fractional "spinon"-like particle pairs. We will show below how the knowledge of these excitations eigenstates can lead to a firmer physical interpretation of their nature.

2.8.1 The spinon pair wavefunction

In the context of the fermionized Heisenberg model eq. 2.4.33, the unprojected spin-$\frac{1}{2}$ fermion particle creation and annihilation operators are simply the bare electronic $c^{\dagger}_{i\sigma}$ and $c_{i\sigma}$ operators. The projected mean-field particle-hole excitations we defined in section 2.6.1 may also

simply be written in the basis of the real space projected particle-hole states

$$\left|\boldsymbol{R},\boldsymbol{r},\sigma\sigma'\right\rangle = P_{D=0}c^{\dagger}_{\boldsymbol{R}+\boldsymbol{r}\sigma}c_{\boldsymbol{R}\sigma'}\left|\psi_{\mathrm{GS}}\right\rangle \tag{2.8.1}$$

with $\boldsymbol{R}$ a real space position on the lattice and $\boldsymbol{r}$ what we will hereby mention as the *spinon pair separation*. Since the system is translation-invariant, whether with doubled unit cell or not, it is convenient to define the two-spinons in crystal momentum space:

$$\left|\boldsymbol{r},\sigma\sigma',\boldsymbol{q}\right\rangle = P_{D=0}\sum_{\boldsymbol{R}} e^{i\boldsymbol{q}\boldsymbol{R}}c^{\dagger}_{\boldsymbol{R}+\boldsymbol{r}\sigma}c_{\boldsymbol{R}\sigma'}\left|\psi_{\mathrm{GS}}\right\rangle \tag{2.8.2}$$

which may be understood as propagating spinon pair with momentum $\boldsymbol{q}$ and spinon separation $\boldsymbol{r}$. In this language, the spin-flip state $\left|\boldsymbol{q},+\right\rangle = P_{D=0}S^{+}_{\boldsymbol{q}}\left|\psi_{\mathrm{GS}}\right\rangle$ is rewritten as

$$P_{D=0}S^{+}_{\boldsymbol{q}}\left|\psi_{\mathrm{GS}}\right\rangle = \left|\boldsymbol{0},\uparrow\downarrow,\boldsymbol{q}\right\rangle \tag{2.8.3}$$

therefore a local spin-flip is understood as a local transverse spinon-pair with zero separation. Of course the spinon pair states $\left|\boldsymbol{r},\sigma\sigma',\boldsymbol{q}\right\rangle$ are not eigenstates but will be used as a reference set of states to quantify the degree of spinon *delocalization* of the eigenstates. By inversing the quasiparticle definition 2.4.81, we can relate the spinon pair wavefunction to the mean-field particle-hole excitations. For instance in the transverse channel we have:

$$\left|\boldsymbol{r},\uparrow\downarrow,\boldsymbol{q}\right\rangle = \sum_{\boldsymbol{k}}\phi^{\boldsymbol{q}+}_{\boldsymbol{k}}(\boldsymbol{r})\left|\boldsymbol{k},\uparrow\downarrow,\boldsymbol{q}\right\rangle \tag{2.8.4}$$

with

$$\begin{aligned}\phi^{\boldsymbol{q}+}_{\boldsymbol{k}}(\boldsymbol{r}) = e^{i\boldsymbol{k}\boldsymbol{r}}\Big[&\epsilon_{\boldsymbol{r}}\left(u^{*}_{\boldsymbol{k}\uparrow+}u_{\boldsymbol{k}-\boldsymbol{q}\downarrow-}+v^{*}_{\boldsymbol{k}\uparrow+}v_{\boldsymbol{k}-\boldsymbol{q}\downarrow-}\right)\\&+\bar{\epsilon}_{\boldsymbol{r}}\left(v^{*}_{\boldsymbol{k}\uparrow+}u_{\boldsymbol{k}-\boldsymbol{q}\downarrow-}+u^{*}_{\boldsymbol{k}\uparrow+}v_{\boldsymbol{k}-\boldsymbol{q}\downarrow-}\right)\Big]\end{aligned} \tag{2.8.5}$$

and

$$\epsilon_{\boldsymbol{r}} = \frac{1}{2}\left(e^{i\boldsymbol{Q}\boldsymbol{r}}+1\right) \tag{2.8.6}$$

$$\bar{\epsilon}_{\boldsymbol{r}} = \frac{1}{2}\left(e^{i\boldsymbol{Q}\boldsymbol{r}}-1\right). \tag{2.8.7}$$

While the set of state $\Omega_{\boldsymbol{q}+} = \{\left|\boldsymbol{k},\uparrow\downarrow,\boldsymbol{q}\right\rangle\}$ is a basis of the transverse particle-hole excitations, the set of states $\{\left|\boldsymbol{r},\uparrow\downarrow,\boldsymbol{q}\right\rangle\}$ is not as it is linearly dependent spanning the same space as $\Omega_{\boldsymbol{q}+}$ but containing twice as much states. This originates from the simple definition of $\left|\boldsymbol{r},\sigma\sigma',\boldsymbol{q}\right\rangle$ in eq. 2.8.2 which is not symmetric upon $\boldsymbol{r}\rightarrow-\boldsymbol{r}$. A symmetric definition could simply be chosen as:

$$\left|\boldsymbol{r},\sigma\sigma',\boldsymbol{q}\right\rangle' = \frac{1}{\sqrt{2}}\left(\left|\boldsymbol{r},\sigma\sigma',\boldsymbol{q}\right\rangle+\left|-\boldsymbol{r},\sigma\sigma',\boldsymbol{q}\right\rangle\right) \tag{2.8.8}$$

and the set of states $\{|\boldsymbol{r},\sigma\sigma',\boldsymbol{q}\rangle'\}$ is a basis of the projected particle-hole excitation subspace provided we only consider half of the plane for the spinon separation $\boldsymbol{r}$. In the following we nonetheless chose the set $\{|\boldsymbol{r},\uparrow\downarrow,\boldsymbol{q}\rangle\}$ but we note that the results presented below are essentially the same in the two formulations.

2.8.2 A real space picture of the projected spinon pair excitations

In the one-dimensional spin chain in the XY limit, we saw in section 2.2 that it was possible to give a simple physical interpretation of the spinless particle-hole excitations as unbound pairs of domain walls. It is an important question to know to which extent a simple picture of the particle-hole excitations can be found in two dimensions. The unprojected mean-field particle-hole excitations by themselves have little significance as it is difficult to see what they become in real space after being Gutzwiller-projected. It is more tractable to look for instance directly at the wavefunction $|\boldsymbol{R},\boldsymbol{r},\uparrow\downarrow\rangle$. To simplify we will consider the QSL groundstate but in the d-wave RVB gauge equivalent to the SF state through a SU(2) transformation (section 2.4.4). The groundstate can be represented as a superposition of various lengths singlets arrangements on the lattice. For simplicity we only represent in fig. 2.29.A arrangements with nearest-neighbours singlets. Along with the singlets arrangements, the unprojected d-wave RVB state will also contain several states with one or more double occupancies.
We now consider the effect of creating particle-hole excitations on these states. When applying a local spin-flip, we will simply promote a singlet into a triplet (fig. 2.29.B). This leaves a new state with the same number of double occupancies, thus the one previously containing double occupancies will be projected out.
The picture for the non-local spinon pair $|\boldsymbol{R},\boldsymbol{r}\neq\boldsymbol{0}\rangle$ is quite different and relies heavily on the fact the creation of the particle-hole is made *before* the Gutzwiller projection. In strong contrast with the local spin-flip, creating a non-local particle-hole state will only work on states which contain exactly one double occupation and one hole. Indeed in the case where $\boldsymbol{R}$ and $\boldsymbol{r}$ are such that the particle-hole excitation annihilates the double occupancy and the hole, then the resulting state is one where a singled out pair of spins sit in the singlet sea separated by $\boldsymbol{r}$ (fig. 2.29.C).

2.8.3 Eigenstates spinon-pair analysis

Using the set of states $\{|\boldsymbol{r},\uparrow\downarrow,\boldsymbol{q}\rangle\}$, we will now characterize the transverse particle-hole excitation eigenstates. An important aspect of our results is that some of the excitations we find seem to have a magnon character, at least when looking at their dispersion relation and intensity. A magnon, considering the simple ferromagnetic groundstate, is simply a Fourier sum of local spin-flips. In an antiferromagnet it is also the case if considering the linear SWT solution. Including further orders of $1/S$ corrections will change this picture as a local spin-flip can now overlap with the multi-magnon continuum. But considering the corrections are small even up to third order $1/S$ perturbation [Syromyatnikov, 2010], it is reasonable still to consider

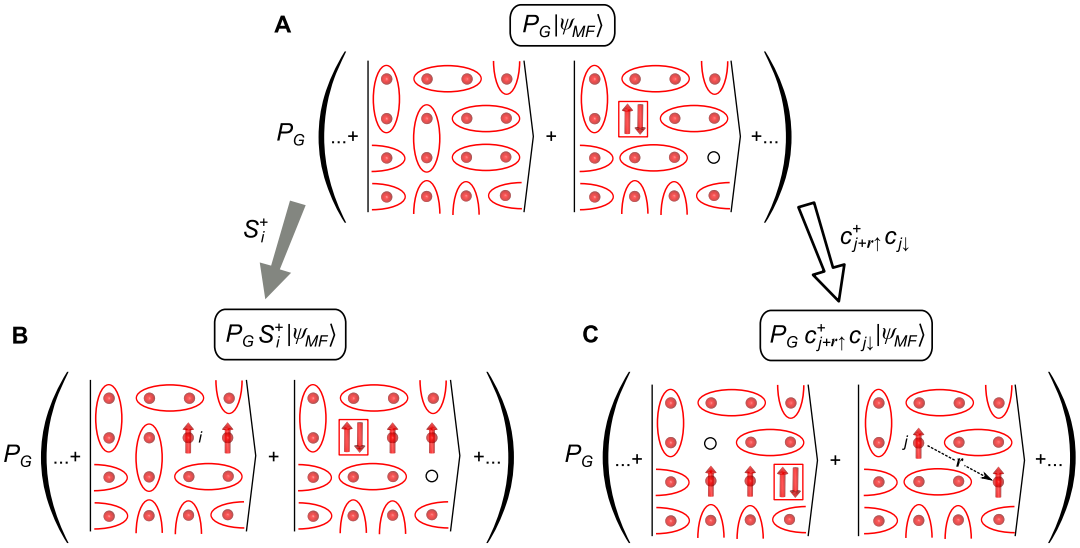

Figure 2.29 – Pictorial representation of the local spin-flip states and the non-local spinon pairs. A: The unprojected ground state in the d-wave RVB gauge represented by a superposition of singlets arrangements. Some of the states contain double occupancies and are discarded by the Gutzwiller projection. B: A local spin-flip corresponds into creating a particle-hole pair on the same site. It promotes a singlet into a triplet and the resulting states have the same number of double occupancies. C: The non-local transverse particle-hole pair will contribute from the unprojected ground state components containing exactly one double occupancy (and one hole) resulting into well separated single spins. Artwork courtesy of Martin Mourigal.

the magnon excitation based on the Fourier sum of local spin-flip picture.
In our variational approach, the Fourier sum of the local spin-flip state is:

$$\sum_{\boldsymbol{R}} e^{i\boldsymbol{q}\boldsymbol{R}} S^{+}_{\boldsymbol{R}} |\mathrm{GS}\rangle = \left|\boldsymbol{0}, \uparrow\downarrow, \boldsymbol{q}\right\rangle \tag{2.8.9}$$

thus expressed as a superposition of local particle-hole pairs. We thus expect the magnon-like excited states to have a strong overlap with this state. We define

$$P^{\boldsymbol{q}+}(\boldsymbol{r}, n) = \left|\left\langle \boldsymbol{r}, \uparrow\downarrow, \boldsymbol{q}\right| n, \uparrow\downarrow, \boldsymbol{q}\right\rangle\right|^2, \tag{2.8.10}$$

the overlap of the n-th transverse eigenstate with the transverse spinon pair separated by $\boldsymbol{r}$. $P^{\boldsymbol{q}+}(\boldsymbol{r}, n)$ gives the spinon-pair separation distribution of the state $\left|n, \uparrow\downarrow, \boldsymbol{q}\right\rangle$. This quantity then provides a picture of the spinon pair separation envelope of some eigenstate $\left|n, \uparrow\downarrow, \boldsymbol{q}\right\rangle$. For instance we expect the magnon-like modes to have most of their overlap contained in the $\boldsymbol{r} = 0$ component and the finite $\boldsymbol{r}$ contributions to decay rapidly. The quantity also allows to quantify how far the spinon-pair states are from being eigenstates. For instance if some eigenstates were to correspond to *delocalized* spinon pairs – the $\left|\boldsymbol{r}, \uparrow\downarrow, \boldsymbol{q}\right\rangle$ states being as far from being eigenstates as possible – then we expect $P^{\boldsymbol{q}+}(\boldsymbol{r}, n)$ to be a very broad distribution of weights as a function of $\boldsymbol{r}$. We also define the following overlap quantity in term of the eigenstates frequency:

$$P^{\boldsymbol{q}+}(\boldsymbol{r}, \omega) = \sum_{n} \left|\left\langle \boldsymbol{r}, \uparrow\downarrow, \boldsymbol{q}\right| n, \uparrow\downarrow, \boldsymbol{q}\right\rangle\right|^2 \delta\left(\omega - E^{\boldsymbol{q}+}_{n} + E_{\mathrm{GS}}\right) \tag{2.8.11}$$

where in practice the delta-function will be widened by a gaussian with a finite width as was done for the dynamic structure factor. This quantity is in practical terms the most handy as what we ultimately want is to link features (i.e. "peaks") of the dynamic structure factor to a corresponding spinon-pair separation distribution. If some eigenstates are nearly degenerate, it defines an average of their spinon separation distribution. Numerically, truly degenerate eigenstates will always crystallize into non-degenerate states chosen at random by the numerical algorithm in the degenerate subspace. This is the motivation behind the definition eq. 2.8.11 as now $P^{\boldsymbol{q}+}(\boldsymbol{r}, \omega)$ is independent of such random choices. We incidentally also note that, for $\boldsymbol{r} = 0$ case, it is actually the same as the transverse dynamic structure factor:

$$P^{\boldsymbol{q}+}(\boldsymbol{r} = 0, \omega) = \sum_{n} \left|\langle \mathrm{GS}| S^{+}_{\boldsymbol{q}} \left|n, \uparrow\downarrow, \boldsymbol{q}\right\rangle\right|^2 \delta(\omega - E^{\boldsymbol{q}+}_{n} + E_{\mathrm{GS}}) = S^{\pm}(\boldsymbol{q}, \omega) \tag{2.8.12}$$

such that $P^{\boldsymbol{q}+}(\boldsymbol{r}, \omega)$ might be understood as a generalization of the dynamic structure factor. In the following figures, the quantity $P^{\boldsymbol{q}+}(\boldsymbol{r}, \omega)$ is normalized such that

$$\sum_{\boldsymbol{r}} P^{\boldsymbol{q}+}(\boldsymbol{r}, \omega) = 1 \tag{2.8.13}$$

We can now come back at the previously obtained results in the transverse channel. We first consider the Néel ordered case in the SF+N groundstate. We show in fig. 2.30 the transverse dynamic structure factor with some regions highlighted. For the highlighted $\boldsymbol{q}$ and ω, we

show the corresponding spinon pair separation distribution using eq. 2.8.11. It is immediately visible that all the modes consist essentially of the spin-flip state $|\mathbf{0},\uparrow\downarrow,\boldsymbol{q}\rangle$ with a small envelope of finite spinon pair separation. We thus conclude that in the Neel ordered case, the particle-hole pairs form a bound state which we might refer to as a magnon. We note that even higher energy states (feature "B" in fig. 2.30) are also two-spinons bound states such that the magnon interpretation relies not only on the bound spinons argument but also on the observed magnon-like dispersion and intensity. We note that the spinon separation distribution in fig. 2.30 panel lacks an inversion symmetry. This is due to the definition 2.8.2. Using the symmetric states 2.8.8 would simply corresponds into symmetrizing the spinon separation distribution upon the inversion $\boldsymbol{r} \to \boldsymbol{r}$.

The situation is very different in the isotropic disordered SF state case. We show in fig. 2.31

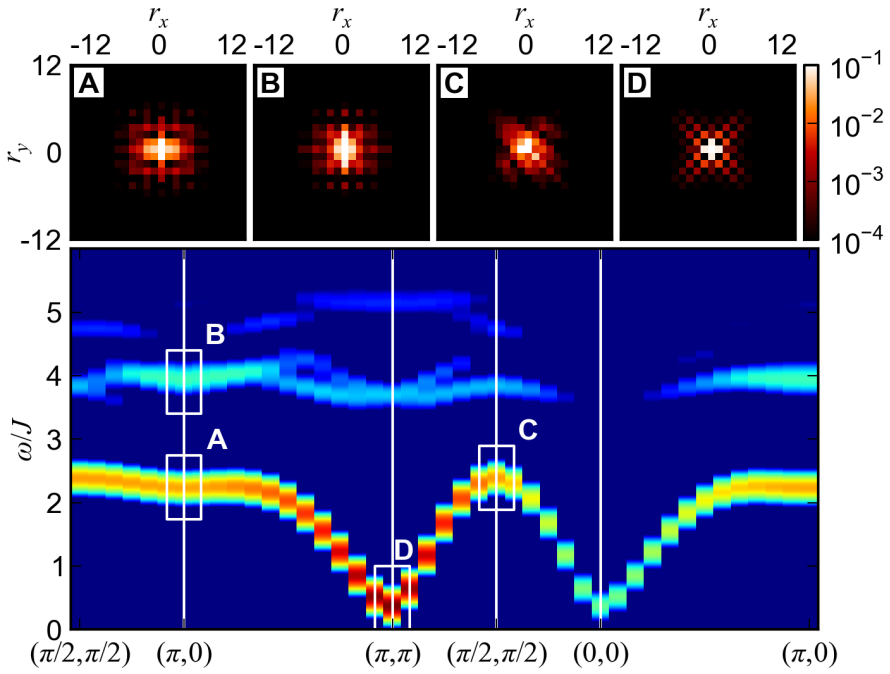

Figure 2.30 – Inspection of the transverse dynamic structure factor features in terms of corresponding spinon pair separation distribution. Bottom: the transverse dynamic structure factor along the high symmetry directions for the Néel SF+N state on a 24×24 lattice. Top: the spinon pair distribution eq. 2.8.11 corresponding to the highlighted features in the transverse dynamic structure factor.

bottom panels the transverse structure factor at the $\boldsymbol{q} = (\pi,0)$ and $\boldsymbol{q} = (\pi/2,\pi/2)$ points again highlighting some features for which the spinon pair separation distribution is shown on the top panels. Note that the color-scale is identical to fig. 2.30 to allow comparison. While the sharp mode still present at $\boldsymbol{q} = (\pi/2,\pi/2)$ still dominantly overlaps with the spin-flip state with a small envelope, the excited states composing the continuum at $\boldsymbol{q} = (\pi,0)$ are much more spread out. In fact the spread is such that it is the system size that bounds the maximum separation, hinting that in the thermodynamic limit the states composing the continuum are made of *delocalized*, unbound spinon pairs. This last affirmation cannot be made firm without

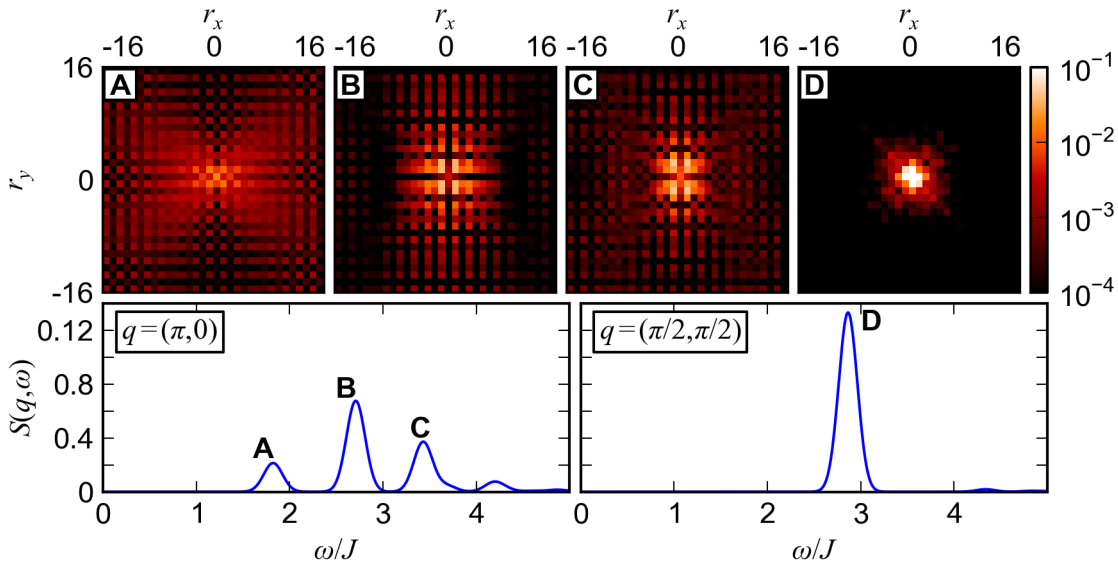

Figure 2.31 – Inspection of the transverse dynamic structure factor features in terms of corresponding spinon pair separation distribution. Bottom left (right): the transverse dynamic structure factor at $\boldsymbol{q} = (\pi,0)$ ($\boldsymbol{q} = (\pi/2,\pi/2)$) for the QSL SF state on a 32×32 lattice. Top: the spinon pair distribution eq. 2.8.11 corresponding to the peaks in the transverse dynamic structure factor.

finite-size analysis which we will develop in section 2.8.5. It is thus seen that our variational calculation yields the two different aspects observed in experiments. The SF+N case allows to recover precisely the observed magnon dispersion, the magnon mode being made out of bound spinons pairs. The SF case on the other hand also recovers a state we might characterize as magnon-like at $(\pi/2,\pi/2)$ but, in strong contrast, finds a continuum at $(\pi,0)$ seemingly corresponding to unbound spinon pairs.

2.8.4 spinon-pair analysis of the $S^+_{\mathbf{q}}|\mathrm{GS}\rangle$ state

Linking the observation of a continuum of excitations to delocalized spinon physics is the most important part of this study. While eq. 2.8.11 seems very suitable to inquire about well-defined, sharp modes, it is not so good for characterizing a continuum. In our finite system calculation the continuum will always appear as a collection of modes growing bigger with system size and eq. 2.8.11 can be used to study the different contributions of the modes. But this has the disadvantage that, the collection evolving with system size, comparing the results across different system sizes is difficult. To allow this comparison we thus need a quantity which is not dependent on a particular collection of modes. We define the following weighted average:

$$\rho^{\boldsymbol{q}^+}(\boldsymbol{r}) = \sum_n \left|\langle \boldsymbol{r},\uparrow\downarrow,\boldsymbol{q}|n,\uparrow\downarrow,\boldsymbol{q}\rangle\langle n,\uparrow\downarrow,\boldsymbol{q}|\boldsymbol{0},\uparrow\downarrow,\boldsymbol{q}\rangle\right|^2, \tag{2.8.14}$$

normalized such that $\sum_{\boldsymbol{r}} \rho^{\boldsymbol{q}+}(\boldsymbol{r}) = 1$. In this quantity, we weight the eigenstates' spinon separation distributions $P^{\boldsymbol{q}+}(\boldsymbol{r}, n) = \left|\langle \boldsymbol{r}, \uparrow\downarrow, \boldsymbol{q} | n, \uparrow\downarrow, \boldsymbol{q}\rangle\right|^2$ with the corresponding mode intensity found in the transverse dynamic structure factor $\left|\langle n, \uparrow\downarrow, \boldsymbol{q} | \boldsymbol{0}, \uparrow\downarrow, \boldsymbol{q}\rangle\right|^2$. This allows to characterize the degree of spinon delocalization attached to the modes proportionally to their intensity in the transverse spectrum at a given momentum $\boldsymbol{q}$. While this definition is simple and functional per se, we give below another interpretation of this quantity.
In the interpretation of the continuum as caused by spinon pair delocalization, the local spin-flip $S^+_{\boldsymbol{q}}$, caused for instance by a probing neutron, delocalizes into more and more extended spinon pairs. This is a dynamic process thus we might be interested into looking at:

$$\rho^{\boldsymbol{q}+}(\boldsymbol{r}, t) = \left|\langle \boldsymbol{r}, \uparrow\downarrow, \boldsymbol{q}| \, e^{-i\mathscr{H}t} \, |\boldsymbol{0}, \uparrow\downarrow, \boldsymbol{q}\rangle\right|^2 \tag{2.8.15}$$

which is the probability, at time t, to find the time-evolved spin-flip state $e^{-i\mathscr{H}t}|\boldsymbol{0}, \uparrow\downarrow, \boldsymbol{q}\rangle$ into the spinon pair state $|\boldsymbol{r}, \uparrow\downarrow, \boldsymbol{q}\rangle$. To resolve the time evolution operator, we simply introduce the eigenstates projector $|n, \uparrow\downarrow, \boldsymbol{q}\rangle\langle n, \uparrow\downarrow, \boldsymbol{q}|$. One might then ask the question of knowing, over all times, how much does the spin-flip state delocalizes? This can be answered by averaging over time the probability distribution $\rho^{\boldsymbol{q}+}(\boldsymbol{r}, t)$:

$$\begin{aligned}
\lim_{T\to\infty} \frac{1}{T}\int_0^T \rho^{\boldsymbol{q}+}(\boldsymbol{r}, t) &= \lim_{T\to\infty} \frac{1}{T}\int_0^T \left|\sum_n \langle \boldsymbol{r}, \uparrow\downarrow, \boldsymbol{q}|n, \uparrow\downarrow, \boldsymbol{q}\rangle\langle n, \uparrow\downarrow, \boldsymbol{q}|\boldsymbol{0}, \uparrow\downarrow, \boldsymbol{q}\rangle \, e^{-iE_n t}\right|^2 \\
&= \sum_n \left|\langle \boldsymbol{r}, \uparrow\downarrow, \boldsymbol{q}|n, \uparrow\downarrow, \boldsymbol{q}\rangle\langle n, \uparrow\downarrow, \boldsymbol{q}|\boldsymbol{0}, \uparrow\downarrow, \boldsymbol{q}\rangle\right|^2 \\
&= \rho^{\boldsymbol{q}+}(\boldsymbol{r}).
\end{aligned} \tag{2.8.16}$$

$\rho^{\boldsymbol{q}+}(\boldsymbol{r})$ can thus also be interpreted as the time-averaged spinon pair separation distribution of the spin-flip state $|\boldsymbol{0}, \uparrow\downarrow, \boldsymbol{q}\rangle$. This interpretation carries the message that, while the spin-flip does naturally overlap with spinon pairs with a small separation, it is the dynamics of the Hamiltonian that might or might not cause delocalization. In other word, while the overlap $\langle \boldsymbol{r}, \uparrow\downarrow, \boldsymbol{q}|\boldsymbol{0}, \uparrow\downarrow, \boldsymbol{q}\rangle$ will decay quickly with $\boldsymbol{r}$ at any momenta, the matrix elements $\langle \boldsymbol{r}, \uparrow\downarrow, \boldsymbol{q}| \, \mathscr{H} \, |\boldsymbol{0}, \uparrow\downarrow, \boldsymbol{q}\rangle$ might not, which will be evidenced by the $\rho^{\boldsymbol{q}+}(\boldsymbol{r})$ quantity.
We show this quantity again for the SF+N (fig. 2.32) and the SF (fig. 2.33) states for the $\boldsymbol{q} = (\pi, 0)$ and $\boldsymbol{q} = (\pi/2, \pi/2)$ momenta. Similarly to the previous section, we see that the $\boldsymbol{q} = (\pi/2, \pi/2)$ momentum spectrum corresponds to bound spinon pair physics in both the SF+N and SF cases. The $\boldsymbol{q} = (\pi, 0)$ momentum displays a contrasted behavior showing again bound spinon pairs physics for the SF+N case and unbound spinon pairs in the SF case. To further quantify the extent of the spinon delocalization as a function of the Néel mean field, we define the disk-integrated spinon-pair separation distribution:

$$R^{\boldsymbol{q}+}(r) = \sum_{|\boldsymbol{r}'|\leq r} \tilde{\rho}^{\boldsymbol{q}+}(\boldsymbol{r}'), \tag{2.8.17}$$

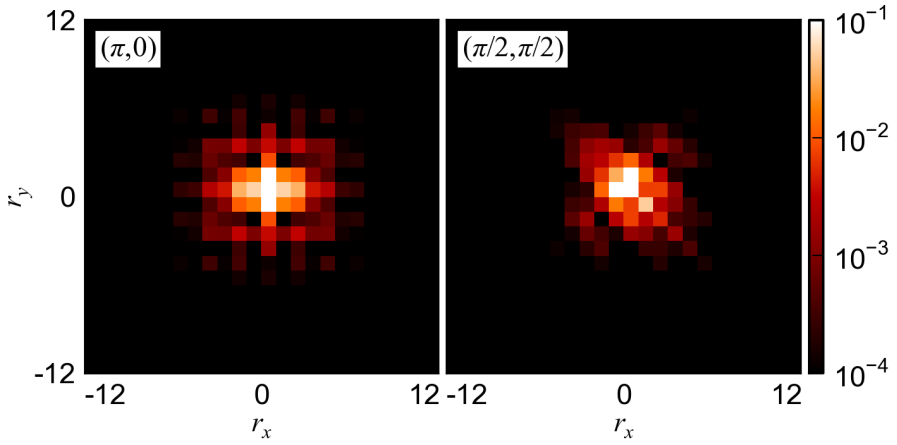

Figure 2.32 – The spinon pair separation quantified using eq. 2.8.14 for $\boldsymbol{q} = (\pi, 0)$ (left) and $\boldsymbol{q} = (\pi/2, \pi/2)$ in the SF+N case on a 24×24 lattice.

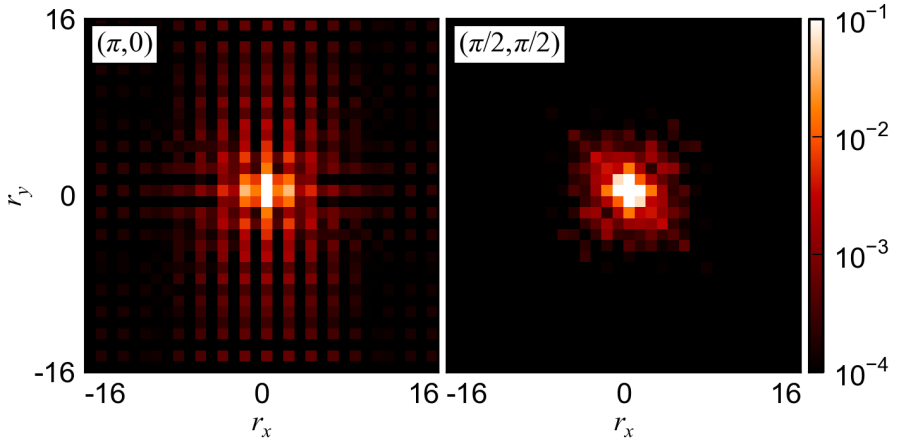

Figure 2.33 – The spinon pair separation quantified using eq. 2.8.14 for $\boldsymbol{q} = (\pi, 0)$ (left) and $\boldsymbol{q} = (\pi/2, \pi/2)$ in the SF case on a 32×32 lattice.

where $\tilde{\rho}^{\boldsymbol{q}+}(\boldsymbol{r})$ is the same quantity than $\rho^{\boldsymbol{q}+}(\boldsymbol{r})$ but restricted to $|\boldsymbol{r}| \leq L/2$ and normalized such that

$$\sum_{|\boldsymbol{r}|\leq L} \tilde{\rho}^{\boldsymbol{q}+}(\boldsymbol{r}) = 1 \tag{2.8.18}$$

in order to work-around the fact that, in a square $L \times L$ lattice, full disks can only have a radius as large as $L/2$. We also define the Root Mean Square (RMS) spinon separation

$$r^{\boldsymbol{q}+} = \sqrt{\sum_{\boldsymbol{r}} \tilde{\rho}^{\boldsymbol{q}+}(\boldsymbol{r})\,|\boldsymbol{r}|^2}. \tag{2.8.19}$$

We note that for these two quantities, whether we use the state $\left|\boldsymbol{r},\uparrow\downarrow,\boldsymbol{q}\right\rangle$ as defined in eq. 2.8.2 or $\left|\boldsymbol{r},\uparrow\downarrow,\boldsymbol{q}\right\rangle'$ in eq. 2.8.8 to calculate $\tilde{\rho}^{\boldsymbol{q}+}(\boldsymbol{r})$ will bring exactly the same result due to the fact that in both quantities $\tilde{\rho}^{\boldsymbol{q}+}(\boldsymbol{r})$ and $\tilde{\rho}^{\boldsymbol{q}+}(-\boldsymbol{r})$ are averaged.
We show these two quantities at $\boldsymbol{q} = (\pi, 0)$ in fig. 2.34 for different strengths of the Néel mean field. Consistently with the overall picture, the Néel mean field gives the disk-integrated separation distributions more weight at short spinon separations and reduces the RMS spinon separation.
To summarize, we thus get a consistent picture for the effect of the artificial symmetry breaking

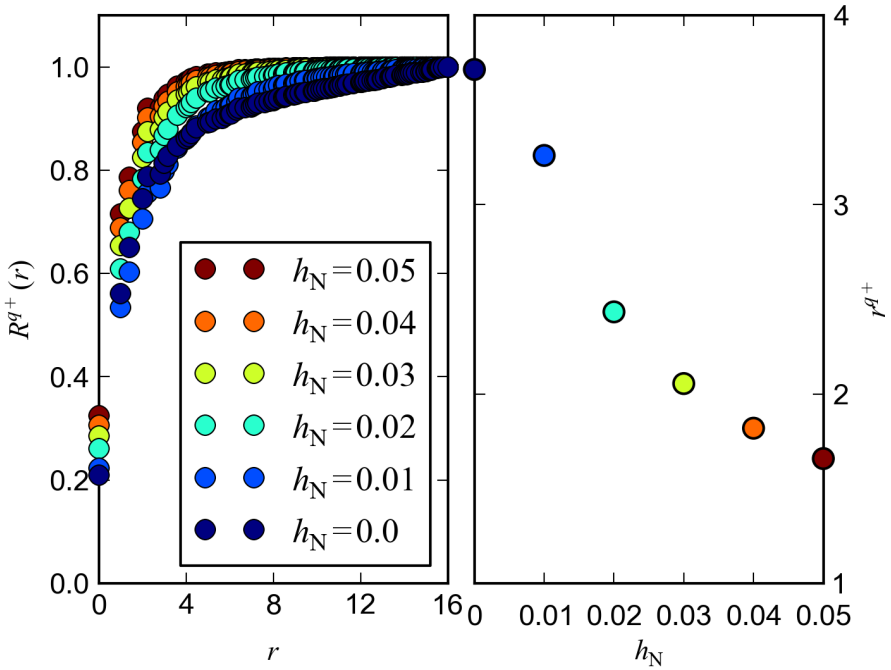

Figure 2.34 – Analysis of the Néel mean field effect on the spinon pair separation. Left panel, the spinon pair separation profile as defined in eq. 2.8.17 for increasing Néel mean fields. Right panel: The root mean square spinon separation eq. 2.8.19 as a function of the Néel mean field. All data is obtained for a 32×32 lattice.

induced by the Néel field. It induces:

– A change from algebraic to exponential decay of the instantaneous transverse spin-spin correlation functions.
– A well-defined magnon-mode.
– A binding of the spinon pairs at $\boldsymbol{q} = (\pi, 0)$.

2.8.5 Finite size-effect analysis

We provide here what we consider the strongest support in favor of spinon delocalization at $\boldsymbol{q} = (\pi, 0)$ in the SF state. If the spinon pairs are indeed unbound, then they are allowed to separate as much as the finite $L \times L$ system size permits. We thus expect a linear dependence of the RMS spinon separation eq. 2.8.19 on system size L. The disk-integrated spinon separation distribution eq. 2.8.17 should also show a constantly changing profile as a function of L. In the opposite case where spinons form a bound state, then the RMS spinon separation and the disk-integrated spinon separation distribution should stay unchanged once a sufficiently large system size to contain the full bound spinon pair envelope is reached.
With these expectations in mind we show the system size dependence of the $\boldsymbol{q} = (\pi, 0)$ and $\boldsymbol{q} = (\pi/2, \pi/2)$ in the SF case in fig. 2.35. While the transverse spectrum size dependence was already shown in fig. 2.26, we show again this size-dependence in fig. 2.35 top panels as we believe the parallel with the spinon separation size-dependence in the bottom panels is remarkable: At $\boldsymbol{q} = (\pi/2, \pi/2)$ all quantities plotted quickly converge with increasing system size, indicating that already at modest sizes the solution we obtain is representative of the thermodynamic limit.
In strong contrast at $\boldsymbol{q} = (\pi, 0)$ the continuous changes against system size observed both in the transverse excitation spectrum and in the spinon separation quantities hints at completely deconfined spinon physics. In particular the linear size-dependence of the RMS spinon separation brings strong support to the unbound spinons interpretation of the observed transverse continuum.

2.9 Conclusion

To conclude this chapter we will state again the results shown in the preceding sections. A strong axis in this work is to explain theoretically the observed magnetic zone boundary anomaly and to provide a physical interpretation. This is covered into section 2.9.1. The success of the variational approach for characterizing the magnetic excitations of the square lattice antiferromagnet calls for further research topics for which we provide a tentative list in section 2.9.2.

2.9.1 Magnetic zone boundary anomaly

The initial motivation for this work was the unambiguous characterization of the magnetic zone boundary quantum anomaly found in the transverse dynamic structure factor. This

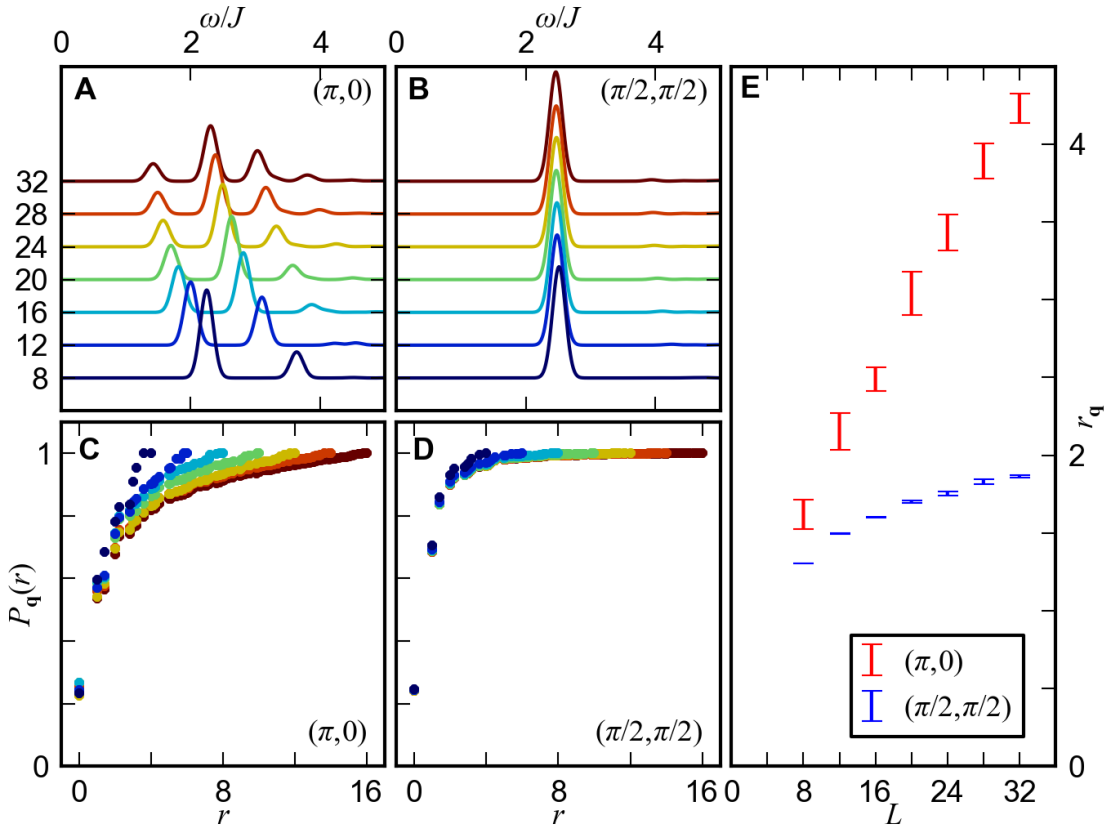

Figure 2.35 – Size dependence of various quantities in the SF case at $\boldsymbol{q} = (\pi,0)$ and $\boldsymbol{q} = (\pi/2,\pi/2)$. A and B: the transverse dynamic structure factor at $\boldsymbol{q} = (\pi,0)$ and $\boldsymbol{q} = (\pi/2,\pi/2)$ respectively for sizes ranging from 8×8 (dark blue) to 32×32 (dark red). C and D: for the same momenta the disk-integrated spinon separation distributions eq. 2.8.17. Same color-code as in A and B. E: The RMS spinon separation eq. 2.8.19 for $\boldsymbol{q} = (\pi,0)$ (red error bars) and $\boldsymbol{q} = (\pi/2,\pi/2)$ (blue error bars) as a function of system size. The error bars are evaluated as explained in appendix A.6.

anomaly is characterized by i) a 7% reduction of the magnon-like mode energy from $\boldsymbol{q} = (\pi/2, \pi/2)$ to $\boldsymbol{q} = (\pi, 0)$, ii) a 50% of the $\boldsymbol{q} = (\pi, 0)$ maximum intensity with respect to $\boldsymbol{q} = (\pi/2, \pi/2)$ and iii) an asymmetric broadening of the $\boldsymbol{q} = (\pi, 0)$ peak towards higher energies, referred to as the continuum. All these observations mark a strong contradiction with the SWT, even when accounting for high-order corrections [Canali and Wallin, 1993; Syromyatnikov, 2010]. On the other hand numerical calculations could reproduce the 7% magnon-like mode energy reduction [Sandvik and Singh, 2001; Zheng et al., 2005] strengthening the hypothesis that the magnetic zone-boundary quantum anomaly is an intrinsic aspect of the square lattice antiferromagnet. An unbiased numerical determination of the transverse dynamic structure factor lineshape at $\boldsymbol{q} = (\pi, 0)$ is still missing due to the limitations of exact numerical approaches, especially the so-called analytical continuation problem [Jarrell and Gubernatis, 1996].

In this context our work brings important contributions by linking the magnetic zone boundary quantum anomaly aspects i)-iii) to physically meaningful variational Ansätze for the square lattice Heisenberg antiferromagnet ground-state and low-energy excitations. Namely we provide two complementary pictures through the Néel ordered SF+N and the QSL SF variational Ansätze.

The SF+N variational Ansatz reproduces the spontaneously broken spin symmetry of the square lattice Heisenberg antiferromagnet by artificially breaking it through a Néel mean field. It has a very good variational energy, only 0.7% higher than the best numerical groundstate energy estimate [Trivedi and Ceperley, 1989; Calandra Buonaura and Sorella, 1998; Runge, 1992] and a staggered magnetization of $0.71S$, higher by 12% from aforementioned references. These groundstate aspects of the SF+N variational Ansatz have been studied before [Gros, 1988; Lee and Feng, 1988; Ivanov and Lee, 2003; Ivanov, 2004]. The completely new result is that this Ansatz perfectly reproduces the observed short wavelength magnon-like excitation energy including the 7% dispersion along the magnetic zone boundary. But it also has limitations tied to the artificial breaking of the spin symmetry. The transverse instantaneous spin-spin correlation function decays exponentially instead of the expected power-law decay (fig. 2.17). Along with the slightly too high staggered magnetization, this shows that the SF+N state underestimates the transverse quantum fluctuations of the true square lattice Heisenberg antiferromagnet groundstate. The most striking aspect of the magnetic zone-boundary quantum anomaly is not reproduced by the SF+N Ansatz: Everywhere on the magnetic zone-boundary, higher energy excitations stay gapped from the magnon-like mode such that there is no trace of a transverse continuum of excitations at $\boldsymbol{q} = (\pi, 0)$. Looking in parallel at the evolution of the transverse dynamic structure factor evolution at $\boldsymbol{q} = (\pi, 0)$ and at the evolution of the transverse instantaneous spin-spin correlation function suggests that the extinction of the transverse quantum fluctuation in the SF+N variational Ansatz is responsible for the disappearance of the transverse continuum.

This leads to the second complementary variational Ansatz we studied, the spin-liquid SF state. With respect to variational energy and staggered magnetization, it is a sub-optimal Ansatz as it has a 5% higher energy than the best numerical estimate and no staggered magnetization. But it also has interesting properties. In particular it is a critical state as the isotropic instantaneous

spin-spin correlation decay as a power-law, in agreement with robust long wave-length SWT prediction. Being a spin-liquid the quantum fluctuations are very large as there are no finite classical order parameter. We found that this state reproduces the magnetic zone boundary quantum anomaly aspects ii) and iii), that is it finds a continuum of excitations at $\boldsymbol{q} = (\pi, 0)$ as evidenced by the finite-size effect analysis in fig. 2.26. Moreover it also finds that at the $\boldsymbol{q} = (\pi/2, \pi/2)$ the magnon-like mode stays sharp as observed in experiments.
The two SF+N and SF Ansätze thus provide a complementary description of all of the experimental aspects of the short wavelength excitations of the square lattice Heisenberg antiferromagnet. It has to be noted however that we presently do not provide a complete picture as it seems we cannot reproduce all the aspects in a single Ansatz. The mean-field approach to describe the spontaneously broken spin symmetry seems to suffer from the strong limitation that it effectively extincts the transverse quantum fluctuations present in the square lattice Heisenberg antiferromagnet groundstate.
Following the achievements of the SF+N and SF Ansätze into reproducing the experimentally established aspects of the magnetic zone boundary quantum anomaly, we developed their physical interpretation based on the complete knowledge of the variational excitation wavefunctions allowed by the variational Monte Carlo approach. Namely we could describe all of the excitations as projected mean-field particle-hole excitations and showed that, in the physical Hilbert space they can be understood as superpositions of spatially-separated spinon-pairs. This naturally lead to the question of knowing whether these spinon-pairs must be seen as a bound-state identifiable to a magnon or if the two spinons are in fact truly independent degrees of freedom. The development of meaningful quantities to tackle this important section allowed to unambiguously link the calculated SF Ansatz continuum of excitations at the $\boldsymbol{q} = (\pi, 0)$ momentum to a deconfinement of the spinon-pairs while, at the $\boldsymbol{q} = (\pi/2, \pi/2)$ momentum the SF Ansatz variational excitation is found to be a spinon-pair bound state. In the SF+N case, all excitations including the magnon-like mode were found to be spinon-pair bound states.
Deconfined fermionic excitations have been observed and predicted in 1D systems. In 2D, deconfined fermionic degrees of freedom has so far mainly been pursued in highly frustrated models such as the triangular model [Coldea et al., 2001b] or the Kagomé lattice [Han et al., 2012; Jeong et al., 2011]. The unambiguous experimental characterization of the square lattice Heisenberg antiferromagnet magnetic zone boundary quantum anomaly and its interpretation in our work in terms of bound and unbound spinon pairs is the first attempt at establishing the existence of deconfined fractional degrees of freedom in the experimentally measured excitation spectrum of an *unfrustrated* 2D magnetic system with a Néel ordered groundstate.

2.9.2 Further research

The success of the variational Monte Carlo approach at calculating the magnetic excitations of the square lattice Heisenberg antiferromagnet calls for more applications. We list here a tentative list of interesting topics where this approach might be useful.

– **Transverse field effect:** Experimentally applying an external field is one of the most obvious approaches to add some controlled parameter into the system and might help to uncover new physics. Early unpublished neutron scattering results from the Laboratory for Quantum Magnetism seem to indicate that, upon applying a magnetic field transverse to the Néel ordering direction, the magnetic zone boundary quantum anomaly disappears and a conventional magnon mode is recovered. While in zero field the magnon mode is two-fold degenerate, the uniform field will split it into an "antiferromagnetic" and a "ferromagnetic" component.
  It is in principle simple to introduce such external magnetic fields into the variational calculation. First, the projected Heisenberg model matrix will need to include a Zeemann term, a simple modification of the calculation. But to truly take account of the effect of the applied field one would also need to introduce it at the projected mean-field wavefunction level. Indeed to be physically relevant the variational wavefunction should be able to get polarized by the applied field. A new wavefunction must therefore be introduce which allow a polarization along the axis where the field is applied. This is a rather trivial modification but will add a new variational parameter – the polarization – which will need to be optimized for each value of the applied magnetic field.
  An interesting aspect is that, in the case where a magnetic field does break the spin rotational symmetry, it is possible that the SF+N becomes a better variational Ansatz since its broken spin symmetry now is a physical ingredient of the system under study. In particular it seems like the exponential decay of the transverse instantaneous spin-spin correlation might be physical in the case where we apply a transverse field and would be consistent with the extinction of the $\boldsymbol{q} = (\pi, 0)$ continuum.
– **Excitation spectra for doped systems:** The interest into the square lattice Heisenberg antiferromagnet physics obviously was in a large part motivated by the discovery of the high-temperature cuprate materials. The projected mean-field wavefunction approach originally was also motivated by the high-T_c problematic following Anderson's proposal of the RVB theory [Anderson, 1987]. It is thus an obvious route to take to try to obtain the magnetic excitation spectrum of doped square-lattice antiferromagnet. There are indeed many experimental results available which the variational approach could or could not reproduce. The development of the reweighing technique by Li and Yang [Li and Yang, 2010] was primarily geared towards describing the so-called $\boldsymbol{q} = (\pi, \pi)$ neutron resonance as a function of doping. The $\boldsymbol{q}$-dependence of the magnetic excitation spectrum was not looked at. Therefore it remains an important question to know if for instance the hour-glass excitation spectrum could be reproduce by a mean-field Ansatz. The interest of variationally reproducing such a feature goes beyond simply reproducing numerically some experimental feature. The fact the calculation is tied to a variational Ansatz brings a strong physical significance by strengthening the Ansatz.
– **ARPES spectra:** If extending the variational calculation to undoped systems, it is then completely possible to calculate variationally the spectral function:

$$A(\boldsymbol{q}, \omega) = \sum_{n\sigma} \left| \langle n, \boldsymbol{q}, \sigma | \, c_{\boldsymbol{q}\sigma} \, |\mathrm{GS}\rangle \right|^2 \delta(\omega - E_n^{\boldsymbol{q}\sigma} + E_{\mathrm{GS}}) \tag{2.9.1}$$

where $|n, \boldsymbol{q}, \sigma\rangle$ is an eigenstate calculated by diagonalizing the generalized eigenvalue problem defined by the Heisenberg Hamiltonian projected on a suitable projected mean-field excitations subspace.

– **Jastrow factor optimization:** An obvious weakness of our work is that we could not, using the Néel mean field approach, reproduce neither the long wavelength properties (the magnon mode we found is gapped) or one of the most important short wavelength property: the development of the $\boldsymbol{q} = (\pi, 0)$ continuum. But the introduction of a Néel mean-field arguably is a rather primitive approach. A much more versatile one is to use an optimized Jastrow factor (see section 2.5.3) to the wavefunction which might introduce non-trivial many-body physics into the variational Ansatz. Of course it has the drawback that one must now numerically optimize a large number of variational parameters. Techniques to perform such an optimization have been devised and might bring interesting results [Sorella, 2005].
– **Extended magnetic interactions (ring-exchange):** If focusing on the relevance of our calculation in the context of the cuprate materials, it is probably interesting to include further magnetic interactions into the physical model. Introducing second- and third-neighbor magnetic interaction should be very simple if one does not account for those at the mean-field level. The four-spin ring-exchange term (see the second chapter of this thesis) might also be introduced, first only into the physical model without modifying the mean-field wavefunction Ansatz. A difficulty is that the ring-exchange term will exchange a pair of up spins with a pair of down spins which, in the variational Monte Carlo technique, corresponding into changing simultaneously two rows or columns of the up and down Slater matrices. But this technical difficulty can now be easily overcome by the use of the generalized rank-r determinant and inverse matrix update formulas we developed in appendix A.2.
  The magnetic zone boundary quantum anomaly has been observed in the cuprate material La_2CuO_4 [Headings et al., 2010]. The ring-exchange term effect seems to kill the 7% magnetic zone boundary dispersion by increasing the $\boldsymbol{q} = (\pi, 0)$ magnon energy compared to $\boldsymbol{q} = (\pi/2, \pi/2)$. It is interesting to see whether, by introducing this ring-exchange term we also get the increased $\boldsymbol{q} = (\pi, 0)$ magnon energy while keeping the continuum above.
– **Raman scattering spectrum:** The asymmetric line shape of the Raman spectrum measured on realizations of the QHSAF is a long standing puzzle which originally inspired to look for fractional excitations [Ho et al., 2001]. In principle this spectrum can as well be calculated using our variational approach. In the so-called B_{1g} geometry, the interaction of light with the magnetic degrees of freedom is [Canali and Girvin, 1992]

$$\Lambda \propto \sum_j \boldsymbol{S}_j \cdot \left(\boldsymbol{S}_{j+\hat{\mathbf{y}}} - \boldsymbol{S}_{j+\hat{\mathbf{x}}}\right) \tag{2.9.2}$$

such that the scattering intensity will be a function of the four spin operator correlation function

$$I(\omega) = \int dt e^{i\omega t} \langle \Lambda(t) \Lambda \rangle. \tag{2.9.3}$$

In our formalism, this could be written in the longitudinal projected particle-hole excitation subspace as:

$$I(\omega) = \sum_n \left| \langle n, \boldsymbol{q}, 0 | \Lambda | \mathrm{GS} \rangle \right|^2 \delta(\omega - E_n^{\boldsymbol{q}0} + E_{\mathrm{GS}}). \tag{2.9.4}$$

But this last equation overlooks the fact that, writing the $\Lambda|\mathrm{GS}\rangle$ state into the projected mean-field states will not only generate particle-hole states, but also two-particles two-holes states. This will therefore dramatically increasing the excitation subspace to be considered. The prospect of increasing the size of the considered projected mean-field excitation subspace is treated in the next point.

– **Higher order spinon excitations:** While calculating the magnetic excitation spectrum we restricted the subspace of excited states to the particle-hole pairs in the transverse and the longitudinal channels. This is of course an approximation and these subspaces are only as much "sufficient" for describing the real system excitations as the variational wavefunction is close to the real groundstate. In fact we already checked that the Gutzwiller projection results in a finite overlap between particle-hole pair excitations and two-particles two-holes excitations, thus in the projected Hilber space four-spinons excitations. These four-spinons excitations have been shown to be responsible of about 30% of the 1D spin chain magnetic spectrum [Mourigal et al., 2013]. It is thus an interesting question to know if this is the case as well in 2D. While adding 4-spinons excitations is simple formally, it does bring significant technical difficulties. Indeed for instance the transverse 4-spinons excitations subspace now has $L^6/2$ states instead of $L^2/2$ for the 2-spinon state (L^2 being the system size). In practice the first technical limitation to come will be the memory problem as the projected Heisenberg model and overlap matrices will likely be too large to hold on a standard computer memory. But we would like to mitigate this issue. In fact the computationally expensive part is to calculate the overlaps $\langle\psi|\alpha\rangle$ and $\langle\beta|\psi'\rangle$ where $|\psi\rangle$ and $|\psi'\rangle$ are two different variational excitations. The number of $|\beta\rangle$ states depends on the quantity being sampled. For the Heisenberg model, this is of order L^2. Each of the overlap calculation still is only of cubic complexity in the system size $\mathcal{O}\left(L^6\right)$. Thus one can imagine a computational scheme where the random walks only calculate the *vectors* of overlaps $\langle\psi|\alpha\rangle$ and $\langle\beta|\psi'\rangle$ and delegate the construction of the large projected Heisenberg and overlap matrices to an other process with access to a large permanent storage to hold the full matrices. There are thus possible ways to push the technical limits.
  Other axes would be to concentrate on quantities which do not require the explicit calculation of the projected matrices. Without much inquiring, we would like to mention information theory quantities which could be used to quantify the degree of entanglement between the two-spinons and four-spinons excitation subspaces. This could potentially indicate how “good” is the approximation of truncating the excitation subspace to two-spinons only.
– **Extrapolation to 1D chain:** This research suggestion aims at giving a more solid footing to the analogy between the 1D spinon excitations and the 2D ones. An interesting question is to know how, upon weakening for instance the magnetic coupling J_y along the y-axis of the

square lattice, the continuum of excitations would evolve towards the exactly known 1D limit. If the 2D spinon excitations are adiabatically connected to the 1D ones, then we should see for $J_y \to 0$ the continuum of excitations at $\boldsymbol{q} = (\pi, 0)$ expand such that it reproduces the 1D two-spinons excitation spectrum (see for instance the XY spectrum fig. 2.3).
It is possible for the variational Monte Carlo approach to bring valuable insight with respect to this problematic. Indeed it has been shown that the projected wavefunction with no flux ($\theta_0 = 0$) and no Néel mean field is a very good variational Ansatz for the 1D spin chain with an energy only 0.2% higher than the exact groundstate energy from the Bethe Ansatz [Gros et al., 1987; Gebhard and Vollhardt, 1987]. It thus would be quite desirable to generalize the SF mean-field wave function such that it can extrapolate to the 1D case. The most likely modification will be to differentiate the two mean-fields:

$$\langle c^\dagger_{i\sigma} c_{i\pm\hat{\boldsymbol{e}}_x\sigma}\rangle = t_x e^{i\theta_{i,i\pm\hat{\boldsymbol{e}}_x}} \tag{2.9.5}$$

$$\langle c^\dagger_{i\sigma} c_{i\pm\hat{\boldsymbol{e}}_y\sigma}\rangle = t_y e^{i\theta_{i,i\pm\hat{\boldsymbol{e}}_y}} \tag{2.9.6}$$

and then carry out the optimization of these mean-fields for each ratio J_y/J_x. Therefore this only amounts into redefining the mean-field Ansatz while the computational framework would stay unmodified.

– **other lattices:** The variational procedure we used can in principle be used on any lattice geometry provided a motivated mean-field variational Ansatz exists. It could possibly make sense for instance to go back to the triangular lattice for which the RVB Ansatz was conceived in the first place and calculate its excitation spectrum.

2.9.3 Summary

In summary we have developed a variational Monte Carlo approach to give a variational determination of the magnetic spectrum of the square lattice Heisenberg antiferromagnet. Using the Néel ordered SF+N variational Ansatz, we could reproduce perfectly the short wave-length magnon-like excitations dispersion, including the 7% zone boundary dispersion. The observed continuum at $\boldsymbol{q} = (\pi, 0)$ however is not found with this Néel ordered wavefunction but could be obtained from the spin-liquid SF Ansatz. Detailed analysis of the obtained variational excitations lead to characterize them as *bound* and *unbound* spinon pairs. The short wave-length magnon-like mode in the SF+N case corresponds to *bound* spinons forming the magnon while the continuum at $\boldsymbol{q} = (\pi, 0)$ found in the SF Ansatz is found to correspond to deconfined spinon pairs.

3 Modeling the Spin-Wave Dispersion of Insulating Cuprate Materials

3.1 introduction

The discovery of high-temperature superconductivity in the cuprate compounds family by Bednorz and Müller [1986] lead to a renewed interest into the quantum magnetism topic as it was soon realized that high-T_c superconductivity was arising in the vicinity of magnetically ordered phases. To address theoretically the physics of the cuprate materials, the Hubbard model was proposed to encompass the most relevant aspects of the CuO_2 square lattice plane physics [Anderson, 1987]. Despite its simplicity, the Hubbard model contains all the ingredients that make the task of describing the physics of high-T_c cuprate materials a great challenge: It mixes spin and charge degrees of freedom and, for the regime relevant to cuprates, lacks a small variational parameter which would allow some simple perturbative approach. These ingredients are nicely represented as the model parameters, respectively the electron filling and the ratio between the electron hopping matrix element and the on-site Coulomb repulsion t/U. This ratio is though to be moderately small for the cuprate materials $t/U \sim 1/10$. Thus a first approach is to consider the states where two electrons with opposite spin sit on the same site as high-energy ones and to project them out from the Hilbert space. For the half-filled case where there is one electron per site, this corresponds to getting rid of the charge degrees of freedom of the model. However this projection cannot be carried out exactly and is performed as an expansion in t^n/U^{n-1}. This leads to another difficult model, the t-J model and its half-filled version, the Heisenberg model. In this last case, the Spin Wave Theory (SWT) can be used to give an approximate solution which can be compared to experiments.
The problematic raised by high-T_c superconductivity lead to designing or dramatically improving experimental techniques. Perhaps the best example is the Angle-Resolved Photo-Emission Spectroscopy (ARPES) technique able to directly probe the electronic physics of the CuO_2 plane. Another whose realization was strongly motivated by the cuprate problem is the Resonant Inelastic X-ray Scattering (RIXS) technique able to probe both magnetic and electronic degrees of freedom. Adding to these the well-established Inelastic Neutron Scattering (INS) and Raman scattering techniques, it appears that there are plenty of different available probes to tackle the spectroscopic properties of the cuprate materials.
This work aims at addressing the conventional aspects of the magnetic excitation spectrum of the insulating cuprate high-T_c parent compounds trying to bring a determination of some microscopic parameters consistent with the constraints set by the ARPES, RIXS, INS and Raman results. Looking at the ARPES and INS results for the La_2CuO_4 (LCO) compound, some inconsistencies appear [Delannoy et al., 2009]: The Fermi surface as determined by ARPES indicates that second and third nearest neighbour hopping matrix elements have a significant amplitude compared to the nearest neighbour hopping matrix element [Damascelli et al., 2003]. On the other hand, the magnon dispersion measured by INS indicates that, in the projection of the Hubbard model onto the no-double-occupancy Hilbert space, fourth order t^4/U^3 correction bring important qualitative modifications of the magnetic excitation spectrum [Coldea et al., 2001a]. The model parameters extracted from these two approaches are incompatible [Delannoy et al., 2009]: In particular the Coulomb repulsion U found in INS for La_2CuO_4[Coldea et al., 2001a] is too small compared to ARPES estimates. Importantly, the

analysis of the INS magnetic spectrum did not include further neighbour hopping matrix elements. New RIXS experimental results soon showed that these discrepancies were not limited to the La_2CuO_4 compound but were in fact even worse considering for instance the $Sr_2CuO_2Cl_2$ (SCOC) or the bi-layer compound $Bi_2Sr_2YCu_2O_8$ (BSYCO).
In this work, we followed the derivation of a low-energy magnetic model as developed in MacDonald et al. [1988] and extended in the case of Hubbard models with extended hoppings in Delannoy et al. [2009] in order to consistently analyze the newly available magnetic spectra as obtained by RIXS following the development of an unprecedented high-resolution spectrometer at the Swiss Light Source in the Paul Scherrer institute. The focus is to use established theoretical techniques in order to extract a detailed determination of the microscopic model parameters from the measurement of magnetic spectra and confront it in particular to the electronic measurements determination.

3.1.1 Overview

We provide here a quick overview of this study.

- **Experimental status:** The cuprate materials LCO and SCOC have been measured by ARPES and, for the former, by INS. The Fermi surface as measured by ARPES (see section 3.2.1) indicates that second and third nearest neighbor hopping amplitudes must be considered in the $t-J$ model (see section 3.3). INS measurements on LCO showed that extended magnetic couplings such as the ring-exchange term must be included in the microscopic magnetic model to account for the magnon dispersion. This corresponds to fourth order terms in the strong coupling perturbation theory of the Hubbard model. The constraints set by the ARPES and INS measurements are inconsistent. For instance considering the $t-J$ model as the effective theory of the Hubbard model (see section 3.3.3), the Coulomb repulsion as found from fitting the Fermi surface measured by ARPES is inconsistent with the one found from fitting the magnetic excitation spectrum from INS. New results of the SCOC material magnon dispersion from RIXS show an even larger discrepancy. In that last case the Hubbard model parameters as found by fitting the magnon dispersion would inconsistently put SCOC out of the Mott insulating phase.
- **Low energy theory:** To reconcile the microscopic parameter determinations from electronic and magnetic excitation spectra, we develop an effective low energy theory for the extended Hubbard model including second and third nearest neighbor hopping amplitudes (see section 3.4). This calculation is carried out through the unitary transform technique to fourth order in t/U. The resulting effective spin model at half filling is a Heisenberg model including extended magnetic interactions. In particular a large family of ring exchange couplings involving first, second and third nearest neighbor hopping amplitudes arise. The effective spin Hamiltonian is approximately diagonalized using SWT including first order $1/S$ quantum corrections (see section 3.5).
- **Experimental data fitting:** Using the SWT result, we fit the dispersion relation of LCO from INS measurements and of SCOC and BSYCO from RIXS measurements (see section 3.6.1 and 3.6.2). The fitting parameters are the microscopic model parameters of the extended

Hubbard model. As the fit is under-constrained, we obtain a family of solutions, more precisely a line of solutions. We choose to parametrize these solutions as a function of the Coulomb repulsion U. The fitting results show that strong constraints are imposed on the amplitude of U while the ratio $t/U \sim 1/10$ stays rather constant for all solutions. These results are then compatible with ARPES ones (see section 3.6.3).

– **Predictions:** Having determined consistent microscopic parameters, we then produce a number of predictions and compare them with available ARPES, RIXS and Raman experimental results (see section 3.6.4 and 3.6.5).

3.1.2 The cuprates materials

The cuprate material class regroups various ceramic compounds which share a layered structure of copper-oxides planes separated by various rare earth elements. A very large interest arose when an unexpectedly high temperature superconductivity was discovered for the compound $Ba_xLa_{5-x}Cu_5O_5$ [Bednorz and Müller, 1986] at $35K$, about $15K$ above the highest superconducting temperature known at that point for Nb_3Ge thin films [Muller, 1980]. Soon similar compounds were found to also achieve superconductivity at higher temperature culminating at about $130K$ [Schilling et al., 1993] less than a decade later. These high critical temperatures are well above $30K$, traditionally accepted as an upper-bound for conventional phonon-mediated superconductivity raising hopes that room temperature superconducting materials could be discovered in the future. After two decades of intensive research, the mechanism driving the electron pairing, a prerequisite for superconductivity, still remains highly controversial as the absence of isotope effect shed important doubts about the possibility of a conventional phonon-based mechanism (for reviews see [Dagotto, 1994] or [Scalapino, 2012]).
The structure of the cuprate materials consists of layers of one or more CuO_2 planes stacked

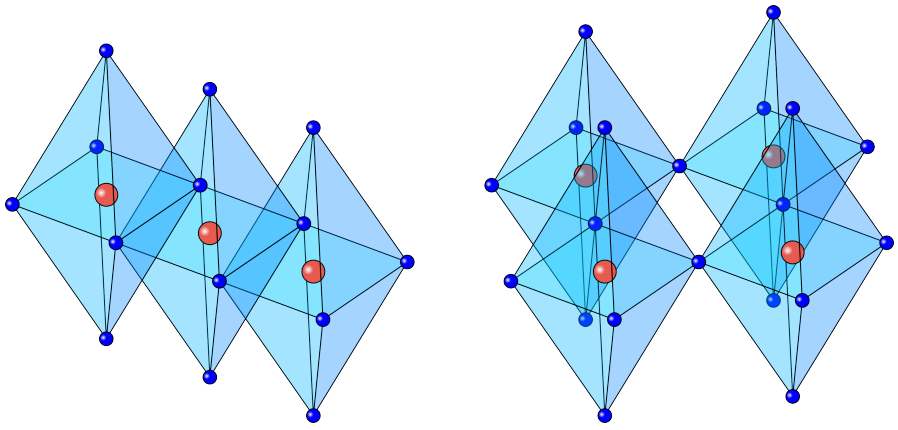

Figure 3.1 – Sketch of the oxygen (blue) octahedra surrounding the copper (orange) ions. Left: edge-sharing octahedra. Right: corner-sharing octahedra.

together with large interstitial rare-earth ions which isolate the copper oxides layers from each others. As a result the physics of the cuprate materials is dominantly two-dimensional. The

copper oxides planes are made of copper embedded in a octahedral cage of oxygens ions. The octahedra can be either edge- or corner-sharing the latter forming a checkerboard pattern (fig. 3.1). The oxidation state of the copper ion is Cu^{2+} which means that 9 electrons populate its 3d valence shell. The octahedral crystal field induced by the oxygens breaks the spherical symmetry of the $3d$ shell and results in the splitting of the 3d energy levels into the two groups of six (spin degree of freedom included) t_{2g} and of four e_g levels (fig. 3.3). In this reduced symmetry, the electronic states are conveniently labeled by the cubic harmonics orbitals. The slight elongation of the octahedra in the perpendicular direction from the plane further causes a splitting between the e_g $3d_{z^2-r^2}$ and $3d_{x^2-y^2}$ orbitals, the latter having the highest energy which can be understood simply considering where the lobes of the copper 3d orbitals point with respect to the neighbouring oxygen 2p orbitals. Filling up the 9 electrons, one sees that the state of the Cu^{2+} ions has a single electron in the $3d_{x^2-y^2}$ orbital with a spin-$\frac{1}{2}$ degree of freedom and all other orbitals are filled. The situation where every copper ion is in this local state is referred as half-filling while situations where some copper ions have either more or less electrons are referred as electron-doped and hole-doped, respectively. It is in the electron- or hole-doped cases that superconductivity has been observed.

We reproduce in fig. 3.2 the generic cuprate phase diagram. A striking aspect of the cuprate

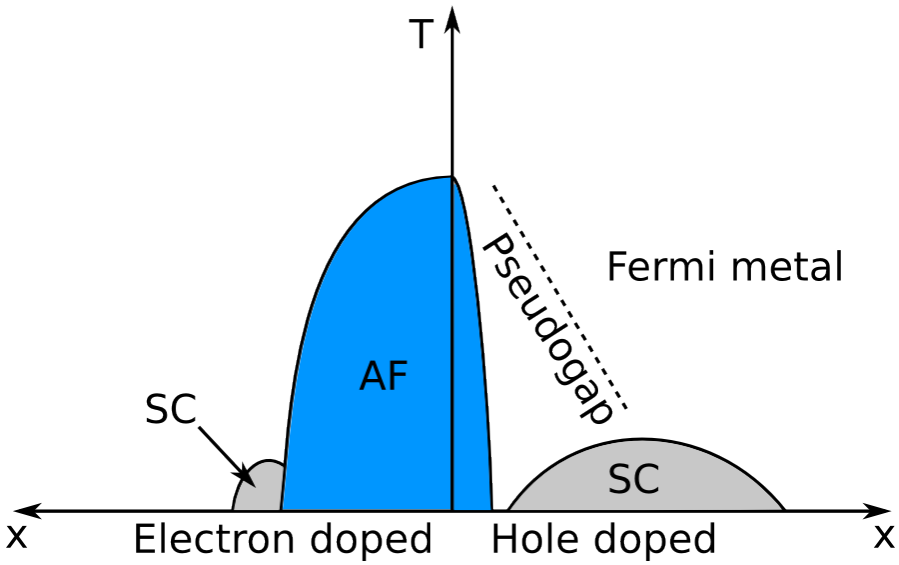

Figure 3.2 – Generic phase diagram for the cuprate materials. SC stands for the superconducting phase and AF for the antiferromagnetic one. The pseudogap phase is a badly metallic one where the density of states close to the Fermi surface is strongly suppressed.

family is the proximity between the superconducting phase and the insulating antiferromagnetic phase where each copper ion hosts on average a spin-$\uparrow$ or a spin-$\downarrow$ in a staggered manner. This proximity inspired the idea that the electron pairing mechanism might be of magnetic origin [Anderson, 1987] in contrast with conventional superconductivity where it is the electron-phonon interaction which results in electron pairing.

In this work we will focus on the antiferromagnetic phase of the cuprate materials seeking a

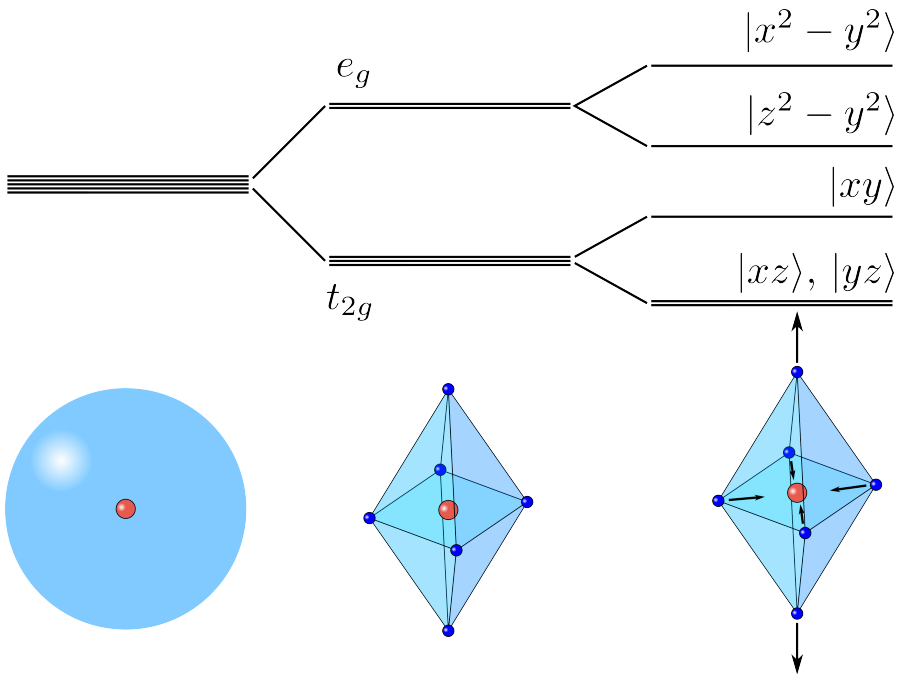

Figure 3.3 – Splitting of the Cu^{2+} 3d orbitals in the reduced symmetry of the octahedral environment.

microscopic model to account for available experimental data.

3.2 Electronic and Magnetic measurements

We give here a short description of some of the different techniques that allowed an experimental insight into the electronic and magnetic properties of the cuprate materials. We also give short reviews of some of the achieved experimental results that we will try to address in the rest of the chapter.

3.2.1 Angle-Resolved Photo-Emission Spectroscopy

Angle-Resolved Photo-Emission Spectroscopy (ARPES) has been a very successful techniques for characterizing materials including, for our topic, the cuprates (for a review see Damascelli et al. [2003] or Lu et al. [2012]). The photoemission process is a fundamental manifestation of the quantum nature of photons and electrons. Historically this effect lead to the discovery of light quantization [Einstein, 1905], a prerequisite for the quantum mechanics revolution of modern physics. In a photoemission event, light is absorbed by a material which as a result emits excited electrons. ARPES additionally keeps track of the emitted electrons energy and angle with respect to the incident light beam and sample orientation. This allows to resolve the momentum of the electrons. The ARPES intensity is then a function of the electron momentum

$\boldsymbol{k}$ and energy $\hbar\omega$ and can be expressed as:

$$I(\boldsymbol{k},\omega) = I_0(\boldsymbol{k},\nu,\mathbf{A})\, f(\omega)\, A(\boldsymbol{k},\omega) \tag{3.2.1}$$

This formula is valid in the so-called sudden approximation, where the photoelectron do not further interact with the material once excited away from its material equilibrium state. I_0 is the matrix element describing the light-matter interaction (the probe function), ν the incident light frequency and $\mathbf{A}$ the electromagnetic vector potential. $f(\omega)$ is the Fermi function which express the fact that only occupied electronic states can give rise to a photoemission event. Finally $A(\boldsymbol{k},\omega)$ is the spectral function associated with the one-particle retarded Green function, an intrinsics property of the material unrelated to the probe

$$G^R(\boldsymbol{k},t) = i\Theta(t)\left\langle \left\{ c_{\boldsymbol{k}}(t), c^\dagger_{\boldsymbol{k}}(0) \right\} \right\rangle \tag{3.2.2}$$

whose time Fourier transform is related to the spectral function as

$$G^R(\boldsymbol{k},\omega) = \int d\epsilon \frac{A(\boldsymbol{k},\omega)}{\omega - \epsilon + i0^+} \tag{3.2.3}$$

$$A(\boldsymbol{k},\omega) = -\frac{1}{\pi}\mathrm{Im}\left[G^R(\boldsymbol{k},\omega)\right]. \tag{3.2.4}$$

More explicitly, the total spectral function is the sum of the electron removal and addition spectral functions $A^-(\boldsymbol{k},\omega)$ and $A^+(\boldsymbol{k},\omega)$

$$A(\boldsymbol{k},\omega) = A^+(\boldsymbol{k},\omega) + A^-(\boldsymbol{k},\omega) \tag{3.2.5}$$

$$A^\pm(\boldsymbol{k},\omega) = \sum_m \left|\left\langle \Psi^{N\pm1}_m \right| c^\pm_{\boldsymbol{k}} \left|\Psi^N_i\right\rangle\right|^2 \delta(\omega - E^{N\pm1}_m + E^N_i) \tag{3.2.6}$$

where $\left|\Psi^N_i\right\rangle$ is the initial material N particles state with initial energy E^N_i, $\left|\Psi^{N\pm1}_m\right\rangle$ a possible final material eigenstate indexed by m with $N\pm1$ particles and energy $E^{N\pm1}_m$, and $c^+_{\boldsymbol{k}} = c^\dagger_{\boldsymbol{k}\sigma}$ and $c^-_{\boldsymbol{k}} = c_{\boldsymbol{k}\sigma}$ are respectively the creation and annihilation operators of an electron with momentum $\boldsymbol{k}$ and spin σ. While in eq. 3.2.1 the ARPES intensity thus seems to include both the electron removal and addition contributions, the latter are formally extinguished by the fermi function $f(\omega)$ at low temperature. Direct ARPES measures the electron removal probability as a function of energy and momentum. If the matrix element $I_0(\boldsymbol{k},\nu,\boldsymbol{A})$ is known, it allows to extract the electron removal spectral function $A^-(\boldsymbol{k},\omega)$ or equivalently at low temperature the total spectral function multipied with the Fermi function $f(\omega)A(\boldsymbol{k},\omega)$. If the $c^\pm_{\boldsymbol{k}}$ operators correspond to the system quasiparticle creation and annihilation operators so the initial and final states could be written as

$$\left|\Psi^N_i\right\rangle = \prod_{\{\boldsymbol{k}\}} c^\dagger_{\boldsymbol{k}}|0\rangle \qquad\qquad \left|\Psi^{N-1}_{m=\boldsymbol{k}}\right\rangle = \prod_{\{\boldsymbol{k}'\neq\boldsymbol{k}\}} c^\dagger_{\boldsymbol{k}'}|0\rangle \tag{3.2.7}$$

Then the ARPES signal would be essentially a delta function

$$I^-(\boldsymbol{k},\omega) \sim \delta(\omega - \omega_{\boldsymbol{k}}) \tag{3.2.8}$$

where $\omega_{\boldsymbol{k}}$ is the electron dispersion relation in the material. In this example the system is made of non-interacting electrons forming bands. For a correlated electron system, the excited state $\left|\Psi^{N-1}\right\rangle = c_{\boldsymbol{k}\sigma}\left|\Psi_i^N\right\rangle$ will not be an eigenstate and therefore overlap with many $\left|\Psi_m^{N-1}\right\rangle$ resulting in a broadening of the ARPES signal. This is often referred to as self-energy effects as the ARPES results are commonly interpreted on the basis of a band picture (non-interacting electrons) and the interaction introduced perturbatively in the Green function formalism. Considering a system Hamiltonian with a diagonal kinetic term and some non-magnetic interaction treated perturbatively:

$$\mathscr{H} = \sum_{\boldsymbol{k}} \omega_{\boldsymbol{k}} c_{\boldsymbol{k}}^{\dagger} c_{\boldsymbol{k}} + \hat{V} \tag{3.2.9}$$

the Green function of the unperturbed system is

$$G_0^R(\boldsymbol{k},\omega) = \frac{1}{\omega - \omega_{\boldsymbol{k}} + i0^+}. \tag{3.2.10}$$

Introducing the perturbation through the Feynman diagram technique leads to the Dyson equation

$$G^R(\boldsymbol{k},\omega) = \left[\left(G_0^R(\boldsymbol{k},\omega)\right)^{-1} - \Sigma(\boldsymbol{k},\omega)\right]^{-1} \tag{3.2.11}$$

where $\Sigma(\boldsymbol{k},\omega)$ is the self energy. Because the above system has only one band and the interaction is non-magnetic, $G^R(\boldsymbol{k},\omega)$, $G_0^R(\boldsymbol{k},\omega)$ and $\Sigma(\boldsymbol{k},\omega)$ are scalars. Introducing the Dyson equation into eq. 3.2.4 leads to the popular form of the spectral function in terms of the self-energy:

$$A(\boldsymbol{k},\omega) = -\frac{1}{\pi}\frac{\mathrm{Im}(\Sigma(\boldsymbol{k},\omega))}{\left[\omega - \omega_{\boldsymbol{k}} - \mathrm{Re}(\Sigma(\boldsymbol{k},\omega))\right]^2 + \left[\mathrm{Im}(\Sigma(\boldsymbol{k},\omega))\right]^2}. \tag{3.2.12}$$

Thus if one can extract from ARPES the total spectral function, it might allow for a determination of the self-energy function, a key quantity encoding the many-body correlation. Of course what direct ARPES really measures is $I_0(\boldsymbol{k},\nu,\mathbf{A})\,f(\omega)\,A(\boldsymbol{k},\omega)$ and approximations must be made to obtain the total spectral function [Norman et al., 1999]. We shortly review below two important results from ARPES experiments on cuprates that will be referred to in the following development.

Single hole dispersion in the antiferromagnetic phase

The motion of a single hole on top of the antiferromagnetic background of the undoped (half-filled) cuprate $Sr_2CuO_2Cl_2$ has been reported in various articles [Wells et al., 1995; LaRosa et al., 1997] and compared to a $t-t'-t''-J$ model using the self-consistent Born approximation [Tohyama and Maekawa, 2000]. A good agreement has been found for the model parameters $t = 0.35$eV, $t' = -0.12$eV, $t'' = 0.08$eV and $J = 0.14$eV. We will discuss in section 3.3.3 and 3.6.4 how this result can be related to our work.

Waterfall feature in the doped and undoped cuprates

The cuprates quasiparticle dispersion measured by ARPES displays a kink between 80 and 400meV [Ronning et al., 2005; Graf et al., 2007] that has been interpreted either as an ARPES matrix element effect on top of a shallow quasiparticle bare band with $t = 0.23$eV [Inosov et al., 2007] or as an intrinsics self-energy effect on top of strongly dispersing quasiparticle bare band with $t = 0.48$eV [Chang et al., 2008]. In the section 3.6.4 we will address whether our results can possibly shed light into this controversy.

3.2.2 Inelastic Neutron Scattering

Inelastic Neutron Scattering (INS) is an extremely successful technique able to probe detailed properties of magnetic materials. Neutrons produced through nuclear events such as fission or proton irradiation get scattered by the sample where the initial and final neutron energy and momentum can be controlled in various experimental geometries. The scattering can either result from nuclear interaction between the neutrons and the sample nuclei or from the small dipole-dipole interaction between the neutron spin-$\frac{1}{2}$ and the magnetic ions of the sample. This last scattering process is the one of interest to us as it gives rise to a signal that can be traced back to the intrinsic magnetic properties of the sample. Compared to other techniques, magnetic INS has the special characteristic that there is nothing unknown about the probing mechanism which is very accurately accounted for by the simple Fermi golden rule. The signal is given by the neutron scattering differential cross-section:

$$\frac{d^2\sigma}{d\Omega d\omega} = (\gamma r_0)^2 \frac{k_f}{k_i} \left| \frac{g}{2} F(\boldsymbol{q}) \right|^2 \exp(-2W(\boldsymbol{q})) \sum_{\alpha\beta} (\delta_{\alpha\beta} - \hat{\boldsymbol{q}}_\alpha \hat{\boldsymbol{q}}_\beta) S^{\alpha\beta}(\boldsymbol{q}, \omega) \tag{3.2.13}$$

where γ is the neutron dipole moment in units of nuclear magneton μ_N, $r_0 = \frac{e^2}{m_e c^2}$ is the classical electron radius, g is the Landé g-factor, $F(\boldsymbol{q})$ is the magnetic form factor, $W(\boldsymbol{q})$ is the Debye-Waller factor and $(\delta_{\alpha\beta} - \hat{\boldsymbol{q}}_\alpha \hat{\boldsymbol{q}}_\beta)$ is a geometric factor related to the form of the dipole-dipole interaction. The most important part of the above formula is the dynamical structure factor $S^{\alpha\beta}(\boldsymbol{q}, \omega)$ which is the material-intrinsic part of the INS signal while all the rest broadly relates to the probing mechanism and is known more or less exactly. The dynamical structure factor is given by:

$$S(\boldsymbol{q}, \omega) = \frac{1}{2\pi} \int dt e^{i\omega t} \sum_{ij} e^{i\boldsymbol{q}(\boldsymbol{R}_j - \boldsymbol{R}_i)} \langle S_i^\alpha(t) S_j^\beta(0) \rangle \tag{3.2.14}$$

$$= \sum_{\lambda\lambda'} \rho(\lambda) \sum_{ij} e^{i\boldsymbol{q}(\boldsymbol{R}_j - \boldsymbol{R}_i)} \langle \lambda | S_i^\alpha | \lambda' \rangle \langle \lambda' | S_j^\beta | \lambda \rangle \delta(\hbar\omega - E_{\lambda'} + E_\lambda) \tag{3.2.15}$$

and can be understood as the time and space Fourier transform of the spin-spin correlation function $\langle S_i^\alpha(t) S_j^\beta(0) \rangle$. Through this quantity, the internal correlated structure of the local spins can be both experimentally probed and theoretically predicted providing a unique platform where experiments and theory can meet on solid ground.

In the context of the cuprates, magnetic neutron scattering brought important information both in the doped and undoped case. We focus here on the undoped results which characterize the properties of the square lattice antiferromagnet. A detailed study of the square lattice antiferromagnet INS magnetic spectrum is carried out in chapter 2 which was motivated by important peculiarities of the INS spectrum which fall out of the scope of this part. The dynamical structure factor takes a quite simple form when the system can be described in the spin-wave approximation. It becomes

$$S(\boldsymbol{q},\omega) = I(\boldsymbol{q})\delta(\omega - \omega_{\boldsymbol{q}}) \tag{3.2.16}$$

where $I(\boldsymbol{q})$ is a $\boldsymbol{q}$-dependent intensity and $\omega_{\boldsymbol{q}}$ is the dispersion relation of bosonic excitations known as spin-waves, a propagating disturbance of the antiferromagnetic order. INS experiments could accurately measure the spin-wave dispersion of the La_2CuO_4 cuprate material [Coldea et al., 2001a; Headings et al., 2010] and consistently relate it to a microscopic one band Hubbard model with parameters $t = 0.3$eV and $U = 2.2$eV. A striking aspect of the measured spin-wave dispersion is the so called magnetic zone boundary dispersion, the variation of the spin-wave energy along the line $\boldsymbol{q} = (l, \pi - l)$, $l \in [0, \pi]$, which is as large as 20meV in La_2CuO_4. This is in complete contradiction with spin-wave theory based on the Heisenberg model which predicts no dispersion at all. This result was the proof that, in the case of the cuprates where the interaction energies are large, more complicated interactions of the magnetic moments must be included in the model. We will come back to this in section 3.6.

3.2.3 Raman scattering

The Raman scattering technique is a photon-in photon-out techniques which uses polarized visible light produced with lasers. Light has the advantage to couple strongly to the valence electrons and can thus probe a large spectrum of excitations ranging from phonons, electronic excitations and magnons. The excitations have zero total momentum because the small momentum carried by visible light photons. For magnetic scattering on the square lattice antiferromagnet, the measurements are most often carried out in the so-called B_{1g} geometry where the incident light is linearly polarized with the electrical and magnetic components of the field point at 45° in-between the square lattice $\hat{\mathbf{x}}$ and $\hat{\mathbf{y}}$ translation vectors [Devereaux and Hackl, 2007]. In this geometry the interaction of light with the magnetic degrees of freedom is [Canali and Girvin, 1992]:

$$\Lambda = \frac{B}{2} P(\mathbf{E}_{in}, \mathbf{E}_{sc}) \sum_j \boldsymbol{S}_j \cdot \left(\boldsymbol{S}_{j+\hat{\mathbf{y}}} - \boldsymbol{S}_{j+\hat{\mathbf{x}}} \right) \tag{3.2.17}$$

where $P(\mathbf{E}_{in}, \mathbf{E}_{sc}$ is a function of the incident and scattered light electrical field vectors. We see that, on top of momentum-conservation, the excitations also conserves the z component of the total spin $\sum_j S_j^z$ so the excitations must carry zero spin $\Delta S = 0$. We can thus already conclude that single magnon which are $\Delta S = 1$ excitations cannot be observed. The lowest order magnetic excitations which can be observed will therefore be two-magnons. We also see

that the correlation functions probed by Raman scattering will be much more complicated as, using the Fermi golden rule, the intensity will be

$$I(\omega) \sim \int d\omega e^{i\omega(t)} \langle \psi_0 | \Lambda(t)\Lambda(0) | \psi_0 \rangle \tag{3.2.18}$$

where, by comparison to the INS cross-section eq. 3.2.14, the operator $\Lambda(t)\Lambda(0)$ is quartic in spin operators instead of quadratic. We follow here Canali and Girvin [1992] to give a brief account of the two-magnon Raman peak. Expressing eq. 3.2.17 using the magnon operators will produce two-magnons terms as well as higher order ones. Restricting to the two-magnons part and neglecting magnon-magnon interaction gives:

$$I(\omega) \sim \sum_{\boldsymbol{k}} \frac{\tilde{\gamma_{\boldsymbol{k}}}^2}{\epsilon_{\boldsymbol{k}}^2} \delta(\omega - 2\epsilon_{\boldsymbol{k}}) \tag{3.2.19}$$

where $\epsilon_{\boldsymbol{k}}$ is the magnon dispersion and $\tilde{\gamma}_{\boldsymbol{k}} = \frac{1}{2}\big(\cos(k_y) - \cos(k_x)\big)$. This is very similar to eq. 3.2.16 except that in the δ-function we have the joint energy of a $\boldsymbol{k}$ and $-\boldsymbol{k}$ magnon pair so the formula looks like a weighted density of states of the zero momentum two-magnons pairs which is peaked at twice the magnetic zone boundary energy $4Z_cJ$. Including the magnon-magnon interaction will, in a Random Phase Approximation (RPA)[Canali and Girvin, 1992], effectively shifts to lower energies the Raman two-magnons peak to $3.37J$, a 36.8% rather large energy renormalization. By approximating the effective model for undoped cuprates to the simple nearest-neighbour Heisenberg model, the position of the measured Raman two-magnon peak then gives an approximate of the magnetic coupling J, found to be of about 124meV in La_2CuO_4, which is small if compared to the magnetic zone boundary energy found by INS indicating J_{NN} = 140meV [Coldea et al., 2001a; Headings et al., 2010]. This issue was further resolved by extending the RPA procedure from Canali and Girvin [1992] including a ring exchange term [Katanin and Kampf, 2003].

3.2.4 Resonant Inelastic X-ray Scattering

Resonant Inelastic X-ray Scattering (RIXS) is a technique made available by the improved brilliance of X-ray radiation produced in third generation sychrotrons. The technique, similarly to Raman scattering, is a photon-in photon-out technique but where the much higher photons energy allows momentum transfer and is thus an angle-resolved technique. Another big difference with Raman scattering is that the scattering event is produced by a second order process (the resonance) not accounted for by the Fermi golden rule. In RIXS, the incoming photon energy is tuned to an absorption edge of the sample material, that is a specific energy which will bring a core electron to the valence shell for one of the elements in the sample. In the context of the cuprates, the absorption edges considered are the Cu L_3-edge and the oxygen K-edge. The most successful experiments used the copper L_3 edge as it allows single magnon scattering. The RIXS process is illustrated on fig. 3.4. The incident photon creates a copper core hole in the Cu $2p$ shell and an excited electron in the Cu $3d$ valence shell. During

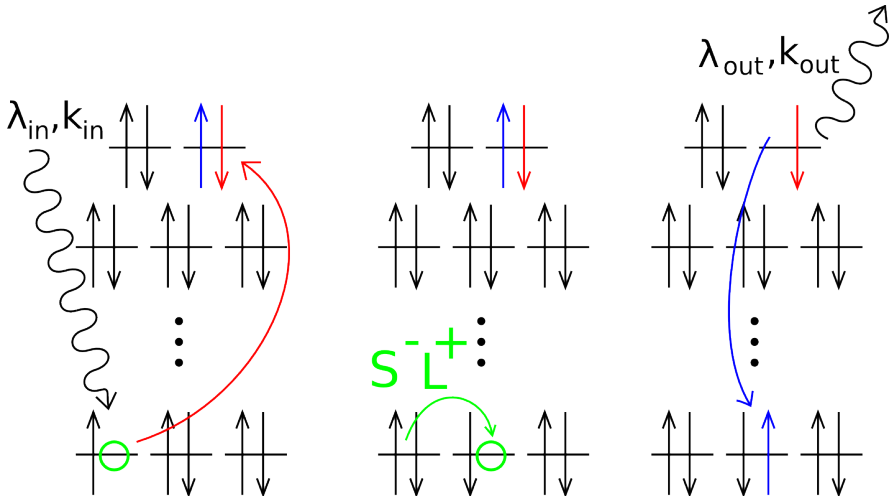

Figure 3.4 – Schematic cartoon of the RIXS second order scattering process. An incoming photon promotes a Cu $2p$ core hole into the valence Cu $3d$ shell. During its life-time, the core hole can exchange spin angular momentum for orbital angular momentum through the spin-orbit interaction. A possible final state has a flipped spin in the Cu $3d$ valence shell corresponding to a $\Delta S = 1$ excitation.

its life-time the copper core hole can exchange spin angular momentum for orbital angular momentum due to spin-orbit coupling. As a result, the core hole might decay with a valence shell electron with opposite spin thus creating a $\Delta S = 1$ excitation. This second order process and the related RIXS intensity can be modeled by the Kraemer-Heisenberg formula [Forte et al., 2008; Ament et al., 2009; Haverkort, 2010]

$$\frac{d^2\sigma}{d\Omega d\omega} \sim \lim_{\eta\to 0^+} \sum_f \left| \langle f | T^\dagger_{\epsilon_o} \frac{1}{\omega_i + E_i + i\eta/2 - H} T_{\epsilon_i} | i \rangle \right|^2 \delta(\omega_i - \omega_o + E_i - E_f) \tag{3.2.20}$$

where the $\epsilon_{i(o)}$ stands for the incoming (outgoing) photon polarization and T_ϵ the optical transition operator $\mathbf{A}\cdot\mathbf{p}$ where $\mathbf{A}$ is the photon vector potential and $\mathbf{p}$ the electron momentum operator. $|i\rangle$ and $|f\rangle$ respectively stand for the initial and final states. H is the intermediate state Hamiltonian describing the excited system with a core-hole and excited electron pair. Various theoretical approaches tackled the theoretical problem of giving practical estimates for eq. 3.2.20[Forte et al., 2008; Ament et al., 2009; Haverkort, 2010; Nomura and Igarashi, 2005].

In the following, we are only interested in the magnon dispersion and not in the intensity nor lineshape analysis of the RIXS spectrum. A typical RIXS spectrum for the $Sr_2CuO_2Cl_2$ is shown in fig. 3.5 (figure from Guarise et al. [2010]). Several energy scales are present. In the range $1.2-2.5$eV are the $d-d$ orbital excitations which are related to the octahedral crystal field. Not shown on the left are the charge transfer excitations corresponding to creating a hole on the oxygen $2p$ valence shell and a fully occupied Cu $3d$ valence shell. But the most interesting energy scale for us is $0-1$eV which shows a dispersing peak for $\boldsymbol{q} = (x,0)$ $x \in [-\pi,\pi]$ which we can identify with the magnon dispersion. In section 3.6 we will show various RIXS results

which we will analyse with the theory developed below.

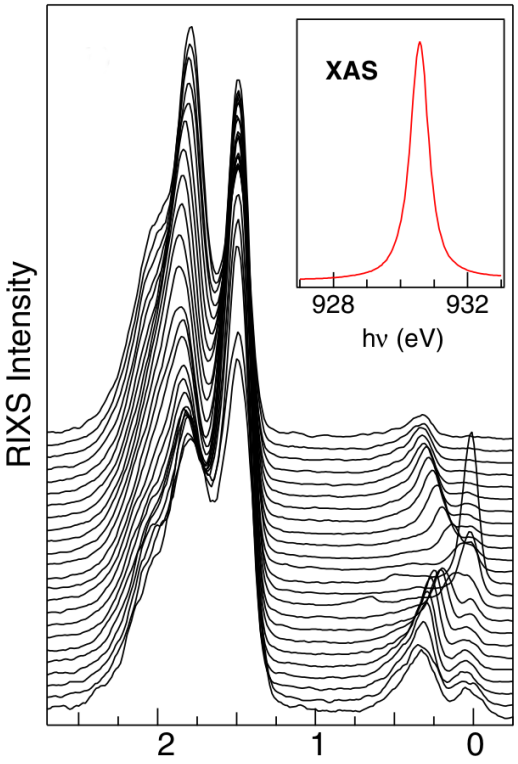

Figure 3.5 – RIXS spectra of the $Sr_2CuCl_2O_2$ cuprate from Guarise et al. [2010]. The insert shows the x-ray absorption spectrum which highlights the absorption edge for incident photons at about $\hbar\nu \sim 930.8$eV.

3.3 Microscopic Electronic Models

I describe here models that are the starting point of the effective theory derived below. These models already are a drastic simplification of the physical system. The atoms position is considered fixed to the lattice points, thus phonon physics is not considered. From all the electronic degrees of freedom, it assumed that only the valence electrons participate in the low-energy physics while the other electrons are left in their atomic orbital state.

3.3.1 The Hubbard model

The Hubbard model is one of the simplest microscopic model to describe electrons on a lattice. The electrons state is written in the basis of one spin-degenerate local orbital per site. The electrons may tunnel from adjacent sites orbital and are repelling each others whenever two occupy the same site, therefore with opposite spins. In second quantized form, the

Hamiltonian is:

$$\mathscr{H} = -t \sum_{\langle i,j\rangle,\sigma} \left(c^{\dagger}_{i\sigma} c_{j\sigma} + \text{h.c.} \right) + U \sum_{i} n_{i\uparrow} n_{i\downarrow} \tag{3.3.1}$$

with t the tunneling probability amplitude and U the on-site Coulomb repulsion. The model parameters are electron filling and the ratio t/U. In this work we will only consider the half-filled case with one electron per site. If t/U is large, then one might introduce the Coulomb repulsion perturbatively. To zeroth order, the Hamiltonian is diagonalized simply by considering the canonical transformation:

$$c_{\boldsymbol{k}\sigma} = \frac{1}{\sqrt{N}} \sum_{i} e^{i\boldsymbol{R}_i \cdot \boldsymbol{k}} c_{i\sigma} \tag{3.3.2}$$

$$c^{\dagger}_{\boldsymbol{k}\sigma} = \frac{1}{\sqrt{N}} \sum_{i} e^{-i\boldsymbol{R}_i \cdot \boldsymbol{k}} c^{\dagger}_{i\sigma} \tag{3.3.3}$$

which leads to a metallic system with a single band:

$$\mathscr{H} = \sum_{\boldsymbol{k}\sigma} \epsilon_{\boldsymbol{k}} c^{\dagger}_{\boldsymbol{k}\sigma} c_{\boldsymbol{k}\sigma} \tag{3.3.4}$$

$$\epsilon_{\boldsymbol{k}} = -\frac{1}{2} \sum_{\boldsymbol{\tau}} t_{\boldsymbol{\tau}} e^{i\boldsymbol{\tau}\cdot\boldsymbol{k}} \tag{3.3.5}$$

where $\boldsymbol{\tau}$ is the hopping translation vector. Turning on U can then be done by for instance the Random Phase Approximation [Hirsch, 1985]. Without going so far, it is interesting to see the case of the half-filled square lattice in the absence of Coulomb interaction. In that case the electron dispersion relation is:

$$\epsilon_{\boldsymbol{k}} = 2t(\cos(\mathrm{k_x}) + \cos(\mathrm{k_y})). \tag{3.3.6}$$

Filling all spin-$\uparrow$ and spin-$\downarrow$ results in the Fermi level being at $\epsilon_{\mathrm{F}} = 0$ which results in a perfectly nesting Fermi surface with the wave-vector $\boldsymbol{Q} = (\pi, \pi)$ (Fig. 3.6). As a result, already looking at the non-interacting Lindhardt magnetic susceptibility:

$$\chi^0(\boldsymbol{q}, \omega) = \lim_{\delta \to 0} \sum_{\boldsymbol{k}} \frac{f(\epsilon_{\boldsymbol{k}}) - f(\epsilon_{\boldsymbol{k}+\boldsymbol{q}})}{\hbar\omega - \epsilon_{\boldsymbol{k}} + \epsilon_{\boldsymbol{k}+\boldsymbol{q}} + i\delta} \tag{3.3.7}$$

we see that the system has an instability towards anti-ferromagnetic ordering since the divergence of $\chi^0(\boldsymbol{q} = (\pi, \pi)$ indicates the linear response to an anti-ferromagnetically alternating applied field.

We now turn to the strong coupling limit with $t/U \ll 1$. In this limit, the number of Double Occupancys (DOs) defines sectors of the Hilbert space separated by the large Coulomb repulsion energy U. Therefore at low temperature the number of double occupations should be a good quantum number and the lowest energy subspace is obtained when there is the minimum of DOs as permitted by the filling. The Coulomb interaction $V = U \sum_i n_{i\uparrow} n_{i\downarrow}$ is diagonal in this subspace while the kinetic term $K = -t \sum_{\langle i,j\rangle,\sigma} \left(c^{\dagger}_{i\sigma} c_{j\sigma} + \text{h.c.} \right)$ can be treated as a perturbation.

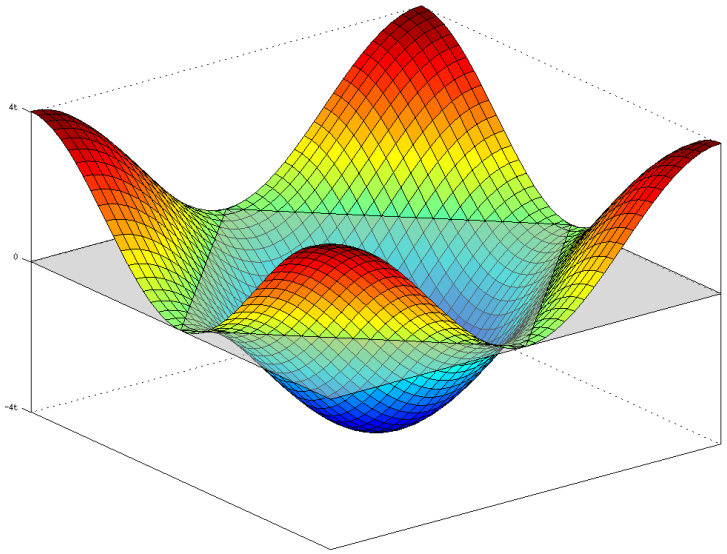

Figure 3.6 – Band structure of the non-interacting Hubbard model on the square lattice. At half-filling the Fermi surface is perfectly nesting with $\boldsymbol{Q} = (\pi, \pi)$.

If we denote $|\alpha\rangle$ and $|\beta\rangle$ two states belonging to the lowest energy sector of the Hubbard model we have:

$$\langle\alpha|\mathscr{H}|\beta\rangle = 0 + \langle\alpha|K|\beta\rangle + \sum_{\gamma} \frac{\langle\alpha|K|\gamma\rangle\langle\gamma|K|\beta\rangle}{E_0 - E_\gamma} + \dots \tag{3.3.8}$$

up to second order perturbation theory. In the case of half-filling, the first order correction does not contribute since $K|\beta\rangle$ must have a DO while $|\alpha\rangle$ has none. In the second order correction, E_0 and E_γ are the energy of the $|\alpha\rangle$ ($|\beta\rangle$) and $|\gamma\rangle$ states in the unperturbed Hamiltonian V respectively. Since K necessarily creates a DO when applied on states without any DO at half-filling, $|\gamma\rangle$ must have a DO to have a finite matrix element $\langle\gamma|K|\alpha\rangle$ and $E_\gamma = U$. The effective Hamiltonian up to second order perturbation theory is therefore

$$\mathscr{H}^{(2)}_{\text{eff}} = \sum_{\alpha,\beta} \frac{1}{U} |\alpha\rangle\langle\alpha|K^2|\beta\rangle\langle\beta| \tag{3.3.9}$$

As $|\alpha\rangle$ and $|\beta\rangle$ have no DO or empty sites, this effective Hamiltonian works on the same Hilbert space as spin operators. It can be "translated" from fermionic operators to spin operators

giving the antiferromagnetic Heisenberg model

$$\mathscr{H}^{(2)}_{\text{eff}} = J \sum_{\langle i,j \rangle} \left(\mathbf{S}_i \cdot \mathbf{S}_j - \frac{1}{4} \right) \tag{3.3.10}$$

$$J = \frac{4t^2}{U}. \tag{3.3.11}$$

It is thus seen that adding the kinetic energy perturbatively will lift the degeneracy between the different spin configurations favoring to first approximation an antiferromagnetic arrangement. The reason for this is that the system can gain energy through the virtual hoppings such as in eq. 3.3.9. But the virtual hoppings are only allowed when nearest-neighbors are of opposite spin, due to the Pauli exclusion principle which forbids two fermions of same spin state to occupy the same site.
Now turning to the doped case where holes are added, one can perform the same kind of effective perturbation theory development. The first order perturbation $\langle \alpha | K | \beta \rangle$ will now contribute by exchanging an electron and a hole while the second order perturbation will generate more complex hops, the so called three-sites term. Altogether the effective Hamiltonian of the Hubbard model in the strong coupling limit with finite doping is a $t-J$-like model:

$$\begin{aligned} \mathscr{H}^{(2)}_{\text{eff}} = & - \sum_{\langle i,j \rangle \sigma} P_{D=0} \left(t_{ij} c^\dagger_{i\sigma} c_{j\sigma} + \text{h.c.} \right) P_{D=0} + J \sum_{\langle i,j \rangle} \left(\mathbf{S}_i \cdot \mathbf{S}_j - \frac{1}{4} n_i n_j \right) \\ & - \frac{J}{4} \sum_{j, \boldsymbol{\tau} \neq \boldsymbol{\tau}', \sigma} P_{D=0} \left(c^\dagger_{j\bar{\sigma}} c_{j\bar{\sigma}} c^\dagger_{j+\boldsymbol{\tau}\sigma} c_{j+\boldsymbol{\tau}'\sigma} + c^\dagger_{j+\boldsymbol{\tau}\bar{\sigma}} c_{j\bar{\sigma}} c^\dagger_{j\sigma} c_{j+\boldsymbol{\tau}'\sigma} \right) P_{D=0} \end{aligned} \tag{3.3.12}$$

where

$$P_{D=0} = \prod_i (1 - n_{i\uparrow} n_{i\downarrow}) \tag{3.3.13}$$

is the Gutzwiller projector. This model, especially due to the presence of the Gutzwiller projection, constitutes a great theoretical challenge and is the starting point of many of the high-T_c theoretical proposals [Lee et al., 2006].

3.3.2 The d-p model

In this model only the copper $3d_{x^2-y^2}$ and the oxygen $2p_x$ and $2p_y$ orbitals are considered. If not considering overlaps between the orbitals, thus no hopping processes, the groundstate has filled oxygen $2p$ orbitals and half-filled copper $3d_{x^2-y^2}$ orbitals (Fig. 3.7a and 3.7c). It is highly degenerate as the half-filled copper orbital retains a spin degree of freedom. When considering overlaps, the relative energy of the half-filled copper orbital with the filled oxygen ones is important as it changes the nature of the lowest energy excitations. In the case where the energy of the filled oxygen orbitals is lower than that of the half-filled copper, the lowest energy excitation corresponds to making an electron hop from a copper site to an other, creating a double occupancy with energy U_d (Fig. 3.7b). This is the Mott-Insulator scenario

where the oxygen bands could simply be projected out in a further effective theory leading to the Hubbard model (3.3.1) where the hopping amplitude t will be some function of the copper-oxygen and oxygen-oxygen hopping amplitudes considered in the d-p model. On the other hand, if the filled oxygen orbitals have a higher energy than the half-filled copper one by Δ_p, then the lowest energy excitation corresponds to bringing an electron from the oxygen to a neighbouring copper orbital. Relative to the previous scenario, the excitation energy is thus $U_d - \Delta_p$ (Fig. 3.7d). This is the charge-transfer insulator scenario. X-ray absorption spectroscopy [Tranquada et al., 1987] experiments showed that the cuprate materials belong to the second case and are thus charge-transfer insulators such that the adequate effective model is the d-p model [Zaanen et al., 1985; Emery, 1987]. Rather than looking at the electron

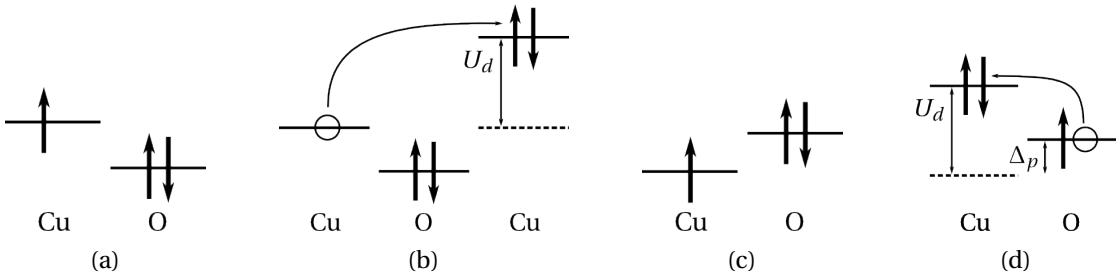

Figure 3.7 – Schematics of the Mott insulator and charge transfer insulator scenario. (a): Ground state of the Mott insulator. (b) Lowest energy excitation of the Mott insulator. The oxygen orbital does not participate and can thus be integrated out of the model. (c) Charge transfer insulator ground state. (d) Lowest energy excitation of the charge transfer scenario. Compared to the direct copper-copper hop, this excitation energy is reduced by Δ_p.

picture, it is also convenient to look at the hole picture on fig. 3.8. The ground state of both the Mott insulator 3.8a and of the charge transfer insulator 3.8c have one hole per copper ion. In the Mott insulator scenario, the lowest energy consists of putting two holes on a copper ion, consequently creating a double occupancy of electrons on a neighbouring copper ion. In the charge transfer scenario, the lowest energy excitation consists of putting a hole on an oxygen ion. This leaves a doubly occupied copper ion costing an energy U_d but releases an energy of Δ_p by putting a hole on the oxygen ion. The total energy of putting a hole on the oxygen ion from a copper one is thus $\Delta = U_d - \Delta_p$. Putting the energy reference at the singly occupied copper ion, if Δ_p is negative, then this is a higher energy excitation than the Mott one (Mott scenario) but if $\Delta_p > 0$ it is lower (charge transfer scenario). The model is written in the hole picture as:

$$\begin{aligned}\mathscr{H}_{dp} = &- t_{dp} \sum_{\langle i,j\rangle\sigma} \left(d^\dagger_{i\sigma} p_{j\sigma} + \text{h.c.} \right) - t_p \sum_{\langle j,j'\rangle\sigma} \left(p^\dagger_{j\sigma} p_{j'\sigma} + \text{h.c.} \right) + t'_p \sum_{\langle\langle j,j'\rangle\rangle\sigma} \left(p^\dagger_{j\sigma} p_{j-\sigma} + \text{h.c.} \right) \\ &+ \Delta \sum_{j\sigma} n_{p,j\sigma} + U_d \sum_i n_{d,i\uparrow} n_{d,i\downarrow} + U_p \sum_j n_{p,j\uparrow} n_{p,j\downarrow} + V \sum_{\langle i,j\rangle} n_{d,i} n_{p,j} \end{aligned} \tag{3.3.14}$$

where $d_{i\sigma}$ and $p_{j\sigma}$ are respectively the destruction operators of a hole with spin σ in copper site i $3d_{x^2-y^2}$ orbital and oxygen site j $2p_x$ or $2p_y$ orbital, $n_{p,j\sigma} = p^\dagger_{j\sigma} p_{j\sigma}$ counts the number

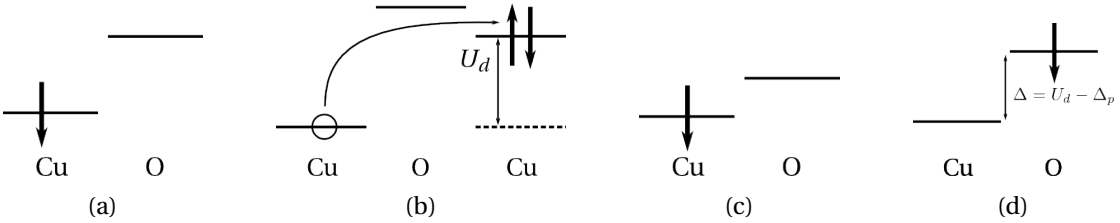

Figure 3.8 – Schematics of the Mott insulator and charge transfer insulator scenario in the hole picture. (a): Ground state of the Mott insulator. (b) Lowest energy excitation of the Mott insulator. Putting two holes on a Cu site means creating another doubly occupied site. The oxygen orbital does not participate and can thus be integrated out of the model. (c) Charge transfer insulator ground state. (d) Lowest energy excitation of the charge transfer scenario. Compared to the direct copper-copper hop, this excitation energy is reduced by Δ_p.

of spin σ holes on the $2p_{x/y}$ orbitals at site j, $n_{d,i\sigma} = d^\dagger_{i\sigma} d_{i\sigma}$ the same for the copper $3d_{x^2-y^2}$ at site i and $n_{d,i} = (n_{d,i\uparrow} + n_{d,i\downarrow})$ and $n_{p,i} = (n_{p,i\uparrow} + n_{p,i\downarrow})$. Other than the constants already defined in Fig. 3.7, we find: a $2p$-orbital Coulomb repulsion U_p is introduced, a neighbouring copper and oxygen Coulomb repulsion V and the hopping amplitudes coming from the orbitals overlap t_{pd}, t_p and t'_p (Fig. 3.9).

We now consider the strong coupling limit at half filling. This limit corresponds to $U_d \gg t_{pd}$

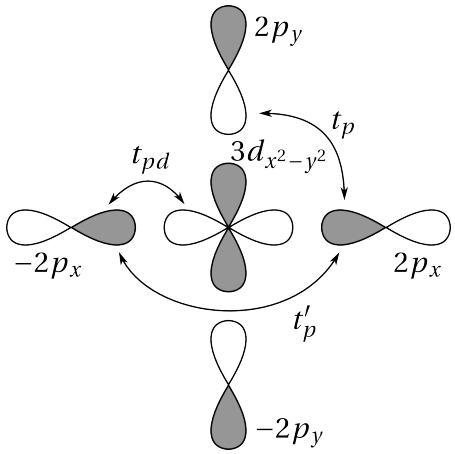

Figure 3.9 – The CuO_2 plane with the relevant orbitals and hopping parameters.

and $U_d - \Delta_p \gg t_{pd}$. In that case we can see that the state which has a double occupancy on the copper ion and a hole on the oxygen (Fig. 3.7d) will be of high energy and should be projected out in an effective theory. To the zeroth order, any copper spin configuration is a groundstate. But introducing virtual hoppings in a perturbative manner in t_{pd}/U_d and $t_{pd}/(U_d - \Delta_p)$ leads to the following Hamiltonian which will lift the degeneracy between the

different spin configurations [Zhang and Rice, 1988]:

$$\mathscr{H} = J \sum_{\langle i,j \rangle} \mathbf{S}_i \cdot \mathbf{S}_j \tag{3.3.15}$$

$$J = \frac{4t_{pd}^4}{U_d - \Delta_p + V} \left(\frac{1}{U_d} + \frac{2}{2(U_d - \Delta_p) + U_p} \right) \tag{3.3.16}$$

which corresponds to the fourth order in perturbation series. The Hamiltonian 3.3.15, up to a constant, is again the Heisenberg model seen previously as the strong coupling expansion of the Hubbard model 3.3.10. Thus, at half-filling, the purely magnetic properties will be independent on whether the underlying electronic model is that of a Mott Insulator or a Charge-Transfer Insulator.

Let us now turn towards the situation where holes are doped into the system. Without considering the intra-orbital overlaps, the hole will simply go on the oxygen site. But turning on the hopping matrix elements perturbatively will result in an effective model where the pure doped hole on the oxygen is not the most favourable state. Zhang and Rice [Zhang and Rice, 1988] showed that rewriting this effective model using a special combination of the oxygen $2p$ orbitals surrounding a copper ion results in an effective magnetic interaction between the copper ion and the surrounding oxygens. The lowest energy state diagonalizing this effective magnetic interaction is called the Zhang-Rice singlet and can be schematically represented as a hole delocalized between a copper ion and its four surrounding oxygen ions. Other terms in the effective Hamiltonian written in the localized Zhang-Rice singlet basis will generate hoppings of the local singlet across neighbouring sites, which may be equivalently regarded as the exchange of a localized copper spin and a hole. The estimation of the hopping integral from the $d-p$ model parameters is quite complex [Matsukawa and Fukuyama, 1989a] such that it may be better accounted for as a parameter which must be fixed by experiments [Tanamoto et al., 1993]. Putting together the half-filled case and the doped case, we obtain the $t-J$ model

$$\mathscr{H} = -\sum_{(i,j)\sigma} P_{D=0} \left(t_{ij} c_{i\sigma}^\dagger c_{j\sigma} + \text{h.c.} \right) P_{D=0} + J \sum_{\langle i,j \rangle} \mathbf{S}_i \cdot \mathbf{S}_j \tag{3.3.17}$$

where $c_{i\sigma}$ and $c_{i\sigma}^\dagger$ are the destruction and creation operators of the localized copper spins. As before, the operator $P_{D=0}$ is the Gutzwiller projection which enforces the no double occupancy constraint.

3.3.3 Relation between the $d-p$ and the Hubbard model

In the Mott insulator scenario, the Hubbard model is simply the effective model one obtains by projecting out the filled oxygen orbitals from the $d-p$ model. But in the relevant case for cuprates, the charge-transfer scenario, the relation between the two models is not so simple. On the other hand, the two models, once taken in the strong coupling limit, both result in a $t-J$-like model. The Hubbard model can nonetheless not be considered as an effective theory of the $d-p$ one. The $t-J$ model eq. 3.3.17 and the strong coupling limit of the Heisenberg

model differ by the two additional terms found in the latter:

$$\frac{J}{4}\sum_{\langle i,j\rangle} n_i n_j \tag{3.3.18}$$

and

$$-\frac{J}{4}\sum_{j,\boldsymbol{\tau}\neq\boldsymbol{\tau}',\sigma} P_{D=0}\left(c^{\dagger}_{j\bar{\sigma}}c_{j\bar{\sigma}}c^{\dagger}_{j+\boldsymbol{\tau}\sigma}c_{j+\boldsymbol{\tau}'\sigma}+c^{\dagger}_{j+\boldsymbol{\tau}\bar{\sigma}}c_{j\bar{\sigma}}c^{\dagger}_{j\sigma}c_{j+\boldsymbol{\tau}'\sigma}\right)P_{D=0}. \tag{3.3.19}$$

At half filling the first term is a constant and the second term identically zero because of the Gutzwiller projection. For small doping, the first term remains nearly a constant and it has been shown by variational Monte Carlo that the second term hardly contributes [Yokoyama and Ogata, 1996]. In this work we will thus consider the Hubbard model as a phenomenological model. A drawback of this approach is that there is no direct link between the phenomenological Hubbard model parameters and the $d-p$ ones. For instance, linking the phenomenological Hubbard model Coulomb repulsion to the $d-p$ model parameters as determined by some electronic measurements will prove to be difficult. In the following, we will take a simpler approach. For instance we will mention ARPES data analysed in terms of a $t-J$ model. To link this analysis to a Hubbard model we will simply deduce the corresponding phenomenological Hubbard model parameters t and U such that its strong coupling limit would result in the same $t-J$ model.

3.4 Effective low-energy theory

In this section we describe the development of the strong coupling effective low-energy theory of the single band Hubbard model with an arbitrary set of hopping amplitudes $t_{\boldsymbol{\tau}}$ along $\boldsymbol{\tau}$ bonds defined as

$$\mathscr{H} = -\sum_{\boldsymbol{r}\sigma\boldsymbol{\tau}} t_{\boldsymbol{\tau}}\hat{T}_{\boldsymbol{r}\boldsymbol{\tau}\sigma} + U\hat{V} \tag{3.4.1}$$

$$\hat{T}_{\boldsymbol{r}\boldsymbol{\tau}\sigma} = c^{\dagger}_{\boldsymbol{r}+\boldsymbol{\tau}\sigma}c_{\boldsymbol{r}\sigma} \tag{3.4.2}$$

$$\hat{V} = \sum_{\boldsymbol{r}} c^{\dagger}_{\boldsymbol{r}\uparrow}c_{\boldsymbol{r}\uparrow}c^{\dagger}_{\boldsymbol{r}\downarrow}c_{\boldsymbol{r}\downarrow} \tag{3.4.3}$$

where $c^{\dagger}_{\boldsymbol{r}\sigma}$ and $c_{\boldsymbol{\tau}\sigma}$ are the creation and annihilation fermion operators. Practical choices for the hoppings can for instance include first, second and third nearest neighbors on a square lattice. This is the case further on when this theory will be applied for the specific case of the cuprates. Here we develop a theory which is completely generic for any considered hoppings on any lattice. As seen before in section 3.3.1, the strong coupling limit $t_{\boldsymbol{\tau}}/U \ll 1$ expresses the fact that putting two fermions on the same site (therefore with opposite spins) costs a very large energy due to the Coulomb repulsion U compared to the energy one gains by letting the fermions delocalize with a bandwidth $W \sim t_{\boldsymbol{\tau}}$.
The number of double occupancies is given by the operator $\hat{V}$ defining subspaces with very

different energies. The Hubbard Hamiltonian in the strong coupling limit, if expressed in a suitable basis, should thus commute with $\hat{V}$. Developing a low-energy theory for the Hubbard model in the strong coupling limit thus only amounts to finding an approximate change of basis $\hat{U}$ such that the condition:

$$\left[\hat{U}\mathscr{H}\hat{U}^{\dagger},\hat{V}\right]=0 \tag{3.4.4}$$

is approximately fulfilled.

3.4.1 The unitary transformation

The change of basis operator $\hat{U}$ defines the new basis states as

$$|\alpha\rangle \rightarrow |\alpha'\rangle = \hat{U}|\alpha\rangle \tag{3.4.5}$$
$$\langle\alpha| \rightarrow \langle\alpha'| = \langle\alpha|\hat{U}^{\dagger}. \tag{3.4.6}$$

In our case the states $|\alpha\rangle$ are real space configurations of $\uparrow$, $\downarrow$, empty and doubly occupied sites. A choice to enumerate them is, for instance on a two by two square lattice:

$$\left|\begin{array}{cc}\uparrow & \uparrow\downarrow\\ \downarrow & -\end{array}\right\rangle = |\ \uparrow - \ \vdots\ \uparrow\downarrow\ \vdots\ -\downarrow\ \vdots\ --\ \rangle \tag{3.4.7}$$
$$= |\ 1,0\ \vdots\ 1,1\ \vdots\ 0,1\ \vdots\ 0,0\ \rangle. \tag{3.4.8}$$

To be sure the transformation is isomorphic and leads to an new orthonormal basis set, we require that

$$\langle\beta'|\alpha'\rangle = \langle\beta|\hat{U}^{\dagger}\hat{U}|\alpha\rangle = \delta_{\alpha,\beta} \tag{3.4.9}$$

which imply that the transformation $\hat{U}$ must be unitary:

$$\hat{U}^{-1} = \hat{U}^{\dagger}. \tag{3.4.10}$$

This is formally achieved by defining the unitary transformation in the following manner:

$$\hat{U} = e^{i\hat{S}} \tag{3.4.11}$$

where $\hat{S}$ is a hermitian matrix. In the new basis set, the transformed Hamiltonian is then written as

$$\mathscr{H}' = e^{i\hat{S}}\mathscr{H}e^{-i\hat{S}} \tag{3.4.12}$$
$$= \mathscr{H} + \frac{1}{1!}\left[i\hat{S},\mathscr{H}\right] + \frac{1}{2!}\left[i\hat{S},\left[i\hat{S},\mathscr{H}\right]\right] + \ldots \tag{3.4.13}$$

where eq. 3.4.13 is a standard combinatorics result (proof in appendix B.1). In eq. 3.4.11-3.4.13, $i\hat{S}$ is an unknown operator for which we ideally require that eq. 3.4.4 is fulfilled which would mean that the transformed Hamiltonian $\mathscr{H}'$ conserves the number of double occupancies. Of course it is doubtful we would find a way to exactly determine $i\hat{S}$ and are thus looking for an approximation. If we suppose $i\hat{S}$ is proportional to a small parameter λ, then it might suffice to only find an approximate transformation

$$\hat{U}^{(n)} = e^{i\hat{S}^{(n)}} \tag{3.4.14}$$

such that only the n first terms of eq. 3.4.13 do fulfill the conservation of the number of double occupancy condition eq. 3.4.13.
In the original Hamiltonian eq. 3.4.1 it is immediatly visible that, applied on a state without double occupancies, the kinetic term eq. 3.4.2 will create a double occupancy. To better tackle the effect of the kinetic operator we split it in parts using the occupation number operators

$$n_{\boldsymbol{r}\sigma} = c^\dagger_{\boldsymbol{r}\sigma} c_{\boldsymbol{r}\sigma} \tag{3.4.15}$$
$$h_{\boldsymbol{r}\sigma} = 1 - n_{\boldsymbol{r}\sigma}. \tag{3.4.16}$$

Left- and right-mutliplying the kinetic term by respectively $n_{\boldsymbol{r}+\boldsymbol{\tau}\bar{\sigma}} + h_{\boldsymbol{r}+\boldsymbol{\tau}\bar{\sigma}}$ and $n_{\boldsymbol{r}\bar{\sigma}} + h_{\boldsymbol{r}\bar{\sigma}}$ results in

$$\hat{T}_{\boldsymbol{r}\boldsymbol{\tau}\sigma} = \hat{T}^1_{\boldsymbol{r}\boldsymbol{\tau}\sigma} + \hat{T}^{-1}_{\boldsymbol{r}\boldsymbol{\tau}\sigma} + \hat{T}^0_{\boldsymbol{r}\boldsymbol{\tau}\sigma} \tag{3.4.17}$$
$$\hat{T}^1_{\boldsymbol{r}\boldsymbol{\tau}\sigma} = n_{\boldsymbol{r}+\boldsymbol{\tau}\bar{\sigma}} c^\dagger_{\boldsymbol{r}+\boldsymbol{\tau}\sigma} c_{\boldsymbol{r}\sigma} h_{\boldsymbol{r}\bar{\sigma}} \tag{3.4.18}$$
$$\hat{T}^{-1}_{\boldsymbol{r}\boldsymbol{\tau}\sigma} = h_{\boldsymbol{r}+\boldsymbol{\tau}\bar{\sigma}} c^\dagger_{\boldsymbol{r}+\boldsymbol{\tau}\sigma} c_{\boldsymbol{r}\sigma} n_{\boldsymbol{r}\bar{\sigma}} \tag{3.4.19}$$
$$\hat{T}^0_{\boldsymbol{r}\boldsymbol{\tau}\sigma} = n_{\boldsymbol{r}+\boldsymbol{\tau}\bar{\sigma}} c^\dagger_{\boldsymbol{r}+\boldsymbol{\tau}\sigma} c_{\boldsymbol{r}\sigma} n_{\boldsymbol{r}\bar{\sigma}} + h_{\boldsymbol{r}+\boldsymbol{\tau}\bar{\sigma}} c^\dagger_{\boldsymbol{r}+\boldsymbol{\tau}\sigma} c_{\boldsymbol{r}\sigma} h_{\boldsymbol{r}\bar{\sigma}}. \tag{3.4.20}$$

The new operators $\hat{T}^m_{\boldsymbol{r}\boldsymbol{\tau}\sigma}$ now have a more adequate meaning as it is easy to see that $\hat{T}^1_{\boldsymbol{r}\boldsymbol{\tau}\sigma}$ creates a double occupancy, $\hat{T}^{-1}_{\boldsymbol{r}\boldsymbol{\tau}\sigma}$ destroys one and $\hat{T}^0_{\boldsymbol{r}\boldsymbol{\tau}\sigma}$ either move a double occupancy or a hole. For instance taking $\sigma = \uparrow$ we have:

$$\hat{T}^1_{\boldsymbol{r}\boldsymbol{\tau}\uparrow}|\alpha\rangle = \hat{T}^1_{\boldsymbol{r}\boldsymbol{\tau}\uparrow} \Big| \ \dots \ \begin{matrix}\boldsymbol{r}\\ \uparrow -\end{matrix} \ \dots \ \begin{matrix}\boldsymbol{r}+\boldsymbol{\tau}\\ - \downarrow\end{matrix} \ \dots \Big\rangle = \epsilon^\alpha_{\boldsymbol{r}\boldsymbol{\tau}\sigma} \Big| \ \dots \ \begin{matrix}\boldsymbol{r}\\ - -\end{matrix} \ \dots \ \begin{matrix}\boldsymbol{r}+\boldsymbol{\tau}\\ \uparrow\downarrow\end{matrix} \ \dots \Big\rangle \tag{3.4.21}$$
$$\hat{T}^{-1}_{\boldsymbol{r}\boldsymbol{\tau}\uparrow}|\alpha\rangle = \hat{T}^{-1}_{\boldsymbol{r}\boldsymbol{\tau}\uparrow} \Big| \ \dots \ \begin{matrix}\boldsymbol{r}\\ \uparrow\downarrow\end{matrix} \ \dots \ \begin{matrix}\boldsymbol{r}+\boldsymbol{\tau}\\ - -\end{matrix} \ \dots \Big\rangle = \epsilon^\alpha_{\boldsymbol{r}\boldsymbol{\tau}\sigma} \Big| \ \dots \ \begin{matrix}\boldsymbol{r}\\ - \downarrow\end{matrix} \ \dots \ \begin{matrix}\boldsymbol{r}+\boldsymbol{\tau}\\ \uparrow -\end{matrix} \ \dots \Big\rangle \tag{3.4.22}$$
$$\hat{T}^0_{\boldsymbol{r}\boldsymbol{\tau}\uparrow}|\alpha\rangle = \hat{T}^0_{\boldsymbol{r}\boldsymbol{\tau}\uparrow} \Big| \ \dots \ \begin{matrix}\boldsymbol{r}\\ \uparrow\downarrow\end{matrix} \ \dots \ \begin{matrix}\boldsymbol{r}+\boldsymbol{\tau}\\ - \downarrow\end{matrix} \ \dots \Big\rangle = \epsilon^\alpha_{\boldsymbol{r}\boldsymbol{\tau}\sigma} \Big| \ \dots \ \begin{matrix}\boldsymbol{r}\\ - \downarrow\end{matrix} \ \dots \ \begin{matrix}\boldsymbol{r}+\boldsymbol{\tau}\\ \uparrow\downarrow\end{matrix} \ \dots \Big\rangle \tag{3.4.23}$$
$$\hat{T}^0_{\boldsymbol{r}\boldsymbol{\tau}\uparrow}|\alpha\rangle = \hat{T}^0_{\boldsymbol{r}\boldsymbol{\tau}\uparrow} \Big| \ \dots \ \begin{matrix}\boldsymbol{r}\\ \uparrow -\end{matrix} \ \dots \ \begin{matrix}\boldsymbol{r}+\boldsymbol{\tau}\\ - -\end{matrix} \ \dots \Big\rangle = \epsilon^\alpha_{\boldsymbol{r}\boldsymbol{\tau}\sigma} \Big| \ \dots \ \begin{matrix}\boldsymbol{r}\\ - -\end{matrix} \ \dots \ \begin{matrix}\boldsymbol{r}+\boldsymbol{\tau}\\ \uparrow -\end{matrix} \ \dots \Big\rangle \tag{3.4.24}$$

where $\epsilon^\alpha_{\boldsymbol{r}\boldsymbol{\tau}\sigma}$ is the fermionic sign attached to the hop of a spin $\uparrow$ from site $\boldsymbol{r}$ to site $\boldsymbol{r}+\boldsymbol{\tau}$ in the state $|\alpha\rangle$. The calculation of the fermionic sign is tied to the arbitrarily chosen state enumeration convention. Defining the index $i = x(\boldsymbol{r},\sigma)$, the fermionic sign attached to a hop

of a fermion from state $i = x(\boldsymbol{r}, \sigma)$ to $j = x(\boldsymbol{r}+\boldsymbol{\tau}, \sigma')$ is

$$\epsilon_{ij}^{\alpha} = (-1)^{N_{ij}^{\alpha}} \tag{3.4.25}$$

$$N_{ij}^{\alpha} = \sum_{k=\mathrm{min(i,j)}+1}^{\mathrm{max(i,j)}-1} \langle\alpha| c_k^{\dagger} c_k |\alpha\rangle. \tag{3.4.26}$$

To ease the notations, we also define the more compact form of the hop operators

$$\hat{T}^m = \sum_{\boldsymbol{r}\boldsymbol{\tau}\sigma} t_{\boldsymbol{\tau}} \hat{T}^m_{\boldsymbol{r}\boldsymbol{\tau}\sigma} \tag{3.4.27}$$

and remark the following properties:

$$\left[\hat{V}, \hat{T}^m\right] = mU\hat{T}^m \tag{3.4.28}$$

$$\left(\hat{T}^m\right)^{\dagger} = \hat{T}^{-m}. \tag{3.4.29}$$

The determination of the approximate unitary transform is then performed iteratively. At order n:

$$\mathscr{H}^{(n)} = \mathscr{H} + \left[i\hat{S}^{(n-1)}, \mathscr{H}\right] + \frac{1}{2!}\left[i\hat{S}^{(n-1)}, \left[i\hat{S}^{(n-1)}, \mathscr{H}\right]\right] + \ldots \tag{3.4.30}$$

such that terms that change the number of double occupancies are of order no less than t^n/U^{n-1} where t^n is a shorthand notation for a n^{th} order product of the various $t_{\boldsymbol{\tau}}$ hopping amplitudes. To second order, we see that using

$$i\hat{S}^{(1)} = \frac{1}{U}(T^1 - T^{-1}) \tag{3.4.31}$$

will indeed result in

$$\mathscr{H}^{(2)} = \hat{V} + \hat{T}^0 + \frac{1}{U}\left(\left[\hat{T}^1, \hat{T}^{-1}\right] + \left[\hat{T}^1, \hat{T}^0\right] + \left[\hat{T}^0, \hat{T}^{-1}\right]\right) + \mathscr{O}(t^3/U^2) \tag{3.4.32}$$

where the first terms changing the number of double occupancies are $\frac{1}{U}\left[\hat{T}^1, \hat{T}^0\right]$ and $\frac{1}{U}\left[\hat{T}^0, \hat{T}^{-1}\right]$. We can further simplify this expression if considering only the subspace with the minimum number of double occupancies allowed by the filling. If $|\alpha_L\rangle$ belongs to this lowest-energy subspace, then

$$\hat{T}^{-1}|\alpha_L\rangle = 0 \tag{3.4.33}$$

or more generally

$$\hat{T}^{m_1}\hat{T}^{m_2}\ldots\hat{T}^{m_k}|\alpha_L\rangle = 0 \tag{3.4.34}$$

if

$$\sum_{i=1}^{k} m_i < 0. \tag{3.4.35}$$

Further on, if now considering specifically the half-filled case, we see that

$$\hat{T}^0|\alpha_L\rangle = 0 \tag{3.4.36}$$

or more generally

$$\hat{T}^{m_1}\hat{T}^{m_2}\ldots\hat{T}^{m_k}|\alpha_L\rangle \equiv 0 \tag{3.4.37}$$

if

$$m_k = 0 \quad \text{or} \tag{3.4.38}$$

$$\sum_{i=l}^{k} m_i < 0 \quad \forall\, l \in \{1,\ldots,k\}. \tag{3.4.39}$$

Applying all these simplifications, we end with

$$\mathscr{H}^{(2)} = -\frac{1}{U}\left(\hat{T}^{-1}\hat{T}^{1} + \hat{T}^{0}\hat{T}^{1}\right). \tag{3.4.40}$$

A systematic scheme to calculate higher order approximates of $i\hat{S}$ can be devised (details in appendix B.2) and leads to:

$$\begin{aligned} i\hat{S}^{(3)} = &\frac{1}{U}\left(\hat{T}^{1} - \hat{T}^{-1}\right) + \frac{1}{U^2}\left(\left[\hat{T}^{1},\hat{T}^{0}\right] - \left[\hat{T}^{0},\hat{T}^{-1}\right]\right) \\ &+ \frac{1}{U^3}\left(\left[\hat{T}^{0},\left[\hat{T}^{0},\hat{T}^{1}\right]\right] - \left[\hat{T}^{0},\left[\hat{T}^{0},\hat{T}^{-1}\right]\right]\right. \\ &+ \frac{1}{4}\left[\hat{T}^{1},\left[\hat{T}^{0},\hat{T}^{1}\right]\right] - \frac{1}{4}\left[\hat{T}^{-1},\left[\hat{T}^{0},\hat{T}^{-1}\right]\right] \\ &\left.+ \frac{2}{3}\left[\hat{T}^{1},\left[\hat{T}^{1},\hat{T}^{-1}\right]\right] - \frac{2}{3}\left[\hat{T}^{-1},\left[\hat{T}^{-1},\hat{T}^{1}\right]\right]\right) \end{aligned} \tag{3.4.41}$$

and to the effective low-energy Hamiltonian

$$\begin{aligned} \mathscr{H}^{(4)} = &-\frac{1}{U}\hat{T}^{-1}\hat{T}^{1} + \frac{1}{U^2}\hat{T}^{-1}\hat{T}^{0}\hat{T}^{1} \\ &+ \frac{1}{U^3}\left(\hat{T}^{-1}\hat{T}^{1}\hat{T}^{-1}\hat{T}^{1} - \hat{T}^{-1}\hat{T}^{0}\hat{T}^{0}\hat{T}^{1}\right. \\ &\left.- \hat{T}^{-1}\hat{T}^{-1}\hat{T}^{1}\hat{T}^{1}/2\right) \end{aligned} \tag{3.4.42}$$

where terms of order t^4/U^3 creating one or more double occupancies have been omitted as they will be destroyed at next order leaving the terms shown here unchanged.

3.4.2 Effective Spin Hamiltonian

At half filling we thus obtain to t^4/U^3 order the Hamiltonian eq. 3.4.42 expressed as a sum of a combination of hopping operators $\hat{T}^m$ which do not create any double occupancy. Therefore the Hilbert space associated with eq. 3.4.42 has only the $\sigma \in \{\uparrow, \downarrow\}$ spin-$\frac{1}{2}$ degrees of freedom per site. It follows that eq. 3.4.42 can be reformulated using the $SU(2)$ invariant spin operators. If we consider a system of N sites, the Hamiltonian eq. 3.4.42 can be represented as a $2^N \times 2^N$ matrix $\mathbf{H}$ in a given basis of states. The matrix itself can be seen as a superposition of matrices with only one element:

$$\mathbf{H} = \sum_{ij} \mathbf{H}_{ij} \mathbf{\Delta}_{ij} \quad \left(\mathbf{\Delta}_{ij}\right)_{kl} = \delta_{ik}\delta_{jl} \tag{3.4.43}$$

or if we associate the matrix $\mathbf{\Delta}_{ij}$ to the unit vectors $\vec{e}_{ij}$ of the basis spanning the complex $2^N \times 2^N$ matrices Ω_{2^N}:

$$\Omega_{2^N} = \left\{\Delta_{ij}\right\} \tag{3.4.44}$$

we can equivalently write the matrix $\boldsymbol{H}$ in a vector form

$$\vec{\boldsymbol{H}} = \sum_{ij} \boldsymbol{H}_{ij} \vec{e}_{ij}. \tag{3.4.45}$$

In this language, reformulating $\mathbf{H}$ in terms of spin operators is identical to performing a change of basis for $\vec{\mathbf{H}}$. Let us define the new basis of the $2^N \times 2^N$ hermitian matrices $\Omega^H_{2^N}$:

$$\Omega^H_{2^N} = \{\sigma[m]\} \tag{3.4.46}$$

$$\sigma[m] = \sigma^{(1)}_{m_1} \otimes \sigma^{(2)}_{m_2} \otimes \cdots \otimes \sigma^{(N)}_{m_N} \tag{3.4.47}$$

where $\sigma^{(l)}_{m_l} \in \left\{\mathbb{1}, \sigma^x, \sigma^y, \sigma^z\right\}$ are the Pauli matrices plus the 2×2 identity $\mathbb{1}$ associated with the site l spin-$\frac{1}{2}$ degree of freedom. The unit vectors of the new $\Omega^H_{2^N}$ basis can be written in the old one Ω_{2^N} as

$$\vec{\sigma}[m] = \frac{1}{2^{N/2}} \sum_{ij} (\sigma[m])_{ij} \vec{e}_{ij}. \tag{3.4.48}$$

We can verify that the new vectors are indeed orthonormal as:

$$\begin{aligned}\vec{\sigma}[m]\cdot\vec{\sigma}[m'] &= \frac{1}{2^N}\sum_{ij}\sum_{i'j'}(\sigma[m'])_{i'j'}(\sigma[m])^*_{ij}\vec{e}_{ij}\cdot\vec{e}_{i'j'}\\ &= \frac{1}{2^N}\sum_{ij}(\sigma[m'])_{ij}(\sigma[m])_{ji}\\ &= \frac{1}{2^N}\mathrm{Tr}\left(\sigma[\mathrm{m}']\sigma[\mathrm{m}]\right)\\ &= \frac{1}{2^N}\prod_l \mathrm{Tr}(\sigma^{(l)}_{m_l}\sigma^{(l)}_{m'_l})\\ &= \prod_l \delta_{m_l m'_l}.\end{aligned} \tag{3.4.49}$$

We can then rewrite $\vec{\mathbf{H}}$ in terms of $\vec{\sigma}[m]$:

$$\vec{\mathbf{H}} = \frac{1}{2^{N/2}}\sum_{\{m\}}\left(\vec{\sigma}[m]\cdot\vec{\mathbf{H}}\right)\vec{\sigma}[m] \tag{3.4.50}$$

or in operator form,

$$\mathbf{H}_S = \frac{1}{2^N}\sum_{\{m\}}\sigma[m]\mathrm{Tr}(\sigma[m]\mathbf{H}). \tag{3.4.51}$$

To reformulate $\mathscr{H}^{(k)}$ in terms of spin operators, we must therefore evaluate its matrix form on a specific cluster of N sites large enough to support the different hopping processes contained in $\mathscr{H}^{(k)}$. This calculation is carried out using an exact computer implementation. To illustrate how it works, let us study the case of the hopping process $\hat{T}^{-1}\hat{T}^0\hat{T}^0\hat{T}^1$:

$$\hat{T}^{-1}\hat{T}^0\hat{T}^0\hat{T}^1 = \sum_{i_1 i_2 i_3 i_4}\sum_{\boldsymbol{\tau}_1\boldsymbol{\tau}_2\boldsymbol{\tau}_3\boldsymbol{\tau}_4}\sum_{\sigma_1,\sigma_2,\sigma_3,\sigma_4}\hat{T}^{-1}_{i_4\boldsymbol{\tau}_4\sigma_4}\hat{T}^0_{i_3\boldsymbol{\tau}_3\sigma_3}\hat{T}^0_{i_2\boldsymbol{\tau}_2\sigma_2}\hat{T}^1_{i_1\boldsymbol{\tau}_1\sigma_1}. \tag{3.4.52}$$

Despite the apparent complexity from the many indices, only a very few subset of those actually give a finite contribution. We consider the cluster of fig. 3.10 with the highlighted spins participating an exchange process. The initial state is denoted

$$|\alpha\rangle = \left|\begin{array}{cc}\uparrow & \downarrow\\ \downarrow & \uparrow\end{array}\right\rangle. \tag{3.4.53}$$

Reading $\hat{T}^{-1}\hat{T}^0\hat{T}^0\hat{T}^1$ from right to left we can illustrate one possible exchange process:

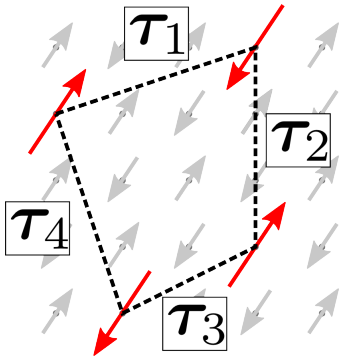

Figure 3.10 – Example of a cluster with the four spins highlighted forming a closed path through the hoppings $\boldsymbol{\tau}_1$, $\boldsymbol{\tau}_2$, $\boldsymbol{\tau}_3$ and $\boldsymbol{\tau}_4$.

$$\hat{T}^{-1}\hat{T}^{0}\hat{T}^{0}\hat{T}^{1}\left|\begin{array}{cc}\uparrow & \downarrow\\ \downarrow & \uparrow\end{array}\right\rangle = \hat{T}^{-1}\hat{T}^{0}\hat{T}^{0}\left|\begin{array}{cc}\uparrow\downarrow & \downarrow\\ - & \uparrow\end{array}\right\rangle \tag{3.4.54}$$

$$= \hat{T}^{-1}\hat{T}^{0}\left|\begin{array}{cc}\uparrow\downarrow & \downarrow\\ \uparrow & -\end{array}\right\rangle \tag{3.4.55}$$

$$= \hat{T}^{-1}\left|\begin{array}{cc}\downarrow & \uparrow\downarrow\\ \uparrow & -\end{array}\right\rangle \tag{3.4.56}$$

$$= \left|\begin{array}{cc}\downarrow & \uparrow\\ \uparrow & \downarrow\end{array}\right\rangle. \tag{3.4.57}$$

The last hop from eq. 3.4.56 to eq. 3.4.57, which must annihilate a double occupancy and a hole, require that the double occupancy and the hole do not separate far enough that no hopping is available for $\hat{T}^{-1}$ to be able to operate. The translation vectors $\boldsymbol{\tau}_i$ must therefore form a closed path for the operator $\hat{T}^{-1}\hat{T}^{0}\hat{T}^{0}\hat{T}^{1}$ to give a contribution. The complicated sum of eq. 3.4.52 thus contains far less terms than apparent. The situation is identical for the $\hat{T}^{-1}\hat{T}^{0}\hat{T}^{1}$ and the $\hat{T}^{-1}\hat{T}^{1}$ operators: they might only contribute on closed paths of three or two sites respectively. The $\hat{T}^{-1}\hat{T}^{-1}\hat{T}^{1}\hat{T}^{1}$ and $\hat{T}^{-1}\hat{T}^{1}\hat{T}^{-1}\hat{T}^{1}$ operators on the other hand might individually contribute on two disjoint pairs of sites. A close inspection of this situation reveals that in that case, one can commute the $\hat{T}^{m}_{i\boldsymbol{\tau}\sigma}$ which do not operate on the same bonds such that the two operators are actually identical up to a combinatorial factor. In the end the sum of their contribution in eq. 3.4.42 cancels out such that only their contributions on closed paths remain.

Using an exact computer implementation to carry out the evaluation of $\mathscr{H}^{(4)}$ on a given cluster

in order to calculate eq. 3.4.51 finally gives the following effective spin Hamiltonian

$$\begin{aligned}\hat{\mathscr{H}}^{(4)} = &\sum_{\left\{\begin{smallmatrix}1\\2\end{smallmatrix}\right\}} \left(\frac{4t_{12}^2}{U} - \frac{16t_{12}^4}{U^3}\right)\left(\mathbf{S}_1\mathbf{S}_2 - \frac{1}{4}\right) + \sum_{\left\{\begin{smallmatrix}1&2\\3\end{smallmatrix}\right\}} \frac{4t_{12}^2 t_{23}^2}{U^3}\left(\mathbf{S}_1\mathbf{S}_3 - \frac{1}{4}\right) \\ &- \sum_{\left\{\begin{smallmatrix}1&2\\4&3\end{smallmatrix}\right\}} \frac{4t_{12}t_{23}t_{34}t_{41}}{U^3}\Big\{\sum_{\substack{i,j=1\\ i\neq j}}^{4} \mathbf{S}_i\mathbf{S}_j - 20\Big[(\mathbf{S}_1\mathbf{S}_2)(\mathbf{S}_3\mathbf{S}_4) \\ &+ (\mathbf{S}_1\mathbf{S}_4)(\mathbf{S}_2\mathbf{S}_3) - (\mathbf{S}_1\mathbf{S}_3)(\mathbf{S}_2\mathbf{S}_4)\Big]\Big\} + E^{(4)},\end{aligned} \tag{3.4.58}$$

where, following the previous discussion, $\left\{\begin{smallmatrix}1\\2\end{smallmatrix}\right\}$, $\left\{\begin{smallmatrix}1&2\\3\end{smallmatrix}\right\}$ and $\left\{\begin{smallmatrix}1&2\\4&3\end{smallmatrix}\right\}$ are the ensembles of every closed loops with two, three and four sites respectively. Here we leave these ensembles undefined as they depend on the specific lattice and hopping parameters $\{\boldsymbol{\tau}\}$ considered. We note that there are no three spins contributions which would come out from the operator $\hat{T}^{-1}\hat{T}^0\hat{T}^1$. The contribution of this operator is always null, which is non-trivial in the case of the three site loops $\left\{\begin{smallmatrix}1&2\\&3\end{smallmatrix}\right\}$. In that case for each hopping process going around the loop, one can find another going in the other direction which will give the same contribution but with an opposite sign of fermionic origin. We conclude this section emphasizing that eq. 3.4.58 is the general effective spin Hamiltonian of the strong coupling Hubbard model at half filling for any lattice and any ensemble of considered hoppings $\{\boldsymbol{\tau}\}$.

3.4.3 Spin operators in the effective theory

The low-energy effective theory defines a change of basis such that the number of double occupancies is approximately conserved and it turns out the effective Hamiltonian can be written in terms of spin operators. But these effective spin operators must not be confused with the bare physical ones as defined in the original basis:

$$\bar{S}_i^z = \frac{1}{2}\left(c_{i\uparrow}^\dagger c_{i\uparrow} - c_{i\downarrow}^\dagger c_{i\downarrow}\right) \tag{3.4.59}$$

$$\bar{S}_i^+ = c_{i\uparrow}^\dagger c_{i\downarrow} \tag{3.4.60}$$

$$\bar{S}_i^- = c_{i\downarrow}^\dagger c_{i\uparrow}. \tag{3.4.61}$$

In the same way as the Hamiltonian, the bare spin operators must be transposed in the new effective basis using the formula:

$$\bar{S}_i^{\alpha(n)} = \bar{S}_i^\alpha + \left[i\hat{S}^{(n-1)}, \bar{S}_i^\alpha\right] + \frac{1}{2}\left[i\hat{S}^{(n-1)}, \left[i\hat{S}^{(n-1)}, \bar{S}_i^\alpha\right]\right] + \ldots. \tag{3.4.62}$$

Looking at $i\hat{S}^{(3)}$ in eq. 3.4.41, we can notice that all terms change the number of double occupancies but on the other hand the bare spin operators do not. It follows that in eq. 3.4.62 the terms with odd power of $1/U$ will necessarily change the number of double occupancies so they will not contribute in the low-energy subspace where double occupancies are forbidden. On the other hand the even terms in $1/U$ will contribute so we expect a correction of order $(t/U)^2$. In the coming discussion, it is more useful to give the spin operator in reciprocal space

$$\tilde{S}^{\alpha}_{\boldsymbol{q}} = \sum_i e^{i\boldsymbol{q}\cdot\boldsymbol{R}_i}\tilde{S}^{\alpha}_i. \tag{3.4.63}$$

In the effective theory this operator becomes

$$\tilde{S}^{\alpha(4)}_{\boldsymbol{k}} = R_{\text{eff}}(\boldsymbol{q})S^{\alpha}_{\boldsymbol{q}} \tag{3.4.64}$$

with the $R_{\text{eff}}(\boldsymbol{q})$ is a charge fluctuation renormalization factor:

$$R_{\text{eff}}(\boldsymbol{q}) = 1 + \sum_{\boldsymbol{\tau}}\left(\frac{t_{\boldsymbol{\tau}}}{U}\right)^2\left(1 - e^{i\boldsymbol{q}\cdot\boldsymbol{\tau}}\right) + \mathcal{O}\left(\frac{t^4}{U^4}\right) \tag{3.4.65}$$

3.5 Spin-Wave Theory

The previous sections were dedicated to produce a low-energy Hamiltonian for general lattices and hopping ensembles. In this section we will restrict our discussion to the square lattice as this development aims at fitting the magnetic excitation spectrum of the cuprate families. While the size of the Hilbert space associated with our problem could already be dramatically reduced by projecting out double occupancies, the spin Hamiltonian eq. 3.4.58 still is a difficult problem. It is in fact difficult already without considering all the complicated terms and restricting it for instance to the simple nearest neighbour Heisenberg model

$$\mathcal{H} = \sum_{\langle i\,j\rangle} \boldsymbol{S}_i \cdot \boldsymbol{S}_j, \tag{3.5.1}$$

a model that has no known exact solution on 2-dimensional systems [Manousakis, 1991]. Here we will use the overall very successful spin-wave theory to approximately diagonalize the Heisenberg model and adapt it to the case of the more complicated effective spin Hamiltonian eq. 3.4.58. The starting point is to note that the minimum classical energy for eq. 3.5.1 is obtained for an antiferromagnetic arrangement of the spins hereafter referred as Néel order. But now considering the complete effective Hamiltonian eq. 3.4.58, it is not the case for any U

and any set of hoppings parameter. But in a situation where the nearest neighbor coupling is dominant, there must be a region where the other parameters only affect the eigenenergies but not the eigenstates. We therefore also start by assuming the classical groundstate of eq. 3.4.58 is the antiferromagnetic Néel order. The spin-wave theory assumes the quantum state can be described as the classical groundstate plus zero-point quantum fluctuations [Bloch, 1930; Anderson, 1952; Kubo, 1952] and is written as an expansion in $1/S$ so is most justified when S is large while we sit actually in the opposite situation with $S = 1/2$. We describe here its application on the effective spin Hamiltonian eq. 3.4.58 in the case of the single and double layer square lattice where the classical groundstate is postulated to be antiferromagnetic.
As the magnetic lattice has doubled unit cell compared to the nuclear lattice, we apply a staggered rotation of the frame of reference around the spin y-axis:

$$S_i^x = e^{i\boldsymbol{Q}\cdot\boldsymbol{R}_i}\tilde{S}_i^x \tag{3.5.2}$$
$$S_i^y = \tilde{S}_i^y \tag{3.5.3}$$
$$S_i^z = e^{i\boldsymbol{Q}\cdot\boldsymbol{R}_i}\tilde{S}_i^z \tag{3.5.4}$$

In the case of a double layer, we proceed similarly but shift the staggered rotation by one unit cell between the layers so they sit antiferromagnetically with respect to each others:

$$S_{i1}^x = e^{i\boldsymbol{Q}\cdot\boldsymbol{R}_i}\tilde{S}_{i1}^x \qquad S_{i2}^x = e^{-i\boldsymbol{Q}\cdot\boldsymbol{R}_i}\tilde{S}_{i2}^x \tag{3.5.5}$$
$$S_{i1}^y = \tilde{S}_{i1}^y \qquad S_{i2}^y = \tilde{S}_{i2}^y \tag{3.5.6}$$
$$S_{i1}^z = e^{i\boldsymbol{Q}\cdot\boldsymbol{R}_i}\tilde{S}_{i1}^z \qquad S_{i2}^z = e^{-i\boldsymbol{Q}\cdot\boldsymbol{R}_i}\tilde{S}_{i2}^z \tag{3.5.7}$$

where $\boldsymbol{Q} = (\pi/a, \pi/a)$ with a the square lattice parameter and, for the spin operators S_{il}^α, i and $\boldsymbol{R}_i$ index the unit cell and $l \in \{1,2\}$ index the layers. In the staggered frame of reference the classical ground state is now ferromagnetic. It simplifies the formalism in the following. We further introduce the Holstein-Primakov transformation [Holstein and Primakoff, 1940]:

$$S_{il}^z = S - a_{il}^\dagger a_{il} \tag{3.5.8}$$
$$S_{il}^+ = \sqrt{2S - a_{il}^\dagger a_{il}}\, a_{il} \tag{3.5.9}$$
$$S_{il}^- = a_{il}^\dagger \sqrt{2S - a_{il}^\dagger a_{il}}. \tag{3.5.10}$$

The classical ground state being ferromagnetic in the staggered frame of reference, we do not need to introduce two species of bosons to represent the even $\boldsymbol{Q}\cdot\boldsymbol{R} = 2n\pi$ from the odd $\boldsymbol{Q}\cdot\boldsymbol{R} = (2n+1)\pi$ sites. The different terms in the effective spin Hamiltonian eq. 3.4.58 are either quadratic or quartic products of spin operators. We develop below their formulation in terms of spin-waves.

3.5.1 Quadratic products of spin operators

The quadratic spin operators products in eq. 3.4.58 written in the staggered frame of reference eq. 3.5.2-3.5.4 and 3.5.5-3.5.7 is:

$$\begin{aligned}\boldsymbol{S}_{il}\cdot\boldsymbol{S}_{i+\boldsymbol{\tau}l'} = (2\epsilon_{\boldsymbol{\tau}ll'}-1)\tilde{S}^z_{il}\tilde{S}^z_{i+\boldsymbol{\tau}l'} + \frac{1}{2}\big[\epsilon_{\boldsymbol{\tau}ll'}\left(\tilde{S}^+_{il}\tilde{S}^-_{i+\boldsymbol{\tau}l'} + \tilde{S}^-_{il}\tilde{S}^+_{i+\boldsymbol{\tau}l'}\right)\\ -\bar{\epsilon}_{\boldsymbol{\tau}ll'}\left(\tilde{S}^+_{il}\tilde{S}^+_{i+\boldsymbol{\tau}l'} + \tilde{S}^-_{il}\tilde{S}_{i+\boldsymbol{\tau}l'}\right)\big]\end{aligned} \tag{3.5.11}$$

where $\boldsymbol{\tau}$ is a translation vector, the l and l' index applies to the double layer square lattice and

$$\epsilon_{\boldsymbol{\tau}ll'} = \begin{cases}\frac{1+e^{i\boldsymbol{Q}\cdot\boldsymbol{\tau}}}{2} & l = l'\\ \frac{1-e^{i\boldsymbol{Q}\cdot\boldsymbol{\tau}}}{2} & l \neq l'\end{cases} \tag{3.5.12}$$

$$\bar{\epsilon}_{\boldsymbol{\tau}ll'} = \begin{cases}\frac{1-e^{i\boldsymbol{Q}\cdot\boldsymbol{\tau}}}{2} & l = l'\\ \frac{1+e^{i\boldsymbol{Q}\cdot\boldsymbol{\tau}}}{2} & l \neq l'\end{cases}. \tag{3.5.13}$$

Note that the vector $\boldsymbol{\tau}$ describes only translations between unit cells, not the layers. If $l \neq l'$, the $\boldsymbol{\tau} = 0$ must be included to account for the nearest neighbour inter-layer interaction. Substituting eq. 3.5.8-3.5.10 into eq. 3.5.11 we obtain a power series of terms in S:

$$\begin{aligned}\boldsymbol{S}_{il}\cdot\boldsymbol{S}_{i+\boldsymbol{\tau}l'} = S^2\Bigg[(\boldsymbol{S}_{il}\cdot\boldsymbol{S}_{i+\boldsymbol{\tau}l'})^{(0)} + \frac{1}{S}(\boldsymbol{S}_{il}\cdot\boldsymbol{S}_{i+\boldsymbol{\tau}l'})^{(1)}\\ + \frac{1}{S^2}(\boldsymbol{S}_{il}\cdot\boldsymbol{S}_{i+\boldsymbol{\tau}l'})^{(2)} + \mathcal{O}\left(\frac{1}{S^3}\right)\Bigg]\end{aligned} \tag{3.5.14}$$

where we kept only terms up to $\frac{1}{S^2}$ in the above notation. We find

$$(\boldsymbol{S}_{il}\cdot\boldsymbol{S}_{i+\boldsymbol{\tau}l'})^{(0)} = (2\epsilon_{\boldsymbol{\tau}ll'}-1), \tag{3.5.15}$$

$$\begin{aligned}(\boldsymbol{S}_{il}\cdot\boldsymbol{S}_{i+\boldsymbol{\tau}l'})^{(1)} =& (1-2\epsilon_{\boldsymbol{\tau}ll'})(a^\dagger_{il}a_{il} + a^\dagger_{i+\boldsymbol{\tau}l'}a_{i+\boldsymbol{\tau}l'})\\ &+ 2\epsilon_{\boldsymbol{\tau}ll'}(a^\dagger_{i+\boldsymbol{\tau}l'}a_{il} + a^\dagger_{il}a_{i+\boldsymbol{\tau}l'})\\ &- 2\bar{\epsilon}_{\boldsymbol{\tau}ll'}(a_{il}a_{i+\boldsymbol{\tau}l'} + a^\dagger_{il}a^\dagger_{i+\boldsymbol{\tau}l'})\end{aligned} \tag{3.5.16}$$

and

$$\begin{aligned}(\boldsymbol{S}_{il}\cdot\boldsymbol{S}_{i+\boldsymbol{\tau}l'})^{(2)} = \quad (2\epsilon_{\boldsymbol{\tau}ll'}-1)n_{il}n_{i+\boldsymbol{\tau}l'} - \tfrac{1}{4} \quad &\Big[\epsilon_{\boldsymbol{\tau}ll'}\Big(a^\dagger_{il}(n_{il}+n_{i+\boldsymbol{\tau}l'})a_{i+\boldsymbol{\tau}l'}\\ &+a^\dagger_{i+\boldsymbol{\tau}l'}(n_{il}+n_{i+\boldsymbol{\tau}l'})a_{il}\Big)\\ &+\bar{\epsilon}_{\boldsymbol{\tau}ll'}\left((n_{il}+n_{i+\boldsymbol{\tau}l'})a_{il}a_{i+\boldsymbol{\tau}l'}\right.\\ &\left.+a^\dagger_{il}a^\dagger_{i+\boldsymbol{\tau}l'}(n_{il}+n_{i+\boldsymbol{\tau}l'})\right)\Big].\end{aligned} \tag{3.5.17}$$

We then proceed by doing a Fourier transform. We use

$$a_{il} = \frac{1}{\sqrt{N}} \sum_{\boldsymbol{k}} e^{i\boldsymbol{k}\cdot\boldsymbol{R}_i} a_{\boldsymbol{k}} \tag{3.5.18}$$

$$a_{il}^{\dagger} = \frac{1}{\sqrt{N}} \sum_{\boldsymbol{k}} e^{i-i\boldsymbol{k}\cdot\boldsymbol{R}_i} a_{\boldsymbol{k}}^{\dagger}. \tag{3.5.19}$$

The quadratic part eq. 3.5.16 becomes:

$$\sum_i (\boldsymbol{S}_{il}\cdot\boldsymbol{S}_{i+\boldsymbol{\tau}l'})^{(1)} = \sum_{\boldsymbol{k}} \sum_{m,m'\in\{l,l'\}} \left(A_{\boldsymbol{k}}^{\boldsymbol{\tau}ll'}\right)_{mm'} a_{\boldsymbol{k}(m)}^{\dagger} a_{\boldsymbol{k}(m')} + \frac{1}{2}\left(B_{\boldsymbol{k}}^{\boldsymbol{\tau}ll'}\right)_{mm'} \left(a_{\boldsymbol{k}m}^{\dagger} a_{-\boldsymbol{k}m'}^{\dagger} + a_{\boldsymbol{k}m} a_{-\boldsymbol{k}m'}\right) \tag{3.5.20}$$

with

$$A_{\boldsymbol{k}}^{\boldsymbol{\tau}ll'} = J_{\boldsymbol{\tau}ll'} \begin{pmatrix} 2(1-2\epsilon_{\boldsymbol{\tau}ll'}) + \delta_{ll'}\epsilon_{\boldsymbol{\tau}ll'}\cos(\boldsymbol{k}\boldsymbol{\tau}) & (1-\delta_{ll'})\epsilon_{\boldsymbol{\tau}ll'}\cos(\boldsymbol{k}\boldsymbol{\tau}) \\ (1-\delta_{ll'})\epsilon_{\boldsymbol{\tau}ll'}\cos(\boldsymbol{k}\boldsymbol{\tau}) & 2(1-2\epsilon_{\boldsymbol{\tau}ll'}) + \delta_{ll'}\epsilon_{\boldsymbol{\tau}ll'}\cos(\boldsymbol{k}\boldsymbol{\tau}) \end{pmatrix} \tag{3.5.21}$$

$$B_{\boldsymbol{k}}^{\boldsymbol{\tau}ll'} = -J_{\boldsymbol{\tau}ll'} \begin{pmatrix} 2\delta_{ll'}\bar{\epsilon}_{\boldsymbol{\tau}ll'}\cos(\boldsymbol{k}\boldsymbol{\tau}) & 2(1-\delta_{ll'})\bar{\epsilon}_{\boldsymbol{\tau}ll'}\cos(\boldsymbol{k}\boldsymbol{\tau}) \\ (1-\delta_{ll'})\bar{\epsilon}_{\boldsymbol{\tau}ll'}\cos(\boldsymbol{k}\boldsymbol{\tau}) & 2\delta_{ll'}\bar{\epsilon}_{\boldsymbol{\tau}ll'}\cos(\boldsymbol{k}\boldsymbol{\tau}) \end{pmatrix}. \tag{3.5.22}$$

In the monolayer case, the above formulas are still valid simply by considering only the $\left(A_{\boldsymbol{k}}^{\boldsymbol{\tau}11}\right)_{11}$ and $\left(B_{\boldsymbol{k}}^{\boldsymbol{\tau}11}\right)_{11}$ or equivalently by letting $J_{\boldsymbol{\tau}l\neq l'} = 0$ such that the two layers are non-interacting.

3.5.2 Quartic products of spin operators

We treat in a similar way the quartic terms, but will keep only the terms quadratic in the boson operators. Doing so we carry out the following approximation:

$$\begin{aligned}(\boldsymbol{S}_i\cdot\boldsymbol{S}_{i+\boldsymbol{\tau}_1})(\boldsymbol{S}_{i+\boldsymbol{\tau}_2}\cdot\boldsymbol{S}_{i+\boldsymbol{\tau}_3}) \simeq S^4 \Big(& (\boldsymbol{S}_i\cdot\boldsymbol{S}_{i+\boldsymbol{\tau}_1})^{(0)} (\boldsymbol{S}_{i+\boldsymbol{\tau}_2}\cdot\boldsymbol{S}_{i+\boldsymbol{\tau}_3})^{(0)} \\ & + \frac{1}{S}\Big((\boldsymbol{S}_i\cdot\boldsymbol{S}_{i+\boldsymbol{\tau}_1})^{(1)} (\boldsymbol{S}_{i+\boldsymbol{\tau}_2}\cdot\boldsymbol{S}_{i+\boldsymbol{\tau}_3})^{(0)} \\ & + (\boldsymbol{S}_i\cdot\boldsymbol{S}_{i+\boldsymbol{\tau}_1})^{(0)} (\boldsymbol{S}_{i+\boldsymbol{\tau}_2}\cdot\boldsymbol{S}_{i+\boldsymbol{\tau}_3})^{(1)} \Big) + \mathcal{O}\left(\frac{1}{S^2}\right) \Big)\end{aligned} \tag{3.5.23}$$

so one can use the formulas found for the case of the quadratic products of spin operators.

3.5.3 Effective Spin Hamiltonian in the spin-wave approximation

We finally sum up all quadratic and quartic products of spin operators to find a Hamiltonian that has the following form:

$$\mathscr{H}^{(4)} \simeq H_{SW}^{(0)} + H_{SW}^{(1)} + H_{SW}^{(2)} \tag{3.5.24}$$

where $H_{SW}^{(0)}$ is a constant, $H_{SW}^{(1)}$ has only terms quadratic in the boson operators and $H_{SW}^{(2)}$ has quartic boson terms. Let us here discuss in what limit exactly the above expansion is justified. Unlike the simple Heisenberg model case where only quadratic products of spin operators must be considered, the limit here cannot be expressed only as a $\frac{1}{S}$ one. We actually work in a mixed $\frac{1}{S}$ and $\frac{t}{U}$ limit. If we denote $[aa]$ and $[aaaa]$ the terms quadratic and quartic in boson operators respectively, we chose to only consider the following terms:

$$\begin{aligned}\mathscr{H}^{(4)} \simeq & \frac{t^2}{U}S^2\left(E_{t^2/U}+\frac{1}{S}[aa]+\frac{1}{S^2}[aaaa]\right)+\mathscr{O}\left(\frac{t^2}{U}\frac{1}{S}\right)\\ & \frac{t^4}{U^3}S^4\left(E_{t^4/U^3}+\frac{1}{S}[aa]\right)+\mathscr{O}\left(\frac{t^4}{U^3}S^2\right)\end{aligned} \tag{3.5.25}$$

so we effectively work in a mixed limit where $\frac{t^2}{US}$ and $\frac{t^4S^2}{U^3}$ are expected to be small enough parameters to be neglected. Using the formalism developed before, we can then write the following quadratic bosonic Hamiltonian

$$\begin{aligned}H_{SW}^{(2)} = & \sum_{\boldsymbol{k}}\sum_{mm'}(A_{\boldsymbol{k}})_{mm'}\left(a_{\boldsymbol{k}m}^{\dagger}a_{\boldsymbol{k}m'}+a_{\boldsymbol{k}m'}^{\dagger}a_{\boldsymbol{k}m}\right)\\ & +\frac{1}{2}(B_{\boldsymbol{k}})_{mm'}\left(a_{\boldsymbol{k}m}^{\dagger}a_{-\boldsymbol{k}m'}^{\dagger}+a_{\boldsymbol{k}m}a_{-\boldsymbol{k}m'}\right)\end{aligned} \tag{3.5.26}$$

where the matrices $A_{\boldsymbol{k}}$ and $B_{\boldsymbol{k}}$ are complicated sums over the ensembles of two-, three- and four-sites closed loops as in eq. 3.4.58. We give the full expressions in the appendix B.3.

3.5.4 Bogoliubov transformation

We diagonalize eq. 3.5.26 using a Bogoliubov transformation. Defining the quasi-particle operators:

$$b_{\boldsymbol{k}n}=\sum_{l}u_{\boldsymbol{k}n}^{l}a_{\boldsymbol{k}l}+v_{\boldsymbol{k}n}^{l}a_{-\boldsymbol{k}l}^{\dagger} \tag{3.5.27}$$

we want $u_{\boldsymbol{k}l}$ and $v_{\boldsymbol{k}l}$ such that the quadratic Hamiltonian can be written as

$$H_{SW}^{(2)}=\sum_{\boldsymbol{k},n}\omega_{\boldsymbol{k}n}b_{\boldsymbol{k}n}^{\dagger}b_{\boldsymbol{k}n}+\frac{1}{2}\sum_{\boldsymbol{k},n}\omega_{\boldsymbol{k}n}-\frac{1}{2}\sum_{\boldsymbol{k},l}A_{\boldsymbol{k}ll}. \tag{3.5.28}$$

In the case of a single layer, the index n is unnecessary. In the bilayer case, $n\in\{a,s\}$ will index the so-called symmetric and anti-symmetric modes. It follows from eq. 3.5.28 that we must have

$$\left[H_{SW}^{(2)},b_{\boldsymbol{k}n}\right]=-\omega_{\boldsymbol{k}n}b_{\boldsymbol{k}n}. \tag{3.5.29}$$

Carrying out the commutator, we arrive at the eigenproblem

$$\begin{pmatrix} \mathbf{A}_{\boldsymbol{k}} & -\mathbf{B}_{\boldsymbol{k}} \\ \mathbf{B}_{\boldsymbol{k}} & -\mathbf{A}_{\boldsymbol{k}} \end{pmatrix} \begin{pmatrix} \mathbf{u}_{\boldsymbol{k}n} \\ \mathbf{v}_{\boldsymbol{k}n} \end{pmatrix} = \omega_{\boldsymbol{k}n} \begin{pmatrix} \mathbf{u}_{\boldsymbol{k}n} \\ \mathbf{v}_{\boldsymbol{k}n} \end{pmatrix} \tag{3.5.30}$$

where $\mathbf{A}_{\boldsymbol{k}}$ and $\mathbf{B}_{\boldsymbol{k}}$ are 2×2 real matrices for the bilayer case and real numbers in the case of a single layer. The $\mathbf{u}_{\boldsymbol{k}n}$ and $\mathbf{v}_{\boldsymbol{k}n}$ are defined in a similar way as

$$\mathbf{u}_{\boldsymbol{k}n} = \begin{pmatrix} u^1_{\boldsymbol{k}n} \\ u^2_{\boldsymbol{k}n} \end{pmatrix} \tag{3.5.31}$$

$$\mathbf{v}_{\boldsymbol{k}n} = \begin{pmatrix} v^1_{\boldsymbol{k}n} \\ v^2_{\boldsymbol{k}n} \end{pmatrix} \tag{3.5.32}$$

$$\tag{3.5.33}$$

for the bilayer case and are simply real numbers in the single layer case. In the single layer case, we get the familiar result

$$\omega_{\boldsymbol{k}} = \sqrt{A^2_{\boldsymbol{k}} - B^2_{\boldsymbol{k}}} \tag{3.5.34}$$

and

$$u_{\boldsymbol{k}} = \sqrt{\frac{1}{2}\left(\frac{A_{\boldsymbol{k}}}{\omega} + 1\right)} \tag{3.5.35}$$

$$v_{\boldsymbol{k}} = \text{sign}\,(B_{\boldsymbol{k}}) \sqrt{\frac{1}{2}\left(\frac{A_{\boldsymbol{k}}}{\omega} - 1\right)} \tag{3.5.36}$$

and for the bilayer case

$$\omega_{\boldsymbol{k}s} = \sqrt{(A_{\boldsymbol{k}11} + A_{\boldsymbol{k}12})^2 - (B_{\boldsymbol{k}11} + B_{\boldsymbol{k}12})^2} \tag{3.5.37}$$

$$\omega_{\boldsymbol{k}a} = \sqrt{(A_{\boldsymbol{k}11} - A_{\boldsymbol{k}12})^2 - (B_{\boldsymbol{k}11} - B_{\boldsymbol{k}12})^2} \tag{3.5.38}$$

and

$$u^1_{\boldsymbol{k}s} = u^2_{\boldsymbol{k}s} = \frac{1}{2}\sqrt{\frac{A^{11}_{\boldsymbol{k}} + A^{12}_{\boldsymbol{k}}}{2} + 1} \tag{3.5.39}$$

$$v^1_{\boldsymbol{k}s} = v^2_{\boldsymbol{k}s} = \frac{1}{2}\text{sign}\left(B^{11}_{\boldsymbol{k}} + B^{12}_{\boldsymbol{k}}\right)\sqrt{\frac{A^{11}_{\boldsymbol{k}} + A^{12}_{\boldsymbol{k}}}{2} - 1} \tag{3.5.40}$$

$$u^1_{\boldsymbol{k}a} = -u^2_{\boldsymbol{k}a} = \frac{1}{2}\sqrt{\frac{A^{11}_{\boldsymbol{k}} - A^{12}_{\boldsymbol{k}}}{2} + 1} \tag{3.5.41}$$

$$v^1_{\boldsymbol{k}a} = -v^2_{\boldsymbol{k}a} = \frac{1}{2}\text{sign}\left(B^{11}_{\boldsymbol{k}} - B^{12}_{\boldsymbol{k}}\right)\sqrt{\frac{A^{11}_{\boldsymbol{k}} - A^{12}_{\boldsymbol{k}}}{2} - 1} \tag{3.5.42}$$

3.5.5 First $\frac{1}{S}$ quantum correction

Here we treat the first $\frac{1}{S}$ corrections to the spin-wave solution. So far we only diagonalized the quadratic part of the spin-wave Hamiltonian allowing us to write it down as a sum of the non-interacting magnon quasiparticles energies. We will only consider the correction coming from magnon-magnon interaction of order $\frac{t^2}{U}S^0$ in eq. 3.5.14. Also we do not calculate the quantum corrections coming from the interlayer magnetic couplings. While they can in principle be calculated simply as shown below, they will bring very little contribution considering the small magnitude of the interlayer coupling in the bilayer material that will be considered. A rough estimate brings $J_\perp/J \sim 2\%$ as discussed on page 3.6.2. The quartic part of the spin-wave Hamiltonian is thus

$$\begin{aligned} H_{SW}^{(4)} =& \frac{1}{2}\sum_i \sum_{\boldsymbol{\tau}} \frac{4t_{\boldsymbol{\tau}}^2}{U}(2\epsilon_{\boldsymbol{\tau}} - 1) n_i n_{i+\boldsymbol{\tau}} \\ & - \frac{1}{4}\Big[\epsilon_{\boldsymbol{\tau}}\left(a_i^\dagger (n_i + n_{i+\boldsymbol{\tau}}) a_{i+\boldsymbol{\tau}} + a_{i+\boldsymbol{\tau}}^\dagger (n_i + n_{i+\boldsymbol{\tau}}) a_i\right) \\ & + \bar{\epsilon}_{\boldsymbol{\tau}}\left((n_i + n_{i+\boldsymbol{\tau}}) a_i a_{i+\boldsymbol{\tau}} + a_i^\dagger a_{i+\boldsymbol{\tau}}^\dagger (n_i + n_{i+\boldsymbol{\tau}})\right)\Big] \end{aligned} \tag{3.5.43}$$

which describes magnon-magnon interactions. The layer index has been dropped as we do not consider interlayer couplings. We will treat it through a Hartree Fock procedure. We start by defining the mean fields:

$$n = \langle a_i^\dagger a_i \rangle \tag{3.5.44}$$

$$\delta = \langle a_i a_i \rangle = \langle a_i^\dagger a_i^\dagger \rangle \tag{3.5.45}$$

$$t_{\boldsymbol{\tau}} = \langle a_i^\dagger a_{i+\boldsymbol{\tau}} \rangle = \langle a_{i+\boldsymbol{\tau}}^\dagger a_i \rangle \tag{3.5.46}$$

$$\Delta_{\boldsymbol{\tau}} = \langle a_i a_{i+\boldsymbol{\tau}} \rangle = \langle a_i^\dagger a_{i+\boldsymbol{\tau}}^\dagger \rangle. \tag{3.5.47}$$

Using those mean fields we can decouple the quartic term in eq. 3.5.43. We give as an example the mean field decoupling of the quartic term $n_i n_{i+\boldsymbol{\tau}}$:

$$\begin{aligned} \frac{1}{2}\sum_i \sum_{\boldsymbol{\tau}} n_i n_{i+\boldsymbol{\tau}} \simeq \sum_i \sum_{\boldsymbol{\tau}} & n(a_i^\dagger a_i + a_{i+\boldsymbol{\tau}}^\dagger a_{i+\boldsymbol{\tau}}) \\ & + t_{\boldsymbol{\tau}}(a_i^\dagger a_{i+\boldsymbol{\tau}} + a_{i+\boldsymbol{\tau}}^\dagger a_i) \\ & + \Delta_{\boldsymbol{\tau}}(a_i^\dagger a_{i+\boldsymbol{\tau}}^\dagger + a_i a_{i+\boldsymbol{\tau}}) \end{aligned} \tag{3.5.48}$$

and by inserting the Fourier transform of the boson operators a_i we obtain

$$\frac{1}{2}\sum_i \sum_{\boldsymbol{\tau}} n_i n_{i+\boldsymbol{\tau}} \simeq \sum_{\boldsymbol{\tau}} \sum_{\boldsymbol{k}} 2\left(n + t_{\boldsymbol{\tau}} \cos(\boldsymbol{k}\boldsymbol{\tau})\right) a_{\boldsymbol{k}}^\dagger a_{\boldsymbol{k}} + \Delta_{\boldsymbol{\tau}} \cos(\boldsymbol{k}\boldsymbol{\tau}) \left(a_{\boldsymbol{k}}^\dagger a_{-\boldsymbol{k}}^\dagger + a_{\boldsymbol{k}} a_{-\boldsymbol{k}}\right). \tag{3.5.49}$$

In principle this just defines a correction to the quadratic Hamiltonian so one could write down mean-field self-consistent equations and use some iterative procedure to find self-consistent mean fields. We don't go so far here and only evaluate the mean fields on the unperturbed

quadratic Hamiltonian. For the monolayer case we obtain:

$$n = \sum_{\boldsymbol{k}} v_{\boldsymbol{k}}^2 \tag{3.5.50}$$

$$\delta = \sum_{\boldsymbol{k}} u_{\boldsymbol{k}} v_{\boldsymbol{k}} \tag{3.5.51}$$

$$t_{\boldsymbol{\tau}} = \sum_{\boldsymbol{k}} \cos(\boldsymbol{k}\boldsymbol{\tau})\, v_{\boldsymbol{k}}^2 \tag{3.5.52}$$

$$\Delta_{\boldsymbol{\tau}} = \sum_{\boldsymbol{k}} \cos(\boldsymbol{k}\boldsymbol{\tau})\, u_{\boldsymbol{k}} v_{\boldsymbol{k}} \tag{3.5.53}$$

Where $u_{\boldsymbol{k}}$ and $v_{\boldsymbol{k}}$ are the Bogoliubov coefficients from the unperturbed Hamiltonian $H_{SW}^{(2)}$ eq. 3.5.26. For the bilayer case we have:

$$n = \sum_{\boldsymbol{k}} v_{\boldsymbol{k}s}^2 + v_{\boldsymbol{k}a}^2 \tag{3.5.54}$$

$$\delta = \sum_{\boldsymbol{k}} u_{\boldsymbol{k}a} v_{\boldsymbol{k}a} + u_{\boldsymbol{k}s} v_{\boldsymbol{k}s} \tag{3.5.55}$$

$$t_{\boldsymbol{\tau}} = \sum_{\boldsymbol{k}} \cos(\boldsymbol{k}\boldsymbol{\tau})\, i\left(v_{\boldsymbol{k}a}^2 + v_{\boldsymbol{k}s}^2\right) \tag{3.5.56}$$

$$\Delta_{\boldsymbol{\tau}} = \sum_{\boldsymbol{k}} \cos(\boldsymbol{k}\boldsymbol{\tau})\, (u_{\boldsymbol{k}a} v_{\boldsymbol{k}a} + u_{\boldsymbol{k}s} v_{\boldsymbol{k}s}) \tag{3.5.57}$$

where $u_{\boldsymbol{k}b} = u_{\boldsymbol{k}b}^1$ and $v_{\boldsymbol{k}b} = v_{\boldsymbol{k}b}^1$ to shorten notations. The mean fields then define corrections to the quadratic Hamiltonian which we give here:

$$\begin{aligned} dA_{\boldsymbol{k}} = &\sum_{\boldsymbol{\tau}} J_{\boldsymbol{\tau}} \epsilon_{\boldsymbol{\tau}} (t_{\boldsymbol{\tau}} - n)\cos(\boldsymbol{k}\boldsymbol{\tau}) \\ &+ \bar{\epsilon}_{\boldsymbol{\tau}} \left[(\Delta_{\boldsymbol{\tau}} - n)\left(\frac{\delta}{2} - t_{\boldsymbol{\tau}}\right)\cos(\boldsymbol{k}\boldsymbol{\tau}) \right] \end{aligned} \tag{3.5.58}$$

$$\begin{aligned} dB_{\boldsymbol{k}} = &\frac{1}{2}\sum_{\boldsymbol{\tau}} J_{\boldsymbol{\tau}} \epsilon_{\boldsymbol{\tau}} \left(-\frac{\Delta_{\boldsymbol{\tau}}}{2} + \left(\Delta_{\boldsymbol{\tau}} - \frac{\delta}{2}\right)\cos(\boldsymbol{k}\boldsymbol{\tau}) \right) \\ &+ \bar{\epsilon}_{\boldsymbol{\tau}} \left((n - \Delta_{\boldsymbol{\tau}})\cos(\boldsymbol{k}\boldsymbol{\tau}) + \frac{t_{\boldsymbol{\tau}}}{2} \right). \end{aligned} \tag{3.5.59}$$

Inserting these corrections to the eigen-energies finally gives the first order quantum corrections. For instance for the single layer case:

$$\tilde{\omega}_{\boldsymbol{k}} = \sqrt{(A_{\boldsymbol{k}}^2 + dA_{\boldsymbol{k}}) - (B_{\boldsymbol{k}} + dB_{\boldsymbol{k}})^2} \simeq \omega_{\boldsymbol{k}} \underbrace{\left(1 + \frac{A_{\boldsymbol{k}} dA_{\boldsymbol{k}} - B_{\boldsymbol{k}} dB_{\boldsymbol{k}}}{\omega_{\boldsymbol{k}}^2}\right)}_{Z_c} \tag{3.5.60}$$

where $\omega_{\boldsymbol{k}}$ is the bare dispersion obtained from eq. 3.5.26. For the bilayer case we obtain:

$$\tilde{\omega}_{\boldsymbol{k}s} \simeq \omega_{\boldsymbol{k}s} \overbrace{\left(1 + \frac{\left(A^{11}_{\boldsymbol{k}} + A^{12}_{\boldsymbol{k}}\right) dA_{\boldsymbol{k}} - \left(B^{11}_{\boldsymbol{k}} + B^{12}_{\boldsymbol{k}}\right) dB_{\boldsymbol{k}}}{\omega^2_{\boldsymbol{k}s}}\right)}^{Z^s_c} \tag{3.5.61}$$

$$\tilde{\omega}_{\boldsymbol{k}a} \simeq \omega_{\boldsymbol{k}a} \underbrace{\left(1 + \frac{\left(A^{11}_{\boldsymbol{k}} - A^{12}_{\boldsymbol{k}}\right) dA_{\boldsymbol{k}} - \left(B^{11}_{\boldsymbol{k}} - B^{12}_{\boldsymbol{k}}\right) dB_{\boldsymbol{k}}}{\omega^2_{\boldsymbol{k}a}}\right)}_{Z^a_c}. \tag{3.5.62}$$

For the single layer square lattice nearest neighbour Heisenberg model, it turns out this quantum renormalization is uniform ($\boldsymbol{k}$-independent) with a value of $Z_c = 1.15$.

3.5.6 Extracted physical quantities

We review here a few physical quantities that can be extracted from the above calculation and confronted with experimental result. To exemplify, we show what these quantities are in the case of the simple square lattice Heisenberg model with nearest neighbour interaction J only. The first obvious quantity is the dispersion relation which will relate the momentum of a spin-wave with its energy. Applying the formalism developed above, we obtain

$$\omega_{\boldsymbol{k}} = 2J\sqrt{1 - \frac{1}{4}\left(\cos(k_x) + \cos(k_y)\right)^2}. \tag{3.5.63}$$

This dispersion has a maximum energy of $2J$ along the magnetic zone boundary $\boldsymbol{k} = (\pi/2 + z, \pi/2 - z)$ $z \in [0, \pi/2]$ which is further uniformly renormalized by the first $\frac{1}{S}$ quantum corrections by approximately $Z_c = 1.15$. Gapless modes appear at $\boldsymbol{k} = (0,0)$ and $\boldsymbol{k} = (\pi,\pi)$ due to the spontaneously broken spin rotational symmetry. The dispersion can be measured through experiments such as inelastic neutron scattering or resonant x-ray scattering. In both cases for each $\boldsymbol{k}$, the mode in the dispersion will appear through a scattering event with some probability amplitude which experimentally corresponds to a measured signal intensity. In the case of INS, the signal is a functional of the dynamical spin structure factor which, at zero temperature, is:

$$S(\boldsymbol{q}, \omega) = \sum_{\lambda} \langle 0 | S^-_{\boldsymbol{q}} | \lambda \rangle \langle \lambda | S^+_{\boldsymbol{q}} | 0 \rangle \delta(\omega + E_0 - E_\lambda) \tag{3.5.64}$$

where $|0\rangle$ is the ground state and $|\lambda\rangle$ are all the intermediate excited states. In our case $|0\rangle$ is the vacuum for the spin-waves quasiparticle operator $b_{\boldsymbol{k}}$ and, to a first approximation, the $|\lambda\rangle = b^\dagger_{\boldsymbol{k}}|0\rangle$ are excited states where a single spin-wave has been created by the spin raising operator.

An important remark is that this spin operator is written in the physical basis, not in the effective spin basis! As seen previously in section 3.4.3, this implies that in the effective spin

basis this operator is renormalized with a $\boldsymbol{q}$-dependent weight eq. 3.4.64:

$$\tilde{S}^{\alpha(4)}_{\boldsymbol{k}} = S^{\alpha}_{\boldsymbol{q}}\left[1-\sum_{\boldsymbol{\tau}}\left(\frac{t_{\boldsymbol{\tau}}}{U}\right)^2\left(1-e^{i\boldsymbol{q}\cdot\boldsymbol{\tau}}\right)\right]+\mathcal{O}\left(\frac{t^4}{U^4}\right). \tag{3.5.65}$$

In the above formula, the operators $S^{\alpha}_{\boldsymbol{q}}$ now are the effective ones from which we derived the spin-wave theory. We can thus rewrite those in terms of the spin-wave operators $b_{\boldsymbol{k}}$:

$$S^{+}_{\boldsymbol{q}} = \frac{1}{2}\left((u_{\boldsymbol{k}}+v_{\boldsymbol{k}})(b_{\boldsymbol{k}}-b^{\dagger}_{-\boldsymbol{k}})+(u_{\boldsymbol{k}+\boldsymbol{Q}}-v_{\boldsymbol{k}+\boldsymbol{Q}})(b_{\boldsymbol{k}+\boldsymbol{Q}}+b^{\dagger}_{-\boldsymbol{k}-\boldsymbol{Q}})\right). \tag{3.5.66}$$

Putting everything together one gets the dynamical structure factor:

$$S(\boldsymbol{q},\omega) = \frac{1}{4}(u_{\boldsymbol{q}}+v_{\boldsymbol{q}})^2\left[1-4\frac{t^2}{U^2}\left(1-\frac{1}{2}\left(\cos(q_x)+\cos(q_y)\right)\right)\right]^2\delta(\omega-\omega_{\boldsymbol{q}}). \tag{3.5.67}$$

Physically, the renormalization is due to the charge fluctuations of the Hubbard model which we integrate perturbatively in our effective theory. It is thus not surprising that a measured magnetic signal will be weakened by these fluctuations as empty and doubly occupied sites have zero spin and thus cannot couple to a magnetic probe such as INS. An important aspect linked to the discussion in the thesis chapter 2 is that this renormalization is constant along the magnetic zone boundary. We show on fig. 3.11 the dispersion and intensity of the spin-waves along the high-symetry directions of the Brillouin zone. In the case of a bilayer square lattice

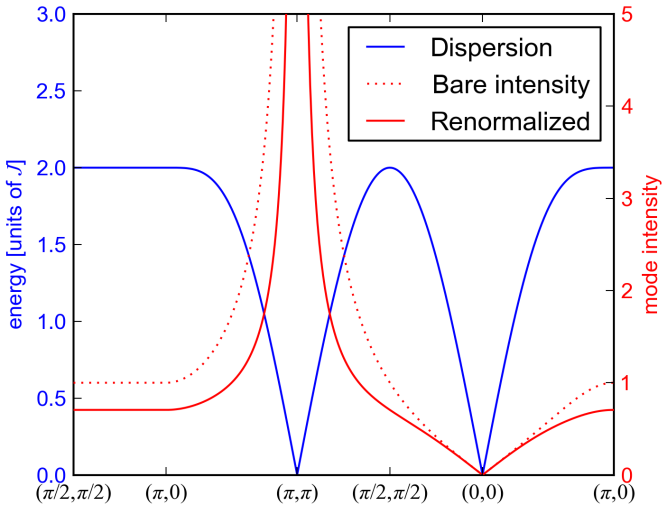

Figure 3.11 – Example of the spin-wave dispersion and intensity for the square lattice Heisenberg antiferromagnet. Y-axis on the left is for energy and y-axis on the right for intensity. Intensity comes as the familiar spin-wave result $I_{\boldsymbol{q}} \sim (u_{\boldsymbol{q}}+v_{\boldsymbol{q}})^2$ (dotted line) and the physically more relevent one where the intensity is renormalized by the Hubbard model charge fluctuations (solid line) as given in eq. 3.5.67. In this example we have used a too large ratio $t/U = 1/5$ so that the renormalization is graphically obvious. A more reasonable ratio for cuprates would be $t/U \sim 1/10$, implying a maximum reduction at $\boldsymbol{q} = (\pi,\pi)$ of 15% of the intensity.

Heisenberg model, the same calculation leads to:

$$S(\boldsymbol{q},\omega) = \left(u_{\boldsymbol{q}s} + v_{\boldsymbol{q}s}\right)^2 \cos^2(\boldsymbol{q}\mathbf{b})\delta(\omega - \omega_{\boldsymbol{q}s}) + \left(u_{\boldsymbol{q}a} + v_{\boldsymbol{q}a}\right)^2 \sin^2(\boldsymbol{q}\mathbf{b})\delta(\omega - \omega_{\boldsymbol{q}a}) \tag{3.5.68}$$

where now for single $\boldsymbol{q}$ momentum one finds the symmetric and anti-symmetric modes, $\mathbf{b}$ is the translation vector between the two layers. For simplicity we dropped here the charge fluctuations renormalization as the effect is small and essentially identical to the monolayer case. The two modes respective intensity is modulated with the perpendicular component of $\boldsymbol{q}$ as $\boldsymbol{q}\mathbf{b} \sim q_z$. Each mode is either gapped at $(0,0)$ or (π,π) and the two are perfectly degenerate along the magnetic zone boundary. By interchanging the modes definition if inside or outside of the magnetic Brillouin zone, we would obtain the more familiar acoustic (gapless at $(0,0)$ and (π,π)) and optical (gapped) modes. We give a representation of the modes with equal out of plane and in-plane couplings $J_\perp = J$ on fig. 3.12. Another important quantity is the

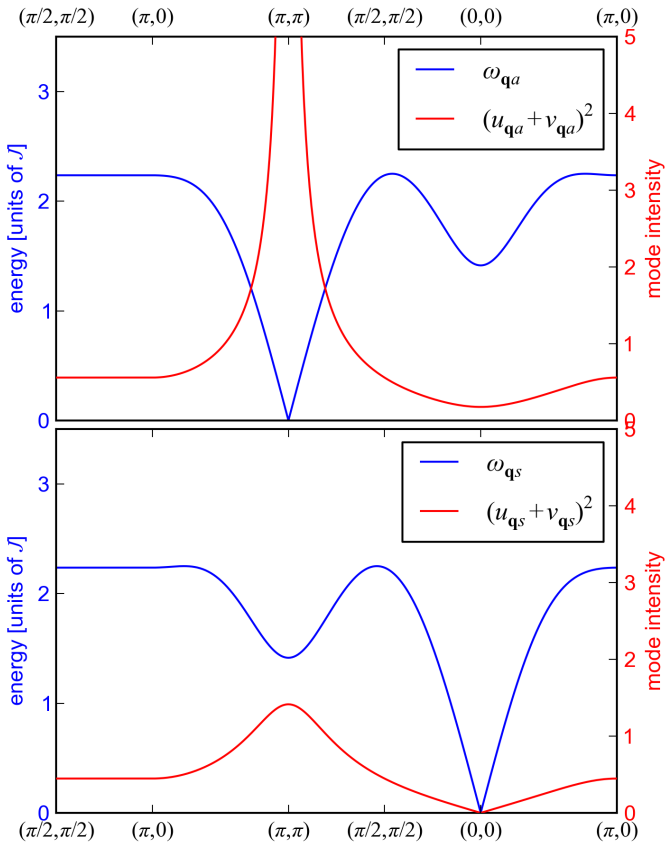

Figure 3.12 – Example of the spin-wave dispersion and intensity for the bilayer square lattice Heisenberg antiferromagnet with equal out of plane and in-plane coupling $J_\perp = J$. Y-axis on the right is for energy and y-axis on the left for intensity.

zero-temperature staggered magnetization:

$$\bar{S}^z_{\boldsymbol{Q}} = \sum_i (-1)^i \langle 0|\bar{S}^z_i|0\rangle. \tag{3.5.69}$$

Again we must be careful to identify that in the above equation the spin operators are the physical ones defined in the Hubbard basis. In terms of the effective spin operators we get:

$$\bar{S}^z_{\boldsymbol{Q}} = S^z_{\boldsymbol{Q}}\left(1 - 8\frac{t^2}{U^2}\right) \tag{3.5.70}$$

Formulating this in term of spin-waves operators and calculating the zero-temperature average gives

$$\langle 0|\bar{S}^z_{\boldsymbol{Q}}|0\rangle = \left(S - \frac{1}{N}\sum_{\boldsymbol{k}} v^2_{\boldsymbol{k}}\right)\left(1 - 8\frac{t^2}{U^2}\right). \tag{3.5.71}$$

Considering the spin-waves fluctuations only, the staggered magnetization is reduced by 40% for spin-$\frac{1}{2}$. For a ratio of $t/U = 1/10$, the charge fluctuations would further reduce it by 8%. Finally, it is interesting to take a closer look at these charge fluctuations directly which could be quantified by the average number of double occupancies. Using the Hellmann-Feynman theorem [Feynman, 1939], we would have for the Hubbard model:

$$\langle \mathrm{GS}|n_{i\uparrow}n_{i\downarrow}|\mathrm{GS}\rangle = \frac{d}{dU}\langle \mathrm{GS}|\mathscr{H}_{\mathrm{Hub}}|\mathrm{GS}\rangle \tag{3.5.72}$$

It means that in our effective theory, taking the derivative of the ground state energy would give an approximate of $\langle n_{i\uparrow}n_{i\downarrow}\rangle$. The ground state energy has many contributions coming from the effective low-energy derivation and the spin-waves approximation. But in the case of the Heisenberg Hamiltonian with $J = 4t^2/U$, all these contributions are of order t^2/U. It follows that the density of double occupancies will be proportional to t^2/U^2 which is consistently the same dependence we found for the charge fluctuation renormalization factor.

3.6 Comparison to experimental data

In this section we will confront the various quantities extracted in section 3.5.6 with experimental results when available. We will focus on the three compounds LCO,SCOC and BSYCO, the first two being monolayers cuprates and the third a bilayer cuprate. We first review the quantities in section 3.5.6.

– Magnon dispersion: $\omega_{\boldsymbol{k}}$ is one of the most accessible properties for spectroscopic probes. In fact the data quality is such that a systematic fit with the theory will results in strong constraints on the model parameters. The other quantities can thus in a later step be evaluated and compared to experiments when possible.
– Magnon intensity: For INS, the magnon intensity is very well known experimentally and theoretically. Below we will therefore give our predicted magnon intensity and compare it to

available INS data which we only have for La_2CuO_4. For the other compounds, we do have a RIXS experimental magnon intensity. The issue is then that it is much more complicated to obtain a theoretical RIXS cross-section prediction [Nomura and Igarashi, 2005; Forte et al., 2008; Ament et al., 2009; Haverkort, 2010] and we did not pursue that direction.

– Staggered magnetization: In a neutron diffraction experiment, magnetic diffraction peaks will show up with an intensity which scale quadratic with the local magnetic ordered moments. This could in principle provide an experimental estimate of the staggered magnetization with the magnetic diffraction peak intensity $I(\boldsymbol{Q})$ taken as:

$$I(\boldsymbol{Q}) \sim \langle S^z_{\boldsymbol{Q}} \rangle^2. \tag{3.6.1}$$

However two difficulties arise. First the antiferromagnetic neutron diffraction peak really measures

$$I(\boldsymbol{Q}) \propto \langle S^z_{-\boldsymbol{Q}} S^z_{\boldsymbol{Q}} \rangle \tag{3.6.2}$$

which in the spin-wave formulation is

$$\langle S^z_{-\boldsymbol{Q}} S^z_{\boldsymbol{Q}} \rangle = S^2 - 2S\langle a^\dagger_i a_i \rangle + \frac{1}{N^2} \sum_{ij} \langle a^\dagger_i a_i a^\dagger_j a_j \rangle. \tag{3.6.3}$$

It follows then that eq. 3.6.1 corresponds to the naive decoupling $\langle a^\dagger_i a_i a^\dagger_j a_j \rangle \sim \langle a^\dagger_i a_i \rangle \langle a^\dagger_j a_j \rangle$ which overlooks two-magnon contributions such as $\langle 0 | b_{-\boldsymbol{k}} b_{\boldsymbol{k}} b^\dagger_{\boldsymbol{k}'} b^\dagger_{-\boldsymbol{k}'} | 0 \rangle$. Experimentally a probably more important difficulty is that the proportionality constant in eq. 3.6.1 is not trivial to determine accurately as it will depend on many details of the experimental setup. A possibility would be to apply a magnetic field large enough to reach a saturated ferromagnetic state where quantum and thermal fluctuations could be neglected. This has been done for instance to establish an experimental absolute scale for the 1D spin chain material $CuSO_4 \cdot 5D_2O$ [Mourigal et al., 2013] using a reasonable field of 5T. However this is in practice impossible to reproduce in the 2D cuprate materials as the very large nearest-neighbour interaction $J \sim 140meV$ is three orders of magnitude stronger than the one in $CuSO_4 \cdot 5D_2O$ and would require an enormous magnetic field of thousands of Tesla. Other possibilities are to carefully calibrate the instrument on some known material or compare the magnetic Bragg peaks to the nuclear peak. Furthermore it will be also important to include the charge fluctuations as in eq. 3.5.71.

– The charge fluctuations: The charge fluctuations $\langle n_{i\uparrow} n_{i\downarrow} \rangle$ can in principle be measured using the neutron scattering sum rule:

$$\sum_{\alpha \in \{x,y,z\}} \int d\boldsymbol{q} d\omega S^{\alpha\alpha}(\boldsymbol{q}, \omega) = NS(S+1), \tag{3.6.4}$$

which is an exact result. But the charge fluctuation will reduce this sum rule as some fraction of the sites are either doubly occupied or empty. Measuring the integrated cross-section thus allows to determine the size of the charge fluctuations as those will reduce the effective total

spin. The charge fluctuations have been calculated to be about $\langle n_{i\uparrow} n_{j\downarrow} \rangle \simeq 5\%$[Lorenzana et al., 2005] in agreement with measurements [Walters et al., 2009].

As enlightened by ARPES measurements analysis [Tohyama and Maekawa, 2000], the single hole dynamics must be described using a $t-t'-t''-J$ model. While this model originate from the strong coupling expansion of the d-p model, it can also be related back to a more simple phenomenological $t-t'-t''-U$ Hubbard model whose strong coupling expansion would be equivalent (see section 3.3.3). In order to be able to relate back to the ARPES electronic spectra from the measured magnetic spectra, we choose to consider the $\{t, t', t''\}$ hopping amplitude as given on fig. 3.13 which in turn defines the set of exchange plaquettes leading to the effective spin Hamiltonian eq. 3.4.58. Some examples of plaquettes are shown on fig. 3.13. In the case of the bilayer system, we also add a perpendicular hopping $t_\perp$ to the hopping ensemble. These rather extended hopping ensembles generate a large number of exchange plaquettes which are determined along with their spin-wave contribution in a systematic way using a computer implementation of the problem. Indeed for the $\{t, t', t''\}$ ensemblse, there are 126 exchange plaquettes to consider and 145 for the $\{t, t', t'', t_\perp\}$ ensemble! Using the formalism developed above, we generate an analytical expression of the magnon dispersion with first order $1/S$ quantum corrections. This analytical expression is parametrized by the hopping parameters and the Coulomb repulsion and is translated in the C programming language in order to provide a fast evaluation mechanism for given wave-vector $\boldsymbol{q}$ and model parameters $\{t, t', t'', (t_\perp), U\}$.

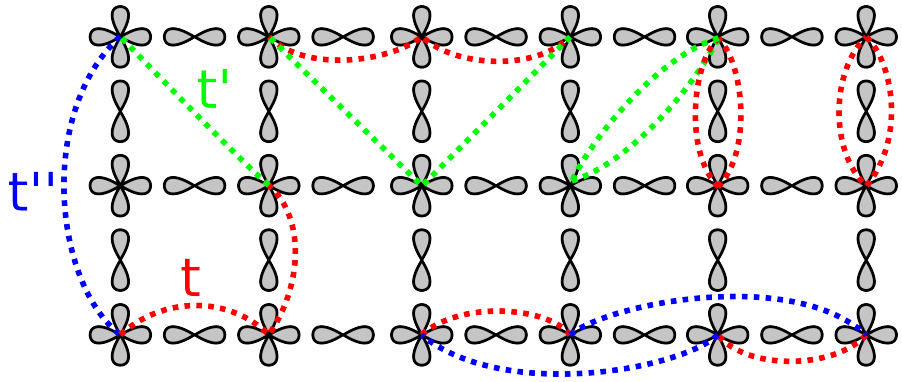

Figure 3.13 – The CuO_2 plane with the t, t' and t'' hopping amplitudes and a few examples of the plaquettes exchange loops that enters the effective spin Hamiltonian eq. 3.4.58.

3.6.1 Experimental data

We give a quick overview of the experimental data that will be used to fit our theory.

La_2CuO_4

Measured by Inelastic Neutron Scattering [Coldea et al., 2001a], this material is famous for providing a strong support for the cyclic ring exchange relevance for the measured magnetic spectrum. Indeed the data evidenced a large magnetic zone boundary dispersion of about 20meV which could be fitted to the effective spin Hamiltonian eq. 3.4.58 where only the nearest-neighbour t is considered. A more recent measurement [Headings et al., 2010] (reproduced on fig. 3.14 bottom panel) also highlighted an anomalous intensity reduction at $\boldsymbol{q} = (\pi, 0)$ compared to $\boldsymbol{q} = (\pi/2, \pi/2)$.

$Sr_2CuO_2Cl_2$

In collaboration with Prof. Grioni's group (Laboratory of Photoelectron Spectroscopy, EPFL) we measured the RIXS magnetic spectrum of this material and extracted the magnon dispersion [Guarise et al., 2010; Guarise, 2012]. The experiment was carried out at the Swiss Light Source ADRESS beamline using the RIXS instrument SAXES. As RIXS will not only pick up single magnon but also two-magnons and in principle further order multi-magnon excitations, the dispersion relation is extracted through an analysis of the spectral lineshape (details available in Marco Guarise's PhD thesis [Guarise, 2012]). We reproduce here the extracted magnon dispersion on fig. 3.14 middle panel. Along the magnetic zone-boundary, the dispersion is even more pronounced than in La_2CuO_4 (LCO) with a 70meV between $\boldsymbol{q} = (\pi, 0)$ and $\boldsymbol{q} = (\pi/2, \pi/2)$.

$Bi_2Sr_2YCu_2O_8$

Lastly we also measured in collaboration with Prof. Grioni's group this bilayer cuprate compound on the SAXES spectrometer. The same lineshape analysis provides the magnon dispersion. As $Bi_2Sr_2YCu_2O_8$ (BSYCO) has two coupled CuO planes, the spectrum should show two magnon modes: an acoustic mode and an optical one as discussed in section 3.5.6 and plotted on fig. 3.12. However the two modes will clearly separate with a finite intensity only at $\boldsymbol{q} = (\pi, \pi)$ which we cannot measure due to the momentum transfer restrictions of the soft x-ray radiation needed for copper L_3 edge RIXS. Elsewhere the two modes lie very close to each others and the SAXES RIXS energy resolution of 130meV could not resolve them separately. We show on fig. 3.14 top panel the obtained dispersion which we can experimentally consider as a nearly doubly degenerate magnon mode.

3.6.2 Fitting procedure

The spin-wave expansion of the effective spin Hamiltonian eq. 3.4.58 with the first $1/S$ quantum corrections provides the magnon dispersion

$$\omega(\boldsymbol{q}) = Z_c(\boldsymbol{q})\omega_0(\boldsymbol{q}) \tag{3.6.5}$$

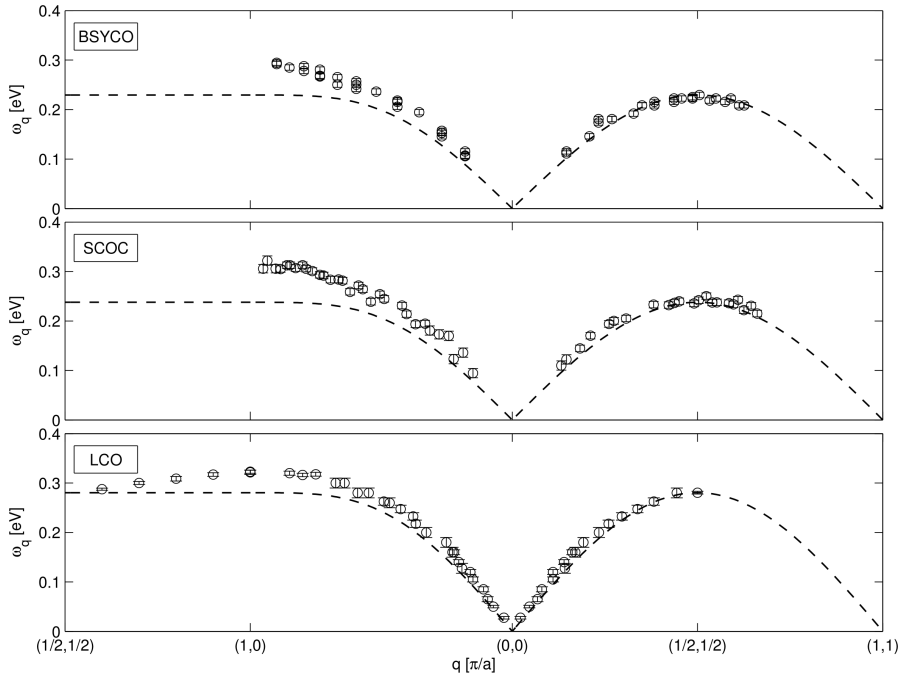

Figure 3.14 – Experimentally measured magnon dispersion relations. Top: BSYCO measured by RIXS[Dalla Piazza et al., 2012], middle: SCOC measured by RIXS[Guarise et al., 2010], bottom: LCO measured by INS[Headings et al., 2010] shifted by (π,π). Dashed lines are the magnon dispersion of the simple Heisenberg model with J adjusted such that the $\boldsymbol{q} = (\pi/2,\pi/2)$ energy matches experiments.

parametrized by the Hubbard model parameters $\{t, t', t'', (t_\perp), U\}$. It can simply be fitted using a least-square minimization algorithm. However the quantum renormalization $Z_c(\boldsymbol{q})$ contains the integrals 3.5.50-3.5.53 which are computationally demanding. To reduce the computational expense of the quantum renormalization, we apply a two-step fitting procedure:

1. Set $Z_c(\boldsymbol{q}) = 1.156$, the first order $\boldsymbol{q}$-independant $1/S$ quantum correction.
2. Fit the experimental data against the $\{t/U, t'/t, t''/t, (t_\perp), U\}$ parameter set using the dispersion formula eq. 3.6.5.
3. With the obtained parameter set $\{t/U, t'/t, t''/t, (t_\perp), U\}$, calculate the quantum renormalization by numerical evaluation of the integrals 3.5.50-3.5.53.
4. Compare the newly obtained $Z_c(\boldsymbol{q})$ to the old one. If the difference is smaller than a given threshold, the fit is said to be converged. If not go back to 2 using the new $Z_c(\boldsymbol{q})$.

Looking at the various dispersions, it can be seen that the fit is under-constraint. One can indeed only identify three independent features in the measured magnon dispersions: The energy at $\boldsymbol{q} = (\pi, 0)$, the energy at $\boldsymbol{q} = (\pi/2, \pi/2)$ and the linear branch slopes at $\boldsymbol{q} = (0,0)$ or $\boldsymbol{q} = (\pi, \pi)$. In the bilayer case, a fourth constraint would be the bilayer splitting at $\boldsymbol{q} = (0,0)$ or $\boldsymbol{q} = (\pi, \pi)$ if available. For BSYCO, as the measured RIXS spectrum cannot resolve the bilayer splitting, we use the value $t_\perp = 54$meV as determined by ARPES[Chuang et al., 2004]. Using this value, it is usefull to give a rough estimate of the respective magnitude of the nearest neighbour coupling and the intralayer one. Taking $J \sim 0.14$eV and $U \sim 3.5$eV from the ARPES estimate for SCOC [Tohyama and Maekawa, 2000] and assuming $J_\perp = 4t_\perp^2/U$ gives $J_\perp/J \sim 2\%$. It is thus expected that the interlayer coupling will bring little contribution to the spin-wave dispersion and very little bilayer splitting.
Counting the number of independent model parameters we see that in the monolayers and bilayer there are four and five respectively while the independent features are only three and four. It follows that one should expect the solutions space to be one-dimensional in parameter space. We choose to set up the fitting procedure such that this line of solutions will be a function of the Coulomb repulsion U. To do so, we first reformulate the model parameters as $\{t/U, t'/t, t''/t, U\}$. We then define a plane of $(t''/t, U)$ pairs and, for each one of those, fit the two other parameters t/U and t'/t. The fit result might be dependent of the starting guess for the fitted parameters $(t/U)_0$ and $(t'/t)_0$ and even completely fail if those are not reasonable. To avoid this issue we choose $(t/U)_0$ such that it reproduce the correct energy scale for the $\boldsymbol{q} = (\pi/2, \pi/2)$ magnon energy that is it must satisfy

$$\omega(\pi/2, \pi/2) \simeq 8\left(\frac{t}{U}\right)^2 U. \tag{3.6.6}$$

The starting parameter $(t'/t)_0$ is considered as a correction and is chosen small. However we found than its sign with respect to t'' is important and thus performed the fit for both $t't'' > 0$ and $t't'' < 0$, keeping the best solution. We then obtain $\chi^2(t''/t, U)$ which quantifies the quality of the fit for each $(t''/t, U)$ pairs. We will show that inspecting the function $\chi^2(t''/t, U)$ will allow to determine the solutions line as a function of U.

3.6.3 Fitting results

For brevity, we show below only the fitting results for SCOC. The BSYCO and LCO fitting results can be found in appendices B.4 and B.5. Performing the fitting procedure, we obtain the following quantities as a function of t''/t and U:
- $\chi^2(t''/t, U)$ quantifying the fit quality.
- $\frac{t}{U}(t''/t, U)$ and
- $\frac{t'}{t}(t''/t, U)$ the fitted parameters.
- $\frac{S-\langle a^\dagger a\rangle}{S}(t''/t, U)$ the reduced staggered magnetization,
- $\langle n_{i\uparrow} n_{i\downarrow}\rangle(t''/t, U)$ the double occupation density,
- $\overline{Z}_c(t''/t, U) = \frac{1}{\Omega_{\mathrm{BZ}}}\int d\boldsymbol{q} Z_c(\boldsymbol{q}, t''/t, U)$ the average first $1/S$ quantum correction and
- $\sigma^2_{Z_c} = \frac{1}{\Omega_{\mathrm{BZ}}}\int d\boldsymbol{q}(Z_c(\boldsymbol{q}, t''/t, U) - \overline{Z}_c(t''/t, U))^2$ its variance on the Brillouin zone.

We plot the fit quality $\chi^2(t''/t, U)$ on fig. 3.15. There is an obvious mirror symmetry between the $t''/t > 0$ and the $t''/t < 0$. It is easily explained as follow: In the magnon dispersion the magnetic exchange energies are either of the form t_i^2/U or $t_1 t_2 t_3 t_4/U^3$ where the electronic exchanges t_i form a closed loop. In the first case the sign of t_i is obviously irrelevant for the magnon energy. In the second case we note that t causes an electronic exchange between the $\uparrow$ and the $\downarrow$ sublattice while t' and t'' associate exchange stays on the same sublattice. Consequently, if t is present in a given term, it must be of a even power as one needs an even number of nearest neighbour hoppings to come back on the starting point sublattice. The sign of t is thus arbitrary explaining fig. 3.15 symmetry. We point out however that the relative signs of t' and t'' are not arbitrary because of terms proportional to $t^2 t' t''/U^3$. For some choices of $(t''/t, U)$ pairs, the fit will completely fail either because varying t/U and t'/t cannot bring a good magnon dispersion or even because for such parameters the spin-wave approach simply fails. This is the case when t'/t and t''/t are so large that the frustration induced by the magnetic couplings destroys the long-range Néel order invalidating the fundamental assumption of the spin-wave approach. These areas a marked on fig. 3.15 in dark red. Elsewhere on the $(t''/t, U)$ plane, a reasonable fit can be obtained. One clearly sees on fig. 3.15 two distinct valleys of good χ^2 solutions. Discarding the mirrored solutions, for a given U one can find two best fit solutions defining two $(t''/t, U)$ best fit lines shown by the white markers on fig. 3.15. The value of χ^2 along these best fit lines strongly constrains $U > 2$eV as seen on fig. 3.16 top panel. Looking at the value of the fitted parameters t'/t and t/U along these best fit lines, we see that the inner line solution corresponds to the $t't'' < 0$ solution while the outer line corresponds to the $t't'' > 0$ solution. We show the evolution of the fitted parameter solutions as a function of U on fig. 3.16. For both $t't'' < 0$ and $t't'' > 0$ solutions, the ratio t/U decreases monotonously from $t/U \sim 0.18$ to $t/U \sim 0.1$ for greater U's while the other parameter amplitudes t'/t and t''/t increase. For each choice of U in the range allowed by fig. 3.16 top panel, a magnon dispersion can be drawn. We plot several of the obtained dispersions on fig. 3.17 along with the original experimental data. Compared to the spin-wave solution of the simple Heisenberg model with J adjusted such that $\omega(\pi/2, \pi/2) = 2J$ (dashed grey line on fig. 3.17), our solution obviously better matches the $\omega(\pi, 0)$ energy as well as the magnon branches slope at $\boldsymbol{q} = (0, 0)$ or $\boldsymbol{q} = (\pi, \pi)$ which should not come as a surprise given the large number of fitting parameters.

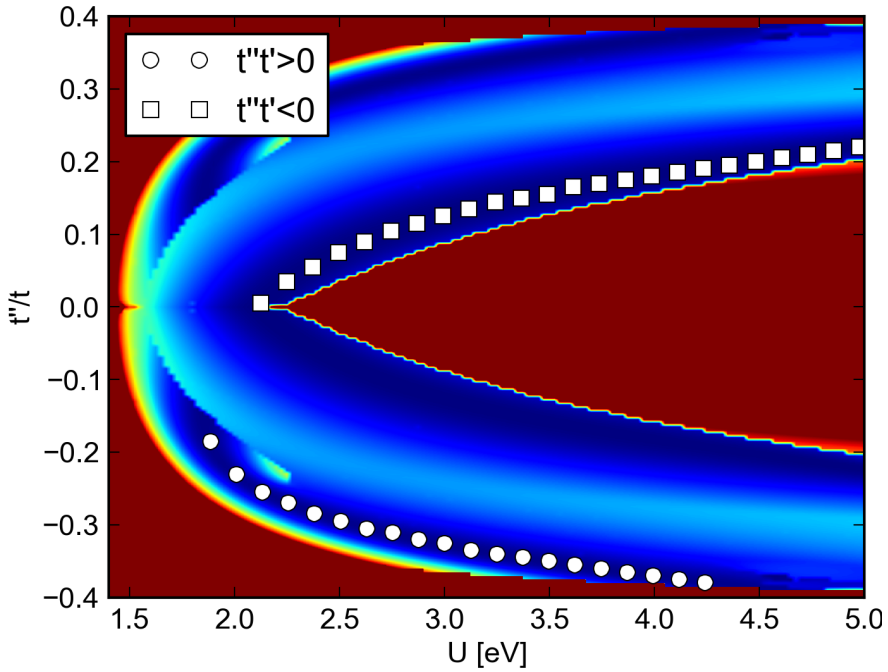

Figure 3.15 – Color map of the fit quality as a function of U and t''/t. In the outer dark red regions the parameters are such that the spin-wave approach fails indicating the breakdown of the long-ranged Néel order hypothesis. In the central area of the displayed $(t''/t, U)$ plane, the spin-wave approach does bring a meaningful solution which results in a good fit quality. In particular, two distinct valleys of best fit solutions can be followed as a function of U. Inspecting the resulting $(t/U, t'/t)$ fitted parameters, we see the inner solution corresponds to $t't'' < 0$ and the outer one to $(t't'' > 0)$.

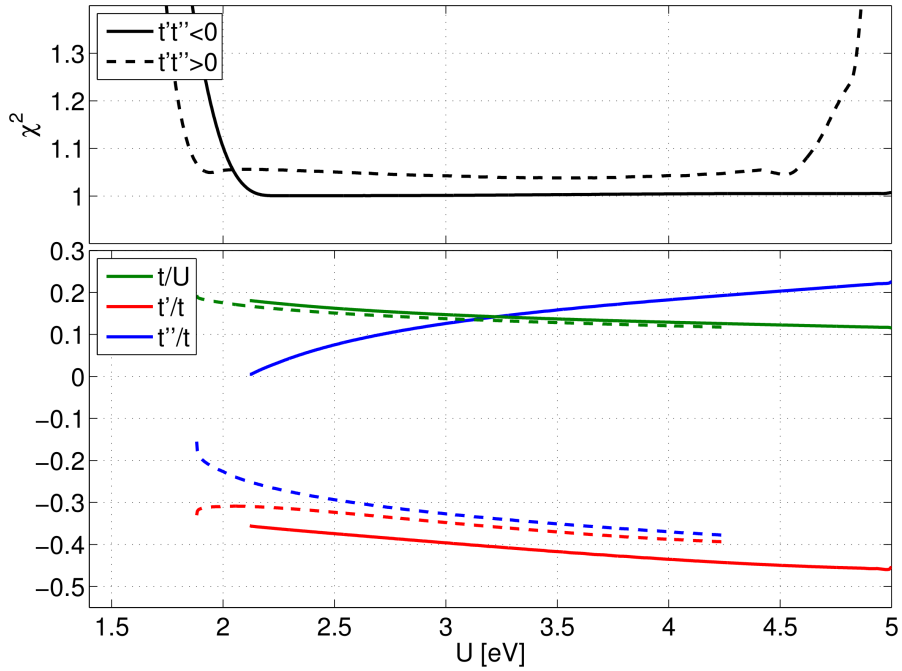

Figure 3.16 – Fitted parameters for the best fit lines defined on fig. 3.15. Top panel shows χ^2 along the inner (solid line) $t't'' < 0$ best fit line and the outer (dashed line) $t't'' > 0$ one. On the bottom panel are show the corresponding fitted parameters $(t''/t, t'/t, t/U)$ as a function of U along the best fit lines, solid line for $t't'' < 0$ and dashed for $t't'' > 0$.

To better view the details of the fit we subtract this simple Heisenberg spin-wave solution from the experimental data and to the fitted dispersion. We obtain fig. 3.17 bottom panel where we also include the fit to a spin-wave solution to the strong coupling limit of the nearest neighbour hopping $t-U$ Hubbard model (eq. 3.4.58 considering only t), the dashed red line. This fit to the $t-U$ Hubbard model corresponds to what was done in Coldea et al. [2001a]. We see that, while it adequately matches the two magnon energies at $\boldsymbol{q} = (\pi, 0)$ and $\boldsymbol{q} = (\pi/, \pi/2)$, it fails to fit the steeper slope at $\boldsymbol{q} = (0,0)$ and $\boldsymbol{q} = (\pi, \pi)$. We can further show the value of the staggered magnetization, the double occupation density and the strength of the first $1/S$ quantum correction along the best fit lines defined in fig. 3.15. We show the results again only for SCOC on fig. 3.18 for the $t't'' < 0$ solution. As seen on fig. 3.16, increasing U's causes the t' and t'' amplitudes to grow in order to still obtain a fit to the experimental data. The induced additional couplings will bring magnetic frustration causing the Néel order to weaken until a point where it becomes zero. At that point the spin-wave theory is not self-consistent anymore. While for SCOC a good fit could be obtained using values of U as large as 5eV, we see on fig. 3.18 top panel that above 4.5eV the staggered magnetization vanishes putting an upper boundary to the allowed range of U. While an experimental determination of the staggered magnetization is a difficult task, some estimate have been provided for SCOC with $S^z(\pi,\pi) = \frac{0.34 \pm 0.04}{g\mu_B}$ [Vaknin et al., 1990] which we added on fig. 3.18 top panel assuming $g = 2$. With the uncertainty of the measurement, we can draw a rough determination of $U \sim 2.8 \pm 0.3$eV which must not be taken too seriously due to the important experimental difficulty of providing such measurement on

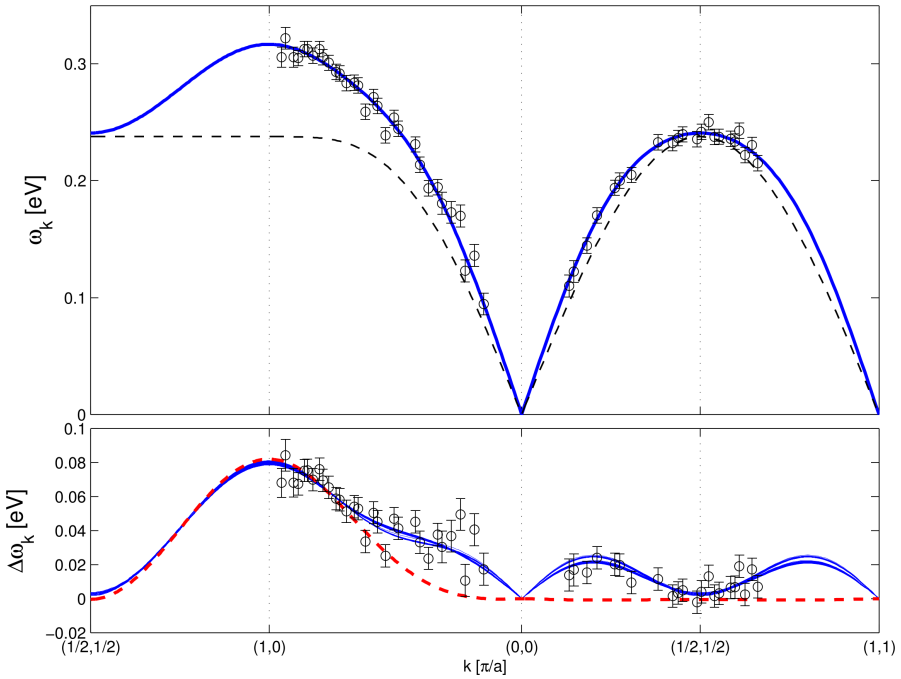

Figure 3.17 – The obtained fitted dispersion for $Sr_2CuCl_2O_2$. Top panel shows the experimental data and a range of fitted solutions (solid blue lines) with the magnon dispersion of a simple Heisenberg model (dashed grey line) with J chosen such that $\omega(\pi/2,\pi/2) = 2J$. On the bottom panel we subtract it to the data and the fitted dispersions and also show the dispersion from a fit to the $t-U$ Hubbard model fourth order strong coupling expansion (dashed red line).

an absolute scale. Another interesting quantity is the average density of doubly occupied sites

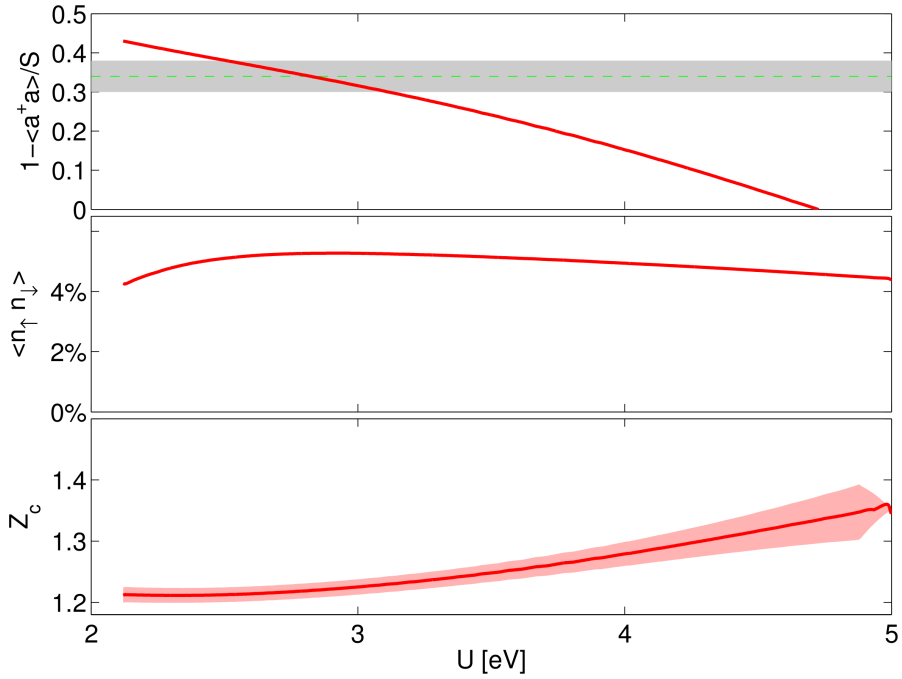

Figure 3.18 – Various physical properties along the $t't'' < 0$ best fit line in fig. 3.15. Top: Reduced staggered magnetization with an experimental determination (dashed black line, shaded area represents the uncertainty). Middle: The doubly occupied site density. Bottom: The $\boldsymbol{q}$-averaged first $1/S$ quantum renormalization of the magnon energy, Shaded area represents the variance σ^2 across the Brillouin Zone.

$\langle n_\uparrow n_\downarrow \rangle$ shown on fig. 3.18 middle panel. It is found it has rather constant value of about 5% indicating that along the best fit line the regime in which the effective strong coupling theory is carried out is not changing. Also this quantity can be put in relation with the electronic shielding factor calculated in Lorenzana et al. [2005]. Lastly, to evaluate the stability of our spin-wave solution, it is interesting to look at the first $1/S$ quantum correction along the best fit line, shown on fig. 3.18 bottom panel. We plot the $\boldsymbol{q}$-averaged renormalization factor Z_c as defined in eq. 3.5.60. Consistently with the decrease of the staggered magnetization, the quantum correction increases along the best fit line for greater U indicating the loss of stability of our solution for larger U. The shaded area on fig. 3.18 indicates the variance of the quantum renormalization on the Brillouin zone. It is also found to grow for larger U's.

3.6.4 Comparison with electronic spectrum

In this section we review the conclusions that can be drawn when comparing the microscopic electronic model parameters as obtained through electronic measurement (ARPES) or magnetic measurements (Raman,RIXS,INS). In the context of the cuprates, the Hubbard model must be thought as a phenomenological one as discussed in section 3.3.3 because it cannot be

considered as an effective theory of the $d-p$ model due charge-transfer energy being smaller than the Cu double occupation one. ARPES spectra are commonly analysed in term of a $t-J$ model which is indeed an effective theory of the $d-p$ model. The related phenomenological Hubbard model is the one from which a strong coupling limit effective model would result in the same $t-J$ model as the one obtained from the $d-p$ one. The quasiparticle dispersion from ARPES measurement of the SCOC material has been analysed and shown to be well accounted for by a $t-t'-t''-J$ model:

$$\begin{aligned}\mathscr{H}_{t-t'-t''-J} = &- t \sum_{\langle i,j\rangle_{1\text{st}}\sigma} i\left(\tilde{c}^{\dagger}_{i\sigma}\tilde{c}_{j\sigma} + \text{h.c.}\right) - t' \sum_{\langle i,j\rangle_{2\text{nd}}\sigma} \left(\tilde{c}^{\dagger}_{i\sigma}\tilde{c}_{j\sigma} + \text{h.c.}\right) \\ &- t'' \sum_{\langle i,j\rangle_{3\text{rd}}\sigma} \left(\tilde{c}^{\dagger}_{i\sigma}\tilde{c}_{j\sigma} + \text{h.c.}\right) + J \sum_{\langle i,j\rangle} \boldsymbol{S}_i \cdot \boldsymbol{S}_j \end{aligned} \tag{3.6.7}$$

where

$$\tilde{c}_{i\sigma} = c_{i\sigma}(1 - n_{i\bar{\sigma}}) \tag{3.6.8}$$

enforces the no double occupancy constraint. The t' and t'' model parameters can be related back to a microscopic description of the CuO_2 plane [Eskes et al., 1989; Hybertsen et al., 1990; Tohyama and Maekawa, 1990; Matsukawa and Fukuyama, 1989b,b]. To relate this model to our work we note that it corresponds to the $t-t'-t''-U$ Hubbard model:

$$\begin{aligned}\mathscr{H}_{t-t'-t''-U} = &- t \sum_{\langle i,j\rangle_{1\text{st}}\sigma} \left(c^{\dagger}_{i\sigma}c_{j\sigma} + \text{h.c.}\right) - t' \sum_{\langle i,j\rangle_{2\text{nd}}\sigma} \left(c^{\dagger}_{i\sigma}c_{j\sigma} + \text{h.c.}\right) \\ &- t'' \sum_{\langle i,j\rangle_{3\text{nd}}\sigma} \left(c^{\dagger}_{i\sigma}c_{j\sigma} + \text{h.c.}\right) + U \sum_{i} n_{i\uparrow}n_{i\downarrow} \end{aligned} \tag{3.6.9}$$

taken in the strong coupling limit up to second order perturbation theory with $J = 4t^2/U$ and the other magnetic coupling $J' = 4t'^2/U$ and $J'' = 4t''^2/U$ neglected. The dispersion of a single hole in the antiferromagnetic background has been measured by ARPES and analysed in terms of the $t-t'-t''-J$ model [Tohyama and Maekawa, 2000] bringing the microscopic model parameters $t = 0.35$eV, $t' = -0.12$eV, $t'' = 0.08$eV and $J = 0.14$eV. Comparing these model parameters to ours imply relating the full complicated effective spin-only Hamiltonian eq. 3.4.58 to the constrained fermionic one eq. 3.6.7. We thus do not expect a detailed agreement but only require major aspects to be consistent. Probably the most important aspect is the amplitude of the Coulomb repulsion U. The phenomenological Hubbard model attached to the above $t-t'-t''-J$ model has $U = 4t^2/J = 3.5$eV.

First we can look at what U we get if we fit the experimental magnon dispersions to an effective spin Hamiltonian derived from the $t-U$ Hubbard model. Having only two parameters, the fit provides a unique solution as was previously done in Coldea et al. [2001a]. This results in table 3.1. It is immediately visible that the obtained Coulomb repulsion for all three materials are very small. For SCOC and BSYCO, it is even less than 2eV and the ratio $U/t \sim 5.5$ places them quite far from the generally accepted ratio $U/t \sim 10$ for cuprate materials. Also these results are in complete disagreement with the ARPES $U = 3.5$eV for the phenomenological

	t [eV]	U [eV]
SCOC	0.28	1.62
BSYCO	0.26	1.46
LCO	0.31	2.2

Table 3.1 – Fit of the experimental dispersion to the effective spin Hamiltonian eq. 3.4.58 considering only nearest neighbour hopping amplitude t.

	t	t'	t''	$\langle S\rangle/S$	c	$\langle n_\uparrow n_\downarrow\rangle$
BSYCO	407(10)	-207(3)	79(4)	0.3	0.146	5.9%
SCOC	480(10)	-200(5)	75(5)	0.29	0.163	5.1%
LCO	492(7)	-207(3)	45(2)	0.4	0.195	5.2%

Table 3.2 – Fitted parameters for the experimental dispersions of SCOC, BSYCO and LCO. Guided by ARPES results, the Coulomb repulsion is chosen to be $U = 3.5$eV for all three materials and only the $t't'' < 0$ solution is kept. Also shown are the reduced staggered magnetization, the spin-wave velocity and the double occupancy density.

Hubbard model. We will see that this discrepancy can be resolved by including the t' and t'' hopping amplitudes in the phenomenological Hubbard model. This leads to the fits shown in the previous section. Requiring $U = 3.5$eV for all three materials, we obtain the microscopic parameters on table 3.2. The obtained rough agreement between our fitted parameters and the SCOC ARPES ones consistently reconciliate the magnetic measurements and the electronic ones in a unified microscopic theory.
Another puzzle attached to the ARPES measurement of the insulating cuprates is the so-called waterfall controversy which we briefly exposed in section 3.2.1. The rather large nearest neighbour hopping amplitude that is found in our work would strongly support the self-energy induced kink scenario [Chang et al., 2008].

3.6.5 Comparison with magnetic measurements

The fit of the magnetic dispersion allowed to put strong constraints on the microscopic model parameters. In this section we consider other 'magnetic' quantities such as the dynamical spin structure factor, the two-magnon oxygen K-edge RIXS spectrum and the Raman scattering spectrum.

Dynamical spin structure factor

Neutron scattering carried on LCO has been very fruitful. First it proved in 2001 that extended magnetic exchanges are relevant for cuprate materials [Coldea et al., 2001a]. Second it evidenced in the context of the cuprate the high energy magnon anomaly [Headings et al., 2010] which was already observed in the CFTD material [Christensen et al., 2007]. This anomaly is the subject of this thesis chapter 2. Briefly, it may be characterized by i) a reduction of the $(\pi, 0)$

magnon energy of 7% with respect to $\boldsymbol{q} = (\pi/2, \pi/2)$, ii) a reduction by 50% of the $\boldsymbol{q} = (\pi, 0)$ magnon intensity and iii) a continuum of excitations extending towards high energy from the $\boldsymbol{q} = (\pi, 0)$ magnon line. This was completely characterized in the context of the CFTD material in Christensen et al. [2007]. For cuprates feature i) is not observable due to the large enlargement of the $\boldsymbol{q} = (\pi, 0)$ magnon energy due to the extended magnetic interactions. But features ii) and iii) have been observed for LCO[Headings et al., 2010]. The magnon description is by definition not suited to tackle feature iii) as it will only predict only as many magnon modes as there are independent sites in the unit cell. But it is worth discussing what happen for feature ii) when accounting from the charge fluctuation renormalization of the dynamical spin structure factor as discussed in section 3.5.6. If only nearest neighbour hopping amplitudes are considered, then we already discussed that the renormalization is constant along the magnetic zone boundary thus cannot explain an intensity difference between $\boldsymbol{q} = (\pi/2, \pi/2)$ and $\boldsymbol{q} = \pi, 0)$. But when the additional next- and next-next-nearest neighbour t' and t'' hopping amplitudes are introduced, this is not strictly the case anymore. We show on fig. 3.19 the experimental magnon intensity of LCO reported in Headings et al. [2010] along with the predicted LCO magnon intensity using the microscopic parameters of table 3.2 with and without the charge fluctuation renormalization. We see that the charge fluctuation renormalization only brings a small 3% intensity variation between $\boldsymbol{q} = (\pi/2, \pi/2)$ and $\boldsymbol{q} = (\pi, 0)$, a much too small effect compared to the 50% reduction experimentally observed. In chapter 2 we argue that the high-energy magnon anomaly has an entirely different origin than an effective model renormalization of a spin-wave result.

Two-magnon quantities

Other important magnetic measurements are the copper K-edge RIXS and Raman scattering experiments. These measurements do not transfer angular momentum to the sample thus cannot probe individual magnon excitations. But conjugated two-magnon excitations are possible. In linear spin-wave theory, the eigenstates are described as a gas of non-interacting magnons which of course is an approximation. The neglected terms in the spin-wave expansion generate magnon-magnon interactions which we already included for the single magnon energy to first order perturbation theory using the Hartree-Fock approach in section 3.5.5. The magnon-magnon interaction becomes even more important when considering two-magnons correlation functions such as those probed by oxygen K-edge RIXS and Raman scattering and lead, in the former case in one theoretical treatment [Canali and Girvin, 1992], to a 36.8% renormalization of the two-magnon peak energy.
The Raman scattering results were briefly introduced in section 3.2.3. In summary, the two-magnon peak energy has been consistently analysed in an RPA treatment of the magnon-magnon interaction on a $t-U$ Hubbard model to the fourth order t/U effective theory (eq. 3.4.58 with only the nearest neighbour hopping amplitude t)[Katanin and Kampf, 2003]. But the asymmetric lineshape of the Raman two-magnon peak could not be reproduced.
Copper K-edge RIXS experiments were carried out on the doped and undoped LCO materials and evidenced a peak in the RIXS signal at $\boldsymbol{q} = (\pi, 0)$ and at a 500meV energy [Ellis et al., 2010].

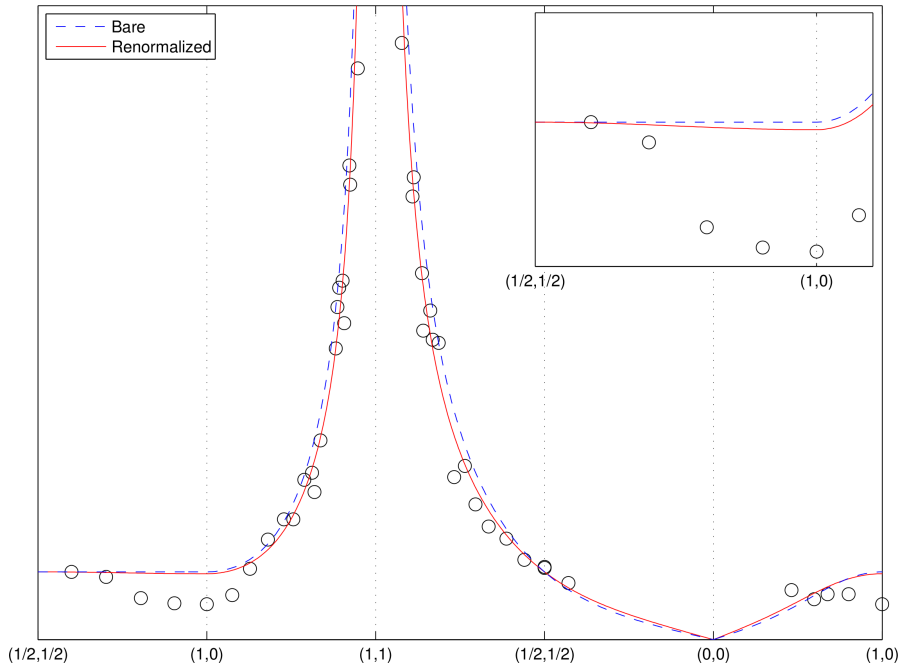

Figure 3.19 – Experimental magnon intensity in LCO as reported in Headings et al. [2010]. Dashed blue line is the predicted magnon intensity without charge fluctuation renormalization with the LCO parameter set of table 3.2. Solid red line is the predicted magnon intensity including the charge fluctuation renormalization. The insert show a zoom in of the magnetic zone boundary intensity variation.

The peak was interpreted as the RIXS equivalent of the Raman two-magnon peak.
To compare our results with these measurements, we calculate the two-magnon density of state and the two-magnon part of the longitudinal dynamical spin structure factor. However we do not go as far as calculating the magnon-magnon interaction effect and only show the results in the non-interacting case. The comparison is based on the differences observed between the non-interacting two-magnon quantities for the simple nearest-neighbour Heisenberg model and for our effective theory. We then postulate that the effect of magnon-magnon interactions would be similar in our effective theory to the one already calculated in the case of the Heisenberg model.
The density of two-magnon states is simply given by:

$$D(\boldsymbol{q},\omega) = \sum_{\boldsymbol{k}} \delta(\omega - \omega_{\boldsymbol{k}} - \omega_{\boldsymbol{k}-\boldsymbol{q}}). \tag{3.6.10}$$

The two-magnon part of the dynamical spin structure factor is obtained using:

$$S^{zz}(\boldsymbol{q},\omega) = \sum_{\lambda} \langle \mathrm{GS}|S^z_{-\boldsymbol{q}}|\lambda\rangle\langle\lambda|S^z_{\boldsymbol{q}}|\mathrm{GS}\rangle \delta(\omega - E_\lambda + E_{\mathrm{GS}}), \tag{3.6.11}$$

expressing the bare $S^z_{\boldsymbol{q}}$ in the effective theory spin operators as in eq. 3.4.64 in turn re-expressed in terms of the magnon quasiparticle operators. The inelastic part is then only composed of two-magnon excitations with the following intensity:

$$S^{zz}(\boldsymbol{q},\omega) = R^2_{\mathrm{eff}}(\boldsymbol{q}) \sum_{\boldsymbol{k}} \frac{1}{2} \left(u_{\boldsymbol{k}} v_{\boldsymbol{k}-\boldsymbol{q}} - u_{\boldsymbol{k}-\boldsymbol{q}} v_{\boldsymbol{k}}\right)^2 \delta(\omega - \omega_{\boldsymbol{k}} - \omega_{\boldsymbol{k}-\boldsymbol{q}}) \tag{3.6.12}$$

where $R_{\mathrm{eff}}(\boldsymbol{q})$ is the charge fluctuation renormalization factor eq. 3.4.65:

$$R_{\mathrm{eff}}(\boldsymbol{q}) = 1 - \sum_{\boldsymbol{\tau}} \frac{t^2_{\boldsymbol{\tau}}}{U^2} \left(1 - \cos(\boldsymbol{q}\cdot\boldsymbol{\tau})\right) \tag{3.6.13}$$

We show the two-magnon density of states in both the case of the simple nearest neighbour Heisenberg model and in the case of our full effective model with the SCOC microscopic parameters from table 3.2 on fig. 3.20. The Heisenberg model J is adjusted such that the $\boldsymbol{q} = (\pi/2\pi/2)$ magnon energy matches the one measured by RIXS for SCOC. At $\boldsymbol{q} = (0,0)$, the sharp $\omega = 4J$ peak observed for the Heisenberg model is brought down in energy and widened. We show an energy cut in fig. 3.21. While magnon-magnon interactions will lower the peak energy, we note that the inclusion alone of the extended magnetic interaction from eq. 3.4.58 lead to a tail of excitations towards high energies from the main peak. It is tempting thus to interpret the measured Raman scattering two-magnon peak asymmetric lineshape as an effect of the extended magnetic interactions. But, while the density of states underlies the Raman scattering signal, the matrix element effects might completely change this picture. Indeed the Raman lineshape has been analyzed using the fourth order low-energy effective theory of the t-U Hubbard model [Katanin and Kampf, 2003] which also includes extended magnetic interactions. This approach did result in a slightly asymmetrical lineshape but not enough compared to experiments. On can speculate that including the larger family of extended

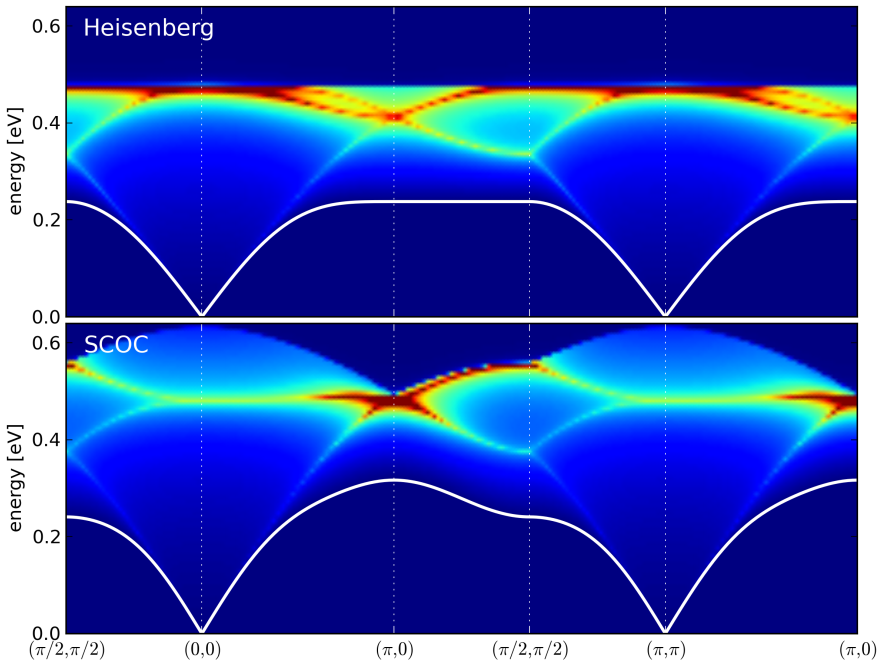

Figure 3.20 – Two magnon density of states in the case of the Heisenberg model (top) and in the case of the full effective model eq. 3.4.58 (bottom) with the SCOC parameters from table 3.2. The Heisenberg model J is adjusted such that the $\boldsymbol{q} = (\pi/2\pi/2)$ magnon energy matches the one measured by RIXS for SCOC.

magnetic couplings for a t-t'-t''-U Hubbard model might increase the asymmetry. But in view of the first chapter of this thesis, one can speculate that the origin of the asymmetrical Raman lineshape has an entirely different origin than effective extended magnetic excitations. In chapter 2 we argued that the asymmetric lineshape measured by INS on the CFTD material at momentum $\boldsymbol{q} = (\pi, 0)$ might be a signature of fractional excitations physics. One can therefore speculate that fractional excitations might also be the explanation for the asymmetric Raman lineshape [Ho et al., 2001]. Lastly we also note that the 500meV copper K-edge RIXS peak can also be interpreted as an extended magnetic interaction effect. Indeed comparing the density of states for the Heisenberg model and for our effective model we see a concentration of two-magnon states exactly at $\boldsymbol{q} = (\pi, 0)$. Again the RIXS matrix elements might change this picture but we note that, at least for the dynamical spin structure factor, this feature survives as shown on fig. 3.22.

3.7 Conclusion

This work is an attempt at using the available theoretical tools to obtain a detailed and unified description of the cuprate superconductor family insulating parent compounds. The goal was to provide a strong experimental footing to the microscopic model parameters. The cuprate superconductors problematic generated a huge worldwide experimental thrust and an as-

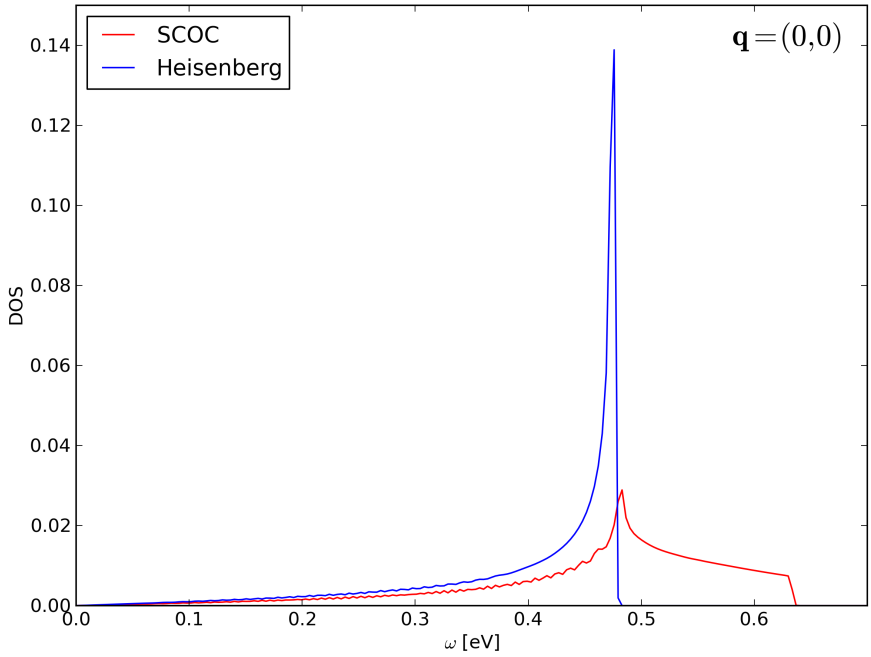

Figure 3.21 – Energy cut of the two-magnon density of states from fig. 3.20 at $\boldsymbol{q} = (0,0)$.

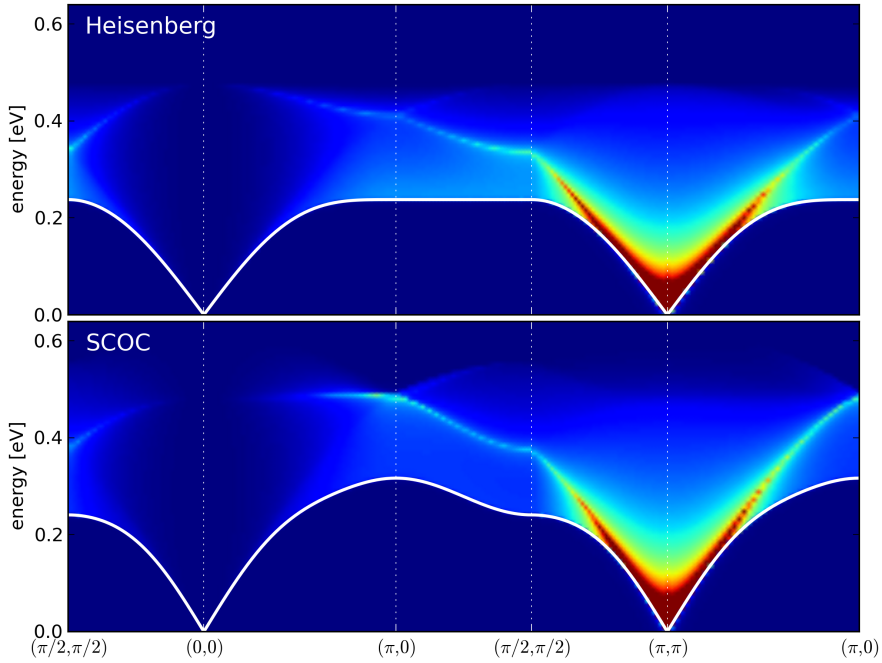

Figure 3.22 – Two magnon part of the longitudinal spin structure factor in the case of the Heisenberg model and in the case of the effective model eq. 3.4.58 with the SCOC parameters from table 3.2. The Heisenberg model J is adjusted such that the $\boldsymbol{q} = (\pi/2, \pi/2)$ magnon energy matches the one measured by RIXS on SCOC.

sociated huge literature. Here we chose to focus on experimental results from the ARPES, INS, Raman scattering and RIXS techniques and show that they consistently constraint the microscopic model parameters. Using the same unified effective theory framework, we could account for the magnetic excitation spectrum of the LCO, SCOC and BSYCO materials and show that it is consistent with the entirely different electronic measurements carried by ARPES. Such a consistency across widely different techniques, while desirable, is rarely achieved. Following this determination of the microscopic model parameters, we discussed their adequacy with the following experimental facts:

– In ARPES measurements, the waterfall feature discussed in section 3.2.1 was controversially described either as an ARPES matrix element effect [Inosov et al., 2007] or an intrinsic self-energy effect [Chang et al., 2008]. In the former case the associated bare band quasiparticle dispersion was shallow corresponding to a small nearest-neighbour hopping $t = 0.23$eV. The size of the nearest neighbour hopping $t = 0.48$eV from our fit of the magnetic spectrum seems to support the latter interpretation of the waterfall feature.
– In copper K-edge RIXS at momentum $\boldsymbol{q} = (\pi, 0)$, a strong peak at 500meV was interpreted a two-magnon excitation. The concentration of states we find in the non-interacting two-magnon density of states at this momentum supports this interpretation although the effect of magnon-magnon interaction and RIXS matrix elements was not accounted for.
– Finally the asymmetric lineshape of the Raman scattering was addressed. While it would seem tempting to link it to the magnetic zone boundary dispersion caused by the extended magnetic interactions, such a course was already attempted in Katanin and Kampf [2003] and did not result in a large enough asymmetry. The inclusion of the larger family of extended magnetic coupling from the t-t'-t''-U Hubbard model low energy effective theory might increase this asymmetry. But it was speculated that the asymmetric Raman lineshape was a result of fractionalized excitations [Ho et al., 2001], a similar phenomenon as the zone boundary anomaly evidenced in chapter 2. It might be very interesting to see if the variational Monte Carlo approach developed in chapter 2 could address the Raman asymmetric lineshape problematic.

A Variational Monte Carlo appendices

A.1 Metropolis Monte Carlo

The metropolis Monte Carlo is a numerical approach to provide an estimate of an integral when the space the integral is carried on is too large for a regular partition. We consider a quantity F:

$$F = \sum_{\alpha} \rho(\alpha) f(\alpha) \tag{A.1.1}$$

where $\rho(\alpha)$ is a normalized probability distribution. The Metropolis Monte Carlo provides a simple way to calculate an estimate of F by summing the contributions $f(\alpha)$ with the α states being generated by a random walk following the probability distribution $\rho(\alpha)$. To define this random walk, we must specify a proposal function $\mathscr{P}(\alpha'|\alpha_n)$ where n index the random walk steps. There is a great freedom into designing this proposal function and we only require that it may generate a transition between any pair of states α and α' in a finite number of steps. We then define the transition probability matrix $\mathscr{A}(\alpha'|\alpha_n)$:

$$\mathscr{A}(\alpha'|\alpha_n) = \min\left[1, \frac{\mathscr{P}(\alpha_n|\alpha')\rho(\alpha')}{\mathscr{P}(\alpha'|\alpha_n)\rho(\alpha_n)}\right]. \tag{A.1.2}$$

The random walk is then generated as follow:

1. A new state α' is generated by the proposal function $\mathscr{P}(\alpha'|\alpha_n)$.
2. A random number $r \in [0,1)$ is drawn.
   - If $r < \mathscr{A}(\alpha'|\alpha_n)$ then the state is *accepted* and $\alpha_{n+1} = \alpha'$.
   - If not then the state is *rejected* and $\alpha_{n+1} = \alpha_n$.
3. Go back to 1.

Defined that way, the random walk conditional probability $P(\alpha_{n+1}|\alpha_n)$ is:

$$P(\alpha_{n+1}|\alpha_n) = \begin{cases} \mathscr{A}(\alpha_{n+1}|\alpha_n)\mathscr{P}(\alpha_{n+1}|\alpha_n) & \alpha_{n+1} \neq \alpha_n \\ 1 - \sum_{\alpha'} \mathscr{A}(\alpha'|\alpha_n)\mathscr{P}(\alpha'|\alpha_n) & \alpha_{n+1} = \alpha_n \end{cases} \tag{A.1.3}$$

and verifies the detailed balance

$$P(\alpha'|\alpha)\rho(\alpha) = P(\alpha|\alpha')\rho(\alpha') \tag{A.1.4}$$

which guaranties that the set of states $\{\alpha_n\}$ drawn by the random walk will follow the probability distribution $\rho(\alpha)$. Using this random walk we will then collect samples $f(\alpha)$ whose average will be an estimate of $F \simeq E(F)$. We then would like to be also able to tell what the uncertainty of this estimate is. If the samples are independent, we could simply use the estimate of the standard deviation $\sigma(F)$:

$$\sigma(F) \simeq E(\sigma(F)) = \sqrt{\frac{1}{L(L-1)} \sum_{\alpha} \big(E(F) - f(\alpha)\big)^2}. \tag{A.1.5}$$

This is only valid if the samples are independent which typically is not the case in a Markov chain. To overcome this difficulty we simply choose to take the samples sufficiently far away from each others in the random walk. Also the statistical average will only be reliable for sufficient statistics. All these remarks are quite hand-wavy and we need a way to know whether we can trust the estimate. We describe in appendix A.6 how we determine the uncertainty of our numerical results.

A.2 Determinant update Formulas

The determinant update formula for a new matrix A' where only one row/column has been changed with respect to A can easily be calculated if one knows the inverse matrix A^{-1} and remembering the inverse matrix is linked to the determinant through the co-factor matrix:

$$A^{-1} = \frac{1}{\mathrm{Det}(A)} \mathrm{cof}(A)^T \tag{A.2.1}$$

where the i,j'th element of the cofactor matrix is:

$$\mathrm{cof}(A)_{ij} = \mathrm{Det}\left(A_{\setminus(ij)}\right) \tag{A.2.2}$$

where $A_{\setminus(ij)}$ is the matrix A where row i and column j have been removed. These considerations lead to the simple determinant update formula where, for definiteness, we changed row k in matrix A to get A':

$$\frac{\mathrm{Det}(A')}{\mathrm{Det}(A)} = \sum_j A'_{kj} A^{-1}_{jk}. \tag{A.2.3}$$

A similar formula can be derived to also find the inverse matrix update $(A')^{-1}$. We note that the determinant update formula involve a simple sum over the columns j of the A' matrix and thus is of linear complexity with respect to the matrix size N thus far better the cubic complexity for calculating the determinant from scratch. In fact these results are only special cases of the two following relations. Let A be a $N \times N$ matrix, U a $N \times m$ matrix and V an $m \times N$ matrix. The rank-m modification of the matrix A is defined as:

$$A' = A + UV \tag{A.2.4}$$

for which we have the two results [Brookes, 2011]:

$$\mathrm{Det}(A') = \mathrm{Det}(A)\mathrm{Det}\left(\mathbb{I} + VA^{-1}U\right) \tag{A.2.5}$$

$$(A')^{-1} = A^{-1} - A^{-1}U\left(\mathbb{I} + VA^{-1}U\right)^{-1} VA^{-1} \tag{A.2.6}$$

where $\mathbb{I}$ is the $m \times m$ matrix identity and it s assumed in A.2.6 that the $m \times m$ matrix $\mathbb{I} + VA^{-1}U$ is invertible. Let's reformulate these results in a more useful way for the problem of changing simultaneously m_r rows and m_c columns. We define the matrices of the new rows and columns

as R and C respectively being $m_r \times N$ and $N \times m_c$. We let $r_1, \ldots, r_{m_r}$ be the indices of the rows to be changed and $c_1, \ldots, c_{m_c}$ the indices of the columns to be changed. Furthermore we define the unit column-vectors $\hat{\boldsymbol{e}}_i$ where the only non-zero element is $(\hat{\boldsymbol{e}}_i)_i = 1$. Then one can see that the following U and V do define a simultaneous change of the r_i'th rows and c_j'th columns of A by the i'th rows of R and the j'th columns of C :

$$U = \begin{pmatrix} C' & E_r \end{pmatrix} \tag{A.2.7}$$

$$V = \begin{pmatrix} E_c \\ R' \end{pmatrix} \tag{A.2.8}$$

with

$$E_r = \begin{pmatrix} \hat{\boldsymbol{e}}_{r_1} & \hat{\boldsymbol{e}}_{r_2} & \ldots & \hat{\boldsymbol{e}}_{r_{m_r}} \end{pmatrix} \tag{A.2.9}$$

$$E_c = \begin{pmatrix} \hat{\boldsymbol{e}}_{c_1}^T \\ \hat{\boldsymbol{e}}_{c_2}^T \\ \vdots \\ \hat{\boldsymbol{e}}_{c_{m_c}}^T \end{pmatrix} \tag{A.2.10}$$

and

$$C' = (1 - E_r E_r^T)(C - A E_c^T) \tag{A.2.11}$$

$$R' = R - E_r^T A. \tag{A.2.12}$$

Then the matrix $K = \mathbb{I} + V A^{-1} U$ has the block form:

$$K = \mathbb{I} + V A^{-1} U = \left(\begin{array}{l|l} E_c A^{-1} C - E_c A^{-1} E_r E_r^T C & E_c A^{-1} E_r \\ \quad + E_c A^{-1} E_r E_r^T A E_c^T & \\ \hline R A^{-1} C - R A^{-1} E_r E_r^T C & R A^{-1} E_r \\ \quad - R E_c^T + R A^{-1} E_r E_r^T A E_c^T & \end{array}\right). \tag{A.2.13}$$

Let's check the computational complexity of each blocks in the case $m_r \ll N$ and $m_c \ll N$. The upper left block has $m_c \times m_c$ elements and its calculation requires $\mathcal{O}(N)$ operations. The lower left block has $m_r \times m_c$ elements and requires $\mathcal{O}\left(N^2\right)$ operations. The upper right block has $m_c \times m_r$ elements and requires $\mathcal{O}\left(N^0\right)$ operations. The lower right block has $m_r \times m_r$ elements and requires $\mathcal{O}(N)$ operations. The complete calculation of the matrix K is of quadratic complexity $\mathcal{O}\left(N^2\right)$. When there are no row changes or no column changes, the above formulas might be modified a little yielding:

$$K = E_c A^{-1} C \quad \text{no row changes} \tag{A.2.14}$$

$$K = R A^{-1} E_r \quad \text{no column changes} \tag{A.2.15}$$

and thus are only of linear complexity $\mathcal{O}(N)$. Once the matrix K is calculated, the determinant update can be obtained from the rank-$(m_c + m_r)$ determinant of the K matrix. The inverse

matrix update will require the inversion of K and additional rank-N matrix multiplications making the inverse update of quadratic $\mathcal{O}(N^2)$ regardless of the fact there might be only rows or only columns being changed. In summary the above formulas allow to calculate the determinant update and the inverse matrix update in quadratic complexity $\mathcal{O}\left(N^2\right)$ at worst. Of course the whole procedure gets increasingly expensive for larger m_r and m_c and is only worth when $m_c \ll N$ and $m_r \ll N$.

A.3 Modified Monte Carlo random walk: details

The random walk is generated by random exchanges of neighbouring anti-parallel spins as explained in section 2.5.2. The calculation of the amplitude $\langle\alpha|\psi\rangle$ involving $N_\uparrow \times N_\uparrow$ and $N_\downarrow \times N_\downarrow$ Slater determinants we store the Slater matrices $M^{\langle\alpha|\psi\rangle}_{i_\uparrow j_\uparrow}$ and $M^{\langle\alpha|\psi\rangle}_{i_\downarrow j_\downarrow}$:

$$M^{\langle\alpha|\psi\rangle}_{i_\uparrow j_\uparrow} = \left\langle \boldsymbol{R}_{i_\uparrow}, \uparrow \middle| \boldsymbol{k}_{j_\uparrow}, \uparrow, b_{\boldsymbol{k}_{j_\uparrow}} \right\rangle \tag{A.3.1}$$

$$M^{\langle\alpha|\psi\rangle}_{i_\downarrow j_\downarrow} = \left\langle \boldsymbol{R}_{i_\downarrow}, \downarrow \middle| \boldsymbol{k}_{j_\downarrow}, \downarrow, b_{\boldsymbol{k}_{j_\downarrow}} \right\rangle \tag{A.3.2}$$

and their inverse calculated once from a standard LU decomposition. The determinant is also obtained that way and stored. These initial inverse matrix and determinant calculation are of cubic complexity. When one proceeds in the random walk, the proposed state amplitudes is obtained through the determinant update formula derived in appendix A.2. When a move is accepted, one must also update the inverse matrix thus using also the previously seen formulas from appendix A.2.

In the special case of the modified Monte Carlo random walk presented in section 2.6.3, one has to take special care. The random walk starts by choosing an arbitrary particle-hole state for $\left|\psi\right\rangle = \left|\boldsymbol{k}_0, \sigma\sigma', \boldsymbol{q}\right\rangle$ as the reference state to define the Slater matrices and their inverse. But it might happen that some special state $|\alpha\rangle$ is a node of this state $\left\langle\alpha\middle|\boldsymbol{k}_0, \sigma\sigma', \boldsymbol{q}\right\rangle = 0$ but not of the other particle-hole states $\left\langle\alpha\middle|\boldsymbol{k} \neq \boldsymbol{k}_0, \sigma\sigma', \boldsymbol{q}\right\rangle \neq 0$. In that case the weight eq. 2.6.28 or 2.6.31 $W^{\boldsymbol{q}\Delta S}(\alpha)$ might still be finite and the move accepted. But because $\left\langle\alpha\middle|\boldsymbol{k}_0, \sigma\sigma', \boldsymbol{q}\right\rangle = 0$ the Slater matrix for $\left|\boldsymbol{k}_0, \sigma\sigma', \boldsymbol{q}\right\rangle$ is not invertible! To ensure this situation never happen we make sure, when accepting a move $|\alpha\rangle \to \left|\alpha'\right\rangle$, that we also choose the particle-hole reference state $\left|\boldsymbol{k}_0, \sigma\sigma', \boldsymbol{q}\right\rangle \to \left|\boldsymbol{k}', \sigma\sigma', \boldsymbol{q}\right\rangle$ such that $\left|\left\langle\alpha'\middle|\boldsymbol{k}', \sigma\sigma', \boldsymbol{q}\right\rangle\right|^2$ is maximum thus making the inverse matrix well-defined.

A.4 Monte Carlo thermalization

The Monte Carlo random walk starts from a completely random state. It is likely this initial state will have very little weight and the random walk will drift towards better states. This is the so-called thermalization process where the visited states might not be representative of the Monte Carlo probability distribution. The states associated with this process should therefore not enter the Monte Carlo sampling as they will introduce a bias from the random

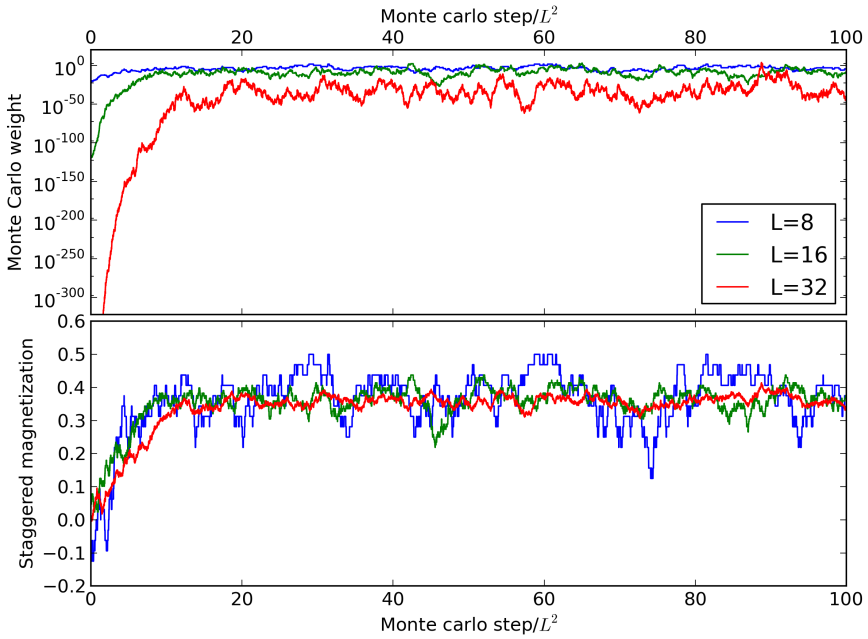

Figure A.1 – Evolution of the Monte Carlo weight and staggered magnetization of the random walk states for the SF+N state with weight $\rho(\alpha) = |\langle\alpha|\text{GS}\rangle|^2$. Top: weight normalized to the average weight of the random walk. Bottom: Staggered magnetization.

initial state. It is therefore important to determine how long in terms of random walk steps the initial thermalization takes, in order to only start sampling quantities safely away. In some cases the thermalization may be as hard as to constitute the main goal of the Monte Carlo procedure. In our case however it turns out to be an extremely fast and easy procedure due to the lack of frustration involved in the square lattice antiferromagnet. We show on fig. A.1 top panel the evolution of the Monte Carlo weight $\rho(\alpha) = |\langle\alpha|\text{GS}\rangle|^2$ as a function of Monte Carlo step for the SF+N wavefunction for different system sizes. The x-axis is scaled by the system size to allow comparison between different sizes. It is seen that the initial state evolves in less than $20 \cdot L^2$ steps to gain a staggered magnetization and get a reasonable weight. We obtain a similar result for the spin-liquid SF state. For calculations in the transverse or longitudinal particle-hole subspace, we also obtain very similar results showing a very fast thermalization. We show it in the SF case on fig. A.2. It is interesting to see that, while in the SF state the $\boldsymbol{q} = (\pi, \pi)$ instantaneous spin-spin correlation function is peaked, the random walk nevertheless alternates between positive and negative staggered magnetization.
The numerical results presented in this thesis were obtained using $100 \times L^2$ thermalization steps to guarantee unbiased results. The very small cost of thermalization in our problem has great advantage for massive parallelization. In the largest calculations we did, we ran up to 3200 parallel random walks each containing only a thousand evaluations of the measured quantities done every L^2 random walk steps where L^2 is the number of lattice sites. We show below that each thermalization step require $\mathcal{O}\left(L^4\right)$ operations while each measurement requires $\mathcal{O}\left(L^6\right)$

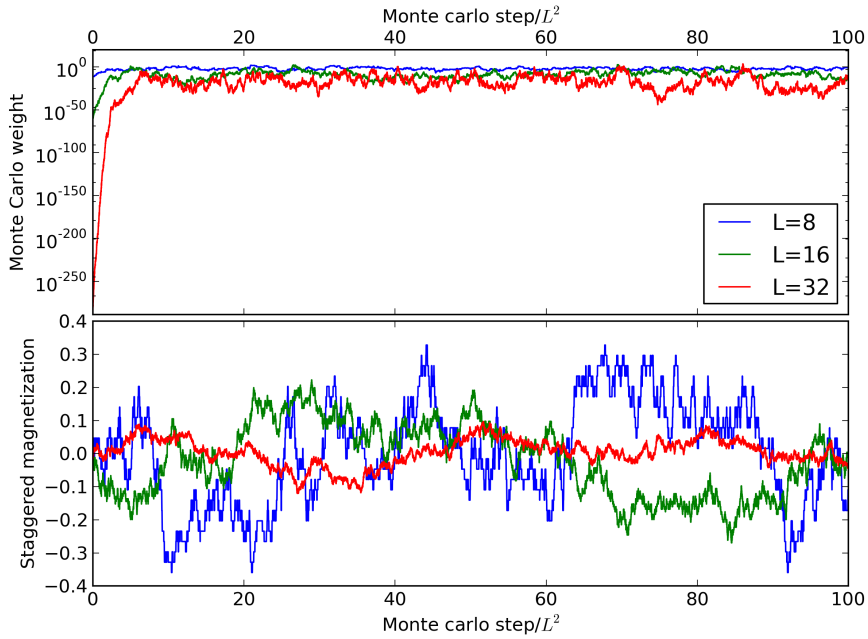

Figure A.2 – Evolution of the Monte Carlo weight and staggered magnetization of the random walk states for the SF state with weight $\rho(\alpha) = \sum_{\boldsymbol{k}} \left|\langle \alpha \left| \boldsymbol{k}\uparrow\downarrow, \boldsymbol{q}\right\rangle\right|^2$. Top: weight normalized to the average weight of the random walk. Bottom Staggered magnetization.

operations. The thermalization thus amounts to a very minor cost in run-time making it profitable to run many short parallel random walks to gather large statistics.

A.5 Calculation run-time scaling

The calculation run-time scaling can be deduced from the algorithmic complexity determined in appendix A.2. For the groundstate and excited subspaces calculations, the random steps cost $\mathcal{O}(N^2)$ operations either from the inverse Slater matrix update or, for the excited subspace calculations, from the determinant update itself. Therefore the thermalization process run-time will scale quadratically with system size as seen on fig. A.3.
The measurements run-time depends on the quantity. The simplest one which have only diagonal contributions $\langle\alpha|O\left|\beta\right\rangle = \langle\alpha|O|\alpha\rangle\,\delta_{\alpha\beta}$ do not involve determinant updates. For instance the staggered magnetization measurement run-time will scale linearly with system size while the longitudinal instantaneous spin-spin correlation function will scale quadratically due to the double sum in eq. 2.5.18.
For the quantities evaluated on the groundstate, quantities with off-diagonal matrix elements $\langle\alpha|O\left|\beta\right\rangle \neq 0$ will involve determinant updates which are of linear complexity for the groundstates if $\left|\beta\right\rangle$ differs from $|\alpha\rangle$ by a unique hop of $\uparrow$ and/or $\downarrow$ spins. For instance the variational energy of the Heisenberg Hamiltonian will scale quadratically with system size due to the sum over sites coupled to the determinant updates. The transverse instantaneous spin-spin

correlation functions measurement will scale in cubically with system size again due to the double sum coupled to the determinant updates.
We finally consider the excitation subspace calculations. The overlap matrix is sampled using, from eq. 2.6.30:

$$f_{O_{\boldsymbol{k}\boldsymbol{k}'}^{\boldsymbol{q}\Delta S}}(\alpha) = \frac{\langle \boldsymbol{k}, \sigma\sigma', \boldsymbol{q} | \alpha \rangle \langle \alpha | \boldsymbol{k}', \sigma\sigma', \boldsymbol{q} \rangle}{\sum_{\boldsymbol{q}} \left| \langle \alpha | \boldsymbol{k}, \sigma\sigma', \boldsymbol{q} \rangle \right|^2} \tag{A.5.1}$$

which, for calculating all $(\boldsymbol{k}, \boldsymbol{k}')$ matrix elements is of quadratic complexity as the determinant update where only rows or columns are changed is of linear complexity. For the case of the projected Heisenberg matrix, the sampling is done using, from eq. 2.6.29:

$$f_{H_{\boldsymbol{k}\boldsymbol{k}'}^{\boldsymbol{q}\Delta S}}(\alpha) = \sum_{\beta} \frac{\langle \boldsymbol{k}, \sigma\sigma', \boldsymbol{q} | \alpha \rangle \langle \alpha | \mathscr{H} | \beta \rangle \langle \beta | \boldsymbol{k}' \sigma\sigma', \boldsymbol{q} \rangle}{\sum_{\boldsymbol{q}} \left| \langle \alpha | \boldsymbol{k}, \sigma\sigma', \boldsymbol{q} \rangle \right|^2} \tag{A.5.2}$$

which involves simultaneous row and column changes in the determinant update from the $\langle \beta | \boldsymbol{k}', \sigma\sigma', \boldsymbol{q} \rangle$ amplitude which are of quadratic complexity. Coupled to the sum over sites in the Heisenberg model and the $\mathscr{O}(N)$ number of $\boldsymbol{k}'$, it looks like the sampling of the projected Heisenberg matrix is of quartic complexity! To fix the ideas let's decide that the change $|\alpha\rangle \rightarrow |\beta\rangle$ involves a row change in the spin-$\uparrow$ and spin-$\downarrow$ Slater matrices. In eq. A.2.13, the quadratic complexity comes from the matrix-vector multiplication

$$R_{\alpha\rightarrow\beta} \left(M^{\langle \alpha | \boldsymbol{k}, \sigma\sigma', \boldsymbol{q} \rangle} \right)^{-1}.$$

It only needs to be calculated once for one $|\alpha\rangle \rightarrow |\beta\rangle$ change. Then the vector-vector product:

$$\left(R_{\alpha\rightarrow\beta} \left(M^{\langle \alpha | \boldsymbol{k}, \sigma\sigma', \boldsymbol{q} \rangle} \right)^{-1} \right) C_{\boldsymbol{k}\rightarrow\boldsymbol{k}'}$$

needs $\mathscr{O}(N)$ operations and must be carried out $\mathscr{O}(N)$ times. Therefore the total complexity is only cubic as there are $\mathscr{O}(N)$ matrix-vector products

$$R_{\alpha\rightarrow\beta} \left(M^{\langle \alpha | \boldsymbol{k}, \sigma\sigma', \boldsymbol{q} \rangle} \right)^{-1}$$

to carry out. The measurement run-time of the projected Heisenberg matrix will therefore scale cubically with system size. The number of Monte-Carlo steps in-between two measurement is given by the system size N such that that it also amounts to a cubically scaling run-time. We confirm in practice these predictions on fig. A.3 where is shown the required run-time per measurement as a function of system size. For the largest system size calculated ($L^2 = 32^2$), one can see that the cost of thermalization steps is 6 orders of magnitude less than a single measurment. Counting that about $100L^2$ thermalization steps must be carried out before starting measurements, the cost of the whole thermalization costs less that 10% of a single measurement, a negiligible cost.

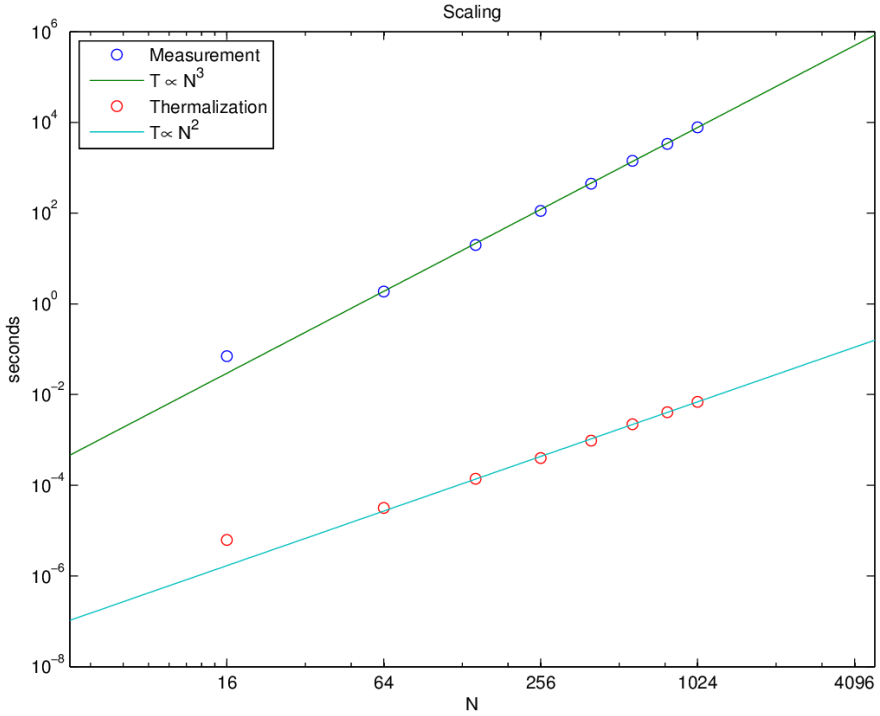

Figure A.3 – Run-time needed versus system size for the excited subspace calculations (here transverse). Thermalization steps (red open circles) scale quadratically with system size (cyan solid line) and measurements (blue open circles) scale cubically with system size (green solid line).

A.6 Evaluation of uncertainties

To evaluate eq. 2.5.3, one sums only on a very small subset of the spin configuration space. This naturally leads to an uncertainty on the end-result. For simple quantities such as the staggered magnetization and the variational energy of the Heisenberg model, the uncertainty can be calculated following Gros [1989]. As the data for large lattices were obtained using massively parallel independant random walks (up to 3200) we usually bunch the obtained data into $N_b \sim 10$ $\langle O \rangle_b$ statistically independant samples. The expectation value is then simply obtained by taking the samples average:

$$\overline{\langle O \rangle} = \frac{1}{N_b} \sum_{b=1}^{N_b} \langle O \rangle_b \tag{A.6.1}$$

and the uncertainty is obtained from the standard deviation

$$\sigma^2(O) = \frac{1}{N_b - 1} \sum_{b=1}^{N_b} \left(\langle O \rangle_b - \overline{\langle O \rangle} \right)^2 . \tag{A.6.2}$$

For more complicated quantities like the projected Heisenberg model matrix eq. 2.6.29 and the overlap matrix eq. 2.6.30, the uncertainty on the matrix elements could be found in the same way. The problem is that the meaningful quantities are then obtained through solving the generalized eigenvalue problem defined by these matrices. It is difficult to know how the uncertainty on the sampled matrices will propagate by the diagonalization process. We thus take the following practical approach: we compare the result obtained through the two different ways:

– We completely collapse the sampled matrices into one projected Heisenberg and overlap matrix pair, diagonalize and extract further quantities from the eigenvectors and eigenvalues. This, for instance in the case of the spinon-pair root mean square separation eq. 2.8.19 gives single points on figure 2.35 panel **E**.
– We bunch the sampled matrices into $N_b = 10$ projected Heisenberg and overlap matrix pairs, diagonalize and extract N_b independant samples of further quantities from the N_b samples of eigenvalues and eigenstates. The average value is then obtained using eq. A.6.1 and the unceratinty eq. A.6.2. In the case of the root-mean-square spinon separation eq. 2.8.19, this gives the errorbars which may or may not be centered on the points calculated from the full collapse of the data in one unique sample.

Comparing these two ways allows to know whether the obtained values can be trusted by making sure they are compatible. On fig. 2.35 panel **E** it is seen that the error propagation is highly non-trivial as the $\boldsymbol{q} = (\pi, 0)$ points display much larger uncertainties than the $\boldsymbol{q} = (\pi/2, \pi/2)$ momentum points.

B Effective low-energy model derivation

B.1 Proof of the unitary transformation expansion formula

We give a short proof of eq. 3.4.13 here written simply as

$$e^X Y e^{-X} = Y + [X,Y] + \frac{1}{2!}[X,[X,Y]] + \frac{1}{3!}[X,[X,[X,Y]]] + \dots \tag{B.1.1}$$

Let

$$f(s) = e^{sX} Y e^{-sX} \tag{B.1.2}$$

where s is a real number. We can write $f(s)$ as a Taylor expansion around $s = 0$:

$$f(s) = Y + \sum_{n=1}^{\infty} \frac{1}{n!} \frac{d^n f}{ds^n}\bigg|_{s=0} s^n. \tag{B.1.3}$$

Then proving that

$$\frac{d^n f}{ds^n} = \overbrace{\big[X,\big[X,\dots\big[X,e^{sX} Y e^{-sX}\big]\dots\big]\big]}^{n \text{ commutators}} \tag{B.1.4}$$

proves (B.1.1) by letting $s = 1$. By recursion:
– $n = 1$:

$$\frac{df}{ds} = X e^{sX} Y e^{-sX} - e^{sX} Y e^{-sX} X \tag{B.1.5}$$

$$= \big[X, e^{sX} Y e^{-sX}\big] \tag{B.1.6}$$

– recursion:

$$\frac{d^{n+1} f}{ds^{n+1}} = \frac{d}{ds} \overbrace{\big[X,\dots\big[X,e^{sX} Y e^{-sX}\big]\dots\big]}^{n \text{ commutators}} \tag{B.1.7}$$

$$= \left[X,\dots\left[X,\frac{d}{ds} e^{sX} Y e^{-sX}\right]\dots\right] \tag{B.1.8}$$

$$= \overbrace{\big[X,\dots\big[X,\big[X,e^{sX} Y e^{-sX}\big]\big]\dots\big]}^{n+1 \text{ commutators}} \quad \# \tag{B.1.9}$$

B.2 Iterative approximate of the unitary transformation

We give here the details of the iterative scheme to derive an approximate of the unitary transformation eq. 3.4.13 which approximately fulfill the conservation of the number of double occupancies condition eq. 3.4.4. Following MacDonald *et al.*MacDonald et al. [1988], we define the following notation:

$$T^{(k)}(m_1, m_2, \dots, m_k) = T^{(k)}[m] = \hat{T}^{m_1} \hat{T}^{m_2} \dots \hat{T}^{m_k} \tag{B.2.1}$$

Then we find that

$$\begin{aligned}\left[\hat{V}, T^{(k)}[m]\right] &= \sum_l \left(\prod_{i=1}^{l-1} \hat{T}^{m_i} \left[\hat{V}, \hat{T}^{m_l}\right] \prod_{i=l+1}^{k} \hat{T}^{m_i} \right) \\ &= U \underbrace{\sum_l m_l}_{=M^{(k)}[m]} T^{(k)}[m]. \end{aligned} \tag{B.2.2}$$

It naturally follows that the terms which do not commute with $\hat{V}$ are those where $M^{(k)}[m] \neq 0$. At a given order k, the previous approximate $i\hat{S}^{(k-1)}$ leaves only terms of order t^k/U^{k-1}. Calling $\mathscr{H}'[k]$ these terms:

$$\mathscr{H}'[k] = U^{1-k} \sum_{\{m\}} C^{(k)}[m] T^{(k)}[m] \tag{B.2.3}$$

where $C^{(k)}[m]$ are simply the coefficients. From eq. B.2.2 it follows that defining:

$$i\hat{S}^{(k)} = i\hat{S}^{(k-1)} + U^{-k} \sum_{\{m\} \in M^{(k)}[m] \neq 0} \frac{C^{(k)}[m] T^{(k)}[m]}{M^{(k)}[m]} \tag{B.2.4}$$

will iteratively define order by order a suitable approximate of $i\hat{S}$. We show on fig. B.1 a short python program which carries out the calculation up to order t^4/U^3.

B.3 Formulas for the spin-wave Hamiltonian

We give here the formulas to calculate the $A_{\boldsymbol{k}}$ and the $B_{\boldsymbol{k}}$ factors in eq. 3.5.26:

$$\begin{aligned} H^{(2)}_{SW} = &\sum_{\boldsymbol{k}} \sum_{mm'} (A_{\boldsymbol{k}})_{mm'} \left(a^\dagger_{\boldsymbol{k}m} a_{\boldsymbol{k}m'} + a^\dagger_{\boldsymbol{k}m'} a_{\boldsymbol{k}m} \right) \\ &+ \frac{1}{2} (B_{\boldsymbol{k}})_{mm'} \left(a^\dagger_{\boldsymbol{k}m} a^\dagger_{-\boldsymbol{k}m'} + a_{\boldsymbol{k}m} a_{-\boldsymbol{k}m'} \right) \end{aligned} \tag{B.3.1}$$

the $A_{\boldsymbol{k}}$ and $B_{\boldsymbol{k}}$ terms are expressed as a sum over the $A^{\boldsymbol{\tau} ll'}_{\boldsymbol{k}}$ and $B^{\boldsymbol{\tau} ll'}_{\boldsymbol{k}}$ terms as defined in eq. 3.5.21 and 3.5.22:

$$A^{\boldsymbol{\tau} ll'}_{\boldsymbol{k}} = \begin{pmatrix} 2(1-2\epsilon_{\boldsymbol{\tau} ll'}) + \delta_{ll'}\epsilon_{\boldsymbol{\tau} ll'}\cos(\boldsymbol{k}\boldsymbol{\tau}) & (1-\delta_{ll'})\epsilon_{\boldsymbol{\tau} ll'}\cos(\boldsymbol{k}\boldsymbol{\tau}) \\ (1-\delta_{ll'})\epsilon_{\boldsymbol{\tau} ll'}\cos(\boldsymbol{k}\boldsymbol{\tau}) & 2(1-2\epsilon_{\boldsymbol{\tau} ll'}) + \delta_{ll'}\epsilon_{\boldsymbol{\tau} ll'}\cos(\boldsymbol{k}\boldsymbol{\tau}) \end{pmatrix} \tag{B.3.2}$$

$$B^{\boldsymbol{\tau} ll'}_{\boldsymbol{k}} = -\begin{pmatrix} 2\delta_{ll'}\bar{\epsilon}_{\boldsymbol{\tau} ll'}\cos(\boldsymbol{k}\boldsymbol{\tau}) & 2(1-\delta_{ll'})\bar{\epsilon}_{\boldsymbol{\tau} ll'}\cos(\boldsymbol{k}\boldsymbol{\tau}) \\ (1-\delta_{ll'})\bar{\epsilon}_{\boldsymbol{\tau} ll'}\cos(\boldsymbol{k}\boldsymbol{\tau}) & 2\delta_{ll'}\bar{\epsilon}_{\boldsymbol{\tau} ll'}\cos(\boldsymbol{k}\boldsymbol{\tau}) \end{pmatrix} \tag{B.3.3}$$

```
#!/bin/env python
from copy import deepcopy
from scipy.misc import factorial

class Op :
    "Class representing T^{(k)}[m]"
    def __init__(self,Tkm=[],Ckm=0):
        self.Tkm=Tkm # operators
        self.Ckm=Ckm # coefficients
    def __repr__(self):
        return '{0}T{1}'\
                .format(self.Ckm,\
                        self.Tkm)
    def __mul__(self,x):
        return Op(self.Tkm, self.Ckm*x)

def commutator(A,B):
    out=[]
    for a in A:
        for b in B:
            if a.Tkm==['v']:
                out+=[Op(b.Tkm,\
                         b.Ckm*\
                         sum(b.Tkm))]
            elif b.Tkm==['v']:
                out+=[Op(a.Tkm,\
                        -a.Ckm*\
                        sum(a.Tkm))]
            else:
                out+=[Op(a.Tkm+b.Tkm,\
                         a.Ckm*b.Ckm),\
                      Op(b.Tkm+a.Tkm,\
                      -a.Ckm*b.Ckm)]
    return out

def simplify(p):
    # Set of unique terms:
    out=[]
    un=set([tuple(o.Tkm) for o in p])
    for t in un:
        c=0
        for o in p:
            if tuple(o.Tkm)==t:
                c+=o.Ckm
        if abs(c)>1e-9:
            out+=[Op(list(t),c)]
    return out

def filter_hf_do(op,order):
    "filters terms for half-filling"
    if op.Tkm[-1]==0 or op.Tkm==['v']:
        return False
    for l in range(1,len(op.Tkm)):
        if sum(op.Tkm[l:])<0:
            return False
        if sum(op.Tkm[l:])==0\
                and op.Tkm[l-1]!=1:
            return False
    return len(op.Tkm)<order\
            or sum(op.Tkm)==0

if __name__=='__main__':
    # initial Hamiltonian
    H0=[Op([1],1.0),Op([-1],1.0),\
        Op([0],1.0),Op(['v'],1.0)]
    # initial (empty) transformation
    S=[]
    # initial transformed Hamiltonian
    Hk=deepcopy(H0)
    # order of the expansion
    order=4
    for k in range(order):
        # bad terms in H and update S
        for o in Hk:
            if o.Tkm!=['v']\
                    and sum(o.Tkm)!=0:
                S+=[Op(o.Tkm,\
                    o.Ckm/sum(o.Tkm))]
        # update H
        Hk=[]
        for t in range(k+2):
            h=deepcopy(H0)
            for s in range(t):
                h=commutator(S,h)
                h=[o for o in h\
                    if len(o.Tkm)\
                        <=(k+1)]
                h=simplify(h)
            Hk=simplify(Hk+\
                [o*(1/factorial(t))\
                    for o in h])
        Hk=simplify(Hk)
    print('Hk=')
    for o in Hk:
        if filter_hf_do(o,order):
            print(o)
    print('\nS(k)=')
    for o in S:
        print(o)
```

Figure B.1 – Full python code to produce the iterative approximate of the unitary transformation

We give the definition for $A_{\boldsymbol{k}}$. The $B_{\boldsymbol{k}}$ is exactly identical just by replacing the $A_{\boldsymbol{k}}^{\boldsymbol{\tau} ll'}$ with $B_{\boldsymbol{k}}^{\boldsymbol{\tau} ll'}$.

$$
\begin{aligned}
A_{\boldsymbol{k}} = & \sum_{\{1\,2\}} \left(\frac{4t_{12}^2}{U} - \frac{16t_{12}^4}{U^3} \right) SA_{\boldsymbol{k}}^{\boldsymbol{\tau}_{12} l_1 l_2} + \sum_{\{1\,2\,3\}} \frac{4t_{12}^2 t_{23}^2}{U^3} SA_{\boldsymbol{k}}^{\boldsymbol{\tau}_{13} l_1 l_3} \\
& - \sum_{\{1\,2\,3\,4\}} \frac{4t_{12}t_{23}t_{34}t_{41}}{U^3} \Bigg\{ \sum_{\substack{i,j=1 \\ i \neq j}}^{4} SA_{\boldsymbol{k}}^{\boldsymbol{\tau}_{ij} l_i l_j} \\
& - 20 \Big[(2\epsilon_{\boldsymbol{\tau}_{12} l_1 l_2} - 1) A_{\boldsymbol{k}}^{\boldsymbol{\tau}_{34} l_3 l_4} + (2\epsilon_{\boldsymbol{\tau}_{34} l_3 l_4} - 1) A_{\boldsymbol{k}}^{\boldsymbol{\tau}_{12} l_1 l_2} \\
& + (2\epsilon_{\boldsymbol{\tau}_{23} l_2 l_3} - 1) A_{\boldsymbol{k}}^{\boldsymbol{\tau}_{41} l_4 l_1} + (2\epsilon_{\boldsymbol{\tau}_{41} l_4 l_1} - 1) A_{\boldsymbol{k}}^{\boldsymbol{\tau}_{23} l_2 l_3} \\
& - (2\epsilon_{\boldsymbol{\tau}_{13} l_1 l_3} - 1) A_{\boldsymbol{k}}^{\boldsymbol{\tau}_{24} l_2 l_4} + (2\epsilon_{\boldsymbol{\tau}_{24} l_2 l_4} - 1) A_{\boldsymbol{k}}^{\boldsymbol{\tau}_{13} l_1 l_3} \Big] \Bigg\}
\end{aligned}
\tag{B.3.4}
$$

where the $\boldsymbol{\tau}_{ij} l_i l_j$ translation and layer indices are determined by the sites included in the two-, three- and four-sites plaquette exchange $\{1\,2\}$, $\{1\,2\,3\}$ and $\{1\,2\,3\,4\}$. The calculation of the $A_{\boldsymbol{k}}$ and $B_{\boldsymbol{k}}$ is then performed using a symbolic algebra software by first enumerating all possible plaquettes exchanges and then defining their corresponding $A_{\boldsymbol{k}}^{\boldsymbol{\tau}_{ij} l_i l_j}$ and $B_{\boldsymbol{k}}^{\boldsymbol{\tau}_{ij} l_i l_j}$ matrices.

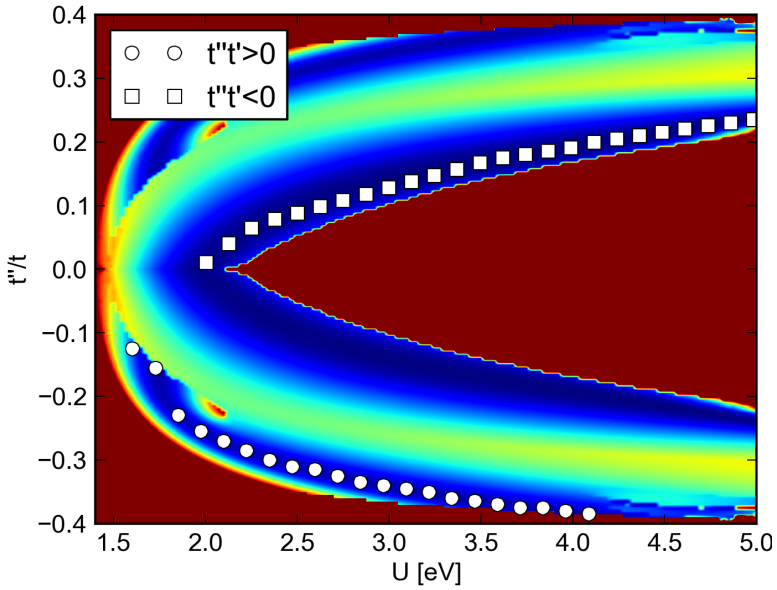

Figure B.2 – Color map of the fit quality as a function of U and t''/t. In the outer dark red regions the parameters are such that the spin-wave approach fails indicating the breakdown of the long-ranged Néel order hypothesis. In the central area of the displayed $(t''/t, U)$ plane, the spin-wave approach does bring a meaningful solution which results in a good fit quality. In particular, two distinct valleys of best fit solutions can be followed as a function of U. Inspecting the resulting $(t/U, t'/t)$ fitted parameters, we see the inner solution corresponds to $t't'' < 0$ and the outer one to $(t't'' > 0)$.

B.4 Fitting results for BSYCO

We provide in this appendix the fitting results in the case of the bilayer cuprate BSYCO. The results are qualitatively identical to those of SCOC discussed in section 3.6.3 and are not further discussed here.

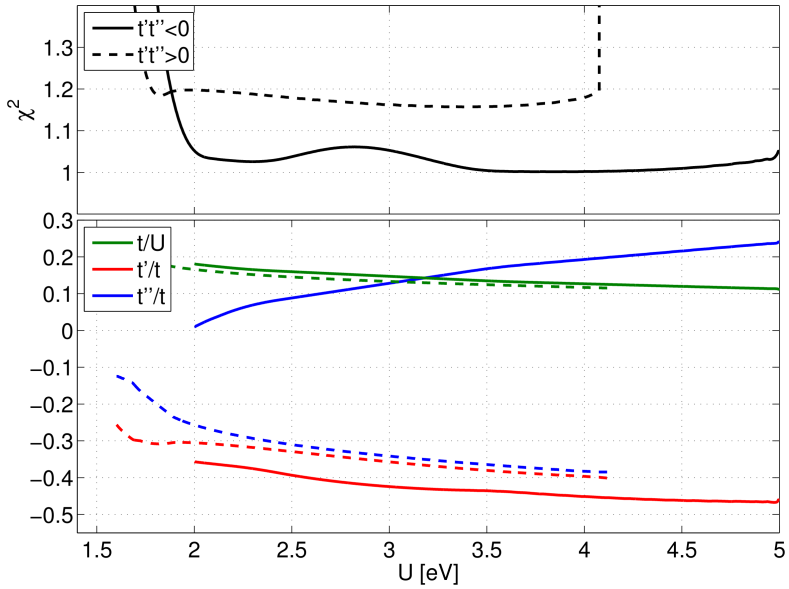

Figure B.3 – Fitted parameters for the best fit lines defined on fig. B.2. Top panel shows χ^2 along the inner (solid line) $t't'' < 0$ best fit line and the outer (dashed line) $t't'' > 0$ one. On the bottom panel are show the corresponding fitted parameters $(t''/t, t'/t, t/U)$ as a function of U along the best fit lines, solid line for $t't'' < 0$ and dashed for $t't'' > 0$.

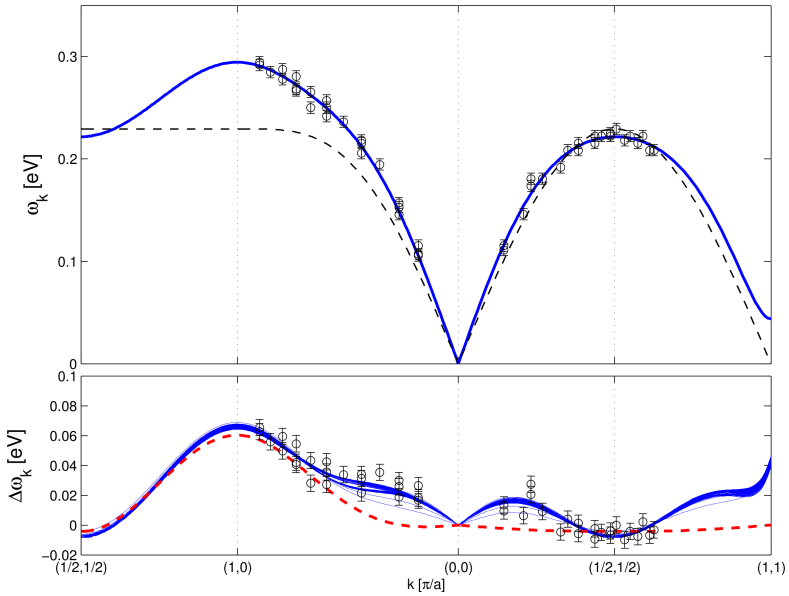

Figure B.4 – The obtained fitted dispersion for BSYCO. Top panel shows the experimental data and a range of fitted solutions (solid blue lines) with the magnon dispersion of a simple Heisenberg model (dashed grey line) with J chosen such that $\omega(\pi/2, \pi/2) = 2J$. On the bottom panel we subtract it to the data and the fitted dispersions and also show the dispersion from a fit to the $t-U$ Hubbard model fourth order strong coupling expansion (dashed red line).

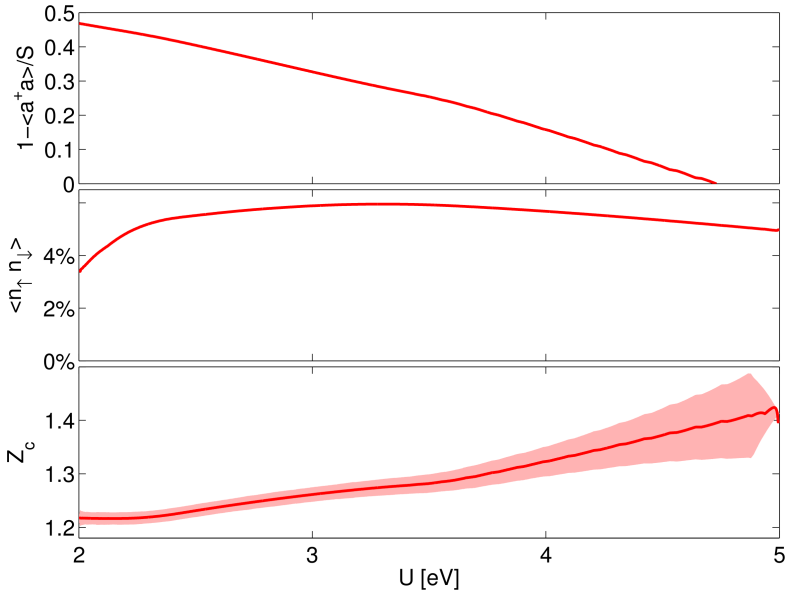

Figure B.5 – Various physical properties along the $t't'' < 0$ best fit line in fig. B.2. Top: Reduced staggered magnetization with an experimental determination (dashed black line, shaded area represents the uncertainty). Middle: The doubly occupied site density. Bottom: The $\boldsymbol{q}$-averaged first $1/S$ quantum renormalization of the magnon energy, Shaded area represents the variance σ^2 across the Brillouin Zone.

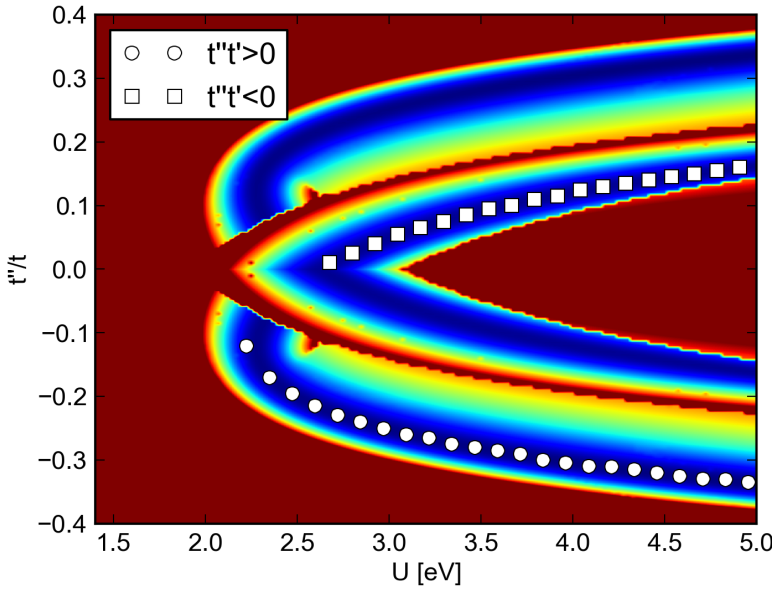

Figure B.6 – Color map of the fit quality as a function of U and t''/t. In the outer dark red regions the parameters are such that the spin-wave approach fails indicating the breakdown of the long-ranged Néel order hypothesis. In the central area of the displayed $(t''/t, U)$ plane, the spin-wave approach does bring a meaningful solution which results in a good fit quality. In particular, two distinct valleys of best fit solutions can be followed as a function of U. Inspecting the resulting $(t/U, t'/t)$ fitted parameters, we see the inner solution corresponds to $t't'' < 0$ and the outer one to $(t't'' > 0)$.

B.5 Fitting results for LCO

We provide in this appendix the fitting results in the case of the single layer cuprate LCO. The results are qualitatively identical to those of SCOC discussed in section 3.6.3 and are not further discussed here.

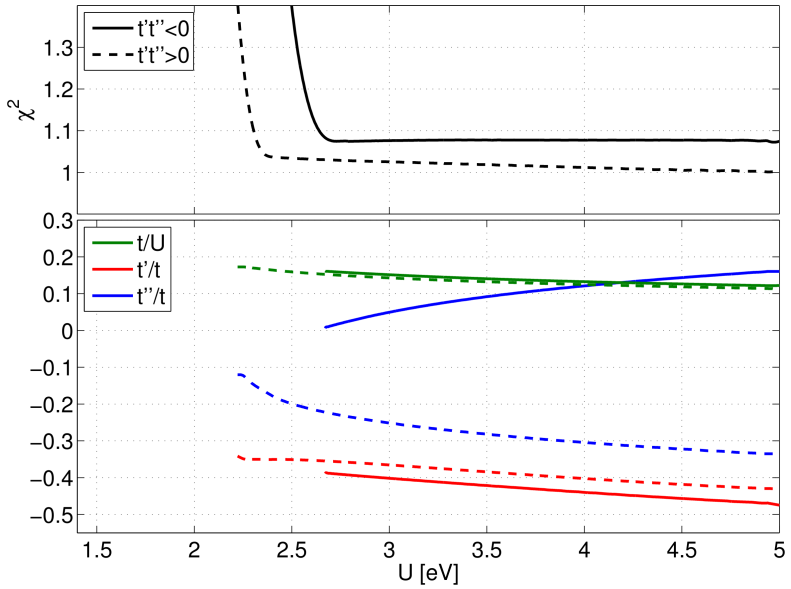

Figure B.7 – Fitted parameters for the best fit lines defined on fig. B.6. Top panel shows χ^2 along the inner (solid line) $t't'' < 0$ best fit line and the outer (dashed line) $t't'' > 0$ one. On the bottom panel are show the corresponding fitted parameters $(t''/t, t'/t, t/U)$ as a function of U along the best fit lines, solid line for $t't'' < 0$ and dashed for $t't'' > 0$.

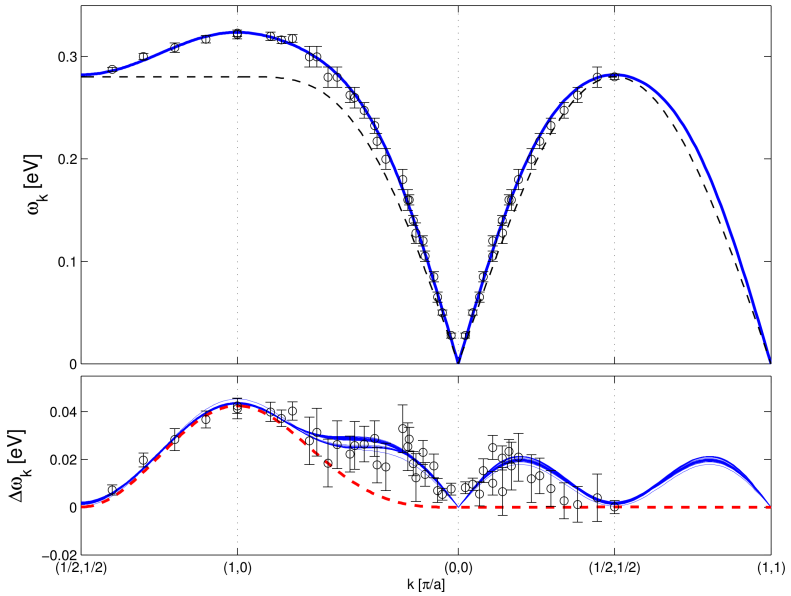

Figure B.8 – The obtained fitted dispersion for LCO. Top panel shows the experimental data and a range of fitted solutions (solid blue lines) with the magnon dispersion of a simple Heisenberg model (dashed grey line) with J chosen such that $\omega(\pi/2, \pi/2) = 2J$. On the bottom panel we subtract it to the data and the fitted dispersions and also show the dispersion from a fit to the $t-U$ Hubbard model fourth order strong coupling expansion (dashed red line).

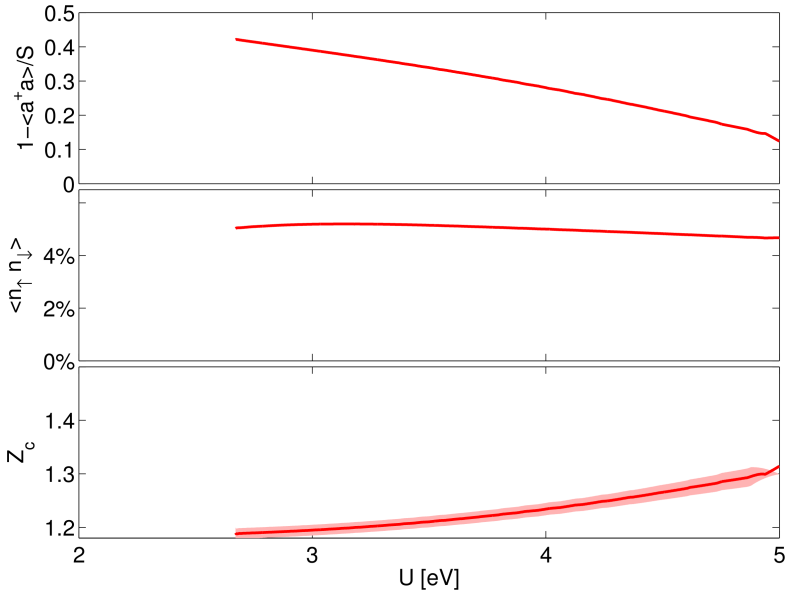

Figure B.9 – Various physical properties along the $t't'' < 0$ best fit line in fig. B.6. Top: Reduced staggered magnetization with an experimental determination (dashed black line, shaded area represents the uncertainty). Middle: The doubly occupied site density. Bottom: The $\boldsymbol{q}$-averaged first $1/S$ quantum renormalization of the magnon energy, Shaded area represents the variance σ^2 across the Brillouin Zone.

C Realization of in-house Quantum Wolf cluster

Components	Model	Number
CPU	Intel i5-3350	96
Motherboard	Gigabyte H61M-S1	96
Memory	Patriot DDR3 1333MHz 2x4GB	96
Power supply	FSP AURUM GOLD 600W	12
Fans	Arctic Cooling F12-PWM	60
Ethernet cables	Roline Kat. 5e Kabel 1m	96
Ethernet switches	Zyxel XGS1910-48	2

Table C.1 – Parts used to build the Quantum Wolf cluster.

In the process of the variational Monte Carlo project covered in chapter 2, the need of a large amount of CPU time quickly rose. This need was partially met by obtaining ten million CPU hours on the Swiss National Supercomputing Center (CSCS) Monte Rosa Cray XE6 cluster. But the constaints linked to the proposal-based CPU time attribution along with my personal interst in computing technical aspects motivated the realization of an in-house loosely interconnected cluster made out of consumer market parts. This kind of cluster is often reffered as "Beowulf" cluster and is a competitive alternative to professionnally-built clusters when the need of a fast-interconnect and of high quality of service are low. Probably following my badly pronounced english and Henrik's wild inspiration, the cluster was named "Quantum Wolf".
Monte Carlo calculations such as the ones described in 2 typically meet these criteria. The Monte Carlo sampling is trivially parallelized by carrying out several random walks in parallel, with essentially no communication needed between the running instances. In case of unexpected termination, there might be essentially no data loss if the Monte Carlo statistics is regularily saved, thus the there is no special reliability needs. Based on these considerations we built a in-house cluster whose key-features are:
– 96 nodes each with a 4-core CPU, totalling 384 computational cores.
– 9.6 TFlops (synthetic from the CPU documentation)
– Energy consumption of 4.8 kW
– Low cost of 312 CHF/node
We show on table C.1 the specific parts which where used. The cluster in simply air-cooled by a front wall of fans and a classic heat-exchanger at the back to thermalize the room the cluster is sitting in. In order to use the power supply in the most energy-efficient way, we power 8 nodes using a single power supply. The local network was setup with two switch interconnected together and with the master node with a 10Gbit/s network speed. The nodes themselves have simple 1Gbit networking. The computational nodes are diskless meaning they completely load in memory a stripped-down debian-based operating system booted from the local network. Standard comnputational libraries such as Message Passing Interface (MPI), Basic Linear Algebra Subroutines (BLAS), lapack of hdf5 for instances.
In terms of reliability the cluster, once setted up, did not suffer major incidents with a constant calculations being carried out over more than 3 months so far.

Figure C.1 – Front view of the cluster. The fans of the top shelf have been removed showing the motherboards stacked vertically in two rows such that each shelf carries 16 nodes powered by two power supplies.

Bibliography

Affleck, I., Zou, Z., Hsu, T., and Anderson, P. W. SU(2) gauge symmetry of the large-u limit of the hubbard model. *Physical Review B*, 38(1):745, July 1988. doi:10.1103/PhysRevB.38.745. URL http://link.aps.org/doi/10.1103/PhysRevB.38.745.

Ament, L. J. P., Ghiringhelli, G., Sala, M. M., Braicovich, L., and van den Brink, J. Theoretical demonstration of how the dispersion of magnetic excitations in cuprate compounds can be determined using resonant inelastic x-ray scattering. *Physical Review Letters*, 103(11): 117003, 2009. doi:10.1103/PhysRevLett.103.117003. URL http://link.aps.org/doi/10.1103/PhysRevLett.103.117003.

Anderson, P. Resonating valence bonds: A new kind of insulator? *Materials Research Bulletin*, 8(2):153–160, Feb. 1973. ISSN 0025-5408. doi:10.1016/0025-5408(73)90167-0. URL http://www.sciencedirect.com/science/article/pii/0025540873901670.

Anderson, P. W. An approximate quantum theory of the antiferromagnetic ground state. *Physical Review*, 86(5):694–701, June 1952. doi:10.1103/PhysRev.86.694. URL http://link.aps.org/doi/10.1103/PhysRev.86.694.

Anderson, P. W. The resonating valence bond state in La2CuO4 and superconductivity. *Science*, 235(4793):1196 –1198, Mar. 1987. doi:10.1126/science.235.4793.1196. URL http://www.sciencemag.org/content/235/4793/1196.abstract.

Auerbach, A. and Arovas, D. P. Spin dynamics in the square-lattice antiferromagnet. *Physical Review Letters*, 61(5):617–620, Aug. 1988. doi:10.1103/PhysRevLett.61.617. URL http://link.aps.org/doi/10.1103/PhysRevLett.61.617.

Balents, L. Spin liquids in frustrated magnets. *Nature*, 464(7286):199–208, Mar. 2010. ISSN 0028-0836. doi:10.1038/nature08917. URL http://www.nature.com/nature/journal/v464/n7286/full/nature08917.html.

Bardeen, J., Cooper, L. N., and Schrieffer, J. R. Theory of superconductivity. *Physical Review*, 108(5):1175–1204, Dec. 1957. doi:10.1103/PhysRev.108.1175. URL http://link.aps.org/doi/10.1103/PhysRev.108.1175.

Bednorz, J. G. and Müller, K. A. Possible highT c superconductivity in the Ba-La-Cu-O system. *Zeitschrift für Physik B Condensed Matter*, 64(2):189–193, June 1986. ISSN 0722-3277, 1431-584X. doi:10.1007/BF01303701. URL http://link.springer.com/article/10.1007/BF01303701.

Bethe, H. Zur theorie der metalle. *Zeitschrift für Physik A Hadrons and Nuclei*, 71(3):205–226, 1931. ISSN 0939-7922. doi:10.1007/BF01341708. URL http://www.springerlink.com/content/g86x6317566uh2x6/abstract/.

Birgeneau, R. J., Greven, M., Kastner, M. A., Lee, Y. S., Wells, B. O., Endoh, Y., Yamada, K., and Shirane, G. Instantaneous spin correlations in la_2cuo_4. *Physical Review B*, 59(21):13788–13794, June 1999. doi:10.1103/PhysRevB.59.13788. URL http://link.aps.org/doi/10.1103/PhysRevB.59.13788.

Bloch, F. Zur theorie des ferromagnetismus. *Zeitschrift für Physik*, 61(3-4):206–219, Mar. 1930. ISSN 0044-3328. doi:10.1007/BF01339661. URL http://link.springer.com/article/10.1007/BF01339661.

Bramwell, S. T. and Gingras, M. J. P. Spin ice state in frustrated magnetic pyrochlore materials. *Science*, 294(5546):1495–1501, Nov. 2001. ISSN 0036-8075, 1095-9203. doi:10.1126/science.1064761. URL http://www.sciencemag.org/content/294/5546/1495. PMID: 11711667.

Bramwell, S. T., Giblin, S. R., Calder, S., Aldus, R., Prabhakaran, D., and Fennell, T. Measurement of the charge and current of magnetic monopoles in spin ice. *Nature*, 461(7266):956–959, Oct. 2009. ISSN 0028-0836. doi:10.1038/nature08500. URL http://www.nature.com/nature/journal/v461/n7266/abs/nature08500.html.

Brookes, M. The matrix reference manual [online], 2011. URL http://www.ee.imperial.ac.uk/hp/staff/dmb/matrix/intro.html.

Burger, N., Fuess, H., and Burlet, P. Neutron diffraction study of the antiferromagnetic phase of copper formate tetradeuterate. *Solid State Communications*, 34(11):883–886, June 1980. ISSN 0038-1098. doi:10.1016/0038-1098(80)90117-9. URL http://www.sciencedirect.com/science/article/pii/0038109880901179.

Calandra Buonaura, M. and Sorella, S. Numerical study of the two-dimensional heisenberg model using a green function monte carlo technique with a fixed number of walkers. *Physical Review B*, 57(18):11446–11456, May 1998. doi:10.1103/PhysRevB.57.11446. URL http://link.aps.org/doi/10.1103/PhysRevB.57.11446.

Canali, C. M. and Girvin, S. M. Theory of raman scattering in layered cuprate materials. *Physical Review B*, 45(13):7127–7160, Apr. 1992. doi:10.1103/PhysRevB.45.7127. URL http://link.aps.org/doi/10.1103/PhysRevB.45.7127.

Canali, C. M. and Wallin, M. Spin-spin correlation functions for the square-lattice heisenberg antiferromagnet at zero temperature. *Physical Review B*, 48(5):3264–3280, Aug. 1993. doi:10.1103/PhysRevB.48.3264. URL http://link.aps.org/doi/10.1103/PhysRevB.48.3264.

Castelnovo, C., Moessner, R., and Sondhi, S. L. Magnetic monopoles in spin ice. *Nature*, 451 (7174):42–45, Jan. 2008. ISSN 0028-0836. doi:10.1038/nature06433. URL http://www.nature.com/nature/journal/v451/n7174/full/nature06433.html.

Caux, J.-S. and Hagemans, R. The four-spinon dynamical structure factor of the heisenberg chain. *Journal of Statistical Mechanics: Theory and Experiment*, 2006(12):P12013, Dec. 2006. ISSN 1742-5468. doi:10.1088/1742-5468/2006/12/P12013. URL http://iopscience.iop.org/1742-5468/2006/12/P12013.

Chang, J., Shi, M., Pailhés, S., Månsson, M., Claesson, T., Tjernberg, O., Bendounan, A., Sassa, Y., Patthey, L., Momono, N., Oda, M., Ido, M., Guerrero, S., Mudry, C., and Mesot, J. Anisotropic quasiparticle scattering rates in slightly underdoped to optimally doped high-temperature $la_{2-x}sr_xcuo_4$ superconductors. *Physical Review B*, 78(20):205103, Nov. 2008. doi:10.1103/PhysRevB.78.205103. URL http://link.aps.org/doi/10.1103/PhysRevB.78.205103.

Christensen, N. B., Rønnow, H. M., McMorrow, D. F., Harrison, A., Perring, T. G., Enderle, M., Coldea, R., Regnault, L. P., and Aeppli, G. Quantum dynamics and entanglement of spins on a square lattice. *Proceedings of the National Academy of Sciences*, 104(39):15264 –15269, 2007. doi:10.1073/pnas.0703293104. URL http://www.pnas.org/content/104/39/15264.abstract.

Chuang, Y.-D., Gromko, A. D., Fedorov, A. V., Aiura, Y., Oka, K., Ando, Y., Lindroos, M., Markiewicz, R. S., Bansil, A., and Dessau, D. S. Bilayer splitting and coherence effects in optimal and underdoped $bi_2sr_2cacu_2o_{8+\delta}$. *Physical Review B*, 69(9):094515, Mar. 2004. doi:10.1103/PhysRevB.69.094515. URL http://link.aps.org/doi/10.1103/PhysRevB.69.094515.

Clarke, S. J., Harrison, A., Mason, T. E., McIntyre, G. J., and Visser, D. Magnetic ordering and fluctuations in the s=1/2 square heisenberg antiferromagnet $cu(dco_2)_2{\cdot}4d_2oi$. *Journal of Physics: Condensed Matter*, 4(4):L71, Jan. 1992. ISSN 0953-8984. doi:10.1088/0953-8984/4/4/003. URL http://iopscience.iop.org/0953-8984/4/4/003.

Coldea, R., Hayden, S. M., Aeppli, G., Perring, T. G., Frost, C. D., Mason, T. E., Cheong, S.-W., and Fisk, Z. Spin waves and electronic interactions in la_2cuo_4. *Physical Review Letters*, 86 (23):5377, June 2001a. doi:10.1103/PhysRevLett.86.5377. URL http://link.aps.org/doi/10.1103/PhysRevLett.86.5377.

Coldea, R., Tennant, D. A., Tsvelik, A. M., and Tylczynski, Z. Experimental realization of a 2D fractional quantum spin liquid. *Physical Review Letters*, 86(7):1335–1338, Feb. 2001b. doi:10.1103/PhysRevLett.86.1335. URL http://link.aps.org/doi/10.1103/PhysRevLett.86.1335.

Dagotto, E. Correlated electrons in high-temperature superconductors. *Reviews of Modern Physics*, 66(3):763–840, July 1994. doi:10.1103/RevModPhys.66.763. URL http://link.aps.org/doi/10.1103/RevModPhys.66.763.

Dalla Piazza, B., Mourigal, M., Guarise, M., Berger, H., Schmitt, T., Zhou, K. J., Grioni, M., and Rønnow, H. M. Unified one-band hubbard model for magnetic and electronic spectra of the parent compounds of cuprate superconductors. *Physical Review B*, 85(10):100508, Mar. 2012. doi:10.1103/PhysRevB.85.100508. URL http://link.aps.org/doi/10.1103/PhysRevB.85.100508.

Damascelli, A., Hussain, Z., and Shen, Z.-X. Angle-resolved photoemission studies of the cuprate superconductors. *Reviews of Modern Physics*, 75(2):473–541, Apr. 2003. doi:10.1103/RevModPhys.75.473. URL http://link.aps.org/doi/10.1103/RevModPhys.75.473.

de Vries, M. A., Stewart, J. R., Deen, P. P., Piatek, J. O., Nilsen, G. J., Rønnow, H. M., and Harrison, A. Scale-free antiferromagnetic fluctuations in the s=1/2 kagome antiferromagnet herbertsmithite. *Physical Review Letters*, 103(23):237201, Dec. 2009. doi:10.1103/PhysRevLett.103.237201. URL http://link.aps.org/doi/10.1103/PhysRevLett.103.237201.

Delannoy, J.-Y. P., Gingras, M. J. P., Holdsworth, P. C. W., and Tremblay, A.-M. S. Low-energy theory of the t-t'-t''-u hubbard model at half-filling: Interaction strengths in cuprate superconductors and an effective spin-only description of la_2cuo_4. *Physical Review B*, 79(23):235130, June 2009. doi:10.1103/PhysRevB.79.235130. URL http://link.aps.org/doi/10.1103/PhysRevB.79.235130.

Devereaux, T. P. and Hackl, R. Inelastic light scattering from correlated electrons. *Reviews of Modern Physics*, 79(1):175–233, Jan. 2007. doi:10.1103/RevModPhys.79.175. URL http://link.aps.org/doi/10.1103/RevModPhys.79.175.

Edegger, B., Muthukumar, V. N., and Gros, C. Gutzwiller–RVB theory of high-temperature superconductivity: Results from renormalized mean-field theory and variational monte carlo calculations. *Advances in Physics*, 56(6):927–1033, 2007. ISSN 0001-8732. doi:10.1080/00018730701627707. URL http://www.tandfonline.com/doi/abs/10.1080/00018730701627707.

Einstein, A. über einen die erzeugung und verwandlung des lichtes betreffenden heuristischen gesichtspunkt. *Annalen der Physik*, 322:132–148, 1905. ISSN 0003-3804. doi:10.1002/andp.19053220607. URL http://adsabs.harvard.edu/abs/1905AnP...322..132E.

Ellis, D. S., Kim, J., Hill, J. P., Wakimoto, S., Birgeneau, R. J., Shvyd'ko, Y., Casa, D., Gog, T., Ishii, K., Ikeuchi, K., Paramekanti, A., and Kim, Y.-J. Magnetic nature of the 500 mev peak in $la_{2-x}sr_xcuo_4$ observed with resonant inelastic x-ray scattering at the cu k-edge. *Physical Review B*, 81(8):085124, Feb. 2010. doi:10.1103/PhysRevB.81.085124. URL http://link.aps.org/doi/10.1103/PhysRevB.81.085124.

Emery, V. J. Theory of high-t_c superconductivity in oxides. *Physical Review Letters*, 58(26):2794–2797, June 1987. doi:10.1103/PhysRevLett.58.2794. URL http://link.aps.org/doi/10.1103/PhysRevLett.58.2794.

Eskes, H., Sawatzky, G., and Feiner, L. Effective transfer for singlets formed by hole doping in the high-tc superconductors. *Physica C: Superconductivity*, 160(5–6):424–430, Oct. 1989. ISSN 0921-4534. doi:10.1016/0921-4534(89)90415-2. URL http://www.sciencedirect.com/science/article/pii/0921453489904152.

Faddeev, L. and Takhtajan, L. What is the spin of a spin wave? *Physics Letters A*, 85(6–7): 375–377, Oct. 1981. ISSN 0375-9601. doi:10.1016/0375-9601(81)90335-2. URL http://www.sciencedirect.com/science/article/pii/0375960181903352.

Feynman, R. P. Forces in molecules. *Physical Review*, 56(4):340–343, Aug. 1939. doi:10.1103/PhysRev.56.340. URL http://link.aps.org/doi/10.1103/PhysRev.56.340.

Forte, F., Ament, L. J. P., and van den Brink, J. Magnetic excitations in la_2cuo_4 probed by indirect resonant inelastic x-ray scattering. *Physical Review B*, 77(13):134428, Apr. 2008. doi:10.1103/PhysRevB.77.134428. URL http://link.aps.org/doi/10.1103/PhysRevB.77.134428.

Foulkes, W. M. C., Mitas, L., Needs, R. J., and Rajagopal, G. Quantum monte carlo simulations of solids. *Reviews of Modern Physics*, 73(1):33–83, Jan. 2001. doi:10.1103/RevModPhys.73.33. URL http://link.aps.org/doi/10.1103/RevModPhys.73.33.

Gebhard, F. and Vollhardt, D. Correlation functions for hubbard-type models: The exact results for the gutzwiller wave function in one dimension. *Physical Review Letters*, 59(13):1472–1475, Sept. 1987. doi:10.1103/PhysRevLett.59.1472. URL http://link.aps.org/doi/10.1103/PhysRevLett.59.1472.

Gelfand, M. P., Singh, R. R. P., and Huse, D. A. Perturbation expansions for quantum many-body systems. *Journal of Statistical Physics*, 59(5-6):1093–1142, June 1990. ISSN 0022-4715, 1572-9613. doi:10.1007/BF01334744. URL http://link.springer.com/article/10.1007/BF01334744.

Giamarchi, T. *Quantum Physics in One Dimension*. Number 121 in International Series of Monographs on Physics. Clarendon Press, Oxford, 2004.

Graf, J., Gweon, G.-H., McElroy, K., Zhou, S. Y., Jozwiak, C., Rotenberg, E., Bill, A., Sasagawa, T., Eisaki, H., Uchida, S., Takagi, H., Lee, D.-H., and Lanzara, A. Universal high energy anomaly in the angle-resolved photoemission spectra of high temperature superconductors: Possible evidence of spinon and holon branches. *Physical Review Letters*, 98(6):067004, Feb. 2007. doi:10.1103/PhysRevLett.98.067004. URL http://link.aps.org/doi/10.1103/PhysRevLett.98.067004.

Greven, M., Birgeneau, R. J., Endoh, Y., Kastner, M. A., Matsuda, M., and Shirane, G. Neutron scattering study of the two-dimensional spinS=1/2 square-lattice heisenberg antiferromagnet $sr_2cuo_2cl_2$. *Zeitschrift für Physik B Condensed Matter*, 96(4):465–477, Dec. 1995. ISSN 0722-3277, 1431-584X. doi:10.1007/BF01313844. URL http://link.springer.com/article/10.1007/BF01313844.

Gros, C. Superconductivity in correlated wave functions. *Physical Review B*, 38(1):931–934, July 1988. doi:10.1103/PhysRevB.38.931. URL http://link.aps.org/doi/10.1103/PhysRevB.38.931.

Gros, C. Physics of projected wavefunctions. *Annals of Physics*, 189(1):53–88, Jan. 1989. ISSN 0003-4916. doi:10.1016/0003-4916(89)90077-8. URL http://www.sciencedirect.com/science/article/pii/0003491689900778.

Gros, C., Joynt, R., and Rice, T. M. Antiferromagnetic correlations in almost-localized fermi liquids. *Physical Review B*, 36(1):381–393, July 1987. doi:10.1103/PhysRevB.36.381. URL http://link.aps.org/doi/10.1103/PhysRevB.36.381.

Guarise, M. *Electronic and Magnetic Resonant Inelastic X-ray Study of Cuprates*. PhD thesis, École Polytechnique Fédérale de Lausanne, 2012. URL http://infoscience.epfl.ch/record/181539.

Guarise, M., Dalla Piazza, B., Moretti Sala, M., Ghiringhelli, G., Braicovich, L., Berger, H., Hancock, J. N., van der Marel, D., Schmitt, T., Strocov, V. N., Ament, L. J. P., van den Brink, J., Lin, P.-H., Xu, P., Rønnow, H. M., and Grioni, M. Measurement of magnetic excitations in the two-dimensional antiferromagnetic $sr_2cuo_2cl_2$ insulator using resonant x-ray scattering: Evidence for extended interactions. *Physical Review Letters*, 105(15):157006, Oct. 2010. doi:10.1103/PhysRevLett.105.157006. URL http://link.aps.org/doi/10.1103/PhysRevLett.105.157006.

Gutzwiller, M. C. Effect of correlation on the ferromagnetism of transition metals. *Physical Review Letters*, 10(5):159–162, Mar. 1963. doi:10.1103/PhysRevLett.10.159. URL http://link.aps.org/doi/10.1103/PhysRevLett.10.159.

Hamer, C. J., Zheng Weihong, and Arndt, P. Third-order spin-wave theory for the heisenberg antiferromagnet. *Physical Review B*, 46(10):6276–6292, Sept. 1992. doi:10.1103/PhysRevB.46.6276. URL http://link.aps.org/doi/10.1103/PhysRevB.46.6276.

Han, T.-H., Helton, J. S., Chu, S., Nocera, D. G., Rodriguez-Rivera, J. A., Broholm, C., and Lee, Y. S. Fractionalized excitations in the spin-liquid state of a kagome-lattice antiferromagnet. *Nature*, 492(7429):406–410, Dec. 2012. ISSN 0028-0836. doi:10.1038/nature11659. URL http://www.nature.com/nature/journal/v492/n7429/full/nature11659.html.

Hastings, W. K. Monte carlo sampling methods using markov chains and their applications. *Biometrika*, 57(1):97–109, Apr. 1970. ISSN 0006-3444. doi:10.2307/2334940. URL http://www.jstor.org/stable/2334940. ArticleType: research-article / Full publication date: Apr., 1970 / Copyright © 1970 Biometrika Trust.

Haverkort, M. W. Theory of resonant inelastic x-ray scattering by collective magnetic excitations. *Physical Review Letters*, 105(16):167404, Oct. 2010. doi:10.1103/PhysRevLett.105.167404. URL http://link.aps.org/doi/10.1103/PhysRevLett.105.167404.

Headings, N. S., Hayden, S. M., Coldea, R., and Perring, T. G. Anomalous high-energy spin excitations in the high-t_c superconductor-parent antiferromagnet la_2cuo_4. *Physical Review Letters*, 105(24):247001, Dec. 2010. doi:10.1103/PhysRevLett.105.247001. URL http://link.aps.org/doi/10.1103/PhysRevLett.105.247001.

Hirsch, J. E. Two-dimensional hubbard model: Numerical simulation study. *Physical Review B*, 31(7):4403–4419, Apr. 1985. doi:10.1103/PhysRevB.31.4403. URL http://link.aps.org/doi/10.1103/PhysRevB.31.4403.

Ho, C.-M., Muthukumar, V. N., Ogata, M., and Anderson, P. W. Nature of spin excitations in two-dimensional mott insulators: Undoped cuprates and other materials. *Physical Review Letters*, 86(8):1626–1629, Feb. 2001. doi:10.1103/PhysRevLett.86.1626. URL http://link.aps.org/doi/10.1103/PhysRevLett.86.1626.

Holstein, T. and Primakoff, H. Field dependence of the intrinsic domain magnetization of a ferromagnet. *Physical Review*, 58(12):1098–1113, Dec. 1940. doi:10.1103/PhysRev.58.1098. URL http://link.aps.org/doi/10.1103/PhysRev.58.1098.

Hsu, T. C. Spin waves in the flux-phase description of the s=1/2 heisenberg antiferromagnet. *Physical Review B*, 41(16):11379, June 1990. doi:10.1103/PhysRevB.41.11379. URL http://link.aps.org/doi/10.1103/PhysRevB.41.11379.

Hybertsen, M. S., Stechel, E. B., Schluter, M., and Jennison, D. R. Renormalization from density-functional theory to strong-coupling models for electronic states in cu-o materials. *Physical Review B*, 41(16):11068–11072, June 1990. doi:10.1103/PhysRevB.41.11068. URL http://link.aps.org/doi/10.1103/PhysRevB.41.11068.

Igarashi, J.-i. 1/s expansion for thermodynamic quantities in a two-dimensional heisenberg antiferromagnet at zero temperature. *Physical Review B*, 46(17):10763, Nov. 1992. doi:10.1103/PhysRevB.46.10763. URL http://link.aps.org/doi/10.1103/PhysRevB.46.10763.

Igarashi, J.-i. and Nagao, T. 1/s-expansion study of spin waves in a two-dimensional heisenberg antiferromagnet. *Physical Review B*, 72(1):014403, July 2005. doi:10.1103/PhysRevB.72.014403. URL http://link.aps.org/doi/10.1103/PhysRevB.72.014403.

Imambekov, A., Schmidt, T. L., and Glazman, L. I. One-dimensional quantum liquids: Beyond the luttinger liquid paradigm. *Reviews of Modern Physics*, 84(3):1253–1306, Sept. 2012. doi:10.1103/RevModPhys.84.1253. URL http://link.aps.org/doi/10.1103/RevModPhys.84.1253.

Inosov, D. S., Fink, J., Kordyuk, A. A., Borisenko, S. V., Zabolotnyy, V. B., Schuster, R., Knupfer, M., Büchner, B., Follath, R., Dürr, H. A., Eberhardt, W., Hinkov, V., Keimer, B., and Berger, H. Momentum and energy dependence of the anomalous high-energy dispersion in the electronic structure of high temperature superconductors. *Physical Review Letters*, 99(23):237002, Dec. 2007. doi:10.1103/PhysRevLett.99.237002. URL http://link.aps.org/doi/10.1103/PhysRevLett.99.237002.

Ivanov, D. A. Antiferromagnetism and phase separation in the t-j model at low doping: A variational study. *Physical Review B*, 70(10):104503, Sept. 2004. doi:10.1103/PhysRevB.70.104503. URL http://link.aps.org/doi/10.1103/PhysRevB.70.104503.

Ivanov, D. A. Resonating-valence-bond structure of gutzwiller-projected superconducting wave functions. *Physical Review B*, 74(2):024525, July 2006. doi:10.1103/PhysRevB.74.024525. URL http://link.aps.org/doi/10.1103/PhysRevB.74.024525.

Ivanov, D. A. and Lee, P. A. Staggered-flux normal state in the weakly doped t-j model. *Physical Review B*, 68(13):132501, Oct. 2003. doi:10.1103/PhysRevB.68.132501. URL http://link.aps.org/doi/10.1103/PhysRevB.68.132501.

Jarrell, M. and Gubernatis, J. Bayesian inference and the analytic continuation of imaginary-time quantum monte carlo data. *Physics Reports*, 269(3):133–195, May 1996. ISSN 0370-1573. doi:10.1016/0370-1573(95)00074-7. URL http://www.sciencedirect.com/science/article/pii/0370157395000747.

Jastrow, R. Many-body problem with strong forces. *Physical Review*, 98(5):1479–1484, June 1955. doi:10.1103/PhysRev.98.1479. URL http://link.aps.org/doi/10.1103/PhysRev.98.1479.

Jaubert, L. D. C. and Holdsworth, P. C. W. Signature of magnetic monopole and dirac string dynamics in spin ice. *Nature Physics*, 5(4):258–261, Apr. 2009. ISSN 1745-2473. doi:10.1038/nphys1227. URL http://www.nature.com/nphys/journal/v5/n4/abs/nphys1227.html.

Jeong, M., Bert, F., Mendels, P., Duc, F., Trombe, J. C., de Vries, M. A., and Harrison, A. Field-induced freezing of a quantum spin liquid on the kagome lattice. *Physical Review Letters*, 107(23):237201, Nov. 2011. doi:10.1103/PhysRevLett.107.237201. URL http://link.aps.org/doi/10.1103/PhysRevLett.107.237201.

Jordan, P. and Wigner, E. Über das paulische Äquivalenzverbot. *Zeitschrift für Physik*, 47(9-10):631–651, Sept. 1928. ISSN 0044-3328. doi:10.1007/BF01331938. URL http://link.springer.com/article/10.1007/BF01331938.

Karbach, M., Müller, G., Bougourzi, A. H., Fledderjohann, A., and Mütter, K.-H. Two-spinon dynamic structure factor of the one-dimensional s= heisenberg antiferromagnet. *Physical Review B*, 55(18):12510–12517, May 1997. doi:10.1103/PhysRevB.55.12510. URL http://link.aps.org/doi/10.1103/PhysRevB.55.12510.

Katanin, A. A. and Kampf, A. P. Theoretical analysis of magnetic raman scattering in la_2cuo_4: Two-magnon intensity with the inclusion of ring exchange. *Physical Review B*, 67(10):100404, Mar. 2003. doi:10.1103/PhysRevB.67.100404. URL http://link.aps.org/doi/10.1103/PhysRevB.67.100404.

Kim, C., Matsuura, A. Y., Shen, Z.-X., Motoyama, N., Eisaki, H., Uchida, S., Tohyama, T., and Maekawa, S. Observation of spin-charge separation in one-dimensional $srcuo_2$. *Physical*

Review Letters, 77(19):4054–4057, Nov. 1996. doi:10.1103/PhysRevLett.77.4054. URL http://link.aps.org/doi/10.1103/PhysRevLett.77.4054.

Kim, J., Casa, D., Upton, M. H., Gog, T., Kim, Y.-J., Mitchell, J. F., van Veenendaal, M., Daghofer, M., van den Brink, J., Khaliullin, G., and Kim, B. J. Magnetic excitation spectra of sr_2iro_4 probed by resonant inelastic x-ray scattering: Establishing links to cuprate superconductors. *Physical Review Letters*, 108(17):177003, Apr. 2012. doi:10.1103/PhysRevLett.108.177003. URL http://link.aps.org/doi/10.1103/PhysRevLett.108.177003.

Kim, Y. J., Aharony, A., Birgeneau, R. J., Chou, F. C., Entin-Wohlman, O., Erwin, R. W., Greven, M., Harris, A. B., Kastner, M. A., Korenblit, I. Y., Lee, Y. S., and Shirane, G. Ordering due to quantum fluctuations in $sr_2cu_3o_4cl_2$. *Physical Review Letters*, 83(4):852–855, July 1999. doi:10.1103/PhysRevLett.83.852. URL http://link.aps.org/doi/10.1103/PhysRevLett.83.852.

Kim, Y. J., Birgeneau, R. J., Chou, F. C., Greven, M., Kastner, M. A., Lee, Y. S., Wells, B. O., Aharony, A., Entin-Wohlman, O., Korenblit, I. Y., Harris, A. B., Erwin, R. W., and Shirane, G. Neutron scattering study of $sr_2cu_3o_4cl_2$. *Physical Review B*, 64(2):024435, June 2001. doi:10.1103/PhysRevB.64.024435. URL http://link.aps.org/doi/10.1103/PhysRevB.64.024435.

Kubo, R. The spin-wave theory of antiferromagnetics. *Physical Review*, 87(4):568–580, Aug. 1952. doi:10.1103/PhysRev.87.568. URL http://link.aps.org/doi/10.1103/PhysRev.87.568.

Lake, B., Tennant, D. A., Frost, C. D., and Nagler, S. E. Quantum criticality and universal scaling of a quantum antiferromagnet. *Nature Materials*, 4(4):329–334, Apr. 2005. ISSN 1476-1122. doi:10.1038/nmat1327. URL http://www.nature.com/nmat/journal/v4/n4/abs/nmat1327.html.

LaRosa, S., Vobornik, I., Zwick, F., Berger, H., Grioni, M., Margaritondo, G., Kelley, R. J., Onellion, M., and Chubukov, A. Electronic structure of cuo_2 planes: From insulator to superconductor. *Physical Review B*, 56(2):R525–R528, July 1997. doi:10.1103/PhysRevB.56.R525. URL http://link.aps.org/doi/10.1103/PhysRevB.56.R525.

Laughlin, R. B. Numerical evidence for electron decay in the two-dimensional t-j model. *Journal of Low Temperature Physics*, 99(3-4):443–466, May 1995. ISSN 0022-2291, 1573-7357. doi:10.1007/BF00752323. URL http://link.springer.com/article/10.1007/BF00752323.

Lecheminant, P., Bernu, B., Lhuillier, C., Pierre, L., and Sindzingre, P. Order versus disorder in the quantum heisenberg antiferromagnet on the kagomé lattice using exact spectra analysis. *Physical Review B*, 56(5):2521–2529, Aug. 1997. doi:10.1103/PhysRevB.56.2521. URL http://link.aps.org/doi/10.1103/PhysRevB.56.2521.

Lee, P. A., Nagaosa, N., and Wen, X.-G. Doping a mott insulator: Physics of high-temperature superconductivity. *Reviews of Modern Physics*, 78(1):17, Jan. 2006. doi:10.1103/RevModPhys.78.17. URL http://link.aps.org/doi/10.1103/RevModPhys.78.17.

Lee, T. K. and Feng, S. Doping dependence of antiferromagnetism in la_2cuo_4: A numerical study based on a resonating-valence-bond state. *Physical Review B*, 38(16):11809–11812, Dec. 1988. doi:10.1103/PhysRevB.38.11809. URL http://link.aps.org/doi/10.1103/PhysRevB.38.11809.

Li, T. and Yang, F. Variational study of the neutron resonance mode in the cuprate superconductors. *Physical Review B*, 81(21):214509, June 2010. doi:10.1103/PhysRevB.81.214509. URL http://link.aps.org/doi/10.1103/PhysRevB.81.214509.

Lieb, E. H. and Wu, F. Y. Absence of mott transition in an exact solution of the short-range, one-band model in one dimension. *Physical Review Letters*, 20(25):1445–1448, June 1968. doi:10.1103/PhysRevLett.20.1445. URL http://link.aps.org/doi/10.1103/PhysRevLett.20.1445.

Lorenzana, J., Seibold, G., and Coldea, R. Sum rules and missing spectral weight in magnetic neutron scattering in the cuprates. *Physical Review B*, 72(22):224511, Dec. 2005. doi:10.1103/PhysRevB.72.224511. URL http://link.aps.org/doi/10.1103/PhysRevB.72.224511.

Lu, D., Vishik, I. M., Yi, M., Chen, Y., Moore, R. G., and Shen, Z.-X. Angle-resolved photoemission studies of quantum materials. *Annual Review of Condensed Matter Physics*, 3 (1):129–167, 2012. doi:10.1146/annurev-conmatphys-020911-125027. URL http://www.annualreviews.org/doi/abs/10.1146/annurev-conmatphys-020911-125027.

Lumsden, M. D., Nagler, S. E., Sales, B. C., Tennant, D. A., McMorrow, D. F., Lee, S.-H., and Park, S. Magnetic excitation spectrum of the square lattice s=1/2 heisenberg antiferromagnet $k_2v_3o_8$. *Physical Review B*, 74(21):214424, Dec. 2006. doi:10.1103/PhysRevB.74.214424. URL http://link.aps.org/doi/10.1103/PhysRevB.74.214424.

MacDonald, A. H., Girvin, S. M., and Yoshioka, D. t/u expansion for the hubbard model. *Physical Review B*, 37(16):9753, June 1988. doi:10.1103/PhysRevB.37.9753. URL http://link.aps.org/doi/10.1103/PhysRevB.37.9753.

Manousakis, E. The spin-$\frac{1}{2}$ heisenberg antiferromagnet on a square lattice and its application to the cuprous oxides. *Reviews of Modern Physics*, 63(1):1–62, Jan. 1991. doi:10.1103/RevModPhys.63.1. URL http://link.aps.org/doi/10.1103/RevModPhys.63.1.

Marston, J. B. and Affleck, I. Large-n limit of the hubbard-heisenberg model. *Physical Review B*, 39(16):11538, June 1989. doi:10.1103/PhysRevB.39.11538. URL http://link.aps.org/doi/10.1103/PhysRevB.39.11538.

Marston, J. B. and Zeng, C. Spin-peierls and spin-liquid phases of kagomé quantum antiferromagnets. *Journal of Applied Physics*, 69(8):5962, Apr. 1991. ISSN 00218979. doi:doi:10.1063/1.347830. URL http://jap.aip.org/resource/1/japiau/v69/i8/p5962_s1.

Matsukawa, H. and Fukuyama, H. Effective hamiltonian for high-$t_\textc$ cu oxides. *Journal of the Physical Society of Japan*, 58(8):2845–2866, 1989a. doi:10.1143/JPSJ.58.2845. URL http://jpsj.ipap.jp/link?JPSJ/58/2845/.

Matsukawa, H. and Fukuyama, H. Local singlet state in effective hamiltonian for a CuO_2 layer: Case of a single cu spin and a hole. *Journal of the Physical Society of Japan*, 58(10):3687–3697, 1989b. doi:10.1143/JPSJ.58.3687. URL http://jpsj.ipap.jp/link?JPSJ/58/3687/.

Mermin, N. D. and Wagner, H. Absence of ferromagnetism or antiferromagnetism in one- or two-dimensional isotropic heisenberg models. *Physical Review Letters*, 17(22):1133–1136, Nov. 1966. doi:10.1103/PhysRevLett.17.1133. URL http://link.aps.org/doi/10.1103/PhysRevLett.17.1133.

Metropolis, N., Rosenbluth, A. W., Rosenbluth, M. N., Teller, A. H., and Teller, E. Equation of state calculations by fast computing machines. *The Journal of Chemical Physics*, 21(6):1087, June 1953. ISSN 00219606. doi:doi:10.1063/1.1699114. URL http://jcp.aip.org/resource/1/jcpsa6/v21/i6/p1087_s1.

Mourigal, M. *Order and Dynamics of Model Quantum Antiferromagnets*. PhD thesis, École Polytechnique Fédérale de Lausanne, 2011. URL https://infoscience.epfl.ch/record/165768.

Mourigal, M., Enderle, M., Klöpperpieper, A., Caux, J.-S., Stunault, A., and Rønnow, H. M. Fractional spinon excitations in the quantum heisenberg antiferromagnetic chain. *Nature Physics*, 9(7):435–441, July 2013. ISSN 1745-2473. doi:10.1038/nphys2652. URL http://www.nature.com/nphys/journal/v9/n7/full/nphys2652.html.

Muller, J. A15-type superconductors. *Reports on Progress in Physics*, 43(5):641, May 1980. ISSN 0034-4885. doi:10.1088/0034-4885/43/5/003. URL http://iopscience.iop.org/0034-4885/43/5/003.

Müller, G., Thomas, H., Beck, H., and Bonner, J. C. Quantum spin dynamics of the antiferromagnetic linear chain in zero and nonzero magnetic field. *Physical Review B*, 24(3):1429–1467, 1981. doi:10.1103/PhysRevB.24.1429. URL http://link.aps.org/doi/10.1103/PhysRevB.24.1429.

Nomura, T. and Igarashi, J.-i. Analysis of resonant inelastic x-ray scattering in la_2cuo_4. *Physical Review B*, 71(3):035110, Jan. 2005. doi:10.1103/PhysRevB.71.035110. URL http://link.aps.org/doi/10.1103/PhysRevB.71.035110.

Norman, M. R., Ding, H., Fretwell, H., Randeria, M., and Campuzano, J. C. Extraction of the electron self-energy from angle-resolved photoemission data: Application to $bi_2sr_2cacu_2o_{8+x}$. *Physical Review B*, 60(10):7585–7590, Sept. 1999. doi:10.1103/PhysRevB.60.7585. URL http://link.aps.org/doi/10.1103/PhysRevB.60.7585.

Reger, J. D. and Young, A. P. Monte carlo simulations of the spin-1/2 heisenberg antiferromagnet on a square lattice. *Physical Review B*, 37(10):5978–5981, Apr. 1988. doi:10.1103/PhysRevB.37.5978. URL http://link.aps.org/doi/10.1103/PhysRevB.37.5978.

Ronning, F., Shen, K. M., Armitage, N. P., Damascelli, A., Lu, D. H., Shen, Z.-X., Miller, L. L., and Kim, C. Anomalous high-energy dispersion in angle-resolved photoemission

spectra from the insulating cuprate $ca_2cuo_2cl_2$. *Physical Review B*, 71(9):094518, Mar. 2005. doi:10.1103/PhysRevB.71.094518. URL http://link.aps.org/doi/10.1103/PhysRevB.71.094518.

Rønnow, H. M., McMorrow, D. F., and Harrison, A. High-temperature magnetic correlations in the 2d s=1/2 antiferromagnet copper formate tetradeuterate. *Physical Review Letters*, 82 (15):3152–3155, Apr. 1999. doi:10.1103/PhysRevLett.82.3152. URL http://link.aps.org/doi/10.1103/PhysRevLett.82.3152.

Runge, K. J. Finite-size study of the ground-state energy, susceptibility, and spin-wave velocity for the heisenberg antiferromagnet. *Physical Review B*, 45(21):12292–12296, June 1992. doi:10.1103/PhysRevB.45.12292. URL http://link.aps.org/doi/10.1103/PhysRevB.45.12292.

Rønnow, H. M., McMorrow, D. F., Coldea, R., Harrison, A., Youngson, I. D., Perring, T. G., Aeppli, G., Syljuåsen, O., Lefmann, K., and Rischel, C. Spin dynamics of the 2d spin 1/2 quantum antiferromagnet copper deuteroformate tetradeuterate (cftd). *Physical Review Letters*, 87 (3):037202, June 2001. doi:10.1103/PhysRevLett.87.037202. URL http://link.aps.org/doi/10.1103/PhysRevLett.87.037202.

Sandvik, A. W. Stochastic series expansion method with operator-loop update. *Physical Review B*, 59(22):R14157–R14160, June 1999. doi:10.1103/PhysRevB.59.R14157. URL http://link.aps.org/doi/10.1103/PhysRevB.59.R14157.

Sandvik, A. W. and Singh, R. R. P. High-energy magnon dispersion and multimagnon continuum in the two-dimensional heisenberg antiferromagnet. *Physical Review Letters*, 86(3): 528–531, Jan. 2001. doi:10.1103/PhysRevLett.86.528. URL http://link.aps.org/doi/10.1103/PhysRevLett.86.528.

Scalapino, D. J. A common thread: The pairing interaction for unconventional superconductors. *Reviews of Modern Physics*, 84(4):1383–1417, Oct. 2012. doi:10.1103/RevModPhys.84.1383. URL http://link.aps.org/doi/10.1103/RevModPhys.84.1383.

Schilling, A., Cantoni, M., Guo, J. D., and Ott, H. R. Superconductivity above 130 k in the Hg–Ba–Ca–Cu–O system. *Nature*, 363(6424):56–58, May 1993. doi:10.1038/363056a0. URL http://www.nature.com/nature/journal/v363/n6424/abs/363056a0.html.

Singh, R. R. P. Transverse-spin correlations and single-mode approximation for the square-lattice s=1/2 heisenberg model. *Physical Review B*, 47(18):12337–12340, May 1993. doi:10.1103/PhysRevB.47.12337. URL http://link.aps.org/doi/10.1103/PhysRevB.47.12337.

Singh, R. R. P. and Gelfand, M. P. Spin-wave excitation spectra and spectral weights in square lattice antiferromagnets. *Physical Review B*, 52(22):R15695–R15698, Dec. 1995. doi:10.1103/PhysRevB.52.R15695. URL http://link.aps.org/doi/10.1103/PhysRevB.52.R15695.

Singh, R. R. P. and Huse, D. A. Ground state of the spin-1/2 kagome-lattice heisenberg antiferromagnet. *Physical Review B*, 76(18):180407, Nov. 2007. doi:10.1103/PhysRevB.76.180407. URL http://link.aps.org/doi/10.1103/PhysRevB.76.180407.

Sorella, S. Wave function optimization in the variational monte carlo method. *Physical Review B*, 71(24):241103, June 2005. doi:10.1103/PhysRevB.71.241103. URL http://link.aps.org/doi/10.1103/PhysRevB.71.241103.

Syljuåsen, O. F. and Rønnow, H. M. Quantum renormalization of high-energy excitations in the 2D heisenberg model. *Journal of Physics: Condensed Matter*, 12(25):L405, June 2000. ISSN 0953-8984. doi:10.1088/0953-8984/12/25/104. URL http://iopscience.iop.org/0953-8984/12/25/104.

Syromyatnikov, A. V. Spectrum of short-wavelength magnons in a two-dimensional quantum heisenberg antiferromagnet on a square lattice: third-order expansion in 1/s. *Journal of Physics: Condensed Matter*, 22(21):216003, June 2010. ISSN 0953-8984, 1361-648X. doi:10.1088/0953-8984/22/21/216003. URL http://iopscience.iop.org/0953-8984/22/21/216003.

Tanamoto, T., Kohno, H., and Fukuyama, H. Magnetic properties of extended t-j model. i. static properties. *Journal of the Physical Society of Japan*, 62(2):717–730, 1993. doi:10.1143/JPSJ.62.717. URL http://jpsj.ipap.jp/link?JPSJ/62/717/.

Tennant, D. A., Cowley, R. A., Nagler, S. E., and Tsvelik, A. M. Measurement of the spin-excitation continuum in one-dimensional $kcuf_3$ using neutron scattering. *Physical Review B*, 52(18):13368–13380, Nov. 1995. doi:10.1103/PhysRevB.52.13368. URL http://link.aps.org/doi/10.1103/PhysRevB.52.13368.

Tohyama, T. and Maekawa, S. Physical parameters in copper oxide superconductors. *Journal of the Physical Society of Japan*, 59(5):1760–1770, 1990. doi:10.1143/JPSJ.59.1760. URL http://jpsj.ipap.jp/link?JPSJ/59/1760/.

Tohyama, T. and Maekawa, S. Angle-resolved photoemission in high tc cuprates from theoretical viewpoints. *Superconductor Science and Technology*, 13(4):R17, Apr. 2000. ISSN 0953-2048. doi:10.1088/0953-2048/13/4/201. URL http://iopscience.iop.org/0953-2048/13/4/201.

Tranquada, J. M., Heald, S. M., Moodenbaugh, A., and Suenaga, M. X-ray absorption studies of $la_2 - x(ba,sr)_x cuo_4$ superconductors. *Physical Review B*, 35(13):7187–7190, May 1987. doi:10.1103/PhysRevB.35.7187. URL http://link.aps.org/doi/10.1103/PhysRevB.35.7187.

Trivedi, N. and Ceperley, D. M. Green-function monte carlo study of quantum antiferromagnets. *Physical Review B*, 40(4):2737–2740, Aug. 1989. doi:10.1103/PhysRevB.40.2737. URL http://link.aps.org/doi/10.1103/PhysRevB.40.2737.

Tsyrulin, N., Pardini, T., Singh, R. R. P., Xiao, F., Link, P., Schneidewind, A., Hiess, A., Landee, C. P., Turnbull, M. M., and Kenzelmann, M. Quantum effects in a weakly frustrated s=1/2

two-dimensional heisenberg antiferromagnet in an applied magnetic field. *Physical Review Letters*, 102(19):197201, May 2009. doi:10.1103/PhysRevLett.102.197201. URL http://link.aps.org/doi/10.1103/PhysRevLett.102.197201.

Vaknin, D., Sinha, S. K., Stassis, C., Miller, L. L., and Johnston, D. C. Antiferromagnetism in $sr_2cuo_2cl_2$. *Physical Review B*, 41(4):1926, Feb. 1990. doi:10.1103/PhysRevB.41.1926. URL http://link.aps.org/doi/10.1103/PhysRevB.41.1926.

Walters, A. C., Perring, T. G., Caux, J.-S., Savici, A. T., Gu, G. D., Lee, C.-C., Ku, W., and Zaliznyak, I. A. Effect of covalent bonding on magnetism and the missing neutron intensity in copper oxide compounds. *Nature Physics*, 5(12):867–872, Dec. 2009. ISSN 1745-2473. doi:10.1038/nphys1405. URL http://www.nature.com/nphys/journal/v5/n12/full/nphys1405.html.

Wells, B. O., Shen, Z. X., Matsuura, A., King, D. M., Kastner, M. A., Greven, M., and Birgeneau, R. J. E versus k relations and many body effects in the model insulating copper oxide $sr_2cuo_2cl_2$. *Physical Review Letters*, 74(6):964–967, Feb. 1995. doi:10.1103/PhysRevLett.74.964. URL http://link.aps.org/doi/10.1103/PhysRevLett.74.964.

Yamada, K., Kakurai, K., Endoh, Y., Thurston, T. R., Kastner, M. A., Birgeneau, R. J., Shirane, G., Hidaka, Y., and Murakami, T. Spin dynamics in the two-dimensional quantum antiferromagnet la_2cuo_4. *Physical Review B*, 40(7):4557–4565, Sept. 1989. doi:10.1103/PhysRevB.40.4557. URL http://link.aps.org/doi/10.1103/PhysRevB.40.4557.

Yamagata, K., Kozuka, Y., and Morita, T. Magnetization process of nearly 2-dimensional $cu(hcoo)_2{\cdot}4h_2o$ and $cu(hcoo)_2{\cdot}2(nh_2)_2co{\cdot}2h_2o$. II estimation of magnetic parameters. *Journal of the Physical Society of Japan*, 50(2):421–425, 1981. doi:10.1143/JPSJ.50.421. URL http://jpsj.ipap.jp/link?JPSJ/50/421/.

Yan, S., Huse, D. A., and White, S. R. Spin-liquid ground state of the s = 1/2 kagome heisenberg antiferromagnet. *Science*, 332(6034):1173–1176, Mar. 2011. ISSN 0036-8075, 1095-9203. doi:10.1126/science.1201080. URL http://www.sciencemag.org/content/332/6034/1173. PMID: 21527676.

Yokoyama, H. and Ogata, M. Phase diagram and pairing symmetry of the two-dimensional $\mib t$-$\mib j$ \ model by a variation theory. *Journal of the Physical Society of Japan*, 65 (11):3615–3629, 1996. doi:10.1143/JPSJ.65.3615. URL http://jpsj.ipap.jp/link?JPSJ/65/3615/.

Zaanen, J., Sawatzky, G. A., and Allen, J. W. Band gaps and electronic structure of transition-metal compounds. *Physical Review Letters*, 55(4):418–421, July 1985. doi:10.1103/PhysRevLett.55.418. URL http://link.aps.org/doi/10.1103/PhysRevLett.55.418.

Zhang, F. C. and Rice, T. M. Effective hamiltonian for the superconducting cu oxides. *Physical Review B*, 37(7):3759–3761, Mar. 1988. doi:10.1103/PhysRevB.37.3759. URL http://link.aps.org/doi/10.1103/PhysRevB.37.3759.

Zheng, W., Oitmaa, J., and Hamer, C. J. Series studies of the spin-1/2 heisenberg antiferromagnet at t=0: Magnon dispersion and structure factors. *Physical Review B*, 71(18):184440, May 2005. doi:10.1103/PhysRevB.71.184440. URL http://link.aps.org/doi/10.1103/PhysRevB.71.184440.

Bastien Dalla Piazza
Rue St-Laurent 14
1003 Lausanne

Tél. : +41 21 311 88 71
Mobile : +41 77 452 30 82
bastien.dallapiazza@gmail.com

Né le 17 avril 1981
Nationalité suisse

Compétences clés

Aisance à communiquer, plaisir à écouter, expliquer et échanger.
Esprit analytique.
Très bonne expérience de programmation (*C++, Java, Python*).
Expérience de programmation en équipe (*Stage au CERN*).
Langues : Français, langue maternelle ; Allemand, connaissances scolaires ; Anglais parlé et écrit (*Séjour à l'Université de Waterloo, Ontario, Canada*).

Formation

2000–2003	**Études de littérature française, de linguistique et de philosophie.** Université de Lausanne. *Études interrompues après 3 ans.*
2003–2004	**Cours de Math Spécial (CMS)** École Polytechnique fédérale de Lausanne.
2006–2007	**Année d'échange universitaire** University of Waterloo, Ontario, Canada.
2009	**Obtention d'un Master de physique** Section de physique, École Polytechnique Fédérale de Lausanne.
2009–...	**Commencement de la thèse de doctorat en physique** Laboratory for Quantum Magnetism, École Polytechnique Fédérale de Lausanne.

Expériences professionnelles

2000	**Ouvrier en microélectronique (fabrication de quartz).** Micro Crystal, Granges. *6 semaines ; expérience en photolithographie.*
2004	**Service civile : Assistant dans un centre d'aide sociale.** Caritas, Lausanne. *14 semaines.*
2007	**Stagiaire au CERN dans le cadre du "Summer Student Program". Équipe de développement du logiciel d'analyse numérique "ROOT".** Centre Européen de Recherche Nucléaire (CERN). *10 semaines.*
2009	**Service civile : Assistant moniteur dans une institution pour handicappé mentaux** Fondation St-Georges, Yverdon-les-bains. *6 mois.*

Expériences non-professionnelles et hobbies.

2000–2005

Caissier du Choeur des Jeunes de Lausanne.
Membre actif de diverses associations dans le champ de la musique.
Violon et violon alto, chant, choeurs et orchestres.
Pratiquant de divers sports.
Montagne, escalade, judo.